

SEMICONDUCTOR MACROATOMS

Basic Physics and
Quantum-device
Applications

edited by

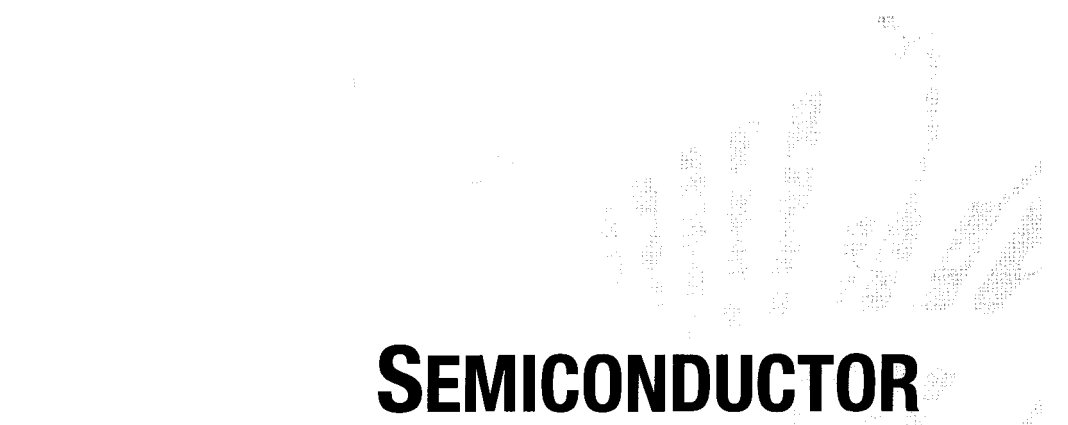
Fausto Rossi

Imperial College Press

SEMICONDUCTOR MACROATOMS

**Basic Physics and
Quantum-device
Applications**

This page intentionally left blank



SEMICONDUCTOR MACROATOMS

Basic Physics and
Quantum-device
Applications

edited by

Fausto Rossi

Politecnico di Torino, Italy

Published by

Imperial College Press
57 Shelton Street
Covent Garden
London WC2H 9HE

Distributed by

World Scientific Publishing Co. Pte. Ltd.
5 Toh Tuck Link, Singapore 596224
USA office: 27 Warren Street, Suite 401-402, Hackensack, NJ 07601
UK office: 57 Shelton Street, Covent Garden, London WC2H 9HE

British Library Cataloguing-in-Publication Data

A catalogue record for this book is available from the British Library.

SEMICONDUCTOR MACROATOMS
Basics Physics and Quantum-Device Applications

Copyright © 2005 by Imperial College Press

All rights reserved. This book, or parts thereof, may not be reproduced in any form or by any means, electronic or mechanical, including photocopying, recording or any information storage and retrieval system now known or to be invented, without written permission from the Publisher.

For photocopying of material in this volume, please pay a copying fee through the Copyright Clearance Center, Inc., 222 Rosewood Drive, Danvers, MA 01923, USA. In this case permission to photocopy is not required from the publisher.

ISBN 1-86094-608-9

Preface

The primary goal of the present volume is to discuss the basic physics of semiconductor macroatoms at the nanoscale as well as their potential application as building blocks for the realization of new-generation quantum optoelectronic devices. The book provides a review state-of-the-art of fabrication and characterization of semiconductor quantum dots aimed at implementing single-electron/exciton devices for quantum information processing and communication. After an introductory chapter on the fundamentals of quantum dots, a number of more specialized review articles will provide a comprehensive picture of this rapidly developing field. More specifically, the strongly multidisciplinary activity presented in the volume includes state-of-the-art nanofabrication and optical characterization, fully microscopic theoretical modeling of non-trivial many-body processes, as well as design and optimization of novel quantum-device architectures. Since most of the scientific activity presented in the book is the result of a number of cross-collaborations within the large-scale European Project *Semiconductor-based implementation of Quantum Information Devices (SQID)* within the *Future and Emerging Technologies (FET)* programme, the volume offers a cohesive perspective on the many research areas involved.

Fausto Rossi

This page intentionally left blank

Contents

<i>Preface</i>	v
1. Fundamentals of Zero-Dimensional Nanostructures	1
1.1 Introduction	1
1.2 Structural Information on Quantum Dots	3
1.3 Single-Particle Electronic States in Quantum Dots	7
1.3.1 Eigenstates in the absence of external perturbations	7
1.3.2 Effect of “external” fields	12
1.3.2.1 Electric field effects	12
1.3.2.2 Magnetic field effects	14
1.3.3 Dot-dot interaction in stacked dots; quantum dot molecules	16
1.4 Optical Properties	17
1.4.1 The idealized quantum dot: a two-level atom. Populations and coherence.	17
1.4.2 Optical properties of dot ensembles. Broadening and selection rules	19
1.4.3 Single dot spectroscopy: the failure of the simple ideas	21
1.5 Phonons and Carrier Coupling to the Phonons in Quantum Dots	26
1.6 Carrier-Carrier Interaction in Quantum Dots	32
1.6.1 Electron-hole interaction in quantum dots	33
1.6.2 Excitonic complexes and optical properties of highly excited quantum dots: new phenomena and a new approach	36

1.6.3 Auger scattering in quantum dots	39
2. Growth and Characterization of Self-Assembled Semiconductor Macroatoms	51
2.1 Introduction	51
2.1.1 Semiconductor quantum dots	53
2.2 Fabrication and Structural Analysis of InGaAs/GaAs Quantum Dots	54
2.3 Nanotechnological Strategies for the Fabrication of Single-Dot Structures	61
2.4 Modeling of the Carrier Wavefunctions	64
2.5 Photoluminescence Experiments	73
2.6 Single-Dot Spectroscopy	78
2.6.1 Wavefunction spectroscopy	78
2.6.2 Optical spectroscopy	85
2.7 Conclusions	92
3. Ultrafast Coherent Spectroscopy of Single Semiconductor Quantum Dots	101
3.1 Introduction	101
3.2 Semiconductor Quantum Dots	104
3.2.1 Interface quantum dots	104
3.2.2 Self-assembled quantum dots	107
3.3 Experimental Techniques	114
3.3.1 Coherent spectroscopy on interface quantum dots . .	115
3.3.2 Coherent spectroscopy on self-assembled quantum dots	119
3.4 Results	123
3.4.1 Coherent control in single interface quantum dots . .	123
3.4.1.1 Ultrafast optical nonlinearities of single interface quantum dots	123
3.4.1.2 Optical Stark effect and Rabi oscillations in a quantum dot: ultrafast control of single exciton polarizations	128
3.4.2 Coherent control in single self-assembled quantum dots	138
3.5 Outlook	143
4. Few-Particle Effects in Semiconductor Macroatoms/Molecules	151

4.1	Introduction	151
4.2	Excitons	152
4.2.1	Semiconductors of higher dimension	152
4.2.2	Semiconductor quantum dots	153
4.2.2.1	Weak confinement regime	153
4.2.2.2	Strong confinement regime	154
4.2.3	Spin structure	155
4.3	Biexcitons	157
4.3.1	Weak confinement regime	157
4.3.2	Strong confinement regime	158
4.4	Few-Particle States	159
4.4.1	Multi excitons	160
4.4.2	Multi-charged excitons	161
4.4.3	Configuration interactions	161
4.5	Optical Spectroscopy	162
4.5.1	Excitons and biexcitons	163
4.5.1.1	Weak confinement regime	163
4.5.1.2	Strong confinement regime	164
4.5.2	Multi excitons	165
4.5.3	Multi-charged excitons	167
4.6	Inter-dot Coupling: Tunneling <i>vs.</i> Coulomb Correlations	167
4.7	Inter-Dot Coupling: Role of the Electric Field	175
5.	Electron-Phonon Interaction in Semiconductor Quantum Dots	183
5.1	Introduction	183
5.2	Energy Relaxation in Bulk and Quantum Well Structures .	185
5.3	Magneto-Absorption in Quantum Dots: the Evidence of Polaron	192
5.4	Energy Relaxation in the Polaron Framework	207
5.5	Excitonic Polaron in Quantum Dots	209
5.6	Diagonal Non-Perturbative Interaction Between Electrons and Acoustic Phonons	212
5.7	Conclusions	215
6.	Phonon-Induced Decoherence in Semiconductor Quantum Dots	221
6.1	Introduction	221
6.2	Model for Phonon-Induced Pure Dephasing	224

6.3	Analytical Results for Excitations with Ultrafast Pulses	226
6.3.1	Linear single-dot spectra	227
6.3.2	The initial decay of four-wave-mixing signals	230
6.3.3	Impact of pure dephasing on electronic and phononic occupations	234
6.4	Influences of Temporal and Spectral Properties of the Laser Excitation on the Decoherence	237
6.4.1	Phonon-induced damping of Rabi oscillations in quantum dots	237
6.4.2	Optimal gating strategy: a trade-off between different types of decoherence	241
6.5	Conclusions	244
7.	All-Optical Schemes for Quantum Information Processing with Semiconductor Macroatoms	249
7.1	Introduction	249
7.2	All-Optical Quantum Information/Computation with Semiconductor Macroatoms	252
7.2.1	Single-dot encoding schemes	252
7.2.2	Coupled-dot encoding schemes	257
7.2.2.1	GaAs-based quantum hardware	257
7.2.2.2	GaN-based quantum hardware	262
7.2.3	Combination of charge and spin degrees of freedom	268
7.2.3.1	Artificial molecules as qubits and Raman adiabatic passages for the optical gating	271
7.3	Summary and Conclusions	278
8.	Novel Devices for the Measurement of Electronic States in Semiconductor Quantum Dots	283
8.1	Introduction	283
8.2	Field-Induced Exciton-Exciton Coupling in Semiconductor Quantum Dots with no Intrinsic Bias	286
8.3	Modeling Few Particle Interactions in Quantum Dots with Intrinsic Bias	294
8.3.1	Engineering electronic structure and optical spectrum in coupled GaN quantum dots	294
8.3.2	Semi-analytical model	297
8.3.2.1	Single exciton system	298

8.3.2.2 Biexciton system	299
8.4 Semiconductor Double Quantum Dot as Storage Qubit	303
8.4.1 Definition	303
8.4.2 Measurement using a STIRAP process	305
8.4.2.1 Failure of the adiabatic condition	308
8.4.2.2 Failure of the energy conservation requirement	310
8.5 All-Optical Read-Out Device	311
<i>Index</i>	317

This page intentionally left blank

Chapter 1

Fundamentals of Zero-Dimensional Nanostructures

G. Bastard

Laboratoire Pierre Aigrain

Ecole Normale Supérieure

24 rue Lhomond F75005 Paris, France

and

INFM National Nanotechnology Laboratory (NNL)

Dipartimento di Ingegneria dell'Innovazione

Università degli Studi di Lecce

via Arnesano, 73100 Lecce, Italy

E. Molinari

INFM Center on nanoStructures and bioSystems at Surfaces (S3)

Dipartimento di Fisica, Università di Modena e Reggio Emilia

Via Campi 213/A, 41100 Modena, Italy

1.1 Introduction

As discussed in Chapter 7, quantum computing is based on our ability to manipulate the quantum superpositions of the eigenstates of an observable which otherwise, i.e. non manipulated, would follow the quantum evolution dictated by Schroedinger's equation [Loss and DiVincenzo (1998)]. Unfortunately, the quantum subsystem performing the computation undergoes random inelastic interactions with its surrounding. These may be very detrimental to quantum computation since they end up replacing the useful but fragile quantum superpositions with very robust statistical mixtures, which however wipe out the eigenstates interference processes and bring

the system back to a stage where it can only produce classical computing. This is why implementing quantum computing in the solid state seems to be self-contradictory at first sight: the requirements for a pure quantum evolution demand the computational variables to be very well buffered from all the other variables (as e.g. realized in atomic physics [Bouwmeester *et al.* (2000)]), while it is well known that solid state is the realm of the intertwining between elementary interactions: electrons interact with phonons, magnons, with other electrons, and so on.

For this reason it has been argued that the use of orbital electronic variables to achieve quantum computation in the solid state requires the most drastic size quantization, the one found in zero-dimensional objects, the so-called “quantum dots” (QDs), where the electrons (holes) are localized in the three directions of space [Woggon (1997); Jacak *et al.* (1998); Bimberg *et al.* (1999)]. The reduction in the phase space so obtained would decrease the role of the interactions with the surrounding, and hopefully make QDs resemble atomic systems – hence their name “macroatoms” [Kastner (1993); Ashoori (1993); Gammon (2000)] – particularly in the context of quantum computation.

In this introductory chapter, we propose a bird’s eye view of the material properties of the semiconductor QDs which hopefully will be used to implement actual quantum bits and gates based on all-optical control. Our aim is firstly to provide the reader with material facts regarding the structural and electronic properties found in QDs, as well as the interactions of the QD electrons with their surrounding. Our second goal is to compare these facts with the predictions of the “macroatomic model”. The chapter is organized as follows. In Section 1.2, we outline the structural properties of quantum dots; we then describe the single-particle electronic states in Section 1.3 and outline the basics of QDs’ optical properties in Section 1.4. In Section 1.5 we discuss the phonons and the electron-phonon interaction in QDs, while the interaction among carriers will be dealt within Section 1.6.

Although most of the considerations which follow are fairly general, we shall concentrate on strongly confined self-organized dots, such as the Ga(In)As/GaAs ones, since these are among the QDs which look most promising for achieving optically-controlled elementary quantum logics operations.

1.2 Structural Information on Quantum Dots

The spontaneous formation of Ga(In)As islands on GaAs was discovered [Kastner (1993)] as a failed attempt to grow by Molecular Beam Epitaxy (MBE) sufficiently thick InAs quantum wells embedded in a GaAs barrier. The lattice mismatch between InAs and GaAs is $\cong 7\%$. As a result, the coherent two-dimensional growth of strained InAs films on a GaAs substrate accumulates elastic energy. The 2D growth proceeds until this energy exceeds the one required to form a dislocation in a relaxed InAs layer. In the InAs/GaAs system this happens when the InAs thickness exceeds $\cong 1.8$ monolayer (roughly 0.5 nm). By suitably controlling the growth parameters (substrate temperature, elemental fluxes of Ga, In, As) islands of InAs or Ga(In)As are formed on the GaAs substrate. The islands are subsequently covered by GaAs (see Figure 1.1a; for reviews see e.g. [Bimberg *et al.* (1999); Zrenner (2000); De Giorgi *et al.* (2003)]). Then, one may iterate the process and grow a second layer of QDs, which may form vertical stacks owing to strain-induced alignment (see Figure 1.1b). An interesting property of this sort of growth is that one can, in principle, vary the separation between the dot planes at will, from zero to several tens of nanometers, thereby spanning a wide range of electronic coupling between vertically aligned dots, from very strong coupling to no vertical coupling at all (see below).

Control of vertical and lateral position of QDs is pursued by growth on patterned substrates with different types of modulations, or by locally modulating the potential by nano-stressors (for a brief review see [Zrenner (2000)]). A class of very interesting systems for optics is represented by dots grown at the apex of inverted pyramids obtained at the intersections of V-grooves [Hartmann *et al.* (2000)].

Nanocrystallites (often made of II-VI semiconductors such as CdS) are dots embedded into a glass or oxide matrix [Woggon (1997); Klimov (2000)]. Compared to self-organized dots, nanocrystallites suffer from much worse interfaces as far as their optical properties are concerned. They are usually smaller (hence display larger size quantization) and easier to produce, but their unsolved interface problem has a very detrimental consequence on their emission property which is known as the *blinking effect* [Shimizu *et al.* (2001)]. This consists in uncontrollable interruptions of the light emission for very long time intervals. At the time of this writing, it seems that nanocrystallites are not well suited to optically controlled quantum logics applications.

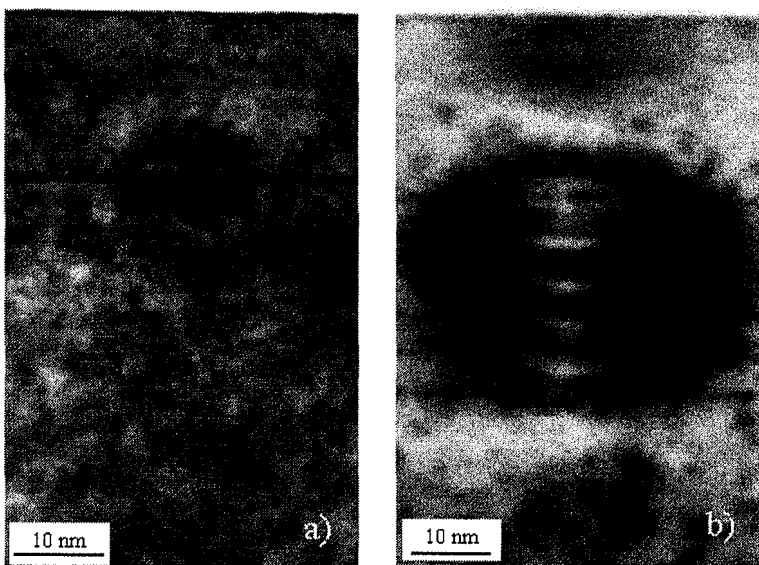


Fig. 1.1 Cross-sectional low-magnification TEM images of a MOCVD grown Ga(In)As/GaAs single dot sample (a) and of a non uniform vertically stacked dot heterostructure (b). Note the anomalous increase of the lateral dot size in (b). Adapted from [De Giorgi *et al.* (2003)].

Self-organized Ga(In)As/GaAs QDs are often lens-shaped or look like truncated pyramids with well defined facets. In a first approximation, lens-shaped dots are modeled by truncated cones (see Figure 1.2) with a small aspect ratio ($h/R \leq 0.3$, with height h , radius R). These dots are thus *very flat* objects and that, as discussed later, has a strong influence on their electronic structure. One should also point out the existence of a Ga(In)As “wetting layer” below the QDs (see Figures 1.1 and 1.2), which is one monolayer thick ($\cong 0.28$ nm) in (nominally) InAs/GaAs dots, but is $\cong 1.2$ nm thick in $\text{Ga}_{0.5}\text{In}_{0.5}\text{As}/\text{GaAs}$ dots [Crozier *et al.* (2001)]. The wetting layer is the source of effective decoherence mechanisms: the electrons moving in the wetting layers are close to the dots and have intermediate energy between bound electron states of the dots and the three-dimensional barrier-like states. The wetting layer states therefore play an important part in electronically connecting the dot to its surrounding.

There have been controversies on whether the In concentration is constant or not in the Ga(In)As dots (see below) and whether or not the interfaces between the QDs and the barrier is sharp. Fry *et al.* [Fry

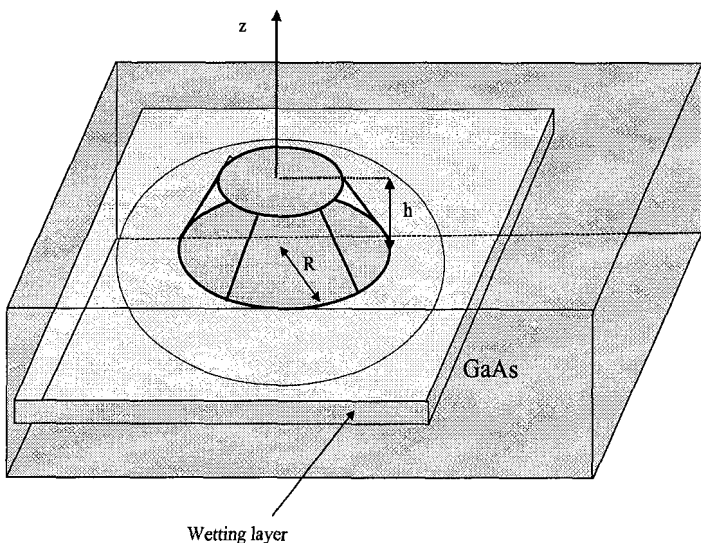


Fig. 1.2 Schematic representation of a single Ga(In)As/GaAs single quantum dot.

et al. (2000)] provided convincing evidence that there exists a pronounced vertical In gradient in (nominally) InAs/GaAs dots, while Crozier *et al.* [Crozier *et al.* (2001)] found little evidence of this vertical grading in (nominally) $\text{Ga}_{0.5}\text{In}_{0.5}\text{As}/\text{GaAs}$ dots. It appears therefore that care has to be exercised when trying to generalize a finding on a given dot to all the other dots.

Considerable strain exists in a Ga(In)As QD and even in the surrounding GaAs barrier (see e.g. [Bimberg *et al.* (1999); De Giorgi *et al.* (2003)]). Again, the exact strain profile should depend on the size, composition, growth conditions, etc. of the dot. Even though the vertical growth may occur along the [001] direction, which is a non piezoelectric direction, the lateral sides of the dot are not parallel to non piezoelectric directions, which implies that strain affects the electronic states via the piezoelectric effect (see e.g. [Stier *et al.* (2000); Williamson and Zunger (1999)]). The piezoelectric field is not homogeneous in the dot and, once again, one must accept that there exist considerable uncertainties regarding the shape and value of the piezoelectric field in actual QDs.

Ga(In)As/GaAs QDs are nominally undoped, which means that in practice a residual p-type doping ($N_A \leq 10^{14} \text{ cm}^{-3}$) takes place in MBE grown

samples and a residual n-type doping ($N_D \leq 10^{16} \text{ cm}^{-3}$) takes place in Low Pressure Metal Organic Chemical Vapour Deposition (LP-MOCVD). In a given charging configuration of the impurities, the residual doping affects very little (a small rigid shift) the lowest lying electronic states of the QDs because they are discrete. The QD situation thus contrasts with that of bulk or quantum well materials, where static impurities in a fixed charge state efficiently scatter the mobile carriers. Note however that a static impurity configuration should not alter the coherence properties of the dots. Nevertheless, residual doping may actually be very detrimental to the coherence lifetimes of the QD optical transitions, because doping introduces electron (hole) traps which may fill and empty during time, thereby changing the electrostatic configuration around a dot (see e.g. [Jankovics *et al.* (2004)]). Thus, residual impurities provide a source of time dependent random electric fields which act on the dot electrons. In doing so they introduce an extra time scale in the QD electronic response which is the typical time it takes to change the electrostatic configuration around one quantum dot. In the limit where this time is much longer than the radiative recombination time, one obtains the *spectral wandering* phenomenon. It consists in a random variation of the QD fundamental transition energy in time, due to the long lived different available electrostatic configurations around the dot. In the limit where one or some of these configurations effectively correspond to no recombination at all, one obtains the blinking effect which is so prevalent in the nanocrystallites.

It is possible to dope the Ga(In)As/GaAs dots selectively at will and thus to store permanently and on purpose electrons (holes) in the dots in a controlled fashion. This is achieved by means of modulation doping of the GaAs barrier, either by inserting a plane of Si (for n-type doping) or a plane of Be (for p-type doping) at some distance D from the dot plane. Residual doping gives also rise to an unintentional loading of the dots by electrons (residual n-type) or holes (residual p-type). The extra electrons (holes) transfer to the dot until (at thermal equilibrium) the dot chemical potential lines up with that in the GaAs barrier. By adjusting D and the concentration of the dopants, one may store from 0 to 6 electrons and from 0 to several holes in (nominally) InAs/GaAs QDs. Note however that the dot storage is only an average value because there exist dot-to-dot fluctuations of the QD charging. This has very detrimental effects on the “quality” of the optical response of these ensemble of charged dots, the broadening being increased with average dot charging. Needless to say, the time dependent trapping/release of charges in the doped dots can very efficiently limit the

coherence of the QD optical transitions.

A controllable (average) loading of the dot by electrons has been achieved in a dot plane [Hartmann *et al.* (2000); Warburton *et al.* (2000); Findeis *et al.* (2001); Fricke *et al.* (1996)], e.g. by inserting it into a M-I-S structure and biasing it (see Figure 1.3). In Reference [Warburton *et al.* (2000)], for example, the capacitance–voltage curves $C(V)$ have revealed the progressive loading of the InAs dots by up to 6 electrons. This useful technique has, however, the drawback of being limited to a single dot plane (to get as homogeneous a doping as possible), which often leads to very small optical absorption.

One of the main sources of troubles associated with self-organized QDs is their size fluctuation. It is clear that one cannot expect that the millions of dots which have spontaneously grown on a substrate will all have the same size (or even the same shape and/or composition). There are fluctuations. This implies that any measurement performed on a *dot ensemble* will display inhomogeneous broadening. Just because the QDs are of nanometric size, this broadening is very significant on the energy scale because the various dots involved in the measurements display quite different electronic spacing. The size distribution of the dots has often been found to be a single Gaussian. Obviously, *single dot* experiments [11] are free of these inhomogeneous broadening effects but they are more involved than those performed on dot ensembles. There is also the risk that measuring a single dot will by misfortune provide information which is not representative of the average properties. Thus, single dot measurements are actually repeated on many different dots to minimize this risk.

Finally, let us mention that the areal density of dots is sufficiently small in $(\text{Ga}, \text{In})\text{As}/\text{GaAs}$ systems (usually in the range $4\text{--}5 \times 10^{10} \text{ cm}^{-2}$) to neglect (on the average) any lateral electronic coupling between QDs. Of course, when performing experiments which involve only few dots, it may well happen that two dots are much closer than the average dot-to-dot distance, and the question of lateral “dot molecules” may show up.

1.3 Single-Particle Electronic States in Quantum Dots

1.3.1 *Eigenstates in the absence of external perturbations*

The GaAs bandgap (≈ 1.5 eV) is much larger than the InAs one (≈ 0.4 eV). Hence, it is expected (and actually observed) that electrons and holes will be confined in the InAs dot in a InAs/GaAs structure. Further, the

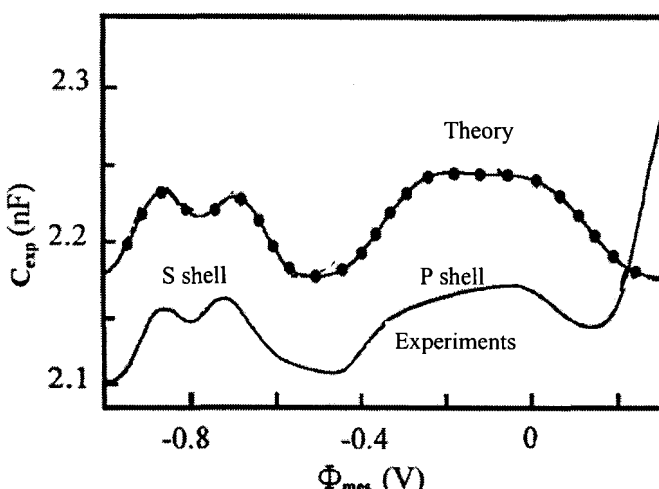


Fig. 1.3 Capacitance/Voltage characteristics of a single (nominally)InAs/GaAs QD plane inserted into a M-I-S structure. The S shell splitting corresponds to a Coulomb energy of ≈ 25 meV. Adapted from [Fricke *et al.* (1996)].

nanometric size of the QDs suggests that their lowest lying electron (hole) states may be discrete and sufficiently well separated from the excited states to make the dots resemble “artificial atoms” or macroatoms. This is nothing but a three-dimensional size-quantization effect. Actually, it turns out that the energy separation between the ground and (discrete) first excited states is not in the eV range like in atoms, but rather falls in the 30–50 meV range in typical (Ga,In)As/GaAs QDs. This is insufficient to prevent thermal population of excited levels at room temperature, and provides a first limitation to the macroatomic model. On the other hand, operating at cryogenic temperatures ($T \approx 10$ K) on the ground state makes the dot properties nearer to the atomic ones. Note that the very existence of discrete states is not warranted by the nanometric size of the dots, since a 3D attractive potential with finite range may fail to support bound states if the confining volume is too small. It is now firmly established that there exist at least three orbital bound states for electrons in (nominally) InAs/GaAs dots, and probably as many holes. As it often occurs, the hole levels are less documented than the electron ones.

Like for other heterostructures, one can attempt to solve the one-electron Schrödinger equation either using the bulk band structure of the hosts material [Stier *et al.* (2000); Jiang and Singh (1997); Pryor (1998);

Stier (2001)] and matching the solutions inside and outside the dot by appropriate boundary conditions (envelope-function approximation), or in real space using an adequate parametrization of the electronic properties of each of the atoms (empirical tight binding [Lee *et al.* (2001)] or pseudopotentials [Williamson and Zunger (1999); Zunger (2002)]). Both kinds of methods should give the same results for actual dots and, in fact, granted the usual uncertainties on the material parameters, both approaches coincide (to our knowledge) when it is meaningful to compare them. It is clear that atomic-like approaches are ideally suited to handle the case of very small dots (e.g. the CdS dots embedded in a glass matrix) while they become numerically cumbersome and physically less transparent than the envelope function approach in the case of larger dots. Very refined dot calculations by means of the bulk band structure have been performed e.g. by Stier *et al.* [Stier *et al.* (2000); Stier (2001)] while accurate atomistic approaches are due to Zunger *et al.* [Williamson and Zunger (1999); Zunger (2002)] and by Lee *et al.* [Lee *et al.* (2001)]. These numerical methods (of both types) are very time-consuming since they attempt to describe finely most of the electronic spectrum of a dot.

In the following, we shall use a cruder but simpler analysis which still allows understanding of the key phenomena of interest. Our approach will be to discard the atomic variations of the host materials and to focus our attention on the slowly varying envelope functions. In addition, we shall retain a single band in our approach. As applied to the conduction band states of the dots, this method states that the conduction band envelope functions are the solutions of a scalar effective Schrödinger equation:

$$\left(\frac{p^2}{2m^*} + V(\vec{r}) \right) F_c(\vec{r}) = \varepsilon F_c(\vec{r}). \quad (1.1)$$

Note that this equation is the limiting case of the more precise multi-band envelope function used in quantum wells and quantum wires (see e.g. [Bastard *et al.* (1991)]) and by Stier *et al.* in QDs [Stier *et al.* (2000); Stier (2001)]. In Eq. (1.1) $V(\vec{r})$ is the sum of the dot confining potential and of the so called “external” perturbations. The former is zero inside the dot and equal to the conduction band discontinuity in the barrier (neglecting any grading). The latter includes the effects of fields that are indeed external to the dot, e.g. a magnetic field or an electric field (such as realized by inserting the dot plane in the intrinsic part of a reversed biased p-i-n junction), but may also result from built-in polarization charges (piezoelectric fields).

A practical way to compute the electron states in a dot consists of writing $V(\vec{r})$ in the separable form

$$V(\vec{r}) = V_{\parallel}(z) + V_{\perp}(\rho), \quad \rho = (x, y), \quad (1.2)$$

where $V_{\perp}(\rho)$ is taken as a parabolic potential (isotropic 2D oscillator)

$$V_{\perp}(\rho) = \frac{1}{2}m * \Omega^2 \rho^2 \quad (1.3)$$

and $V_{\parallel}(z)$ is e.g. a square-well potential describing the vertical confinement. Here m^* is the effective mass of the carrier under consideration. Under such circumstances, the eigenvalues of Eq. (1.1) are

$$\varepsilon = \varepsilon_n + (n_x + n_y + 1)\hbar\Omega \quad n_x, n_y = (0, 1, 2, \dots), \quad (1.4)$$

where, in (nominally) InAs/GaAs dots, there is only a single bound state for the vertical motion: $n = 1$ due to the small height of the actual dots. If we set $N = n_x + n_y$, the eigenvalues labeled by N are $(N + 1)$ fold degenerate. The envelope eigenfunctions associated to the eigenvalues (1.4) are

$$F_c(\vec{r}) = \chi_1(z)\varphi_{n_x}(x)\varphi_{n_y}(y), \quad (1.5)$$

where φ_p is the p^{th} Hermite function of a one-dimensional harmonic oscillator with angular frequency Ω . Instead of Cartesian coordinates, one may wish to emphasize the rotational invariance around the z axis labeling the eigenstates by means of the eigenfunctions of L_z , the z projection of the pseudo-angular momentum along the growth axis.¹ Then for an isotropic parabolic confinement and the same z confinement as above one gets

$$F_c(z, \rho, \theta) = \chi_1(z)g_N(\rho)e^{im\theta}; L_z |F_c\rangle = m\hbar |F_c\rangle. \quad (1.6)$$

In this cylindrically symmetric approach, the labeling of the eigenstates in terms of m is appealing since it calls for using the well-known atomistic notation. Notice however that we deal in the Ga(In)As/GaAs dots with *flat* atoms (only L_z is a good quantum number). So, neglecting spin variables, one finds S, P, D, ... shells corresponding to $m = 0, \pm 1, \pm 2$ respectively. A typical energy separation in (nominally) InAs/GaAs dot is 40 meV. Holes are much less documented but have apparently smaller

¹The pseudo-angular momentum acts on envelope functions while the angular momentum acts on the complete wave functions. The pseudo-angular momentum may commute with the effective Hamiltonian. The angular momentum never commutes with the complete dot Hamiltonian.

energy separations. Taking into account the spin degeneracy, the ground S shell becomes filled with 2 electrons, the next shell is a P one which can accommodate 4 electrons. It is not clear whether at zero magnetic field a D shell may be bound. So as mentioned above, one can load 6 electrons in typical (nominally) InAs/GaAs dots [Warburton *et al.* (2000)].

The 2D parabolic confinement has often been used because it allows to include analytically the effect of a vertical external magnetic field on the single-particle eigenstates (giving rise to the Fock-Darwin states), thereby forming a convenient basis to handle electron-electron interactions. Its accuracy is however limited to qualitative discussions since far-infrared magneto-optical data [Fricke *et al.* (1996); Hameau *et al.* (1999)] have shown that the P states of the conduction band are split even at zero magnetic field by symmetry-breaking effects, the dots being elongated. A typical zero field splitting of 3–4 meV has been measured in (nominally) InAs/GaAs dots between P_X and P_Y states where (X, Y) labels the orientations respectively. This is comparable to the typical exchange energy between two electrons bound to the dot.

Much less is known for holes. Due to the degeneracy of the bulk valence band edge and to the large spin-orbit coupling, the effective hole Hamiltonian is not a scalar but a 4×4 matrix corresponding to the pseudo total angular momentum $J = 3/2$ [Bastard *et al.* (1991)]. The three-dimensional (3D) confinement specific to quantum dot structures prevents that one can find a quantization axis for J where the effective Hamiltonian would be diagonal. So one should either turn to numerical solutions of the effective Hamiltonian matrix or make approximations. In the most simplified approach, the lowest lying hole states are taken as heavy hole-like ($m_J = \pm 3/2$). The rationale behind this approximation (besides convenience) is that the size quantization on the one hand and the stress effects on the other hand, split the light hole and the heavy hole levels by a large energy ($\cong 100$ meV or so), the light hole series of states starting at higher energy than the heavy hole one. If one accepts this first order description, the heavy hole states are the solution of an effective Schrödinger equation like Eq. (1.1), but with an anisotropic effective mass: $m_x = m_y < m_z$ (the so-called mass-reversal effect). In spite of the light hole level repulsion above the heavy hole levels one cannot expect a zero valence band mixing in the valence envelope functions of actual QDs. Indeed, clear cut absorption experiments [32] performed in wave-guide geometry have shown that the lowest lying hole state is indeed predominantly heavy hole like, as expected, but does possess a non zero ($\approx 10\%$) light hole admixture.

As mentioned above, there exists a 2D electronic continuum located at energies between the QD discrete states and the bulk-like states of the surrounding matrix. This continuum is associated with the wetting layer below the dot. The wetting layer can be considered as a very thin quantum well merging with the dot at the dot base. It shows up in the photoluminescence spectra as a relatively broad line below the GaAs-related optical features. Very far away from the dot, the wetting layer states look like plane waves for the in-plane motion and like the ground state of a narrow quantum well for the vertical motion. However, the dot is a huge perturbation to this idealized picture of factorized wave functions, and at least orthogonalized plane waves to the bound dot states have to be used instead of plane waves to cope with the problem.

The wetting layer plays a decisive part in all the non-resonant inter-band optical spectroscopies of QDs, since the QD emission is fed by the carriers created in this continuum which have first to be captured by the dots. Subsequently, relaxation down to the QD first excited state takes place before the QD light emission brings the dot to its ground state. The wetting layer is also expected to play an important part in some of the decoherence aspects of the QD-related emission line. This is because such a thin quantum well such as the wetting layer contains many defects. These defects can store, permanently or not, charges which can randomly affect the dot. Even in a perfect wetting layer, the moving carriers lose their coherence very quickly (on a sub-ps time scale). In turn, these incoherent carriers can affect (by Auger effect, see below) the carriers bound to the dot, thereby limiting again the lifetime of the QD inter-band coherence.

1.3.2 *Effect of “external” fields*

1.3.2.1 *Electric field effects*

Piezoelectric fields have a strong effect on the lower lying hole states (which are predominantly heavy hole-like). In particular it was shown that the ground hole state is shifted toward the corners of truncated pyramids with well-defined facets [Klimov (2000); Jankovics *et al.* (2004); Bastard *et al.* (1991)] while the much lighter electrons are quite insensitive to these effects and display a ground envelope function which is quite centered in the dot. Such a feature has obvious implications on the optical properties (a weakening of the ground transition). It also influences the coupling of the optically created electron-hole (e-h) pair to the opti-

cal phonons [Stier *et al.* (2002)]. The lens shaped dots appear much less sensitive to this piezoelectric field effect.

As mentioned previously, a vertical In grading was convincingly deduced by Fry *et al.* [Fry *et al.* (2000)] in (nominally) InAs/GaAs QDs from the Stark effect displayed by the ground inter-band transitions of a dot ensemble. If a constant and homogeneous electric field F is applied parallel to the growth (z) direction, one expects a *linear* Stark effect to take place at small enough electric fields in QDs [De Giorgi *et al.* (2003); Lelong and Bastard (1996); Vasanelli *et al.* (2001); Vasanelli *et al.* (2002a)]. This contrasts with the quantum well case and occurs because the confining potential in the dot lacks an inversion center. Since there are two different particles involved in the optical transition, there is no possibility that one might cancel this effect by an appropriate shift of the origin of the electrostatic potential. In other words, one expects to find an inter-band transition energy $\hbar\omega$ which will vary with field like

$$\hbar\omega(F) = \hbar\omega(0) - FD_z; D_z = e(\langle z_h \rangle - \langle z_e \rangle); e > 0, \quad (1.7)$$

where D_z is the zero-field electron-hole dipole. The z axis is directed from the basis to the top of the QD. D_z was always calculated to be negative in Ga(In)As dots (essentially because the hole is a heavier particle than the electron and is therefore nearer to the potential minimum). Hence, the expectations were that the ground inter-band transition energy would increase linearly with F . The reverse effect was observed, which led Fry *et al.* [Fry *et al.* (2000)] to conclude that the electron-hole dipole was inverted, the most likely cause of this effect being an In grading inside the dot. To account for the observed features Fry *et al.* had to invoke a strong In depletion near the apex of the dots.

To conclude with the vertical Stark effects, let us stress that they necessarily lead to small shifts [De Giorgi *et al.* (2003); Lelong and Bastard (1996); Vasanelli *et al.* (2001); Vasanelli *et al.* (2002a)] because the dots are rather flat objects. For a field of 10kV/cm one finds a linear Stark shift of 0.3 meV for an already very large electron-hole separation of 0.3 nm. Of course, when increasing the electric field strength, a negative term, quadratic in F , should be added to $\hbar\omega(F)$ to account for the *induced* dipoles. This means that the transition energy versus F will have a maximum for a negative value of the field (again if the electron-hole dipole is positive) and will decrease monotonically with increasing field if $F>0$. Efforts have been made to infer the In grading from the magnitude of the Stark shifts

[Vasanelli *et al.* (2002a)]. All the simulations point to very large modulations of the conduction band edge inside the dot.

Lateral electric fields are expected to redshift more significantly the ground electron, hole and thus inter-band optical transitions in a QD than a vertical field of the same magnitude because the dots are broader than high. The physics is the same as in quantum wells, i.e. that of field-induced dipoles. For circular dots the zero field average in plane separation between electron and hole is zero in the ground and excited states. Thus, there can only exist quadratic Stark shifts. For non-circular dots a linear Stark effect should show up and, in addition, one can expect anisotropic Stark shifts for excited states. Lateral Stark effects of a few dots sample were measured by Rinaldi *et al.* [Rinaldi *et al.* (2001)]. These dots were inserted in a sub-micron gap opened in a metallic contact. They were substantially less confining than the self-organized ones (the lateral confinement was provided by stressors). Stark shifts larger than 1 meV were observed for fields of only 2 kV/cm, showing the expected enhanced polarizability of the eigenstates by a lateral field compared to a vertical one. However, it is difficult to disentangle the part played by the smaller confinement (which also enhances the Stark effect) from that arising from a lateral size being bigger than the vertical one.

1.3.2.2 Magnetic field effects

An external magnetic field is known to completely reorganize the electronic spectrum of bulk or quantum well structures. This leads to spectacular physical phenomena such as the quantum Hall effect. The application of a magnetic field parallel to the growth axis of a quantum well structure changes the 2D continuum attached to each of the bound levels for the z motion into a series of evenly spaced discrete energies, separated by the cyclotron energy $\hbar\omega_c = \hbar\frac{eB}{m^*}$. These energies are however macroscopically degenerate.

In QDs with nanometric sizes, the strong quantization at zero field prevents such a reorganization. Actually, like in atoms, the orbital effects of a constant magnetic field, the Zeeman effects, can be treated as perturbations. Within such a perturbative approach, assuming a circular symmetry and for $B // z$, one finds the S states shift quadratically with B (diamagnetic shift) while the P states become split by $\hbar\omega_c$ (orbital Zeeman effect). It is not difficult to work out the B dependence of the P states in anisotropic

dots. One finds [Hameau *et al.* (1999)]

$$\varepsilon_{P\pm} = \langle \varepsilon_P \rangle \pm \frac{1}{2} \sqrt{\delta^2 + \hbar^2 \omega_c^2} + \gamma_P B^2, \quad (1.8)$$

where $\langle \varepsilon_P \rangle$ is the average energy of the P shell at $B = 0$, δ is the zero field splitting and γ_P the diamagnetic coefficient. Note that even at 25 T the diamagnetic contribution to the S-P transition energy is only a few meV's [Hameau *et al.* (1999)]. This has to be compared with an orbital Zeeman splitting of ≈ 42 meV. In experiments performed on a dot ensemble, the zero field splitting is visible only if all (or most of) the dots display the same anisotropy, otherwise a random anisotropy contributes only to a line broadening. This is why the observation of such an anisotropy in the far-infrared light absorption associated with S-P transitions (with a 100% linearly polarised absorption along the x and y directions) allows us to conclude that the (nominally) InAs dots are, as a rule, elongated (along the [1,-1,0] direction). Note that a morphological deformation seems the most likely explanation to the data, but the experiments could as well be interpreted by assuming that all (or most of) the dots experience an extra potential energy which contains a large d-like component capable of supplying the $2\hbar$ difference between the P_+ and P_- components (i.e. varies like $\cos 2\theta$ or $\sin 2\theta$, where θ is the polar angle). There is no report on a correlation between the magnitude of the $P_+ - P_-$ splitting at zero field and the energy distance $\langle \varepsilon_P \rangle - \varepsilon_S$.

Information on the conduction band effective mass can be extracted [Fricke *et al.* (1996); Hameau *et al.* (1999)] from the orbital effect of the S-P transition since

$$(\varepsilon_{P_+} - \varepsilon_S) - (\varepsilon_{P_-} - \varepsilon_S) \approx \frac{\hbar e B}{m^*} \quad \text{if} \quad \frac{\hbar e B}{m^*} \gg \delta. \quad (1.9)$$

Lens-shaped (nominally) InAs/GaAs quantum dots with an average S-P energy separation of 40–50 meV display an orbital Zeeman effect which corresponds to $m^* \approx 0.07 m_0$. This mass is much closer to the GaAs mass than to the InAs one at the conduction band edge. Aside from grading effects, we note that it is not too far from what one would expect from the known band non-parabolicity of InAs and the large electron confinement in these QDs.

To conclude this section we just mention that magnetic fields with a component that is not parallel to the growth directions are much more complex to deal with since all the symmetries are broken, and must be

treated numerically. They may, however, be relevant in the present context since they can effectively induce a modification in the barrier between stacked dots (see below). For details see e.g. [Bellucci *et al.* (2004)].

1.3.3 Dot-dot interaction in stacked dots; quantum dot molecules

So far we have sketched what can happen to carriers of a single dot, arguing that most of the QDs within a dot plane are independent. The dots can, however, be very effectively stacked vertically due to the strain field which exists around an already grown dot. This strain field actually favors the growth of a second dot at the vertical of the first one. So columns of dots (up to 7–10) can successfully be grown in this manner (see Figure 1.1). The lateral size of the dots grown vertically is not constant but increases slightly with increasing height. As mentioned, the dot-to-dot distance in such column can be varied at will from zero (attached dots) to several tens of nm where the consecutive dots can be considered as electronically isolated. There is therefore in the vertical stacking of QDs a physics of “macro-molecules” obtained from interacting macroatoms. Note the existence of a new regime (the attached dots [Vasanelli *et al.* (2002a)]) which cannot be found in conventional molecules where the distance between the nuclei cannot be made arbitrarily small due to the filled shell and/or Coulomb repulsion. The bonding/antibonding splitting in double dot systems is easily shown to decrease exponentially with the dot-to-dot distance. The attached dots are characterized by eigenstates which are extended along the whole stack. Hence they become more polarized by an electric field applied parallel to the z axis (for details see [Vasanelli *et al.* (2002a)]). Contrary to other categories of dots (e.g. those obtained by electrostatic gating of a 2D electron gas) where lateral coupling has been studied extensively, there are very few studies of lateral QD-molecules from self-assembled growth approaches. This is because QD-molecules occur at random and are not very numerous since the QDs are quite diluted (see however [Schedelbeck *et al.* (1997); Johal *et al.* (2002)]). Numerical estimates point toward very small lateral couplings between dots.

Very weakly coupled dots, either vertically or laterally, are at the core of several proposals of semiconductor-based quantum hardware, i.e. hardware for quantum computing (see Chapter 7). The essence of these proposals is to exploit the QD-molecule not by relying on the tunnel coupling (which may require difficult sample preparation) but rather on particle-particle

(Coulomb) interactions in the molecule. They have a longer range than the tunneling effect (power law *versus* exponential decays), which makes them more tolerant to design imperfections. Suppose such a weakly coupled asymmetrical molecule has two inter-band resonances at frequencies ω_1 and ω_2 if the molecule is singly excited. As described in Chapter 7, it is thus possible by using ultrafast two-color laser pulses (centered at ω_1 and $\omega_2 + \delta\omega$) to create a photon absorption at $\omega_2 + \delta\omega$ *conditional* to the occupancy of the molecule by one electron-hole pair created by the absorption of a first photon in the QD-molecule at ω_1 ; hence the possible use of this QD-molecule in optically controlled logical operations.

1.4 Optical Properties

The symmetry of the conduction and valence band edges of bulk Ga(In)As being such that inter-band transitions are electric dipole-allowed, one may expect that Ga(In)As/GaAs QDs will be efficient light absorbers or emitters and, in fact, they are. In this section we focus on the linear optical response; non linear effects will be more extensively discussed in Section 1.6 and thoroughly on the theoretical side in other chapters of this book (see Chapters 4, 6, and 7) (see also [Rossi and Kuhn (2002)]). In the linear regime, where the dot is either empty or contains one electron-hole pair, the Coulomb effect between the electron and the hole can be ignored since its amounts to a rigid shift of the uncorrelated e-h pair states (see Section 1.6). Hence, in the following we discard it.

1.4.1 *The idealized quantum dot: a two-level atom. Populations and coherence.*

For a single quantum dot, one expects an “atomically” sharp ground inter-band absorption or emission line centered at the energy

$$\hbar\omega_{11} = E_1 + HH_1 \quad (1.10)$$

with a Lorentzian line shape characteristic of a two-level system

$$L(\omega) = L_0 \frac{\Gamma/\pi}{\Gamma^2 + \hbar^2(\omega - \omega_{11})^2}, \quad (1.11)$$

where L_0 is a constant and Γ is the radiative broadening: $\Gamma = \hbar/\tau_{rad}$, τ_{rad} being the radiative lifetime. The diagonal element of the single-particle

density matrix corresponding to the excited QD, which represents the population of the excited state where there is no photon and one electron-hole pair in the dot, is denoted with ρ_{11} . The ground state of this macroatom consists in an empty dot (no electron and no hole in the QD): $\rho_{00} = 1$, $\rho_{11} = 0$. The radiative lifetimes τ_{rad} are known to be in the nanosecond range for the Ga(In)As/GaAs dots (since they are governed by the dimensions of the dots that one knows or guesses relatively well, and otherwise depend only on known material parameters in this system). Hence, the absorption/emission lines are expected to display energy widths $\Gamma \approx 1\mu\text{eV}$. The coherence lifetime τ_c , that is to say the time constant of the exponential decay of the off-diagonal term of the density matrix ρ_{01} is, in this idealized two-level atom, twice as long as τ_{rad} [Rossi and Kuhn (2002)], the relaxation time of the population in the excited state. In fact, it is quite easy to evaluate the time dependence of the inter-band dipole in the two-level system. Taking an inter-band dipole d which has only off-diagonal matrix elements in the $\{|0\rangle, |1\rangle\}$ basis, one finds readily that

$$\langle \vec{d} \rangle = \rho_{01}(t)\vec{d}_{10} + hc = \exp(-1/\tau_c) \left(\rho_{01}(0)\vec{d}_{10} + hc \right). \quad (1.12)$$

Finally, it is worth noting that such μeV broadenings are considerably smaller than what is found in excellent quantum wells (where the luminescence linewidth is hardly smaller than ≈ 0.2 meV).

Single-dot optical experiments have indeed revealed very sharp recombination lines but not as sharp as expected from the radiative broadening of a two-level atom [Zrenner (2000)]. Low temperature linewidths range from \approx a few μeV to \approx several hundreds of μeV and it is not clear (to us) that all the parameters which govern the outcome of a narrow or a broad recombination line on a given sample have been identified (since all the Ga(In)As/GaAs QD samples should display the same kind of radiative decay). There seems to be a relationship between the ground optical transition and the presence of the wetting layer [Kammerer *et al.* (2002)]; however, a physical mechanism which would explain this correlation has still to be found. A coherence lifetime τ_c close to that dominated by the sole radiative recombination has however been reported by Borri *et al.* [Borri *et al.* (2001)] using non linear optical experiments performed on an ensemble of (Ga, In)As /GaAs natural dots.

1.4.2 Optical properties of dot ensembles. Broadening and selection rules

In dot ensembles and assuming no thermalization between the dots ($T < 77\text{K}$), the atomic-like structure is washed out by the *inhomogeneous broadening*. Because every dot has its own ω_{11} , $L_{11}(\omega)$ should be replaced by its average over a probability density that a dot emits at energy $\hbar\omega_{11}$

$$\langle L(\omega) \rangle = \int d\omega_{11} L(\omega) P(\omega_{11} - \langle \omega_{11} \rangle). \quad (1.13)$$

Since $P(\omega)$ is usually a Gaussian function considerably broader than the Lorentzian of any given dot, the averaged $\langle L_{11}(\omega) \rangle$ is also a Gaussian with an energy width $\hbar\Delta\omega$ which is *unrelated* to the natural (*homogeneous*) linewidth, but depends on the parameters of the system and the growth conditions. Typically, one finds $\hbar\Delta\omega \approx 50 \text{ meV}$ in Ga(In)As/GaAs dots for inter-band transitions. Smaller inhomogeneous linewidths have been recently reported, indicating that there still exists room for improvements in the size control of the dots.

The linewidth of the S-P intraband transition in QD ensembles is much smaller than inter-band ones, as might have been intuitively expected: intraband linewidths of $\approx 4\text{-}5 \text{ meV}$ have been reported [Fricke *et al.* (1996); Hameau *et al.* (1999); Hameau *et al.* (2002)] in (nominally) InAs/GaAs dots loaded by one electron and whose inter-band broadening fell in the usual 50 meV range (see Figure 1.4).

If the dots were exactly circular, the selection rules for the ground inter-band transitions based on the previous one band model would be that only two radiative transitions out of the four available are observable. This is easily seen by noting that:

(i) The spin projection along the z axis must be conserved. Hence, only transitions connecting $-3/2$ (hole) with $+1/2$ (electron) or $+3/2$ (hole) with $-1/2$ (electron) are possible. This leaves aside two dark transitions which involve a spin projection change of $\pm 2\hbar$. Despite the fact that they are optically inactive, the dark e-h pairs affect the optical properties (e.g. by means of their role on the population of the excited state).

(ii) In addition, the electron and hole envelope functions should have a non zero overlap. Hence, only $L_{ze} + L_{zh} = 0$ transitions are allowed.

It is true that the photoluminescence lines of dot ensembles are consistent with this rule: one systematically observes strong $S_e\text{-}S_h$, $P_e\text{-}P_h$, ... transitions in the QD luminescence spectra [Bimberg *et al.* (1999);

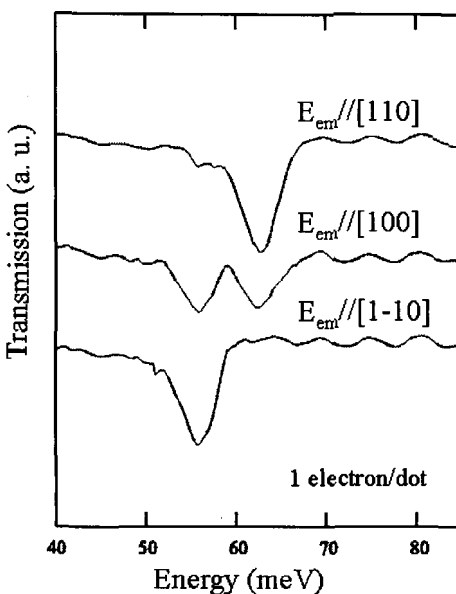


Fig. 1.4 Measured far-infrared absorption of a 30 stacks sample of modulation doped (nominally) InAs/GaAs QDs with 1 electron per dot on the average. Note the linear polarization of the absorptions around 56 meV and 63 meV. From [Hameau *et al.* (2002)].

De Giorgi *et al.* (2003); Schmidt *et al.* (1996)]. Quite often photoluminescence excitation (PLE) experiments are performed where, by detecting the variation of the luminescence intensity versus the frequency of the exciting line, one finds a much larger number of peaks than expected from a circular dot. One way or the other, these peaks are related to absorption (hence to the selection rules), even though one knows that PLE experiments are not identical to absorption experiments. It has been convincingly demonstrated that LO phonon “replica” were involved in the PLE spectra of dot ensembles (see e.g. [Heitz *et al.* (1997)]). This feature is reminiscent of numerous such observations in bulk materials, but it also hints that the simple macroatomic picture where the electronic excitations are decoupled from the others is an oversimplification of the actual state of matter in QDs.

There are several ways one can improve on the previous selection rules. Note that the Coulomb interaction between the electron and hole does not change anything because of its high symmetry. However, its smaller companion, the so-called electron-hole exchange, may change the situation because it involves the electron and hole spins. Without entering into de-

tails (for a review see [Andreani (1995)]) we mention that the electron-hole interaction splits the dark from the bright states. This could be very detrimental to the QD optical properties and to the optical control of the dots if it would happen that the dark states were at significantly lower energy than the bright ones, for the excited pairs would end up in them and the e-h recombination would become mostly non-radiative. Fortunately, it does not seem that this is the case in Ga(In)As QDs.

The shape anisotropy of quantum dots affects the selection rule of the luminescence. In fact, starting from the cylindrically symmetric one particle eigenstates, the anisotropy lifts the $P_+ - P_-$ degeneracy of the electron and hole states. Then Coulomb mixing brings a small admixture of the anisotropic P shell back into the first excited level. This results in the observation of a linear polarization of the ground state emission. This effect was observed by Paillard *et al.* [Paillard *et al.* (2001)] who performed photoluminescence experiments under strictly resonant excitation on arrays of (nominally) InAs/GaAs QDs. The dots were inserted into a planar microcavity to enhance the collection efficiency. Paillard *et al.* observed a very long lifetime of the linear polarization (with a relaxation time longer than the recombination time).

1.4.3 Single dot spectroscopy: the failure of the simple ideas

In spite of improvements in the QD uniformity, it remains true that it is difficult to check the accuracy of the macroatomic description and to implement any quantum-hardware design by performing linear optical experiments on QD ensembles: there, the inhomogeneous linewidth remains much larger than all the effects and departures from the expected behaviors one is looking for. Marzin *et al.* [Marzin *et al.* (1994)] have first shown that it is possible to reveal the atomic lines starting from the broad macro-luminescence line of a dot ensemble by creating mesas at the dot surface, thereby restricting further and further the number of emitting dots present in the exciting light spot and, finally, revealing the discrete lines (see Figure 1.5). Observation of single quantum dots has also been obtained through fixed nano-apertures in an opaque film or through near-field approaches, as recently reviewed by A. Zrenner [Zrenner (2000)]. The use of STM tips has also proven to be a useful tool to investigate restricted (10nm x 10nm) areas of a QD array (see e.g. [Johal *et al.* (2002)]). Hence, probing a few dots (ideally a single one) has become feasible and is by now a very powerful

tool to investigate the electronic properties of QDs.

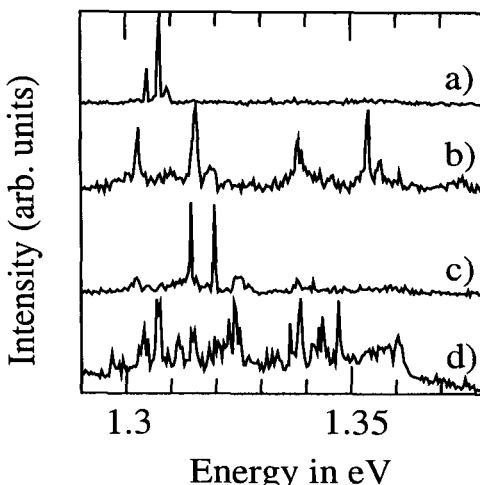


Fig. 1.5 Low temperature photoluminescence of mesas containing a decreasing number of (nominally) InAs/GaAs QDs showing the appearance of discrete lines out of an inhomogeneously broadened transition. From [Marzin *et al.* (1994)].

In fact, single-dot spectroscopy does not really support the simple picture of circular dots isolated from the rest of the world. Firstly, “forbidden” transitions in PLE spectra which lay in energy between the S_e - S_h and P_e - P_h peaks are frequently observed (see Figure 1.6). They are often interpreted as S_e - P_h and/or S_h - P_e transitions. Their existence does not challenge the macroatomic model as they could be taken into account by assuming non-circular dots (which is anyway most likely the case). More puzzling was the discovery by Toda *et al.* [Toda *et al.* (1999)] and others [Kammerer *et al.* (2002); Htoon *et al.* (2001); Oulton *et al.* (2003)] that the PLE signal showed sharp features superimposed on a smooth background taking place around and above the P_e - P_h transition and increasing with photon energy (however for a counter example see [Bayer *et al.* (2000)]). Some of the sharp features have been linked to local modes of LO phonons [Toda *et al.* (1999)]. The smooth increasing background was recently interpreted as the signature of “crossed” transitions [Vasanelli *et al.* (2002b)].

The widths of the discrete excited inter-band transitions, as revealed by single-dot spectroscopy, are as a rule larger or much larger than the

width of the ground inter-band transition. Since the radiative lifetimes of the excited states are known to be of the same order of magnitude as that of the ground state, this finding is a clear indication that the macroatomic scheme does not apply so simply to QDs. There are several good reasons which explain such a systematic breakdown. Firstly, one may expect that the e-h system will always find a way to relax down non radiatively to less excited states, as it is invariably the case in all semiconductor heterostructures and bulk materials. Thus, this non radiative decrease of the excited states populations adds to (and is most often much faster than) the radiative decay. The origins of the non radiative decays can be very diverse; but if the e-h pair loses energy this is necessarily to the benefit of other elementary excitations, which points out an inelastic coupling between the QD electronic variables and the other degrees of freedom (of the dot or of the external world) and thus a failure of the “macro-atom” scheme. The effectiveness of these non radiative channels has, however, to be re-appraised in dot structures because of the discrete nature of the electron (hole) states. Secondly, one has to be aware that excited optical transitions between discrete states, say $P_e - P_h$, can occur at higher energies than those connecting one bound state to a continuum, the so-called “crossed” transitions, say $S_e - \text{Cont}_h$ or $\text{Cont}_e - S_h$ where Cont_e and Cont_h denote the edge of the wetting layer continuum for electrons and holes respectively (see Figure 1.7). This fact recalls that a quantum dot is not really a two-level atom since there is no particle in its ground state while two particles are present in the excited state. An excited discrete-to-discrete transition can thus be degenerate with a continuum. Under such circumstance, this particular two-particle state will autoionize (i.e. disintegrate into the continuum). This behavior is reminiscent of, say, the He spectra, which shows discrete excited transitions (e.g. $(1s, 1s) \rightarrow (2p, 2p)$) superimposed to a continuum ($(1s, 1s) \rightarrow (1s, \text{cont})$). In both the QD and He cases two particles are involved in the optical process. Calculations [Andreani (1995)] show that the autoionization width is indeed much larger than the radiative broadening in typical Ga(In)As/GaAs dots. Single-dot experiments performed by Kammerer *et al.* [Kammerer *et al.* (2002); Kammerer *et al.* (2001)] and by Oulton *et al.* [Oulton *et al.* (2003)] have clearly revealed this enhanced broadening of the excited transitions, together with the continuous increase of the PLE background signal.

Most of the single-dot experiments are usually performed at a low temperature (10 K or so). It is however instructive to follow the evolution of the inter-band spectra with increasing T. As a rule, all the linewidths increase

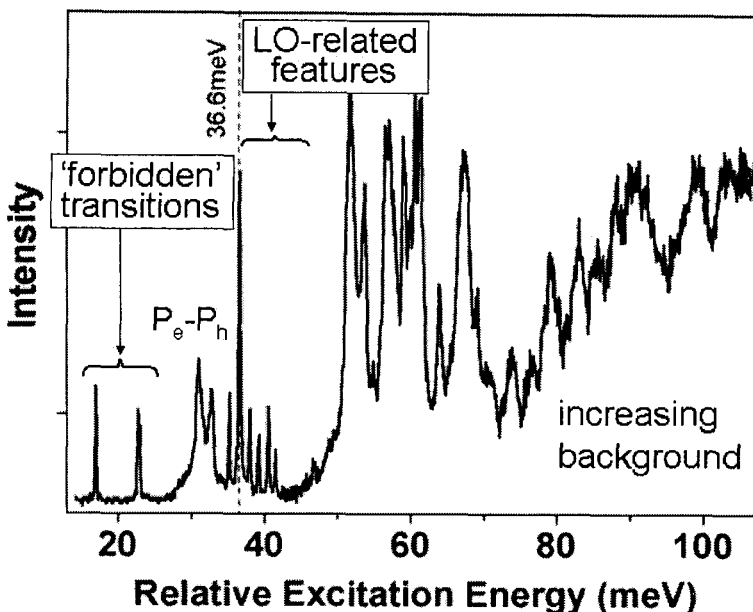


Fig. 1.6 Low temperature photoluminescence excitation spectrum of a single (nominally) $\text{Ga}_0.5\text{In}_0.5\text{As}/\text{GaAs}$ QD showing “forbidden transitions” before Pe-Ph , sharp LO phonon-related features, increasing broadening of the PLE lines at higher energy and a smooth continuum beyond the Pe-Ph line. The detection energy is set at the Se-Sh luminescence line. Courtesy R. Oulton [Oulton *et al.* (2003)].

with increasing T . A popular fit, reminiscent of the findings in quantum well structures, consists in writing

$$\Gamma(T) = \Gamma_0 + \alpha T + \frac{\gamma}{\exp(\beta\Delta\varepsilon) - 1} \quad (1.14)$$

where the first term represents a temperature-independent broadening, ideally arising from the radiative broadening but very often dominated by uncontrolled fluctuations of the QD surrounding. The second term represents the coupling to acoustic phonons. If in Eq. (1.14) $\Delta\varepsilon = \hbar\omega_{LO}$ the last term would describe the interaction with the LO phonons. In Eq. (1.14) all the constants Γ_0 , α , γ depend on the particular transition one is investigating. We mention again that it is non trivial to justify Eq. (1.14) because one deals with discrete transitions. Kammerer *et al.* [Kammerer *et al.* (2001)] found that α is the larger when the ground dot transition is the closer to the wetting layer edge and can reach values comparable to

those found in quantum well structures (see Figure 1.8). Urbaszek *et al.* [Urbaszek *et al.* (2004)] found a similar linear increase of the linewidth of multiply charged excitons in QDs between 4K and 30K, with α increasing when going from the neutral exciton to doubly charged exciton. Such a linear increase of the homogeneous broadening with temperature is common in a QW where there is a continuum of extended electronic states. One can thus easily believe (and in fact calculate) that the population of one excited state will decrease exponentially with time because of the irreversible emission of phonons. The population lifetime of one particular level can in a QW structure be evaluated in the usual way (Fermi Golden Rule) and, for instance, one quantitatively justifies in this way the increase of the population relaxation rate by a term which is linear in T (like in Eq. (1.14)) as the result of the linear increase of the acoustic phonon population with temperature. In QDs instead, the electronic states are discrete and very well energy separated, which makes the coupling to the phonons *a priori* much less efficient than in quantum wells. *A posteriori*, however, it turns out that the coherence of the ground inter-band transition of a single QD is strongly affected by acoustic phonons but in a way which is conceptually very different from what prevails in bulk or QW structures (see Chapters 5 and 6).

A series of time-dependent degenerate four-wave-mixing experiments was performed by Borri *et al.* [Rossi and Kuhn (2002)] (see also Chapter 6) on ensembles of $\text{Ga}_{0.3}\text{In}_{0.7}\text{As}/\text{GaAs}$ dots. Four-wave-mixing is a non-linear optical technique which allows, in principle, the retrieval of the homogeneous broadening from an inhomogeneously broadened line. In contrast to Kammerer *et al.*, Borri *et al.* worked on samples with a large (≈ 0.2 eV) distance between the ground transition and the wetting layer. They derived from their experiments a homogeneous linewidth comparable to the predicted radiative one at cryogenic temperatures ($T \approx 5\text{K}$). This linewidth increases with temperature. However, Eq. (1.13) was not particularly well followed. Instead, each time an activation energy could be deduced from the experiments, it was much smaller than the optical phonon energy.

To close this short review of the salient optical properties of QDs it is worth mentioning that $(\text{Ga},\text{In})\text{As}/\text{GaAs}$ QDs can be efficient, room temperature operated, electrically pumped semiconductor diode lasers [Bimberg *et al.* (1999)]. Their development, now close to industrial application, shows at least that non radiative losses can be kept at a reasonably low level. Note that this feature does not necessarily imply that QDs will make their way to implementing quantum logic functions based on the coherent control

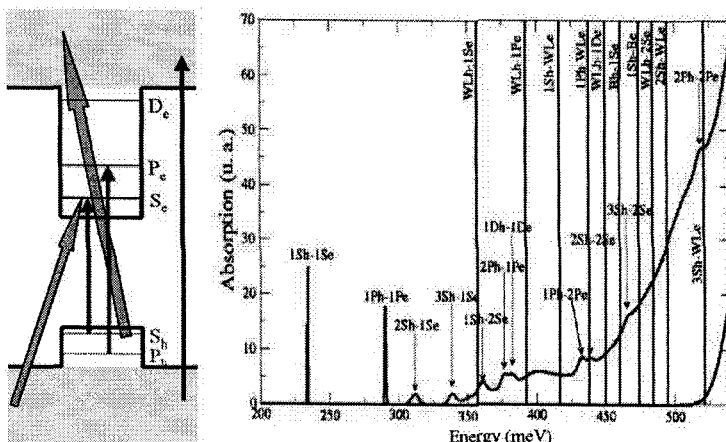


Fig. 1.7 Calculated inter-band absorption spectrum of a single QD showing the existence of quasi discrete transitions superimposed to the continua of “crossed” transitions. In the right-hand panel, the upper curve includes contributions from all transitions while the lower curve only includes transitions between states in the continuum. From [Vasanelli *et al.* (2002b)].

of the optical transitions. The requirement for the latter purpose is the achievement of a very long coherence time of the optical transition. This represents a much more stringent demand than maintaining population inversion between the conduction and valence states.

1.5 Phonons and Carrier Coupling to the Phonons in Quantum Dots

Being solid state heterostructures, quantum dots naturally display phononic excitations. It is however quite clear that the phonon spectra of actual InAs/GaAs quantum dots are very difficult to calculate because of the awkward dot geometry, the unknown In grading and strain state in the dot. One might be tempted to believe that a QD is just like a deep impurity in a semiconductor matrix. This analogy is, however, invalid because of the very large number of unit cells present inside a QD. In contrast to the deep-impurity case, the large number of dot unit cells makes all the confined phonon modes form a quasi continuum. In addition, in Ga(In)As/GaAs QDs, the boundary between the dot and the barrier is chemically and geometrically “smooth”: tetrahedral bonds on both sides, with very similar

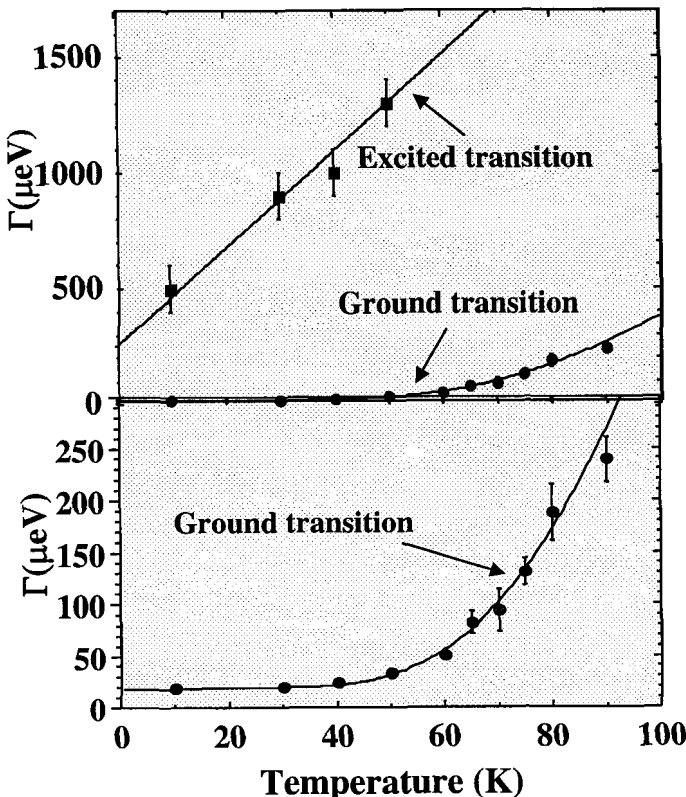


Fig. 1.8 Measured temperature dependences of the ground and excited inter-band transitions in a single (nominally) InAs/GaAs QD. From [Kammerer *et al.* (2001)].

bonds between anions and cations. This smooth interface suggests rather delocalized acoustic modes. As for the optical modes, Raman scattering or PLE experiments performed on QD arrays have revealed the existence of an optical phonon frequency close to the one expected from a highly strained InAs material (31–32 meV). The participation of GaAs-like LO phonons to QDs electronic properties is also established (for a recent review on phonons in quantum heterostructures including QDs see [Jusserand (2002)]).

The coupling between the carriers and the phonons is a topic which has attracted much attention: this is not because one expects it to be inherently different from what is observed in other heterostructures but because the discrete nature of the electronic states seems to (and does) change drastically the results of the electron-phonon coupling. In the early

nineties Bockelmann *et al.* [Bockelmann and Bastard (1990)] and Benisty [Benisty *et al.* (1991)] remarked that the emission of optical phonons by electrons (via Fröhlich coupling) was virtually impossible in quantum dots because the optical phonons are almost dispersionless. Hence, there is in practice no energy match between the optical phonon energy and the energy difference between the electronic states, making energy conservation of the electron-phonon system impossible. In addition, it was shown that the emission of acoustic phonons was very inefficient, as soon as the electronic energy difference exceeds a few meVs. The conclusion was that quantum dots should display the *phonon bottleneck* effect: the reduction in phase space due to the discrete nature of the electronic state would in fact prevent the energy relaxation (see Figure 1.9). Such a strong and clear-cut prediction is in mediocre agreement with experiments. It is true that examples of poor relaxation can be found [Urayama *et al.* (2001); Heitz *et al.* (2001)], but the excellent performances of QD lasers show that ways to bypass the phonon bottleneck exist. In the particular case of QD lasers, where numerous carriers are electrically injected, it is the Auger effect (see Section 1.6) which most likely ensures the relaxation.

Actually, as discussed in Chapter 5, the early analysis missed an important point, namely that the usual way to handle the electron-optical phonon interaction may be not appropriate in QDs. In short, it is the straightforward use of the Fermi Golden Rule which is questionable to describe the electron-LO phonon coupling in QDs. Fröhlich coupling is so strong and the electron-LO phonon mixed continuum is so narrow, that the very idea of irreversible emission of one optical phonon by the electron loses any meaning. What in fact happens is the creation of a mixed elementary excitation between the interacting electron and phonon, the polaron [Inoshita and Sakaki (1997); Li *et al.* (1999)]. Note that the prominent part played by the polaron (*versus* the usual picture of an electron alone emitting LO phonons) is not due to the particular strength of the Fröhlich coupling in III-V QDs (it is only slightly enhanced in quantum dots with respect to the bulk situation). Rather, it is associated with the almost coincidence of the LO phonon energy with the energy difference between discrete electronic states, which considerably magnifies the importance of the coupling: an interaction between degenerate or quasi degenerate levels cannot be treated perturbatively.

The existence of electronic polarons in QDs has been unambiguously proved by far-infrared magnetoabsorption [Hameau *et al.* (1999); Hameau

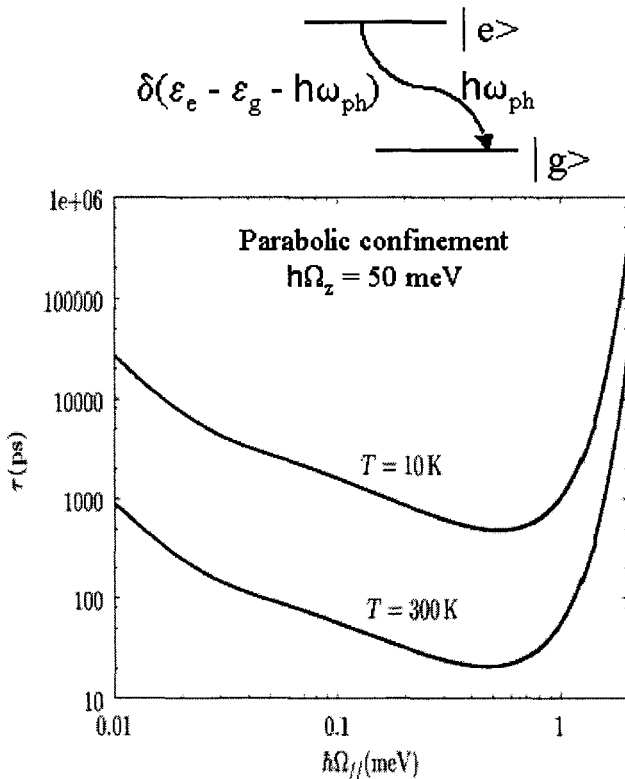


Fig. 1.9 Calculated population relaxation time due to LA phonon emission from the first excited state to the ground state of a quantum dot with parabolic confinement versus the lateral energy spacing. The phonon bottleneck effect corresponds to energy spacings $\geq 1\text{-}2 \text{ meV}$.

et al. (2002)] and the new way to interpret the energy relaxation in QDs in terms of polaron relaxation has been analyzed [Li and Arakawa (1998); Verzelen *et al.* (2000)] (see Chapter 5). The polaron relaxes because it acquires a finite lifetime due to the anharmonic decay of its LO phonon component. It is important to realize at this stage that the decay time of the one-phonon polaron is always larger or equal to twice the phonon lifetime, the bound being reached when the detuning between the zero-phonon level with the one LO phonon replica of the second level vanishes. Recent studies [Sauvage *et al.* (2002); Zibik *et al.* (2003)] of the spectral hole burning of the S-P transitions in ensembles of (nominally) InAs/GaAs dots have given access to the relaxation time τ_P of the excited state *versus*

its energy. A very good agreement with the polaron model was found and the variation of τ_P versus detuning has shown that the most likely polaron decay path is that associated with the disintegration of the LO phonon into two LA phonons (see Figure 1.10). There is also quite convincing PLE evidence [Toda *et al.* (1999); Heitz *et al.* (2001)] that the coupling between e-h pairs and optical phonons is also polaron-like, which at first sight was not obvious since an e-h pair is an electrically neutral entity (for theoretical discussions of e-h polarons see [Krummheuer *et al.* (2002); Fomin *et al.* (1998); Verzelen *et al.* (2002)]).

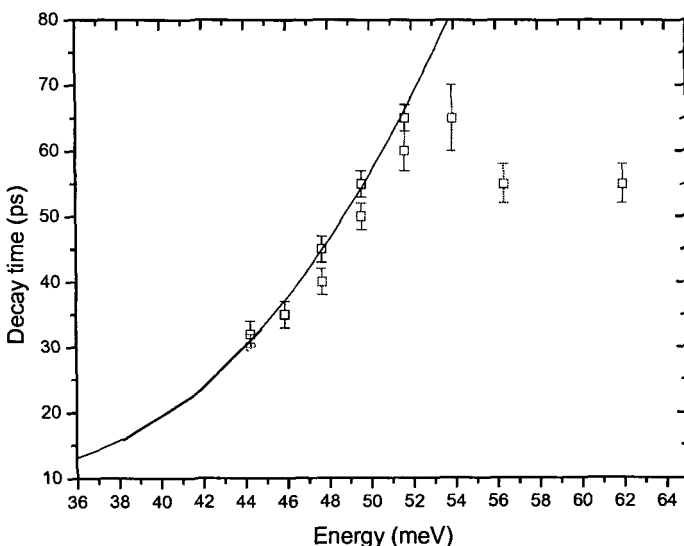


Fig. 1.10 Measured polaron relaxation time versus polaron energy in an ensemble of (nominally) InAs/GaAs QDs. Courtesy L. Wilson [Zibik *et al.* (2003)].

Carrier coupling to acoustic phonons in QDs is also much discussed, particularly in connection with the coherence lifetime of the inter-band transitions. In contrast to the LO phonons, the acoustic-phonon bandwidth together with the weaker deformation potential make it possible to handle the interaction between the carriers and the acoustic phonons like in bulk or QW structures, i.e. by means of the Fermi Golden Rule. In InAs QDs it turns out that the irreversible emission of acoustic phonons is not efficient, as already discussed within the phonon bottleneck approach: for energy separation of ≈ 30 meV, the population and coher-

ence (τ_c) lifetimes exceed by far the μs . The virtual absorption/re-emission of one or several acoustical phonons without changing the e-h quantum numbers (coined as a “pure dephasing” mechanism) is by far a more efficient electron-phonon coupling mechanism [Krummheuer *et al.* (2002); Vagov *et al.* (2002)] that will be analyzed in detail in Chapters 5 and 6. A signature of the “pure dephasing” mechanism is the appearance of multi-phonon sidebands in the absorption or luminescence spectra. These were first observed in II-VI QDs [Besombes *et al.* (2001)]. Clear experimental evidence of acoustic phonon pedestal in the luminescence spectra of single (nominally) InAs QDs has recently been obtained [Favero *et al.* (2003)], (see Figure 1.11). This, together with the study of the temperature dependence of the integrated four-wave-mixing signal in QD’s ensembles [Borri *et al.* (2001)], points to the necessity of reconsidering the way to handle the electron-acoustic phonon in QDs.

The physics behind the acoustic phonon-related pedestal is a particular vibronic coupling. In the excited state of the crystal, say the S_e-S_h pair state, the electron-phonon and hole-phonon couplings modify the energy of the non interacting electronic and phonon systems. In particular, if the e-h pair is assumed to remain in the same quantum state, one can describe the electron-phonon and hole-phonon interaction by means of an *effective* operator which acts on the phonons only, and which depends explicitly on the electron and hole quantum numbers. Such a projection on a given electronic state is expected to work well when the electronic energies are much larger than the phonon energies (Huang–Rhys model), which is certainly the case of acoustic phonons in Ga(In)As/GaAs QDs. This effective operator leads to changes in the phonon energies and wavefunctions. It turns out that its effects can be exactly taken into account. Since the phonon frequencies change when the electronic state changes, it is clear that the radiative recombination of a dressed e-h pair no longer requires the conservation of the phonon number. The existence of phonon sidebands then ensues. Correlatively, on the time scale, one can show [Vagov *et al.* (2002)] within the Huang–Rhys approach that the decoherence of the ground inter-band transition is closely associated with the generation of phonons. Borri *et al.* [Borri *et al.* (2001)] very clearly showed this feature experimentally and how the partial loss of inter-band coherence is fast (a few ps even at low T). Their measurements also show the dramatic decrease of the surviving coherence with increasing T. This points to the failure of the macroatomic model at room temperature in QDs, even for the ground optical transition.

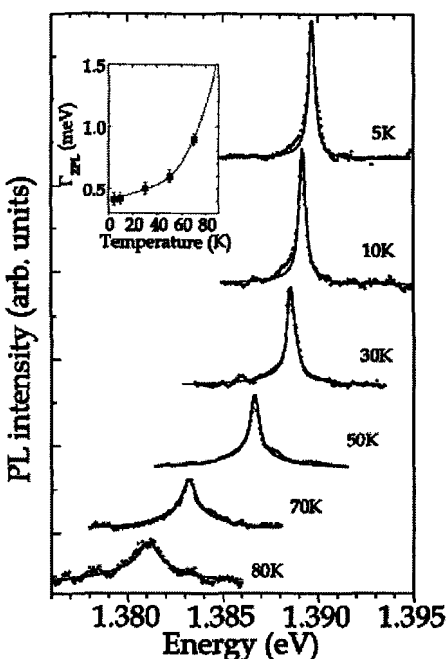


Fig. 1.11 Measured luminescence line of a single (nominally) InAs/GaAs QD at different temperatures. The solid line is the theoretical lineshape. From [Favero *et al.* (2003)].

1.6 Carrier-Carrier Interaction in Quantum Dots

The quantum logics operations resulting from the control of inter-band optical transitions require strong light fields. Thus, it is quite likely that more than one electron-hole pair will be present in the dot. A study of the carrier-carrier interaction is therefore crucial to an understanding their effect on the optical spectra and their coherent manipulation by light pulses. In addition, the study of charged dots under laser illumination requires the quantitative understanding of electrons interacting with other electrons and holes, all localized in the dots. Besides, single dot optical experiments actually correspond to injecting a lot of photons which not only create e-h pairs in the dot but may also create carriers elsewhere. These unwanted carriers may decrease the inter-band coherence of the QD carriers by carrier-carrier (Auger) interactions.

In the following, we first discuss the energy shifts induced by e-h interaction by standard perturbation calculus. This method is well suited to

the energy level calculations of the lowest lying excited state (see Section 1.6.1), but is not satisfactory to handle more excited states nor to interpret the changes of the optical spectra with increasing laser flux or QD occupancy. A better suited method will be highlighted in Section 1.6.2. Finally, Section 1.6.3 will briefly discuss the Auger effects in QDs.

1.6.1 *Electron-hole interaction in quantum dots*

It is well known that the e-h interaction is responsible for the creation of bound states for the relative e-h motion in bulk, quantum wells and quantum wire structures. This reorganization of the spectrum of the relative motion cannot be handled perturbatively, since there is no way one can build up a localized state (say the 1s state of the e-h relative motion) out of a finite number of plane waves (the eigenstates of relative motion of the non interacting pair). Thus, the e-h interaction changes the energy levels and the optical properties not only quantitatively but also qualitatively. Not only does it alter the strength of the absorption in the continuum of the relative motion (Sommerfeld factor), but it creates sharp lines which correspond to discrete states for the relative motion below the edge of the non interacting continuum (exciton lines). In QDs instead, the electron and hole lowest states are discrete and very well energy separated from the excited states compared to a typical Coulomb interaction (as measured by the effective Rydberg). Thus, treating the Coulomb interaction in perturbation is well justified and provides accurate results [Lelong and Bastard (1996)]. Exact results have been obtained by quantum Monte Carlo studies [Tsuchiya (2000)] and “direct diagonalization” approaches (see next paragraph). Note that Coulomb effects do not produce any qualitative change for the lowest lying pair state (without and with Coulomb interaction this state is discrete) but only an energy shift. This in particular implies that the notion of exciton binding energy may be considered meaningless in quantum dots for the reason that there is no dissociation continuum for the exciton into running electrons and holes (the term “exciton binding energy” is sometimes used in dots to indicate the energy shift between the interacting electron-hole energy and the energy of the lowest transition between single-particle states). Furthermore, it can be shown that in a typical InAs/GaAs QD the Coulomb correlation on the ground ($S_e - S_h$) e-h pair state amounts to arising from the zeroth order contribution (expectation value of $1/r_{eh}$) for more than $\approx 95\%$. Thus, one can expect a quick convergence of the perturbation series for the correlation energy of a bound

e-h pair. Such is not the case for more complicated complexes; e.g. the trions which consist of two electrons plus one hole (X^-) or two holes plus one electron (X^+) or the bi-excitons (2 electrons and 2 holes). This is because of an almost exact cancellation between the attractive and repulsive carrier-carrier interactions.

The salient characteristics of the excitonic complexes in QDs (a short hand notation for the Coulomb interacting electrons and holes bound to a QD) is that they always exist and are always observable. This striking feature contrasts with the bulk and QW situations and arises from the lack of continuum spectra at low energy in a QD. Take for instance the trion X^- and compute its ground state. When the trion recombines radiatively, a photon is created and the extra electron is left, say, in the ground state E_1 . Thus, the trion line shows up at an energy E_{X_-} equal to

$$E_{X_-} = \langle \psi_{X_-} | H_{e_1} + H_{e_2} + V_{e_1 e_2} + H_h + V_{he_1} + V_{he_2} | \psi_{X_-} \rangle - E_1. \quad (1.15)$$

This energy E_{X_-} is separated from the excitonic one, E_X ,

$$E_X = \langle \psi_X | H_e + H_h + V_{eh} | \psi_X \rangle \quad (1.16)$$

by a quantity δ which (1) is small because, compared to E_X , there is almost a cancellation between the repulsion between the two electrons and the extra Coulomb attraction between the hole and the second electron and (2) can be either positive or negative depending on the material parameters (carrier effective mass), the size, shape of the dot, *etc.* Irrespective of the sign of δ , nothing particular happens: a X^- recombination line appears on the high (low) energy side of the X line in the photoluminescence spectra. This is, however, a striking effect compared to what we are used to observing in bulk or QW structures where the same situation ($\delta < 0$) would imply the disappearance of the X^- line in these structures. In QW or bulk materials any e-h complex located at higher energy than another one is actually degenerate with the continuum of this other complex (because there exists one or several directions of space where the complex (like the carriers) displays a continuous spectrum. Thus, it auto-ionizes much more quickly than the recombination time, which makes its observation almost impossible (in our X^- example, the unbound trion in a QW would break into a running electron and a running neutral exciton on a \approx ps time scale). Similar situations can happen for the bi-excitons and, in fact, “bound” bi-excitons as well as “unbound” bi-excitons have been observed in InAs/GaAs QDs depending on the dot size (see Figure 1.12), the smaller dots exhibiting a

bi-exciton line at higher energy than the single exciton line.

A QD optical property, which could be very useful for quantum cryptography, is closely associated with the exciton-exciton interaction. For an efficient encoding of information it is necessary to be sure that one and only one photon has been emitted by a source. Now, if two excitons are bound in a single QD, their recombination energy differs from the case when there is a single exciton in the dot. So, by very weakly exciting (at $\hbar\omega_1$) the excitonic resonance only at low temperature (to get the lines as narrow as possible), one could in principle ensure by a spectral discrimination that one and only one photon will be re-emitted. Usually, however, one excites several excitons in the dot (strong injection in the wetting layer) and it is not easy to ensure the single-photon regime [Michler *et al.* (2000); Moreau *et al.* (2001); Santori *et al.* (2001)]. As time flows the excitons recombine and finally only two remain in the dot (see Figure 1.13). One disappears radiatively by emitting a photon at the bi-exciton line ($\hbar\omega_2$). Then a single pair remains and the single-photon regime takes place. This sequential emission of one photon at ω_2 followed by one at ω_1 has recently been convincingly established by measuring the time dependence of the cross correlations between the emissions at ω_1 and ω_2 [Moreau *et al.* (2001)]. It was very clearly observed that the signal at ω_1 occurs after the one at ω_2 .

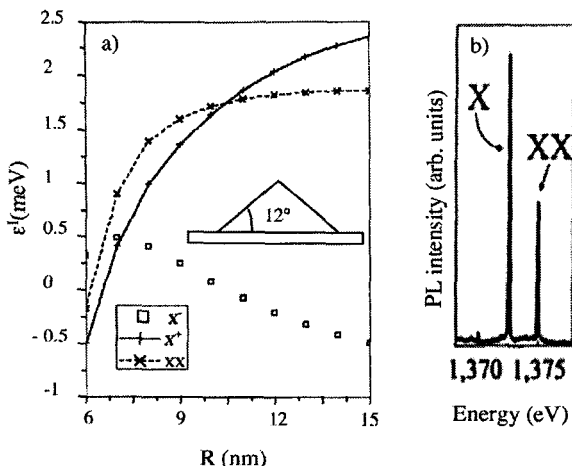


Fig. 1.12 (a) Calculated energy difference between the bi-exciton (XX) the charged excitons (X+ and X-) the exciton recombination lines versus dot radius for InAs cones floating on a one monolayer thick wetting layer. (b) An example of “unbound” bi-exciton (adapted from [Moreau *et al.* (2001)]).

Although perturbation methods can be used to compute the correlation energies of excitonic complexes of arbitrary sizes, they become very cumbersome for large complexes. Under such circumstances it is more advantageous to use a more powerful method, which will also provide us not only with the energy states of the complexes but also with the absorption (or emission) spectra.

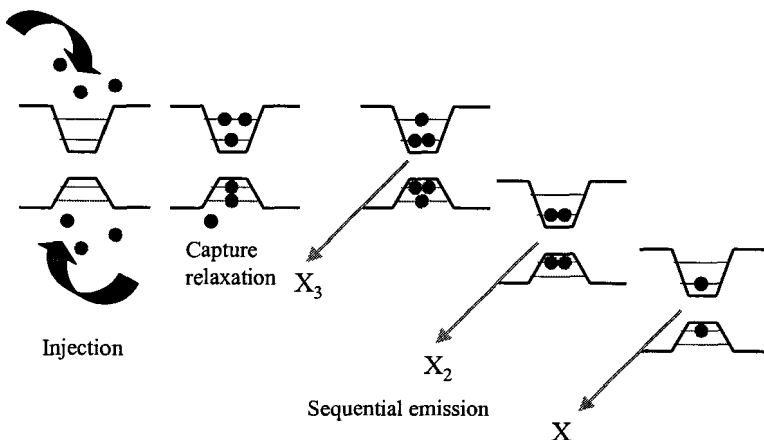


Fig. 1.13 Sequential emission of excitons by a strongly excited dot (schematic).

1.6.2 *Excitonic complexes and optical properties of highly excited quantum dots: new phenomena and a new approach*

In systems of higher dimensionality, strong excitation regimes essentially result in renormalization of the interactions which leads to the modification of the bandgap (the so-called bandgap renormalization) with respect to the linear-excitation regime, and to continuous variations in the oscillator strength and line shapes as a function of the photoexcitation intensity. With increasing photoexcitation power, additional spectral features may arise owing to successive band filling, but no discrete appearance and disappearance of characteristic peaks is observed as a function of the density of photoexcited carriers.

The situation in quantum dots was found to be completely different as soon as single- or few-dot experiments *vs.* density of photoexcited

carriers became available [Motohisa *et al.* (1998); Landin *et al.* (1998); Dekel *et al.* (1998)]. With increasing photoexcitation intensity, one observes the progressive appearance of higher energy spectral peaks, involving QD electron shells that become filled due to Pauli exclusion principle. However, the fine structure of the spectra shows a much more complex behavior: sharp features exist that are characteristic of a specific range of photoexcitation intensity and are not present at other values of the intensity. Exciton and bi-exciton peaks are just one particular manifestation of this phenomenon.

The origin of such excitations can be qualitatively understood just by considering that confinement in self-organized dots is so strong that only few electrons and holes are present. Moreover, owing to carrier localization Coulomb interaction is so strong that each electron and hole aggregate will give rise to a different few-particle complex with its characteristic spectral features.

To test this hypothesis and gain quantitative understanding, it is clear that perturbative approaches are not helpful. Fortunately, however, it is precisely the small number of electrons and holes that allows the use of an “exact” approach [Hohenester and Molinari (2000a); Hohenester and Molinari (2000b); Jacak *et al.* (1998)]: a novel scheme in the field of semiconductors that could not be used for systems of higher dimensionality. The idea is simply to write the full Hamiltonian of the system including the single-particle Hamiltonians and all possible electron-electron, hole-hole, and electron-hole Coulomb interactions

$$H = H_{0e} + H_{0h} + H_{ee} + H_{hh} + H_{eh}, \quad (1.17)$$

and to expand them on the basis $|l\rangle$ of all single-particle states of electrons and holes. The latter are calculated as outlined in the previous sections, or by numerical solution of the Schrödinger equation in an arbitrary geometry and arbitrary external fields on a plane-wave basis. In practice only a finite number of single-particle states with energy below a given energy cutoff E_{cut} can be taken into account in the expansion. Direct diagonalization of $\langle l | H | l' \rangle$ then yields the eigenenergies, E_λ , and the corresponding eigenstates, $|\lambda\rangle$, of the few-particle aggregate, in analogy with the Configuration Interaction (CI) approach well known for molecular systems. From E_λ and $|\lambda\rangle$ not only the energy spectrum but also the emission and absorption spectra are obtained [Hohenester and Molinari (2000a)]. Note that this approach is in principle exact, in the sense that it contains no assumption.

tions about the interactions; however, the cutoff energy must be controlled carefully since it may introduce approximations, particularly when many higher lying single-particle states are important, as in the case of strong coupling with a wetting layer. Also, the implementation is computationally heavy, and soon becomes intractable with increasing number of particles. On the other hand, this scheme is not limited to treating an equal number of electron and holes, but can deal on the same footing with any aggregate of few electrons and holes [Hartmann *et al.* (2000); Bayer *et al.* (2000); Findeis *et al.* (2001); Lomascolo *et al.* (2002)] (including systems composed of electrons only or holes only, see e.g. [Rontani *et al.* (1999); Rontani *et al.* (2004)]), and dots with arbitrary confinement profiles including coupled dots.

The results show that each aggregate has its characteristic energy spectrum. For example, the exciton and bi-exciton states are immediately found as solutions for the one electron and one hole (1e–1h) and the two-electron and two-hole (2e–2h) aggregates with no need of uncontrolled assumptions. The calculated spectra are shown e.g. in Figure 1.14, together with results for other multi-exciton aggregates, for a prototype cylindrical quantum dot [Hohenester and Molinari (2000a)]. The insets show the configuration of electrons in the ground state before emission (hole configurations are the same): for a detailed analysis of each emission spectrum we refer to [Hohenester and Molinari (2000a)]. A similar behavior is found for charged electron and hole aggregates, as displayed e.g. in Figure 1.15(b) for a pyramidal QD (see Figure 1.15(c)). Based on these results, it has been possible to account for a number of very interesting experimental results on charged quantum dots under controlled carrier injection/depletion (see e.g. [Hartmann *et al.* (2000); Bayer *et al.* (2000); Findeis *et al.* (2001); Lomascolo *et al.* (2002)]) that were previously unexplained (see Figures 1.15 and 1.16).

It is clear that in a given quantum dot, for a given number of injected or photoexcited carriers, only the spectral features corresponding to the appropriate “electron and hole cluster” are present at a time. (Sometimes the coexistence of spectral features associated to different clusters is observed in intermediate regimes: this is due to time averaging over configurations with a different number of particles, or to the fact that more than one dot with different configurations is probed at the same time.) As discussed in Chapter 7, the few-particle regime of neutral and/or charged dots is then particularly interesting since it offers a well defined Hilbert space not only for possible implementations based on orbital degrees of freedom [Troiani

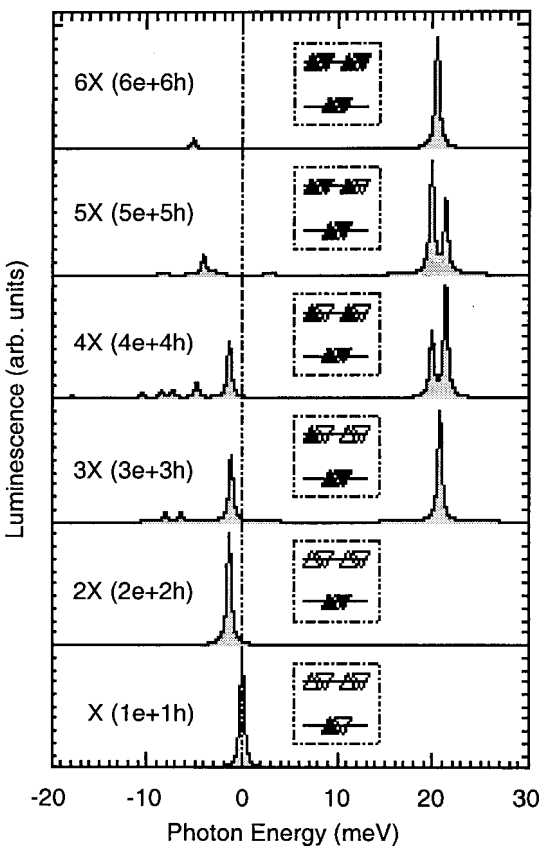


Fig. 1.14 Calculated luminescence spectra for multiple electron-hole pairs confined in a prototype cylindrical GaAs dot (single-particle level splitting of 20 and 3.5 meV for electrons and holes respectively). Adapted from [Hohenester and Molinari (2000a)].

et al. (2000)], but also for schemes based on spin and coupled orbital/spin degrees of freedom [Troiani *et al.* (2003)].

1.6.3 Auger scattering in quantum dots

The Auger effect consists in redistributing the energy among carriers via carrier-carrier interaction. One electron gains some energy while a second one loses the same amount. Very soon, the hot electron loses some of its extra energy to the phonons. Auger processes have long been known in semiconductor physics to be very effective interactions if there are enough

carriers, typically under lasing action conditions. Their role has to be re-appraised in the QDs because again the low energy spectrum of QD carriers is discrete. Calculating an Auger rate explicitly calls for the use of Fermi Golden Rule, implying the existence of a continuum of states for at least one particle (and thereby for the multiparticle Hamiltonian). If there were only discrete states in QDs, the Auger effect would never cause any scattering and thus would not alter the inter-band coherences. At most, if created at $t = 0$ in an arbitrary superposition of the eigenstates of the many electron Hamiltonian, the carriers would oscillate between the available multi-particle states but 'strictly speaking' there would not exist an irreversible departure from the initial state, *viz.*, the survival probability $|\langle \psi(t=0) | \psi(t) \rangle|^2$ would never decay to zero when $t \rightarrow \infty$. This picture may have to be reconsidered if, in addition to carrier-carrier interaction, one includes carrier-phonon interaction: the discrete nature of the electronic states is now transformed into mixed electron-phonon continua. In a Huang-Rhys type of approach, the electron states dress the acoustic phonons. This results in phonon frequencies which depend on the electronic state and thus are no longer orthogonal. Hence, transitions with a change of the phonon number can take place, even if induced by carrier-carrier interactions which are phonon-independent. This feature is reminiscent of the appearance of phonon sidebands in the luminescence spectra. The magnitude of such phonon assisted Auger effects in QDs have, however, to be quantitatively evaluated.

There are situations where the two (or more) particle states of a QD form an electronic continuum even without the participation of phonons (see Figure 1.17). For instance (i) the initial state may correspond to a bound two-particle state and in the final state one of the particles is ejected from the dot, say in the wetting layer 2D continuum, while the second particle has relaxed to a lower energy state [Ferreira and Bastard (1999)]. Another possibility (ii) corresponds to having initially two particles in wetting layer states while in the final state one particle has been captured while the second has increased its kinetic energy [Uskov *et al.* (1998)]. The scattering events (i) or (ii) can be treated by means of the Fermi Golden Rule. One usually finds that (i) is very efficient if energy-allowed. This is because having two particles bound to a dot corresponds to quite a large particle density [Ferreira and Bastard (1999)]. Mechanism (ii) is efficient only at large density. Another mechanism (iii) corresponds to having in the initial state one bound and one unbound particle [Bockelmann and Egeler (1992)]. In the final state the bound particle has relaxed and given its energy to the

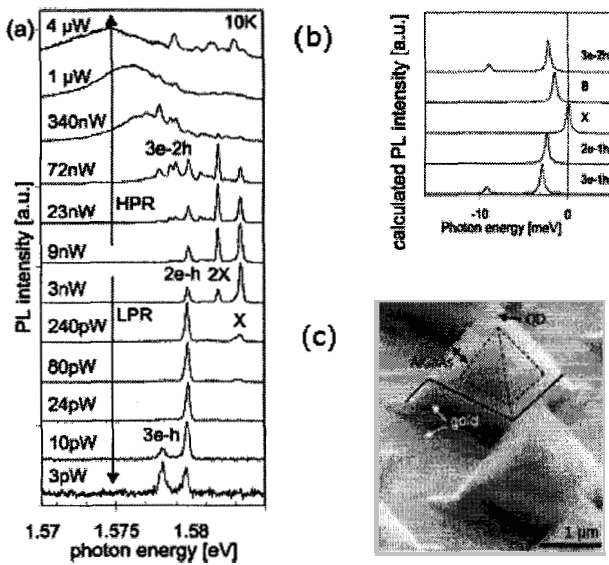


Fig. 1.15 Experimental (a) and calculated (b) photoluminescence spectra as a function of carrier occupation for charged quantum dots self-organized at the apex of inverted pyramids (c) on V-grooved substrates. Adapted from [Hartmann *et al.* (2000)].

second particle. This mechanism is efficient only at large carrier concentration. These scattering mechanisms correspond typically to non resonant excitation of the QD (one excites far above the ground recombination energy). When performing single-dot spectroscopy under resonant condition, one should keep in mind that carriers can be generated in the barrier by two-photon absorption. Their concentration is certainly much smaller than the one generated by strong non resonant excitation but may create parasitic charges around the dot.

A broad class of dephasing mechanisms linked to carrier-carrier interactions involves traps [Jankovics *et al.* (2004)] which can randomly empty or fill as time flows. It is not immediately obvious that this should lead to decoherence of the ground inter-band transition, to the extent that one could conceive the small number of particles (in the dot and in the trap) as a closed and discrete system, therefore not prone to inelastic interactions.

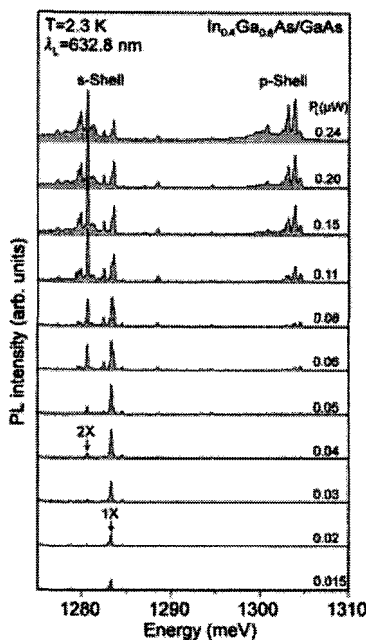


Fig. 1.16 Power-dependent PL spectra from a single isolated self-organized quantum dot. Contributions from the s-shell and p-shell can be clearly distinguished. In the spectral region of the s-shell, the single exciton (1X) and biexciton lines (2X) are labeled. After [Findeis *et al.* (2001)].

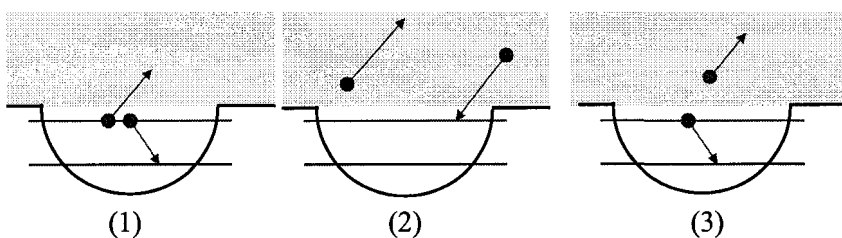


Fig. 1.17 Three possible Auger effects in a quantum dot (schematic).

This is, however, not a very good description of the actual phenomena, because once the extra particle(s) are released from the trap, they undergo random inelastic events with others in the wetting layer or with phonons, etc. Thus, the pure quantum evolution of the dot plus trap particles is

a fiction which should be replaced by a more realistic and stochastic description. We note that the trap occupation changes the Hamiltonian of the e-h pair in the dot in comparison to the one which prevails when the trap is empty: for an electron trapped to a Coulomb impurity, the trap-dot interaction is the effect of a point charge (a dipole) on an exciton when the electron trap is empty (filled). Thus, even in the absence of coupling to the light, the QD is subject to a random time-dependent Hamiltonian, hence the possibility (and realization) of decoherence. We remark that this conditional energy shift of the ground inter-band transition recalls the proposal outlined earlier of optically manipulated quantum hardware formed by QD molecules. In both cases one plays with carrier-carrier interactions but in one case this conditional interaction is completely monitored from the outside by suitably shaping optical pulses, while in the trap case the particle-particle interactions occur at random.

There are now a number of established facts for the Ga(In)As/GaAs QDs. We know their approximate shape and size, as well as their approximate energy level structure. We also know a lot of their optical properties and we have learned how to correctly describe the carrier-phonon interaction in these zero-dimensional systems. Significant progress has been made in recent years on the assessment of the dot capability of implementing optically controlled quantum hardware. We now know that the solid state environment implies that the macroatomic scheme operates accurately only on the ground optical transition and at cryogenic temperatures. Once these facts are acknowledged, the road becomes cleared to effectively realize the designed quantum hardware. In fact optical control of a QD inter-band transition has already been achieved at low temperature [Stiewater *et al.* (2001); Kamada *et al.* (2001); Htoon *et al.* (2002)].

Acknowledgments

We would like to thank all the members of the SQID consortium for the constant fruitful interactions. The LPA-ENS is “Laboratoire associé au CNRS et aux Universités Paris 6 et Paris 7”. One of us (GB) wishes to express his gratitude to R. Ferreira for his continuing collaboration and illuminating insights and to Prof. R. Cingolani for his kind invitation in Lecce where part of this review was written. He is also indebted to a number of students and collaborators for their participation in the work summarized

in this chapter: J. N. Isaia, A. Jankovics, C. Kammerer, Ph. Lelong, A. Vasanelli, O. Verzelen; G. Cassabois, C. Delalande, E. Deleporte, L. A. de Vaulchier, Y. Guldner, S. Hameau, Ph. Roussignol and H. Sakaki. EM is particularly indebted to U. Hohenester and F. Troiani for their key contributions to the work summarized here, and for continued and very pleasant collaborations in this field; to G. Abstreiter, R. Cingolani, E. Kapon and their groups for very fruitful interactions on the experimental side; and to F. Rossi with whom theoretical research on quantum dot optics in Modena was initiated.

Bibliography

- Andreani, L.C. (1995). In: Confined Electrons and Photons, edited by E. Burstein and C. Weisbuch, *NATO ASI Series B: Physics* **340**, p. 57, Plenum Press, New York, and references therein.
- Ashoori, R.C. (1993). Electrons in artificial atoms, *Nature* **379**: 413.
- Bastard, G., Brum, J.A. and Ferreira, R. (1991). Electronic states in semiconductor heterostructures, *Solid State Physics* **44**: 229, and references therein.
- Bayer, M., Stern, O., Hawrylak, P., Fafard, S. and Forchel, A. (2000). Hidden symmetries in the energy levels of excitonic “artificial atoms”, *Nature* **405**: 923.
- Bellucci, D., Rontani, M., Goldoni, G., Troiani, F. and Molinari, E. (2004). Spin-spin interaction in artificial molecules with in-plane magnetic field, *Physica E* **22**: 482.
- Benisty, H., Sotomayor-Torrès, C.M. and Weisbuch, C. (1991). Intrinsic mechanism for the poor luminescence properties of quantum-box systems, *Phys. Rev. B* **44**: 10945.
- Besombes, L., Kheng, K., Marsal, L. and Mariette, H. (2001). Acoustic phonon broadening mechanism in single quantum dot emission, *Phys. Rev. B* **63**: 155307.
- Bimberg, D., Grundmann, M. and Ledentsov, N.D. (1999). *Quantum Dot Heterostructures*, Wiley, New York.
- Bockelmann, U. and Bastard, G. (1990). Phonon scattering and energy relaxation in two-, one-, and zero-dimensional electron gases, *Phys. Rev. B* **42**: 8947.
- Bockelmann, U. and Egeler, T. (1992). Electron relaxation in quantum dots by means of auger processes, *Phys. Rev. B* **46**: 15574.
- Borri, P., Langbein, W., Schneider, S., Woggon, U., Sellin, R.L., Ouyang, D. and Bimberg, D. (2001). Ultralong Dephasing Time in InGaAs Quantum Dots, *Phys. Rev. Lett.* **87**: 157401.
- Bouwmeester, D., Ekert, A. and Zeilinger, A. (Eds.) (2000). *The physics of quantum information*, Springer, Berlin.
- Cortez, S., Krebs, O., Voisin, P. and Gérard, J.M. (2001). Polarization of the interband optical dipole in InAs/GaAs self-organized quantum dots, *Phys.*

- Rev. B* **63**: 233306.
- Crozier, P.A., Catalano, M., Cingolani, R. and Passaseo, A. (2001). Direct quantitative measurement of compositional enrichment and variations in In_yGa_{1-y}As quantum dots, *Appl. Phys. Lett.* **79**: 3170.
- de Giorgi, M., Rinaldi, R., Johal, T., Pagliara, G., Passaseo, A., de Vittorio, M., Lomascolo, M., Cingolani, R., Vasanello, A., Ferreira, R. and Bastard, G. (2003). In: Advanced Semiconductor and Organic Nano-Techniques (Part II), edited by H. Morkoç, Elsevier, New York, and references therein.
- Dekel, E., Gershoni, G., Ehrenfreud, E., Spector, D., Garcia, J.M. and Petroff, P.M. (1998). Multiexciton Spectroscopy of a Single Self-Assembled Quantum Dot, *Phys. Rev. Lett.* **80**: 4991.
- Favero, I., Cassabois, G., Darson, J.D., Voisin, C., Tignon, J., Delalande, C., Roussignol, P., Ferreira, R., Bastard, G. and Gérard, J.M. (2003). Acoustic phonon sidebands in the emission line of single InAs/GaAs quantum dots, *Phys. Rev. B* **68**: 233301.
- Ferreira, R. and Bastard, G. (1999). Phonon-assisted capture and intradot Auger relaxation in quantum dots, *Appl. Phys. Lett.* **74**: 2818.
- Findeis, F., Baier, M., Zrenner, A., Bichler, M., Abstreiter, G., Hohenester, U. and Molinari, E. (2001). Optical excitations of a self-assembled artificial ion, *Phys. Rev. B* **63**: 121309.
- Fomin, V.M., Gladilin, V.N., Devreese, J.T., Pokatilov E.P., Balaban, S.N. and Klimin, S.N. (1998). Photoluminescence of spherical quantum dots, *Phys. Rev. B* **57**: 2415.
- Fricke, M., Lorke, A., Kotthaus, J.P., Madeiros-Ribeiro, G. and Petroff, P.M. (1996). Shell structure and electron-electron interaction in self-assembled InAs quantum dots, *Europhys. Lett.* **36**: 197.
- Fry, P.W., Itskevich, I.E., Mowbray, D.J., Skolnick, M.S., Finley, J.J., Barker, J.A., O'Reilly, E.P., Wilson, L.R., Larkin, I.A., Maksym, P.A., Hopkinson, M., Al-Khafaji, M., David, J.P., Cullis, A.G., Hill, G. and Clark, J.C. (2000). Inverted Electron-Hole Alignment in InAs-GaAs Self-Assembled Quantum Dots, *Phys. Rev. Lett.* **84**: 733.
- Gammon, D. (2000). Semiconductor physics: Electrons in artificial atoms, *Nature* **405**: 899.
- Goldstein, L., Glas, F., Marzin, J. Y., Charasse, M. N. and Le Roux, G. (1985). Growth by molecular beam epitaxy and characterization of InAs/GaAs strained-layer superlattices, *Appl. Phys. Lett.* **49**: 1099.
- Hameau, S., Guldner, Y., Verzelen, O., Ferreira, R., Bastard, G., Zeman, J., Lemaitre, A. and Gerard, J. M. (1999). Strong Electron-Phonon Coupling Regime in Quantum Dots: Evidence for Everlasting Resonant Polarons, *Phys. Rev. Lett.* **83**: 4152.
- Hameau, S., Isaia, J. N., Guldner, Y., Verezelen, O., Ferreira, R., Bastard, G., Zeman, J. and Gérard, J. M. (2002). Far-infrared magnetospectroscopy of polaron states in self-assembled InAs/GaAs quantum dots, *Phys. Rev. B* **65**: 085316.
- Hartmann, A., Ducommun, Y., Kapon, E., Hohenester, U. and Molinari, E. (2000). Few-particle effects in semiconductor quantum dots: Observation

- of multicharged excitons, *Phys. Rev. Lett.* **84**: 5648.
- Heitz, R., Veit, M., Ledentsov, N. N., Hoffmann, A., Bimberg, D., Ustinov V. M., Kop'ev, P. S. and Alferov, Z. I. (1997). Energy relaxation by multiphonon processes in InAs/GaAs quantum dots, *Phys. Rev. B* **56**: 10435.
- Heitz, R., Born, H., Guffarth, F., Stier, O., Schliwa, A., Hoffmann, A. and Bimberg, D. (2001). Existence of a phonon bottleneck for excitons in quantum dots, *Phys. Rev. B* **64**: 241305.
- Hohenester, U. and Molinari, E. (2000). Role of Coulomb Correlations in the Optical Spectra of Semiconductor Quantum Dots, *Physica Status Solidi* (b) **221**: 19.
- Hohenester, U. and Molinari, E. (2000). Excitonic and Biexcitonic States in Semiconductor Quantum Dots, *Physica Status Solidi* (a) **178**: 277.
- Htoon, H., Kulik, D., Baklenov, O., Holmes Jr., A. L., Takagahara, T. and Shih, C. K. (2001). Carrier relaxation and quantum decoherence of excited states in self-assembled quantum dots, *Phys. Rev. B* **63**: 241303.
- Htoon, H., Takagahara, T., Kulik, D., Baklenov, O., Holmes Jr., A. L. and Shih, C. K. (2002). Interplay of Rabi Oscillations and Quantum Interference in Semiconductor Quantum Dots, *Phys. Rev. Lett.* **88**: 087401.
- Inoshita, T. and Sakaki, H. (1997). Density of states and phonon-induced relaxation of electrons in semiconductor quantum dots, *Phys. Rev. B* **56**: 4355.
- Jacak, L., Hawrylak, P. and Wojs, A. (1998). Quantum dots, Springer, Berlin.
- Jankovics, A., Ferreira, R. and Bastard, G. (2004). Non-perturbative optical response of a “fluctuating” single quantum dot, *Physica E* **21**: 252.
- Jiang, H. and Singh, J. (1997). Strain distribution and electronic spectra of InAs/GaAs self-assembled dots: An eight-band study, *Phys. Rev. B* **56**: 4696.
- Johal, T. K., Pagliata, G., Rinaldi, R., Passaseo, A., Cingolani, R., Lomascolo, M., Taurino, A., Catalano, M. and Phaneuf, R. (2002). Spectroscopy of an ensemble of $\text{In}_{0.50}\text{Ga}_{0.50}\text{As}$ quantum dots following highly localized hole injection by a scanning tunneling microscope, *Phys. Rev. B* **66**: 155313.
- Jusserand, B. (2002). “Electron and Photon Confinement in Semiconductor Nanostructures”, *Proceedings of the Varenna Summer School. Course CL*, p. 63, and references therein.
- Kamada, H., Gotoh, H., Temmyo, J., Takagahara, T. and Ando, H. (2001). Exciton Rabi Oscillation in a Single Quantum Dot, *Phys. Rev. Lett.* **87**: 246401.
- Kammerer, C., Cassabois, G., Voisin, C., Delalande, C., Roussignol, P., Lemaitre, A. and Gérard, J. M. (2001). Efficient acoustic phonon broadening in single self-assembled InAs/GaAs quantum dots, *Phys. Rev. B* **65**: 033313.
- Kammerer, C., Voisin, C., Cassabois, G., Delalande, C., Roussignol, P., Klopf, F., Reithmaier, J. T., Forchel, A. and Gérard, J. M. (2002). Line narrowing in single semiconductor quantum dots: Toward the control of environment effects, *Phys. Rev. B* **66**: 041306.
- Kastner M. (1993). Artificial atoms, *Physics Today* **46**: 24.
- Klimov, V. I. (2000). Optical Nonlinearities and Ultrafast Carrier Dynamics in Semiconductor Nanocrystals, *J. Phys. Chem.* **B104**: 6112, and references therein.

- Krummheuer, B., Axt, V. M. and Kuhn, T. (2002). Theory of pure dephasing and the resulting absorption line shape in semiconductor quantum dots, *Phys. Rev. B* **65**: 195313.
- Landin, L., Miller, M. S., Pistol, M. E., Pryor, C. E. and Samuelson, L. (1998). Optical studies of individual InAs quantum dots in GaAs: Few-particle effects, *Science* **280**: 262.
- Lee, S., Jönsson, L., Wilkins, J. W., Bryant, G. W. and Klimeck, G. (2001). Electron-hole correlations in semiconductor quantum dots with tight-binding wave functions, *Phys. Rev. B* **63**: 195318.
- Lelong, P. and Bastard, G. (1996). Binding energies of excitons and charged excitons in GaAs/Ga(In)As quantum dots, *Solid State Commun.* **98**: 819.
- Li, X. Q. and Arakawa, Y. (1998). Anharmonic decay of confined optical phonons in quantum dots, *Phys. Rev. B* **57**: 12285.
- Li, X. Q., Nakayama, H. and Arakawa, Y. (1999). Phonon bottleneck in quantum dots: Role of lifetime of the confined optical phonons, *Phys. Rev. B* **59**: 5069.
- Lomascolo, M., Vergine, A., Johal, T. K., Rinaldi, R., Passaseo, A., Cingolani, R., Patanè, S., Lombardi, M., Allegrini, M., Troiani, F., and Molinari, E. (2002). Dominance of charged excitons in single-quantum-dot photoluminescence spectra, *Phys. Rev. B* **66**: 41302.
- Loss, D. and Di Vincenzo, D. P. (1998). Quantum computation with quantum dots, *Phys. Rev. A* **57**: 120.
- Marzin, J. Y., Gérard, J. M., Izraël, A., Barrier, D. and Bastard, G. (1994). Photoluminescence of Single InAs Quantum Dots Obtained by Self-Organized Growth on GaAs, *Phys. Rev. Lett.* **73**: 716.
- Michler, P., Kiraz, A., Becker, C., Schoenfeld, W. V., Petroff, P. M., Zhang, L. D., Hu, E. and Imamoglu, A. (2000). A quantum dot single-photon turnstile device, *Science* **290**: 2282.
- Moreau, E., Robert, I., Manin, L., Thierry-Mieg, V., Gérard, J. M. and Abram, I. (2001). Quantum Cascade of Photons in Semiconductor Quantum Dots, *Phys. Rev. Lett.* **87**: 183601.
- Motohisa, J., Baumberg, J. J., Heberle, A. P. and Allam, J. (1998). Anomalous excitation intensity dependence of photoluminescence from InAs self-assembled quantum dots, *Solid State Electron.* **42**: 1335.
- Oulton, R., Finley, J. J., Tartakowski, A. I., Mowbray, D. J., Skolnick, M. S., Hopkinson, M., Vasanelli, A., Ferreira, R. and Bastard, G. (2003). Continuum transitions and phonon coupling in single self-assembled Stranski-Krastanow quantum dots, *Phys. Rev. B* **68**: 235301.
- Paillard, M., Marie, X., Renucci, P., Amand, T., Jbeli, A. and Gerard, J. M. (2001). Spin Relaxation Quenching in Semiconductor Quantum Dots, *Phys. Rev. Lett.* **86**: 1634.
- Pryor, C. (1998). Eight-band calculations of strained InAs/GaAs quantum dots compared with one-, four-, and six-band approximations, *Phys. Rev. B* **57**: 7190.
- Rinaldi, R., de Giorgi, M., de Vittorio, M., Melcarne, A., Visconti, P., Cingolani, R., Lipsanen, H., Sopanen, M., Drufva, T. and Tulkki, J. (2001). Longi-

- tudinal Stark Effect in Parabolic Quantum Dots, *Jpn. J. Appl. Phys.* **40**: 2002.
- Rontani, M., Rossi, F., Manghi, F. and Molinari, E. (1999). Coulomb correlation effects in semiconductor quantum dots: The role of dimensionality, *Phys. Rev. B* **59**: 10165.
- Rontani, M., Amaha, S., Muraki, K., Manghi, F., Molinari, E., Tarucha, S. and Austing, D. G. (2004). Molecular phases in coupled quantum dots, *Phys. Rev. B* **69**: 085327.
- Rossi, F. and Kuhn, T. (2002). Theory of ultrafast phenomena in photoexcited semiconductors, *Rev. Mod. Phys.* **74**: 895.
- Santori, C., Pelton, M., Solomon, G., Dale, Y. and Yamamoto, Y. (2001). Triggered Single Photons from a Quantum Dot, *Phys. Rev. Lett.* **86**: 1502.
- Sauvage, S., Boucaud, P., Lobo, R. P. S. M., Bras, F., Fishman, G., Prazeres, R., Glotin, F., Ortega, J. M. and Gérard, J. M. (2002). Long Polaron Lifetime in InAs/GaAs Self-Assembled Quantum Dots, *Phys. Rev. Lett.* **88**: 177402.
- Schedelbeck, G., Wegscheider, W., Bichler, M. and Abstreiter, G. (1997). Coupled quantum dots fabricated by cleaved edge overgrowth: From artificial atoms to molecules, *Science* **278**: 1792.
- Schmidt, K. H., Medeiros-Ribeiro, G., Oestreich, M., Petroff, P. M. and Döhler, G. H. (1996). Carrier relaxation and electronic structure in InAs self-assembled quantum dots, *Phys. Rev. B* **54**: 11346.
- Shimizu, K. T., Neuhauser, R. G., Leatherdale, C. A., Empedocles, S. A., Woo, W. K. and Bawendi, M. G. (2001). Blinking statistics in single semiconductor nanocrystal quantum dots, *Phys. Rev. B* **63**: 205316.
- Stier, O., Grundmann, M. and Bimberg, D. (2000). Electronic and optical properties of strained quantum dots modeled by 8-band k·p theory, *Phys. Rev. B* **59**: 5688.
- Stier, O. (2001). Electronic and Optical Properties of Quantum dots and Wires, Wissenschaft & Technik Verlag, Berlin.
- Stier, O., Heitz, R., Schliwa, A. and Bimberg, D. (2002). Shape and composition effects on excitons and biexcitons in quantum dots, *Phys. Stat. Sol. A* **190**: 477.
- Stiewater, T. H., Li, X., Steel, D. G., Gammon, D., Katzer, D. S., Park, D., Piermarocchi, C. and Sham, L. J. (2001). Rabi Oscillations of Excitons in Single Quantum Dots, *Phys. Rev. Lett.* **87**: 133603.
- Toda, Y., Mariwaki, O., Nishioka, M. and Arakawa, Y. (1999). Efficient Carrier Relaxation Mechanism in InGaAs/GaAs Self-Assembled Quantum Dots Based on the Existence of Continuum States, *Phys. Rev. Lett.* **82**: 4114.
- Troiani, F., Hohenester, U. and Molinari, E. (2000). Exploiting exciton-exciton interactions in semiconductor quantum dots for quantum-information processing, *Phys. Rev. B* **62**: 2263.
- Troiani, F., Hohenester, U. and Molinari, E. (2003). High-Finesse Optical Quantum Gates for Electron Spins in Artificial Molecules, *Phys. Rev. Lett.* **90**: 206802.
- Tsuchiya, T. (2000). Biexcitons and charged excitons in quantum dots: a quantum Monte Carlo study, *Physica E* **7**: 470.

- Urayama, J., Norris, T. B., Singh, J. and Bhattacharya, P. (2001). Observation of Phonon Bottleneck in Quantum Dot Electronic Relaxation, *Phys. Rev. Lett.* **86**: 4930.
- Urbaszek, B., McGhee, E. J., Krueger, M., Warburton, R. J., Karrai, K., Amand, T., Gerardot, B. D., Petroff, P. M. and Garcia, J. M. (2004). Temperature-dependent linewidth of charged excitons in semiconductor quantum dots: Strongly broadened ground state transitions due to acoustic phonon scattering, *Phys. Rev. B* **69**: 035304.
- Uskov, A. V., McInemey, J., Adler, F., Schweitzer, H. and Pilkuhn, M. H. (1998). Auger carrier capture kinetics in self-assembled quantum dot structures, *Appl. Phys. Lett.* **72**: 58.
- Vagov, A., Axt, V. M. and Kuhn, T. (2002). Electron-phonon dynamics in optically excited quantum dots: Exact solution for multiple ultrashort laser pulses, *Phys. Rev. B* **66**: 165312.
- Vasanelli, A., Ferreira, R., Sakaki, H. and Bastard, G. (2001). Stark effects and electro-optical properties of strongly stacked dots, *Solid State Commun.* **118**: 459.
- Vasanelli, A., Ferreira, R., Cingolani, R., Sakaki, H. and Bastard, G. (2002). Electric field effects in stacked dots, *Phys. Stat. Sol. A* **190**: 551.
- Vasanelli, A., Ferreira, R. and Bastard, G. (2002). Continuous Absorption Background and Decoherence in Quantum Dots, *Phys. Rev. Lett.* **89**: 216804.
- Verzelen, O., Ferreira, R. and Bastard, G. (2000). Polaron lifetime and energy relaxation in semiconductor quantum dots, *Phys. Rev. B* **62**: 4809.
- Verzelen, O., Ferreira, R. and Bastard, G. (2002). Excitonic Polarons in Semiconductor Quantum Dots, *Phys. Rev. Lett.* **88**: 146803.
- Warburton, R. J., Schäfein, C., Haft, D., Bickel, F., Lorke, A., Karrai, K., Garcia, J., Schoenfeld, W. and Petroff, P. M. (2000). Optical emission from a charge-tunable quantum ring, *Nature* **405**: 926.
- Williamson, A. J. and Zunger, A. (1999). InAs quantum dots: Predicted electronic structure of free-standing versus GaAs-embedded structures, *Phys. Rev. B* **59**: 15819.
- Woggon, U. (1997). Optical properties of semiconductor quantum dots, Springer, Berlin.
- Zibik, E. A., Wilson, L. R., Green, R. P., Wells, J. P. R., Phillips, P. J., Carder, D. A., Cockburn, J. W., Skolnick, M. S., Steer, M. J., Liu, H. Y. and Hopkinson, M. (2003). *Proceedings of the ITQW 2003*, Evolene (Switzerland).
- Zrenner, A. (2000). A close look on single quantum dots, *J. Chem. Phys.* **112**: 7790.
- Zunger, A. (2002). On the Farsightedness (hyperopia) of the Standard $k \cdot p$ Model, *Phys. Stat. Sol. A* **190**: 467, and references therein.

This page intentionally left blank

Chapter 2

Growth and Characterization of Self-Assembled Semiconductor Macroatoms

R. Rinaldi

INFM National Nanotechnology Laboratory (NNL)

Dipartimento di Ingegneria dell’Innovazione

Università degli Studi di Lecce

via Arnesano, 73100 Lecce, Italy

2.1 Introduction

As discussed in Chapter 1, the study of the optical and electronic properties of zero-dimensional semiconductor heterostructures has been the subject of intense investigation in the last few years. The interest for such nanostructures is mainly due to their potential application to optoelectronic devices (lasers, far-infrared detectors, memories) [Weisbuch and Vinter (1991); Bimberg *et al.* (1999)] and semiconductor-based quantum computing [Kane (1998)]. As discussed in Chapter 7, in a quantum computer the straightforward sequences of binary digits or “bits” that have served computing well for over half a century are abandoned. Generally speaking, a working quantum computer uses a collection (register) of identical physical systems that can be in either of two quantum states – representing “0” and “1” – known as quantum bits or “qubits”. But quantum mechanics also allows these qubits to be placed in a superposition of the two states. In principle, therefore, a superposition of the states of a large collection of qubits can contain an enormous amount of information. Quantum computing directs the evolution of the superposition toward a final state that contains a result that depends on all of the original information, such as a number to

be factored. Unwanted interactions (other than those between the qubits) destroy the planned evolution of the computational wavefunctions and are known as “decoherence”. A powerful architecture that could benefit from the remarkable potential of quantum computing would need at least many thousands of qubits. Although qubits have been made with trapped photons, atoms and ions, it is generally thought that it should be easier to build working devices with solid-state systems. Several teams have made significant progress within the superconducting approach to solid-state quantum computing.

As anticipated, a quantum computer processes quantum information which is stored in “qubits”. If a small set of fundamental operations, or “universal quantum logic gates”, can be performed on the qubits, then a quantum computer can be programmed to solve an arbitrary problem [Steane (1998)]. The implementation of large scale quantum computers is recognized to be a technological challenge of unprecedent proportions. The qubits must be well defined and isolated from decohering influences of their environment, but must also be manipulated individually to initialize the computer, perform quantum logic operations, and measure the result of the computation [DiVincenzo (1995)]. It is well known that the major obstacle to implementing this ideal scheme is “decoherence”: the spoiling of the unitary character of quantum evolution due to uncontrollable coupling to the environmental, i.e. non computational degrees of freedom. Implementation of universal quantum logic gates and quantum computers has been proposed using atomic beams [Sleator and Weinfurter (1995)], trapped atoms [Pellizzari *et al.*(1995)] and ions [Cirac and Zoller (1995)], bulk nuclear magnetic resonance [Gershenfeld and Chuang (1997)], nanostructured semiconductors [Kane (1998); Burkard *et al.* (1999); Imamoglu *et al.* (1999)] and Josephson junctions [Averin (1998); Shnirman *et al.* (1997)]. Coherent carrier control in semiconductor nanostructures allows the coherent manipulation of carrier wave functions on a time scale shorter than the typical dephasing times [Heberle *et al.* (1995)]. To this aim, the so-called “wavefunction engineering” is an essential prerequisite for a successful implementation of ultrafast optical switching and quantum information processing in a pure solid state system. In this respect semiconductor quantum dots (QDs) appear to be among the most promising candidates, since the strong quantum confinement gives rise to a discrete atomic-like density of states and, in turn, to a reduced coupling to the solid-state environment [Jacak *et al.* (1998); Gammon *et al.* (2001)]. As discussed in Chapter 7, it has been envisioned

that optical excitations in QDs could be successfully exploited for quantum information processing [Zanardi and Rossi (1998); Quiroga and Johnson (1999)]. Some of the major advantages in using QDs are: (i) the possibility of exploiting their charge i.e. orbital and/or spin degrees of freedom to identify a “quantum bit”, (ii) the solid state large-scale integration, (iii) the potential operation at higher temperatures than in superconducting mesoscopic junctions and (iv) the long dephasing time. On the other side the disadvantages are the coupling with the environment and the low signal to noise ratio in single QDs.

In this chapter we will focus on the implementation steps and technological issues for the fabrication of quantum dot based structures for quantum information processing in quantum dots. Many theoretical ideas have been published concerning the possibility of performing universal quantum information operations by using single and coupled semiconductor quantum dots. In these proposals the computational degrees of freedom are identified with the electronic states [Imamoglu *et al.* (1999)], electron spin states [Salis *et al.* (2001)] or with energy selected inter-band optical transitions (excitons) [Troianni *et al.* (2000); Biolatti *et al.* (2000); Li *et al.* (2003); Rinaldi *et al.* (2001)].

2.1.1 *Semiconductor quantum dots*

Semiconductor QDs are also of particular interest for the study of basic quantum mechanical effects. Carriers in quantum dots are confined in three dimensions since their de Broglie wavelength is comparable to the dot size. This leads to energy quantization and to the formation of electronic shells which resemble those of natural atoms. For this reason the QDs are often referred to as “artificial atoms” [Kastner (1993); Ashoori (1996); Gammon (2000)]. The atomic-like properties of such systems can be fully exploited only through the complete control of the geometry (shape, size) and composition of the dots. The simultaneous knowledge of these parameters is necessary to engineer the wavefunctions and to exploit the dot properties in functional devices. This is a tremendous task, as it requires the refinement of growth methods and nanoscale structural, optical and electrical characterizations at the forefront of the present technologies. In this chapter, we discuss the latest developments of the field, with special attention to the methodologies developed for the control and the engineering of the electron states of InGaAs/GaAs quantum dots. We also present some technological processes aimed at the creation of single dot structures to be

embedded in quantum processing devices. Valuable information on the shape and size of the QDs can be obtained by a proper combination of electron microscopy techniques, like transmission electron microscopy (TEM) and scanning electron microscopy (SEM), and scanning probe microscopy techniques, such as scanning tunneling microscopy (STM) and atomic force microscopy (AFM). To probe the atomic-like optical properties of a single dot, local spectroscopy methods and nanotechnological processing are necessary, involving local excitation and light collection from a single quantum dot. Near-Field Scanning Spectroscopy on nanomesas containing a few dots (possibly a single dot) is normally used for spatially resolved luminescence spectroscopy. However, a better resolution which allows a direct wavefunction imaging can presently be accomplished only by Tunneling Current induced Luminescence and Scanning Tunneling Spectroscopy. Modeling is another important ingredient for the design of artificial atoms. The solution of a full three-dimensional Schroedinger equation including different contributions to the dot confining potentials, like the strain field and the existence of built-in electric fields induced by the piezoelectricity, becomes indeed crucial for the complete understanding of the artificial atom properties. In what follows we provide a brief review of these topics, in the attempt of describing the strategy for the engineering and fabrication of artificial atoms suitable for solid state implementation of quantum computation logic gates.

2.2 Fabrication and Structural Analysis of InGaAs/GaAs Quantum Dots

Different techniques are used for the fabrication of quantum dots, namely: lithographic patterning and etching of quantum well structures [Beaumont (1991); Snow *et al.*(1993); Fujita *et al.* (1995)], growth on patterned substrates [Sugawara (1995); Hartmann *et al.* (1997)] or by using stressors [Lipsanen *et al.* (1995)]. Quantum dots have also been obtained from mono-layer fluctuations of the well-barrier interface in quantum well structures [Gammon (1996)]. However, the most successful technique is the self-assembled growth by the Stranski-Krastanov (SK) mode [Ledentsov (1996); Rinaldi (1998); Passaseo *et al.* (2001)], which allows the realization of quasi-zero-dimensional semiconductors of excellent structural quality. In such a growth mode, the formation of three-dimensional islands (QDs) is driven by the strain field induced by the deposition of a few mono-layers (MLs) of

a highly strained material on a buffer layer. When the deposited layer (wetting layer, WL) exceeds a critical layer thickness (CLT), a transition from the two-dimensional (2D) to the three-dimensional (3D) growth occurs. At the CLT, the accumulated strain energy due to the lattice mismatch makes the island surfaces energetically more favorable than the flat surface, resulting in a uniformly islanded surface. The islanding process has been described using a strain-induced roughened growth front model, in which a roughened surface is stable for wavelengths above a minimum value. Since the islands are generally capped both the QDs, the wetting layer (WL) and the barrier around the QDs are elastically strained [Xie *et al.* (1994)] thus influencing the carrier confinement properties [Grundmann *et al.* (1994); Cusack *et al.* (1996)]. To increase the optical density of quantum dot structures [Solomon *et al.* (1996)], several QD layers should be grown in the structures. Since the local strain in the barrier above the dots is responsible for the vertical stacking of the dots, the top islands preferentially nucleate above the lower ones, forming vertical columns of dots [Solomon *et al.* (1996); Xie *et al.* (1995)]. The distance among the layers is a very important parameter. When this distance is comparable to the dot height, tunnel coupling occurs and a sort of dot-molecule is formed. On the other hand, for dot distances larger than 10 nm, vertically stacked dots turn out to be uncoupled. The prototype samples discussed in this chapter consist of InGaAs/GaAs single, double and 6-fold stacked quantum dots, grown by metal-organic chemical vapor deposition (MOCVD) in the Stranski-Krastanov growth mode on (001) exactly oriented GaAs substrates. Details about the growth conditions can be found in Reference [Passaseo *et al.* (2001)]. In some cases it was necessary to anneal the sample after the growth to 750°C. This post-growth annealing resulted in a tuning of the QDs emission around 1.22 eV at low temperature, which is in the detection range of the Si charge coupled device (CCD) used in the experiments (see Section VI).

The first step in the study of quantum dot sample is the structural characterization of the samples, which provides the relevant information about the dot shape and size. AFM and STM [Passaseo *et al.* (2001); Xie *et al.* (1994); Grundmann *et al.* (1994); Cusack *et al.* (1996); Solomon *et al.* (1996); Xie *et al.* (1995); Wu *et al.* (1997); Marquez *et al.* (2001); Xue *et al.* (1999); De Giorgi *et al.* (2000)] are techniques commonly used to investigate the structure of un-capped quantum dots. The first one gives important information about dot density and size dispersion. Figure 2.1

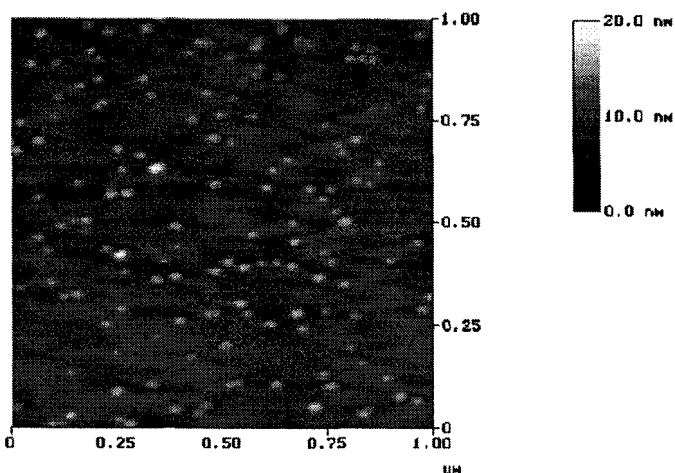


Fig. 2.1 Topographic plan view AFM image of un-capped MOCVD InGaAs/GaAs QDs.

displays a typical plan view AFM image of a planar array of QDs. In this particular sample, the dot density is about 5×10^9 dots/cm² and the size dispersion is reduced to some $\pm 10\%$, resulting in a spectral broadening of the order of ± 15 meV. Detailed information about the shape of un-capped quantum dots can be obtained by high resolution STM images which visualize the exact crystallographic faceting of the nanostructures. In Figure 2.2 a typical topographic image [bias = 2.0 V, tunneling current = 0.5 nA; [Figure 2.2(a)], together with the plan view STM image [Figure 2.2(b)] and a line-scan across the center of the single QD [Figure 2.2 (c)], is shown. In the image displayed in Figure 2.2(a), the QD shape exhibits a complex arrangement of crystal facets resulting in a slightly asymmetric shape. The side-walls are a combination of {111} and {110} planes resulting in steep inclinations with respect to the [100] plane. The base is an octagon with elongated sides aligned along the [001] and [010] directions of the substrate crystal. To obtain structural information on capped quantum dots, TEM investigation is fundamental. In particular, two beam and on zone multi-beam plan-view TEM images are routinely used to investigate such nanostructures [Zou *et al.* (1999); Liao *et al.* (1998); Ruvimov *et al.* (1995); Ledentsov *et al.* (1997)]. Figure 2.3 shows a representative (001) plan-view TEM image performed on a capped quantum dot sample. In spite of the large contrast achieved by the technique, the

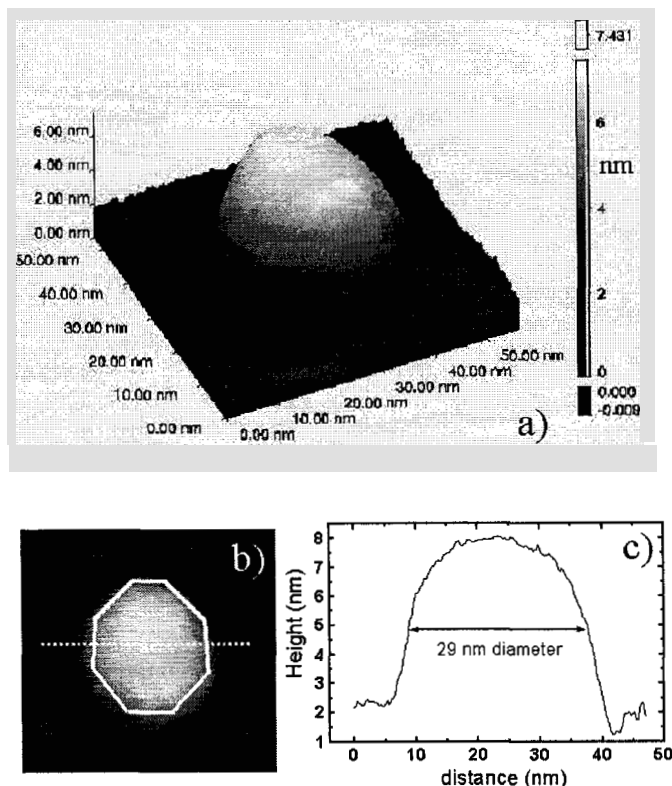


Fig. 2.2 Topographic STM image (a) on single un-capped quantum dot together with the plan view of the STM image (b) and the line-scan profile across the QD (c).

interpretation of the diffraction image is very difficult, due to the convolution of strain contrast and composition dependent contrast. This makes the experimental determination of the capped QD shape still rather controversial [De Giorgi *et al.* (2000); Ruvimov *et al.* (1995); Lian *et al.* (1998); Georgsson *et al.* (1995)]. To overcome this difficulty, high-resolution TEM (HRTEM) measurements are performed along different crystallographic directions. In Figure 2.4(a) a HRTEM image of one dot in the $\langle 001 \rangle$ zone axis is shown. Due to the chemical sensitivity of such zone axis, it is possible to distinguish from the phase contrast features the regions where In is located and, consequently, to get information about the real dot shape [De Giorgi *et al.* (2001)]. In fact, the diffraction pattern of the GaAs lattice exhibits spots arranged in squares with a bright spot at the center [Figure 2.4(b)],

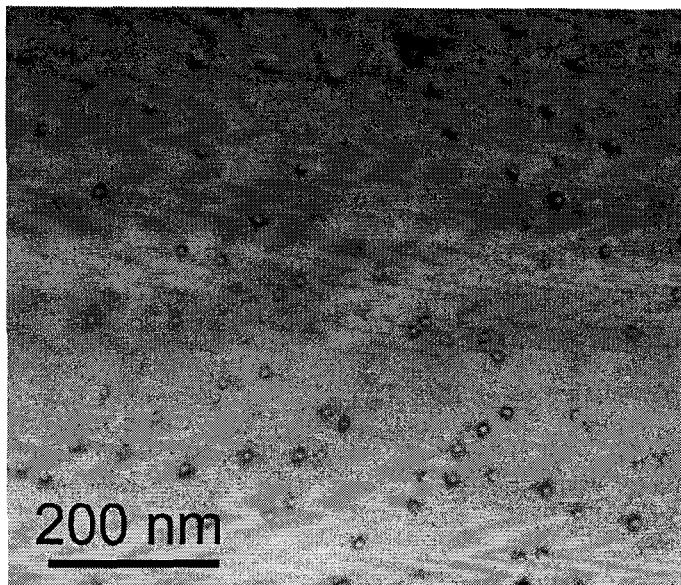


Fig. 2.3 (001) plan view TEM image of capped InGaAs/GaAs quantum dots.

whereas in the InGaAs lattice the central diffraction spot disappears [Figure 2.4(c)]. A detailed analysis of the HRTEM images shows that the capped MOCVD InGaAs/GaAs quantum dots have a cross section similar to a truncated cone, with an angle between the dot base and the dot side equal to 54 degrees. The sizes of the dots strongly depend on the growth conditions. In vertically stacked quantum dot samples, TEM measurements give additional information about the uniformity of the islands along the stack. Figure 2.5 shows the cross-sectional low-magnification TEM images obtained from three samples, consisting, respectively, of a single [Figure 2.5(a)] and six-fold stacked dot layers [Figs. 2.5(b) and 2.5(c)]. The comparison between the images of the vertically stacked quantum dot samples [Figs. 2.5(b) and 2.5(c)] shows that, although the dimensions of the bottom layers are nearly the same, the vertical size dispersion can be quite different. In particular, the sample in Figure 2.5(b) shows dots which are vertically aligned without extended defects and with a rather uniform size (only the topmost dots exhibit a small enlargement). Conversely, the sample in Figure 2.5(c) exhibits an increase of the dot size. These important differences are related to the different growth conditions which influence the quality of

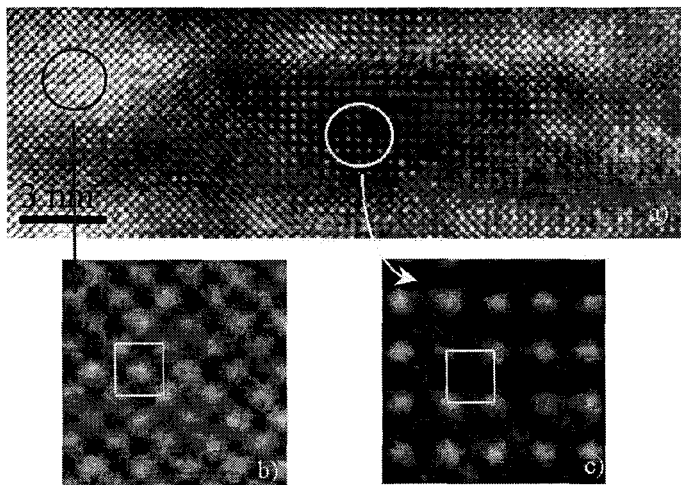


Fig. 2.4 (a) High resolution cross-section TEM image of a single dot along the $\langle 001 \rangle$ zone axis. Diffraction pattern in the GaAs barrier region (b) and in the InGaAs dot region (c).

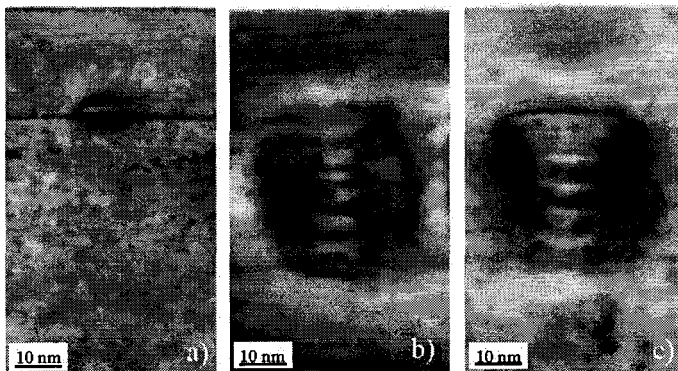


Fig. 2.5 $\langle 001 \rangle$ Cross-sectional low magnification TEM images of a single dot sample (a), and of a uniform (b) and non-uniform (c) vertically stacked dot heterostructure.

the stacked structures in terms of the vertical size uniformity. The quantum dots are formed after the deposition of only 4 monolayers (MLs) of InGaAs in the sample shown in Figure 2.5(b) and 6 MLs in the sample of Figure 2.5(c), resulting in a different total strain in the structure. The

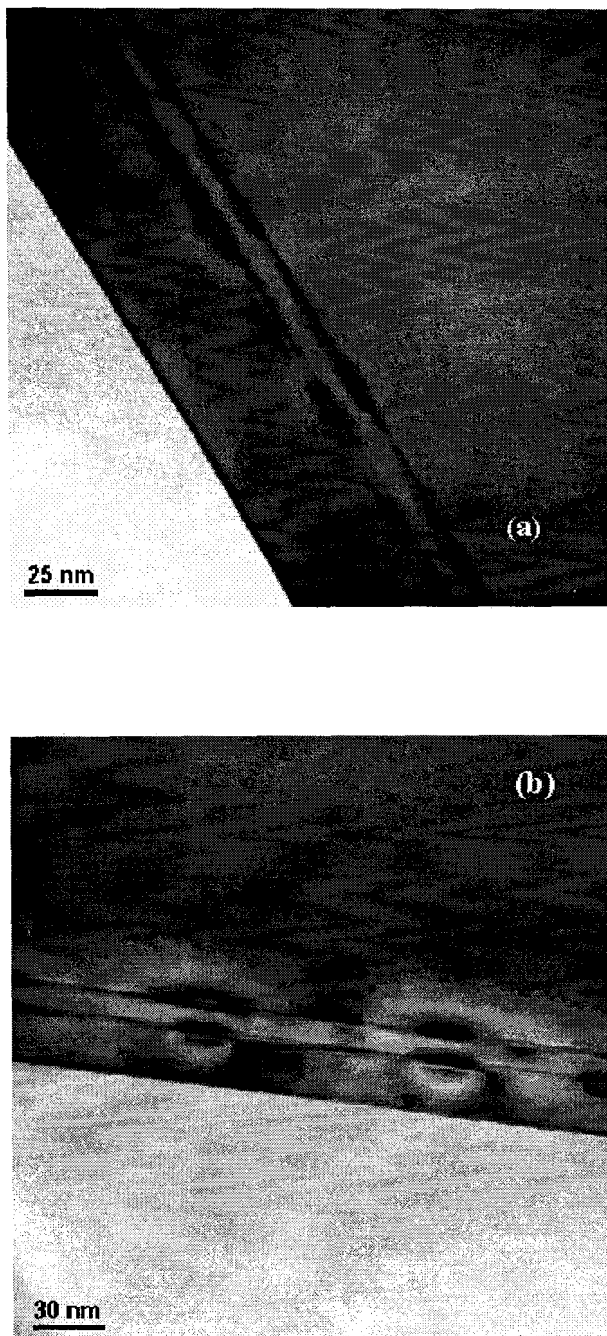


Fig. 2.6 Cross-sectional TEM pictures of annealed (a) and not annealed (b) double dot layers.

occurrence of size dispersion along the stack [like in Figure 2.5(c)] causes in fact considerable inhomogeneous broadening of the optical spectra thus preventing the use of these materials for quantum dot lasers. The achievement of uniform stacked dots is thus a crucial pre-requisite to increase the optical density of the active material without introducing large inhomogeneous broadening. Double dot layers were produced in order to realize the basic structures proposed in theoretical papers [Troiani *et al.* (2000); Biolatti *et al.* (2000)]. TEM pictures of annealed and not annealed are reported in Figures 2.6(a) and (b), respectively. Double dot layers with the same or different sizes were grown by finally tuning the growth parameters.

2.3 Nanotechnological Strategies for the Fabrication of Single-Dot Structures

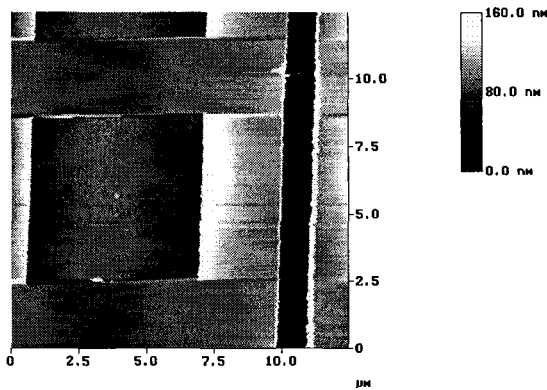


Fig. 2.7 Atomic force microscopy image of a mesa structure produced by a combination of electron beam lithography and chemical wet etching. There are a $5\text{ }\mu\text{m}$ square etched sections (where there are no QDs), at the center of which there are 100 nm diameter, 60 nm high mesa islands (where there should be a single QD).

To produce insulated single and vertically coupled quantum dots, the grown samples were processed to obtain small MESA structures, by means of electron beam lithography and wet chemical etching. The sample surface was covered by an electron beam resist 50nm thick. Then, after the exposure to the electron beam and the development in a suitable solution, a pattern consisting of a two-dimensional array of small resist circles remain on the sample surface (100-200nm in diameter). The samples were

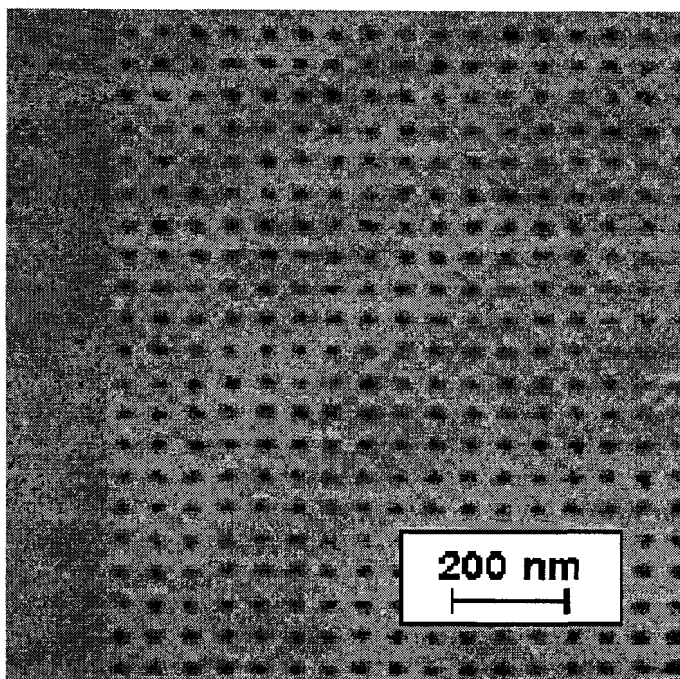


Fig. 2.8 Nanopatterned metallic mask with two-dimensional array of pin-holes

then rinsed in an ammonia hydroxide and hydrogen peroxide solution with a controlled pH in order to chemically remove the semiconductor material outside the resist circles. At the end of this step a two-dimensional array of cylindrical pillars (the MESA structures) containing single InGaAs dots remain on the sample. In Figure 2.7 the AFM micrograph of one of the realized sample is reported. Another method to operate on a single dot structure is to excite the sample through a thick metallic mask with nanometer sized holes. Masks with ordered pin-hole arrays ranging from 600 nm down to 50nm were produced (Figure 2.8) with a combination of optical lithography electron beam lithography and electrochemical deposition. The hole periodicity was in the range of few microns to provide samples for spatially resolved optical spectroscopy experiments based on microphotoluminescence and near-field luminescence. In some cases the application of an external electric field on the single and coupled dots is also needed [Biolatti *et al.* (2000)]. In this case metallic nanoelectrodes

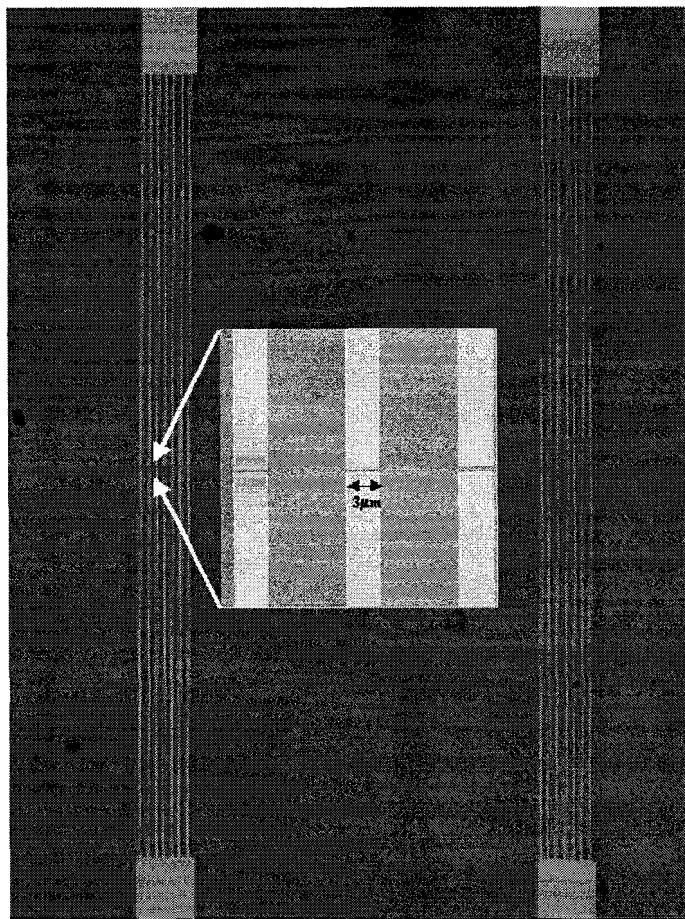


Fig. 2.9 Scanning electron microscopy image of gold electrodes of 100nm thickness, on the surface of a capped InGaAs quantum dots sample produced by a combination of electron beam lithography, chemical wet etching and gold evaporation.

separated by a gap of few hundred of nanometers were produced on the quantum dot samples by electron beam lithography and lift-off. A typical SEM image of comb shaped gold electrodes produced on the surface of a QDs sample is reported in Figure 2.9. By means of these nano electrodes it is possible to apply an in-plane electric field to the quantum dot structures [Rinaldi *et al.* (2001)].

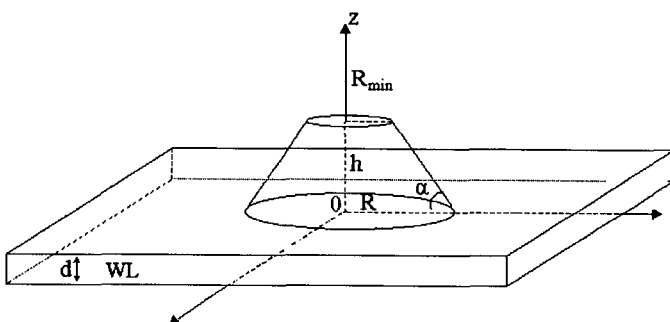


Fig. 2.10 Schematics of the quantum dot nanostructure and wetting layer.

2.4 Modeling of the Carrier Wavefunctions

For a meaningful interpretation of the experimental results obtained in quantum dots, electronic structure calculations must be correlated to the precise information about the structural properties of the QDs discussed previously. A large effort has been spent on the theoretical modeling of QD systems using different approaches: effective masses [Cusack *et al.* (1996); Fonseca *et al.* (1998)], eight-band $\mathbf{k} \cdot \mathbf{p}$ theory [Jiang and Singh (1997); Pryor (1998)] and empirical pseudopotential theory [Zunger (1998)]. The calculations of the electronic structure of QDs have been performed at various levels of approximation, assuming different quantum dot shape such as lens-shape [Lelong and Bastard (1996)] or disc-shape [Marzin and Bastard (1994)], pyramids with different facets and truncated pyramids. The differences in the predicted quantum dot ground state and excited-state emission lines, as well as in the inter-sublevel energies, reflect the different dependencies on the geometry (shape, aspect ratio) and material parameters assumed in the calculations. A model based on effective mass calculations was developed. Details can be found in Reference[Vasanelli *et al.* (2001); De Giorgi *et al.* (2003)]. The single-band effective mass-like calculation has already been used to describe several experiments such as far-infrared magneto transmission [Hameau *et al.* (1999)], and capacitance voltages curves [Lelong *et al.* (1998)]. It has also been used to describe the electronic levels of both single and stacked [Vasanelli *et al.* (2001); De Giorgi *et al.* (2003)] dot layers and satisfactorily employed to interpret the photoluminescence spectra of quantum dot samples. In the model, non

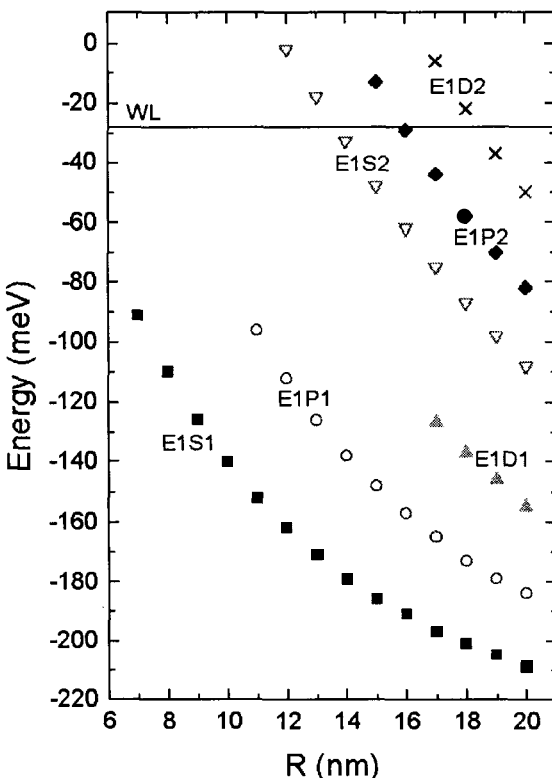


Fig. 2.11 Bound electron states of a single InGaAs/GaAs quantum dot as a function of the dot base radius, R . The aspect ratio is $h/R = 1/4$ whereas the angle $\alpha = 54^\circ$. The solid line shows the WL bound state.

interacting electrons (e) and holes (h) are subjected to three-dimensional confinement potentials $V_e(\mathbf{r}_e)$ and $V_h(\mathbf{r}_h)$. The structural analysis, performed on MOCVD InGaAs/GaAs quantum dot samples and discussed in the previous section, shows that the dots have a truncated cone shape (Figure 2.10) of height h , base radius R , and basis angle $\alpha = 54^\circ$. The dot lies on a InGaAs wetting layer of thickness d . Since the dot density is approximately $10^9 \div 10^{10} \text{ cm}^{-2} \ll 1/R^2$ for $R \sim 10 \text{ nm}$, one can neglect lateral coupling among the dots. Figure 2.11 shows the calculated energies

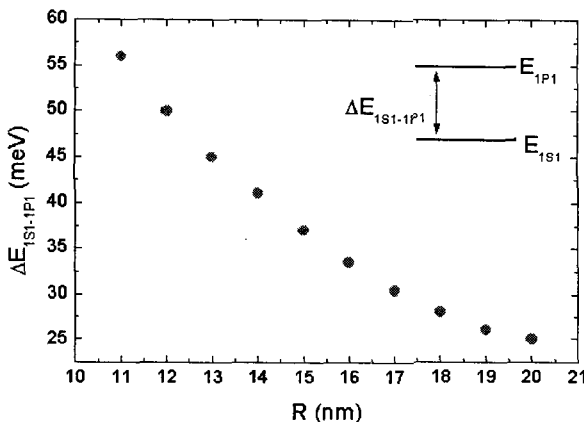


Fig. 2.12 Energy separation between the ground state $1S1$ and the first excited state $1P1$ as a function of the dot radius, R .

of the first few electron levels of a single dot as a function of its radius, R ($h/R = 1/4$ and $\alpha = 54^\circ$). At small R values (not shown in the figure) the ground level saturates toward the energy of the WL. With increasing R , the number of the bound electron states increases, whereas the energy separation decreases. This is more evident in Figure 2.12 where we plot the energy separation between the $1P1$ state and $1S1$ state as a function of the dot radius. It is clear that only the states of energy below the WL edge are localized in the dot. In addition to the truly bound states, the calculation also shows a few levels energetically located between the WL edge and the GaAs barrier (Figure 2.11). These states resemble dot resonances in the WL continuum. The electron density contour plots of the bound levels of dots are shown in Figure 2.13. The ground state ($1S1$) [Figure 2.13(a)] has a peak at the center of the dot and decays steeply toward the barrier regions. Quite generally, the ground state of actual Ga(In)As dots was found to be very well localized inside the dot. The excited states exhibits node lines and/or node plane: the $1P1$ state [Figure 2.13(b)] has a node line along the z direction, the $1S2$ state [Figure 2.13(c)] has a node plane and, finally, the $1P2$ state [Figure 2.13(d)] presents both a node line and a node plane. Moreover, the corresponding wavefunctions are more and more de-

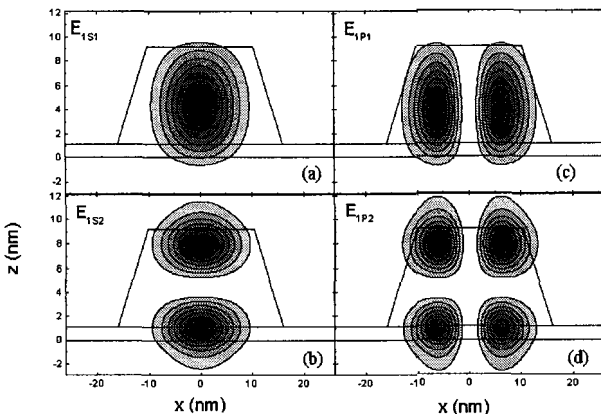


Fig. 2.13 Electron density contour-plots of a $\text{In}_{0.5}\text{Ga}_{0.5}\text{As}/\text{GaAs}$ quantum dot of dimensions $R = 16 \text{ nm}$, $h = 8 \text{ nm}$, $\alpha = 54^\circ$, $d = 4 \text{ MLs}$. E_{1S1} is the ground state of the electrons, whereas E_{1P1} , E_{1S2} and E_{1P2} are the first, second and third excited states, respectively.

localized in the (x,y) plane with increasing l . Note that the bound electron wavefunctions extend very little into the WL. For a given dot size, the binding energy of electrons and holes increases nearly linearly with increasing In content. This results in a redshift of the ground inter-band transition (Figure 2.14) since the electrons and hole become more tightly bound to the dot. The accuracy of this approach has been checked by comparison to the model of Stier *et al.* for pyramidal dots [Stier *et al.* (1999)]. In our case the dots are approximated by cones of radius such that their basal area is the same as that of the pyramid and with the same heights. Using the same material parameters, a good quantitative agreement with Stier *et al.* has been found for the ground state: the two calculations differ by less than 5 meV over the entire R range. Degenerate $1P$ levels differ at most by 15 meV. Such a good agreement with a multiband formalism witnesses that the one-band problem describes the essential features of the physics of electron states in quantum dots.

Let us now describe the electron structure of vertically stacked quantum dots. For stacked dots which are sufficiently separated along z , a molecular-like description applies. In particular, the levels of the structure can easily be assigned to the tunnel coupling of states belonging to different dots. For

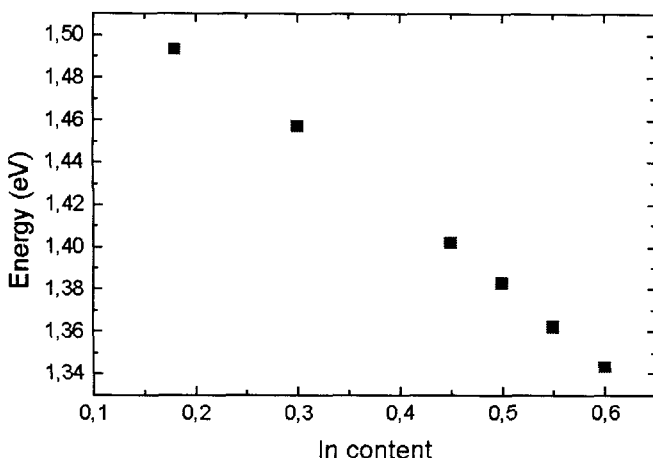


Fig. 2.14 Ground level transition energy as a function of the In content in a dot.

tightly coupled structures; on the contrary, a description in terms of an effective cylinder-like confinement profile is more adequate, since the envelopes are well delocalized along the stacking direction and exhibit only small lateral oscillations nearby the WL regions (this regime for quantum dots is the equivalent of the pseudo/alloy regime of short period superlattices). Figure 2.15 shows the $1S$ and $1P$ electron energies of a two dots structure (barrier potential equal to 697 meV, $R = 3$ nm and $\alpha = 30^\circ$) versus the distance D separating the two wetting layers. The WL edge is also plotted (solid curve) and corresponds to the ground solution of a two thin coupled quantum wells problem. For $D \leq 3$ nm the two dots are attached. The height of the first dot is kept constant ($h = 3$ nm) while the height of the lower one varies from 0 to 3 nm. For $D = 0$ one has the solutions of a single dot floating on a WL of thickness $2d$, which binds only one $1S$ and one $1P$ levels (like the single dot-single WL situation). For $D \geq 3$ nm the two identical dots are separated by an increasingly thick barrier. The energy curves for the $1S1$ and $1P1$ states exhibit a pronounced kink versus D (at $D = 3$ nm). This might seem surprising since, according to the Feynman-Hellmann theorem, one would expect the energy and its derivative to be continuous versus the dot separation. Actually, there is no contradiction since the two dots Hamiltonian changes drastically when the dots become detached: there is an extra step-like barrier which widens with increasing D . In contrast, the $1S2$, $1P2$ versus D curves do not exhibit appreciable

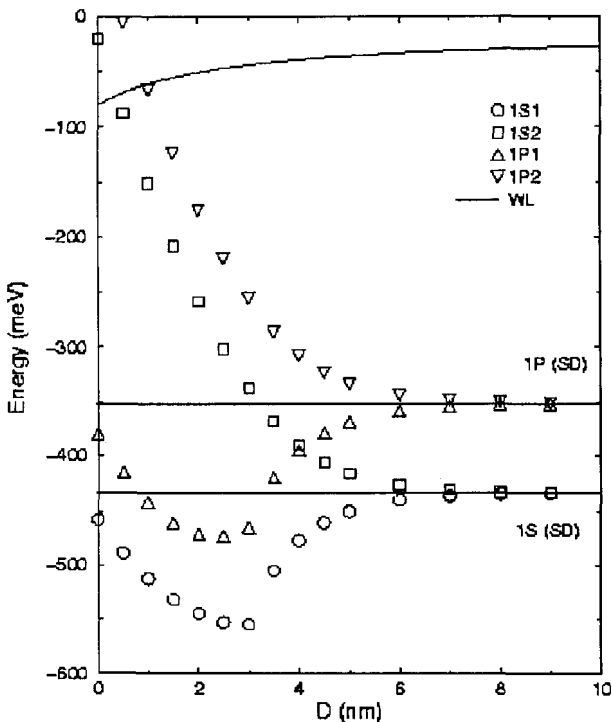


Fig. 2.15 Energies of the $1S$ -like and $1P$ -like states for the two coupled dots ($R = 10$ nm) as a function of the separation D between the two wetting layers. The height of the second dot is $h_2 = 3$ nm. The height h_1 of the first dot varies from 0 to 3 nm.

kinks. This is associated with the fact that a node in the z dependence of their envelope functions is expected in the vicinity of the middle of the structure, where the effect of the dots' detachment should be important. In the $D > 3$ nm region the envelopes of the two $1S1$ and $1S2$ (or $1P1$ and $1P2$) levels increasingly localize inside the dot regions, and resemble more and more the symmetric and anti-symmetric mixture of the two single dot solutions (energies $E_{1S1(SD)} \approx -433$ meV or $E_{1P1(SD)} \approx -351$ meV). The large dot-to-dot separation ($D > 3$ nm) corresponds to the molecular

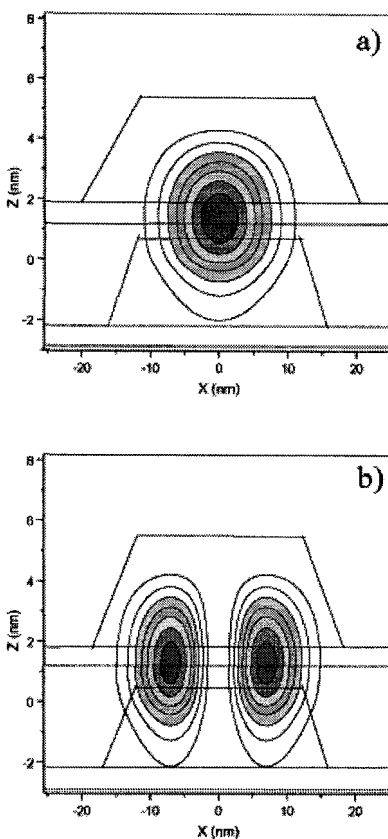


Fig. 2.16 Electron density contour plots of the first two bound states in a double-dot structure with a distance D between the two WLs equal to 3.5 nm.

regime in which atomic orbitals localized in a given dot start to hybridize at large D to give rise to bonding and anti-bonding levels, of increasingly large separation versus $1/D$. The $D < 3$ nm region has on the other hand no counterpart in molecular physics, since in the latter case the nuclei are point-like particles (while dots have a non-zero size) whose Coulomb (or filled shell) repulsion overshadows the transfer integrals at small distance (while dots are neutral). In the case of multi-dot structures in which there is no barrier the picture of a cylindrical-like three-dimensional profile for the confining potential gives a good first estimate for the $1Sj$ electron eigenstates. This is essentially due to the fact that the dots touch each other

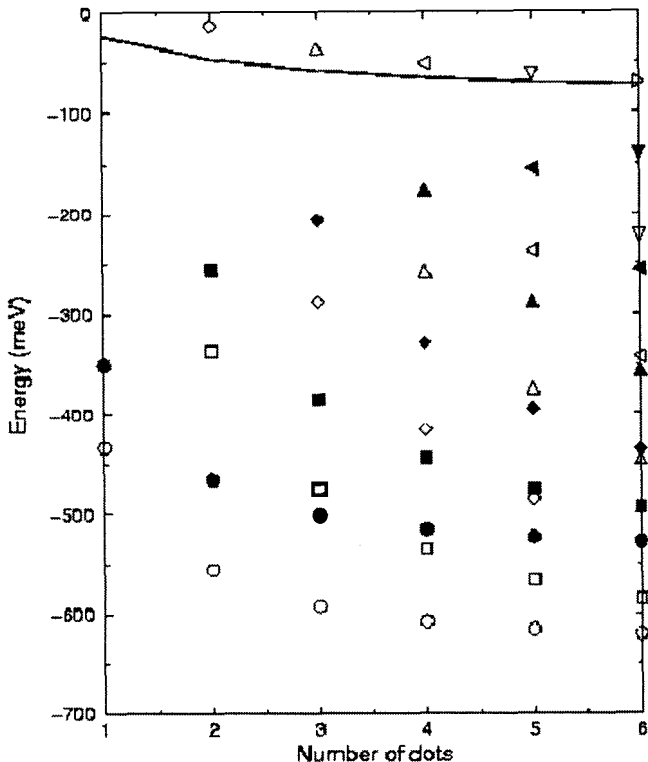


Fig. 2.17 1S-like (open symbols) and 1P-like (bold symbols) levels of a multi-dot structure as a function of the number of (identical) dots. $R = 10$ nm, $h = 3$ nm, and $\alpha = 30^\circ$.

and the InAs region form a small corridor inside the GaAs barrier. The small departures from this result come mainly from the corrections to the cylindrical profile (or to the departures of $V_{1S}(z)$ from a square well shape $V_{SW}(z)$) near the WL regions between the dots. Note that such a "cylindrical" picture becomes less valid for the excited (P, D, \dots) dot levels, for which $V_{n,l}(z) V_{SW}(z)$ become rather different inside the dot regions. Actually, the calculated wavefunctions for more excited states differ significantly from the square well solution: they display a localization inside

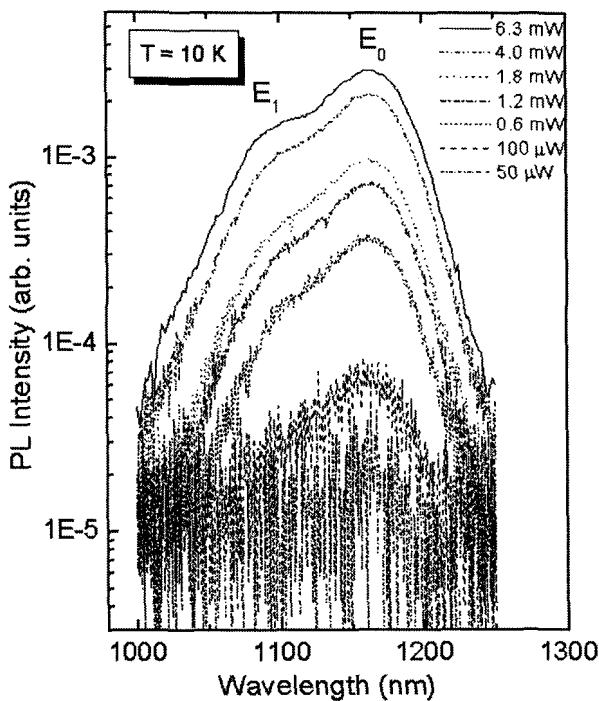


Fig. 2.18 Photoluminescence spectra performed at 10 K for different excitation power intensity (from 50 μ W to 6.3 mW). E_0 and E_1 label the ground state and the first excited state peak transitions, respectively.

different dot regions, as due to the higher value of $V_{n,l>0}(z)$ inside the dots, as compared to $V_{1S}(z)$. Figure 2.16 shows the contour plot of the first two bound electron states in a double-dot structure separated by $D = 3.5$ nm. The calculated energies of the bound 1S and 1P states as a function of the number of dots N_{dot} are shown in Figure 2.17. A single dot ($N_{dot} = 1$) binds only one 1S and one 1P levels. For two dots, the symmetric-like and anti-symmetric-like solutions discussed above are obtained. For large N_{dot} , the energies of the N_{dot} 1S-like and N_{dot} 1P-like levels pack within a finite energy range with increasing N_{dot} . The energies of the 1S-like and 1P-like ground states become N_{dot} -independent after a few dot periods,

as shown in Figure 2.17, but the convergence is slower for the energies of the topmost $1S$ -like and $1P$ -like states (it is reached only if $N_{dot} \geq 15$). For $N_{dot} \rightarrow \infty$, the effective potential $V(z)$ becomes periodic (identical dots are assumed) and the eigenstates are Bloch-like. The calculations of $1S$ and $1P$ miniband widths have been performed: $\Delta_{1S} = 492.4$ meV and $\Delta_{1P} = 473.9$ meV. We found that: (i) the minibands are very broad, a direct consequence of the strong vertical coupling between the dots; and (ii) $\Delta_{1S} > \Delta_{1P}$, due to the differences between $V_{1S}(z)$ and $V_{1P}(z)$. The calculations also predict, in agreement with Pryor, that for $D > 4$ nm the gap between the first and second miniband is greater than 30 meV while the width of the first miniband is less than 20 meV. Finally, the effect of strain field, composition disomogeneity and internal piezoelectricity have been also taken into account in the bound state calculations. Details on the effect of those parameters on the optical and electronic properties of the self-assembled InGaAs dots can be found in Reference [De Giorgi *et al.* (2003)].

2.5 Photoluminescence Experiments

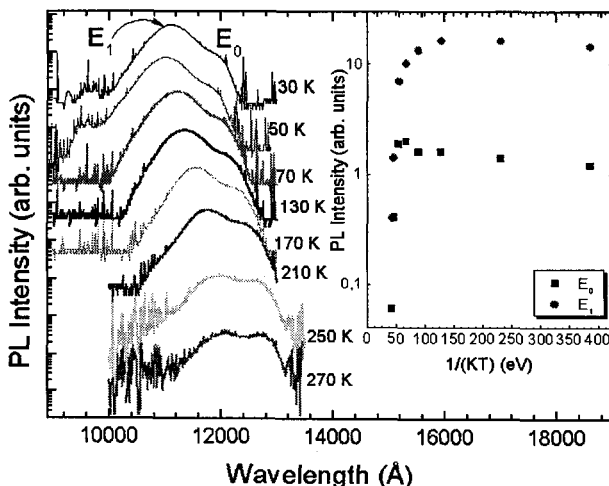


Fig. 2.19 Photoluminescence spectra performed at different temperatures. Inset: Arrhenius plot for the ground level and the first excited transition.

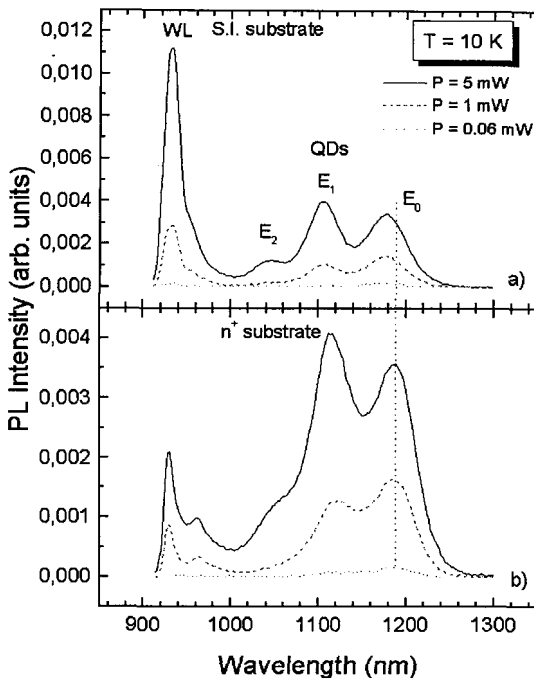


Fig. 2.20 Photoluminescence spectra of two quantum dot samples grown under the same growth conditions on S.I. (a) and n^+ -type (b) substrate. The spectra have been recorded at 10 K for different excitation power intensities, ranging between 0.06 mW and 5 mW.

As discussed so far, the calculation of the dot electronic structure is very useful not only to study dependence of the dot properties on size, shape and composition but also to interpret the photoluminescence experiments. Representative photoluminescence spectra measured at 10 K for different excitation power intensities are shown in Figure 2.18. With increasing the excitation intensity, the PL spectra show a clear band filling dynamics, which is characteristic of quantum dots with uniform size distribution. This monomodal size distribution is typical of samples having a low dot density ($\approx 10^9 \text{ cm}^{-2}$). On the contrary, samples with dot density in excess of 10^{10} cm^{-2} often show a bimodal size distribution resulting in emission spectra which exhibit structures of constant intensity ratio, independent of the excitation intensity. The ground level emission (E_0) peak is

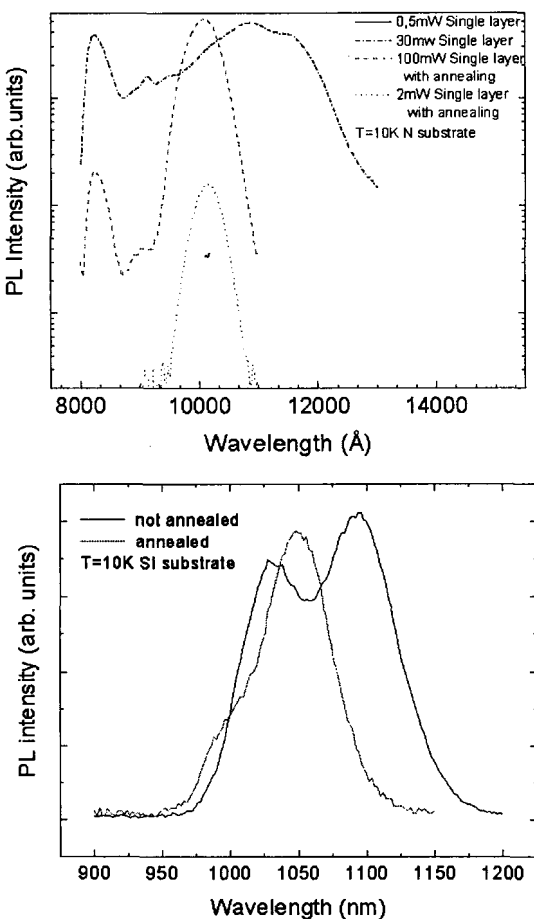


Fig. 2.21 Photoluminescence spectra of single (a) and double (b) quantum dots samples with and without the post growth annealing process

at 1167 nm with a full width at half maximum (FWHM) of about 46 meV, whereas the first excited states (E_1) is observed at 1104 nm (FWHM equal to 66 meV) as obtained by the Gaussian deconvolution of the PL spectra. The spectra show a inhomogeneous broadening due to the non-uniformity of the quantum dot size as well as the composition and shape. Even very high quality samples display this type of broadening. The energy splitting between the ground level and the first excited level is about 60 meV. The

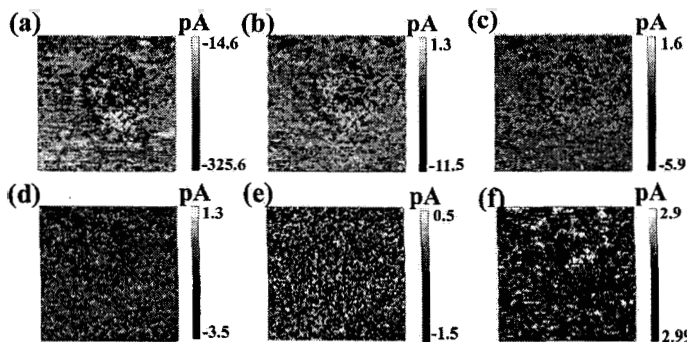


Fig. 2.22 Current images, $80 \times 80 \text{ nm}^2$, of a single, isolated quantum dot as a function of the bias voltage (a) -1.50 V, (b) -0.79 V, (c) -0.65 V, (d) -0.54 V, (e) 0.00 V and (f) 0.61 V. The tunneling set-point, defining the tip-sample separation, is given by a bias voltage of 2.0 V and tunneling current of 0.5 nA

theoretical results for this sample confirm the existence of only two bound levels in the conduction band (CB), (E_{1S1}^e, E_{1P1}^e) and of more than two bound levels in the valence band (VB), ($E_{1S1}^h, E_{1P1}^h, E_{1S2}^h$ and so on). The optical transitions involving levels of different symmetry are very weak, whereas those involving levels of same symmetry are more intense. Among these, the main transitions are those between the ground levels and the first excited levels in CB and VB, respectively, that is $E_0 = E_{1S1}^e \rightarrow E_{1S1}^h$ and $E_1 = E_{1P1}^e \rightarrow E_{1P1}^h$, the others having much smaller oscillator strengths. The theoretical energy splitting ($E_1 - E_0$) is estimated to be 65 meV, in good agreement with the experimental data. The PL spectra of the QD structure for different temperatures are shown Figure 2.19. With increasing temperature it is possible to observe two main effects: (i) a red-shift of the peaks and (ii) a reduction of the luminescence intensity. The red-shift of the peaks is due to the energy-gap reduction with temperature [Paul *et al.* (1991)] whereas the intensity reduction is due to the thermal escape of the carriers from the dot levels and to the thermal activation of non radiative recombination channels. Plotting the integrated emission intensity of the luminescence peaks (obtained by the Gaussian deconvolution) versus $1/(kT)$ (see Arrhenius plot in the inset of Figure 2.19), we found that the depletion of the first excited state corresponds to a small increase of the integrated intensity of the ground level. This is due to the capture in the ground level of carriers escaped from the excited state. Above 180 K, the ground state also begins to empty due to the thermal escape effect. Since

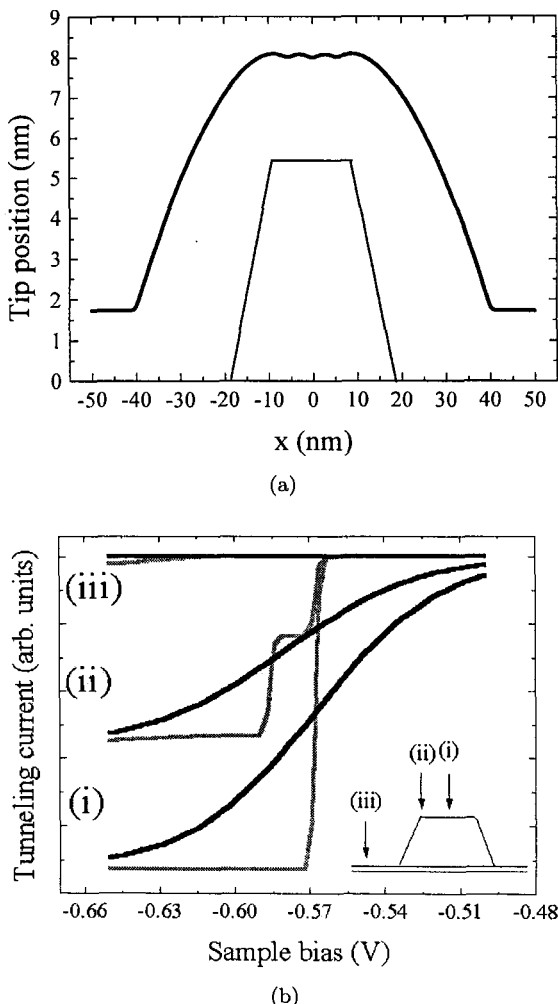


Fig. 2.23 (a) The calculated tip variation, $z(x)$, across the QD, and (b) calculated tunneling spectra, $I(\phi)$, for (i) the center, (ii) periphery of the QD and (iii) the WL region at 300 K (black) and 10 K (gray).

for the realization of a real dot device it is necessary to grow the nanostructures on doped substrates, the study of the optical properties of the dots on different substrates, namely semi-insulating (SI) and n^+ -type (Si doped), is very important. In Figure 2.20, we display the PL spectra at different excitation intensities of two dot samples, grown in the same growth conditions,

on a semi-insulating (SI) [Figure 2.20(a)] and n^+ -type (Si doped) [Figure 2.20(b)] substrate. The emission efficiency with respect to the WL is very different in the two samples. This is due to a small change of the strain field experienced by the InGaAs layer grown on the different substrates, which results in a slightly different critical layer thickness (CLT). In fact, in the heavily doped substrates, the strain field is increased by a very small quantity with respect to the SI substrate, due to the smaller covalent radius of the Si atoms (preferentially incorporated on Ga sites in the GaAs lattice) with respect to Ga atoms. This results in a slightly lower lattice parameter (by a factor 10^{-5}), which was measured by X-ray diffraction in the doped substrate with respect to the undoped GaAs. The difference of the strain field also induces a small variation of the dot size which in turn causes a small energy shift of the luminescence peaks (see Figure 2.20).

Finally, in Figure 2.21 we show typical spectra recorded on single (Figure 2.21(a)) and double (Figure 2.21(b)) with and without the post growth annealing process. The blue shift of the emission of the annealed samples is clearly visible in both structures.

2.6 Single-Dot Spectroscopy

As discussed in the previous section, the study of the electronic and optical properties of an ensemble of quantum dots has been hindered by the inhomogeneous broadening of the spectral features (usually >30 meV in the spatially averaging techniques such as photoluminescence), due to the non-uniformity in the dot size (usually $\approx 10\%$), shape and composition. This broadening obscures Coulomb effects involving energy shifts at approximately the meV level. More recently, the development of spatially resolved techniques has circumvented these problems, enabling the investigation of the optical properties of individual dots for which the broadening is purely homogeneous (<50 μ eV) [Marzin *et al.* (1994); Gammon *et al.* (1995); Empedocles *et al.* (1996); Bacher *et al.* (1999); Landin *et al.* (1999); Dekel *et al.* (2000); Thompson *et al.* (2001)]. Sharp, narrow lines, as in gas-phase spectroscopy, are observed in the single dot spectra where energy separations and intensities reflect the shell-like structure and population of the QD states. However, there is a departure from the analogy with atomic physics due to the appearance of multi-peaked structures which arise as consequence of the charging [Hartmann *et al.* (2000); Karlsson *et al.* (2001); Regelmann *et al.* (2001)] and the multi-particle capture characteristics of

the QDs [Dekel *et al.* (1998); Bayer *et al.* (2000)]. In this section recent reports of single dot scanning tunneling microscopy spectroscopy (STS), scanning near-field optical microscopy (SNOM) and tunneling current induced luminescence (TCIL) are presented.

2.6.1 Wavefunction spectroscopy

Scanning tunneling spectroscopy (STS) of isolated QDs, produced by colloidal synthesis [Alperson *et al.* (1995); Banin *et al.* (1999); Alperson *et al.* (1999); Millo *et al.* (2000); Millo *et al.* (2001)] as well as cross-sectional studies of epitaxially self-assembled QDs have been reported in recent years [Legrand *et al.* (1998); Grandidier *et al.* (2000)]. In these studies, the discrete nature of the electronic structure and the spatial variation of the confined electronic wavefunctions of single QDs was demonstrated. In the following we present the STS imaging of intact un-capped $\text{In}_{0.5}\text{Ga}_{0.5}\text{As}$ QDs grown by strain-driven self-assembled epitaxy on a GaAs matrix. The origins and nature of the measured tunneling current is investigated by comparing with calculated tunneling current spectra [Johal *et al.* (2002a); Johal *et al.* (2002b)].

Tunneling spectra have been measured simultaneously with topographic images of single QDs. During the spectroscopy imaging measurements, that is, the spatial variation of the tunneling current, as a function of the sample bias, the tunneling current feedback loop is switched off and the set point which established the tip-sample distance was that of the tunneling conditions for the topographic images. In this way all purely topographic dependencies of the tunneling current were removed.

Typical I-V curves measured on the QD and in the WL region are shown in Figure 2.22. Since in this quantum dot the chemical composition of the WL and QD is nominally the same, the differences in the tunneling current spectra, such as the smaller zero current gap of the QD with respect to the WL, can be indicative of the smaller electronic gap which results in quantum confinement and the formation of QD states [Franceschetti and Zunger (2000)]. At negative sample biases [Figure 2.22(a-d)], which correspond to tunneling out of occupied states, there is a clear contrast in the current signal between the region of the QD and the WL. This current contrast persists and exhibits a spatial variation within the structure of the QD over the voltage range -1.50 V to -0.51 V [Figure 2.22(a-d)] and then disappears abruptly. In the voltage range between -0.51 V to 0.60 V [Figure 2.22(d-f)] there is an absence of contrast within the noise levels of these

measurements. This voltage range extends over the region of the QD energy gap and the Fermi level resides at the middle of this gap. Very little or no current contrast is observed in the positive voltage range corresponding to tunneling into the unoccupied states of the QD. The spatially resolved spectroscopic features at negative sample biases (such as those shown in Figure 2.22) were observed from QDs of different samples as well as using different tips (both W and Pt-Ir tips). Therefore it can be assumed that these features are independent of the tip density of states and tip effects. Since current contrast was observed only in the negative bias range, when tunneling out of the occupied states, the proceeding discussion shall be confined to the occupied states of the QD and WL, that is, the “hole” states.

In seeking to interpret the measured tunneling current images the spatially resolved tunneling current of an isolated InAs QD situated above a WL in vacuum has been calculated. Following Tersoff and Hamann, the

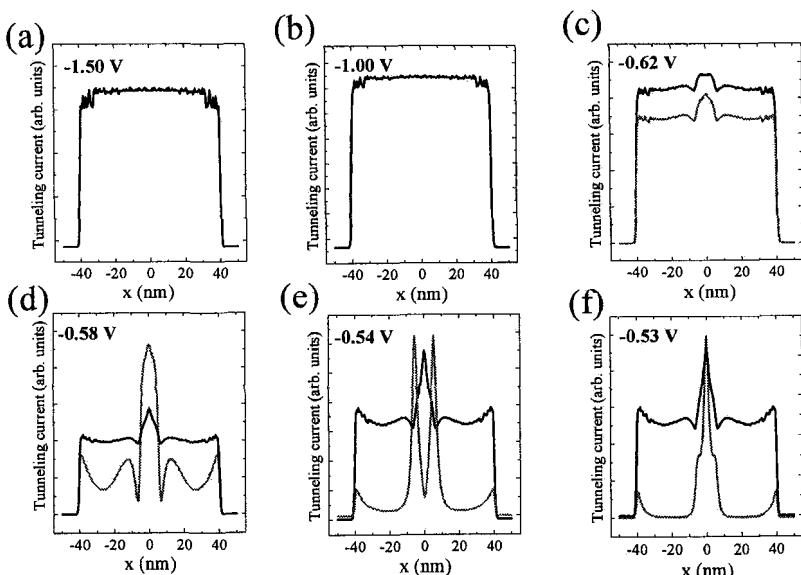


Fig. 2.24 The calculated tunneling current profiles, $I(x)$, for bias voltages of (a) -1.50 V , (b) -1.00 V , (c) -0.62 V , (d) -0.58 V , (e) -0.54 V , and (f) -0.53 V at 300 K (black) and 10 K (gray).

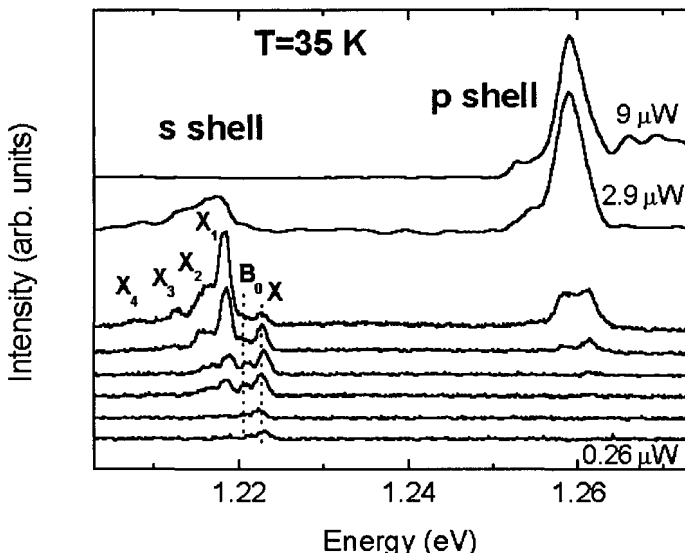


Fig. 2.25 Photoluminescence spectra of a single InGaAs quantum dot, excited by the 514.5 nm line of an Argon laser at 35 K, as a function of the excitation intensity, with increasing intensity from the bottom upward ($0.26 \mu\text{W}$, $0.40 \mu\text{W}$, $1.3 \mu\text{W}$, $1.7 \mu\text{W}$, $2.0 \mu\text{W}$, $2.89 \mu\text{W}$, $4.4 \mu\text{W}$).

tunneling current is given by

$$I(\mathbf{r}_t, E, \phi) \approx \sum_{n, l \geq 0, j} g_l \left[\frac{1}{1 + \exp(-\beta E_{nlj})} - \frac{1}{1 + \exp(-\beta(E_{nlj} + \phi))} \right] |F_{nlj}(\mathbf{r}_t)|^2 + \frac{S}{4\pi^2} \int d^2k \left[\frac{1}{1 + \exp(-\beta E_k)} - \frac{1}{1 + \exp(-\beta(E_k + \phi))} \right] |\Psi_k(\mathbf{r}_t)|^2 \quad (2.1)$$

where the QD bound states, $F_{nlj}(\mathbf{r}_t)$, are described by quantum numbers n , l , j , and the WL eigenstates, $\Psi_k(\mathbf{r}_t)$, by the 2D wavevector \mathbf{k} ; $\beta = 1/k_B T$ and the applied bias, ϕ , is defined as $\phi = \phi_t - \phi_s$ where ϕ_t is the tip chemical potential and ϕ_s is the sample chemical potential.

The QD bound states can be calculated following the envelope function approach developed in the previous section. Since the quantum dots are un-capped the influence of the vacuum is treated by using a high (2 eV) potential barrier. The tunneling junction comprises both the vacuum barrier and the surface of the QD and the WL, which will

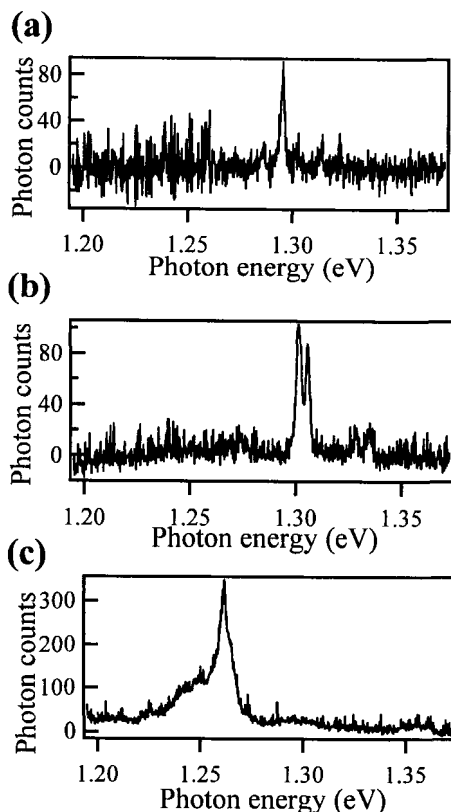


Fig. 2.26 Tunneling current induced luminescence spectra, gap voltage of -1.5 V and tunneling current of 5 nA, where tunneling contact has been made at different locations on the GaAs cap surface, (a) from a single QD, (b) from a pair of coupled QDs and (c) from an ensemble of adjacent quantum dots.

invariably be oxidized. To a first approximation, this oxide can be treated as an insulating layer. There exists a large body of work on tunneling spectroscopy of such junctions, where when treating the insulator barrier as a vacuum barrier the gross features of the calculated tunneling current spectra have been qualitatively correct [Duke (1969); Wiesendanger (1998)]. For the calculation of the spatially defined tunneling current the tip-sample distance has been defined for a constant tunneling current for an applied bias of $\phi = 2$ eV. In these conditions, the tip position variation simulates the spatial extent of the charge density associated with

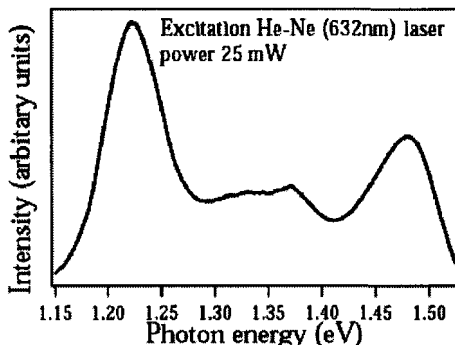


Fig. 2.27 Ensemble photoluminescence spectrum of the $\text{In}_{0.5}\text{Ga}_{0.05}\text{As}$ quantum dot (main peak 1.22 eV), the wetting layer (1.37 eV) and GaAs (\approx 1.51 eV).

the localized, confined states of the QD and is accordingly shown in Figure 2.23(a) and compared with the geometric shape of the QD. The lateral extent of the charge density is accentuated in these calculations which do not accurately account for the decay of the wave functions outside the QD. Calculated tunneling current spectra are shown in Figure 2.23(b) together with the calculated tunneling current intensity profiles (Figure 2.24) for a series of biases for different locations in the QD and WL. At a low bias of -0.53 eV (Figure 2.24(f)) the contribution to the tunneling current is due solely to the 1S-like state which is spherically symmetric and gives rise to a sharp, localized contribution to the tunneling current at the center of the QD. With increasing bias to -0.54 eV (Figure 2.23(e)), there is the contribution due to the 1P-like states which results in an additional tunneling current signal encircling the centered 1S signal. Further increasing the bias leads to the onset of tunneling current originating from the higher level eigenstates and then due to the delocalized WL states. The influence of finite temperature results in the mixing of these contributions, the consequence of which, at room temperature, is the inability to distinguish the onset of tunneling current due to the different eigenstates. However, it is the spatial resolution afforded by the STM which allows these states, to some degree, to be identified. In comparing the measured tunneling current images with the calculated tunneling current profiles there are similarities in the spatial extent and symmetry. The highly localized structure at the center of the QD observable at a voltage of -0.54 V compares well with the calculated contribution due to the 1S- and 1P-like eigenstate of the single QD. The increase in the spread of the intensity at the center of the QD for

the -0.65 V bias together with the appearance of the current intensity at the periphery of the QD can be identified with the higher eigenstates of the QD and the contribution due to the delocalized WL states. The absence of current contrast in the positive bias range together with the very measurement of a sizeable, permanent tunneling current when tunneling into or out of the localized, confined states of the QD requires further discussion. The electronic structure of the single QD is best described by occupied and unoccupied, highly localized, atomic-like states. The maximum number of electrons or holes that the single QDs can host when excited is, in the case of the QDs reported here, sixteen and this charge density is delocalized over the volume of the QD. This would imply, when considering a QD in complete isolation, that tunneling into these states, will result in a tunneling current density well below the detection limit of the STM. The clear observation of an increase in the tunneling current at the QD implies that, as in the case of point defects at semiconductor surfaces [De la Broise *et al.* (2000)], to achieve a permanent tunneling current measurable by STM the QD needs to exchange carriers with the bands of the host GaAs crystal and the WL continuum by the emission and capture of electrons and holes. When tunneling out of the occupied states of the QD (the negative bias) the rate of capture of electrons has to be efficient and vice versa when tunneling into the unoccupied states (the positive bias), the evacuation of electrons should be efficient. Carrier relaxation in QD by phonon scattering [Heitz *et al.* (1997)], Auger scattering [Ferreira and Bastard (1999)] and electron phonon coupling leading to the formation of “ever-lasting” polarons have been reported, as well as escape of electrons and holes by thermal activation and tunneling into the WL [Kapteyn *et al.* (2000)]. From these STS measurements alone it is not possible to distinguish the dominant mechanism for the carrier relaxation in the QD. However, it is clear that hole escape from the QD is sufficiently fast. And since below the dot layer there is a reservoir of free carriers due to the n-type doping of the GaAs layer, the hole states are filled in a time scale faster than the tunneling out of these states (estimated to be of the order of picoseconds [Fertig (1993)]). So there is an effective higher density of occupied states resulting in a measurable tunneling current from the occupied QD state. In the case of the unoccupied states there are a number of conspiring factors, which may give rise to a real, and an apparent, occupation of the unoccupied states, thus reducing the contrast between the QD and the WL in the current images in positive bias. At room temperature there is a finite probability that these states are partially occupied due to intrinsic and extrinsic carriers.

Alternatively defects at the surface of the dot act as trapping centers which prevent the population of the unoccupied states of the QD. Although, this process will reduce the tunneling current, it should not completely prevent tunneling into the unoccupied states of the dot. A further explanation for the absence of a strong contrast in the positive bias is the absence of an efficient evacuation process of the QD electrons. The time scale of electron escape from charged, completely isolated QDs has been predicted to be of the order of hours [Martorell *et al.* (2001)]. However in the case of QDs embedded in a GaAs matrix there is the possibility of radiative recombination, de-excitation by coupling to the lattice phonons [Heitz *et al.* (1997)] and/or tunneling into the GaAs barrier [Kapteyn *et al.* (2000)]. For radiative recombination to be a major de-excitation path there is a need for the availability of hole states into which the electron can fall. For this argument doping becomes an important issue. To date, the relaxation processes in the QD are not completely understood; therefore at this point conclusive explanations are not forthcoming and further work is required, for example STS measurements of QDs grown on p-type substrates are desirable.

In conclusion, in the voltage dependent current images the charge density associated with the discrete occupied states of the QD, the hole wavefunctions, can be identified by comparison with theoretical calculations of the tunneling current. The analogy with point defects is instructive in understanding the origins of the measured tunneling current from the discrete, localized states of the QDs. The important consideration is that an exchange of carriers with the hosting material, the bulk GaAs and the InGaAs WL, is required to form a measurable, permanent current. This suggests that STS imaging of zero-dimensional structures, such as quantum dots, can only be interpreted correctly when not treating the QD as an isolated entity but very much part of the complete system which involves the hosting crystal.

2.6.2 *Optical spectroscopy*

Near-field Scanning Optical Microscopy (NSOM) is another powerful technique to study single dot optical properties with a sub-wavelength spatial resolution [Betzig *et al.* (1991)]. There are two distinct ways of operating an NSOM: (i) the sample is excited in near-field by using a tip of sub-wavelength aperture and the luminescence is collected in far-field (emission mode), as it will be shown in the following; (ii) the luminescence is collected in near-field through the tip (collection mode). In collection mode the spa-

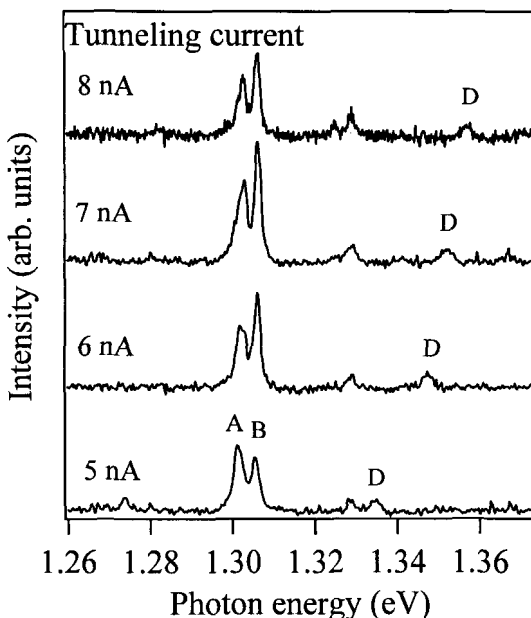


Fig. 2.28 Tunneling current induced luminescence spectra of laterally coupled $\text{In}_{0.50}\text{Ga}_{0.50}\text{As}$ quantum dots, at a gap voltage of -1.5 V, as a function of tunneling current.

tial resolution is determined by the dimension of the tip, whereas in emission mode the diffusion of the generated carriers and excitons dominates the resolution of the technique. This effect can be removed by isolating the single dot in a nanomesa, of typical dimensions $200 \times 200 \times 30 \text{ nm}^3$, realized by Electron Beam Lithography (EBL) at the center of a typically $6 \times 6 \mu\text{m}^2$ window. The single dot luminescence is excited in near-field condition by the continuous wave 514.5 nm line of an Argon laser and it is collected in far-field and dispersed by a 0.3 m of focal length spectrograph equipped by a cooled low noise CCD detector (Andor Technologies). Time integration of the order of several minutes (5- 10 min) is used in most experiments. In Figure 2.25 the excitation intensity dependence of the single dot PL spectra is shown. Sharp lines associated with single dot recombination processes can be observed. The main features of the spectra are: (i) at very low excitation intensity ($0.26 \mu\text{W}$) a single sharp line, of full width half maximum (FWHM) of 1.5 meV, appears at 1.223 eV (Figure 2.25, bottom line); (ii) with increasing excitation intensity five spectral features appear in the

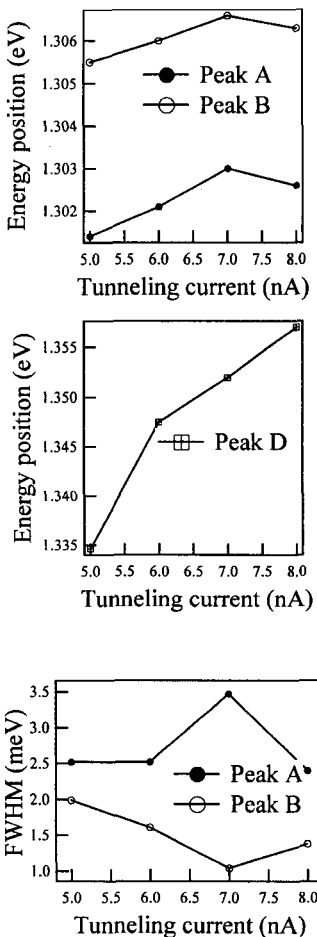


Fig. 2.29 (a) The energy position of *A* and *B* peaks, and (b) the energy position of *D* peak as a function of tunneling current. (c) FWHM as a function of tunneling current.

energy range of 10 meV below the fundamental line. All these lines are related to the s-shell of the QD; (iii) a further increase of pumping intensity causes the saturation of the s-shell lines and the appearance of two p-shell bands at 1.258 eV, which are split by about 3 meV. When the excitation intensity is varied between 2.9 μ W to 9.0 μ W, the p lines are dominated by the emergence of components which are red-shifted by 3.5 meV with respect to the original p-shell signal; (iv) at very high excitation intensity

(9 μW) the s-shell disappears, the p-shell becomes more structured, with a shoulder in the low energy tail of the high intensity feature at 1.258 eV. The appearance of the spectral features as a function of the excitation density is a clear signature of the progressive shell filling and of the few-particle effects occurring in the dot with increasing carrier occupation [Lomascolo *et al.* (2002)]. The identification of the different peaks is possible by means of detailed theoretical calculations [Dekel *et al.* (2000); Rontani *et al.* (1999); Brasken *et al.* (2001)]. Taking into account the Coulomb interaction and correlation between few particles, the optical spectra can be determined as a function of the exact number of electrons and holes in a single quantum dot. Nevertheless, due to the continuous wave nature of the optical excitation in many experiments, a steady state condition in the creation-recombination mechanisms of electron-hole pairs in the dot is achieved. It is therefore reasonable to expect that the measured optical spectra, by temporal averaging, encompass contributions due to transitions involving different numbers of carrier captured by QD. With this assumption, and analyzing the variation of the integrated intensities of the salient components of the spectra (determined by fitting the spectra peaks with Lorentzian and Gaussian line-shape) with increasing power intensity, we determined the recombination nature of the peaks. The single peak X_0 at 1.223 eV (Figure 2.25) arises from the recombination of the exciton ground state, which corresponds to the configuration where the carriers occupy the respective s-shells. With increasing photoexcitation intensity, recombination from the multiexciton states are expected to show up in the optical spectra. The peak B at 1.221 eV (Figure 2.25) corresponds to the transition between the neutral biexciton and the exciton ground, whereas the peak at 1.218 eV to the isoenergetic transition between the charged biexciton and the exciton ground state, X_1 , and between the charged exciton and the neutral exciton ground state. As the number of carriers is further increased, the interaction and correlation between the carriers induce new peaks in the s-shell and the p-shell is progressively filled.

A further enhancement of the spatial resolution can be achieved by tunneling current-induced luminescence (TCIL). The high spatial resolution is afforded by the use of a scanning tunneling microscope tip to inject carriers, either electrons or hole, into capped quantum dots [Johal *et al.* (2002c)]. A planar geometry is employed where carriers are injected into the cap layer directly above the plane of QDs. In unprocessed samples the multitude of QDs are accessed, so that spectral diffusion, excitation transfer and inter-dot tunneling can occur. The TCIL was measured by using an STM

operating in ultra-high vacuum (UHV) equipped with a liquid helium flow cryostat and platinum-iridium tips. The luminescence signal was collected by a lens and dispersed by a 0.3 m monochromator and detected by a cooled Si charge coupled device. The spectral resolution in the region of 1 μm was measured to be 0.25 meV and the typical integration time for individual spectra was 1000 seconds. In Figures 2.26(a), 2.26(b), and 2.26(c) TCIL spectra collected when the tip is in tunneling contact at different points of the cap surface, with tunneling conditions of a gap voltage of -1.5 V and a tunneling current of 5 nA, are shown. No TCIL signal was detected for gap voltages less than -1.5 V, nor for positive biases. The first spectra, Figure 2.26(a), exhibits a single well-defined peak at 1.294 eV with a full width half maximum (FWHM) of 2.0 meV. Figure 2.26(b), at another point of tunneling contact on the sample surface, shows a doublet at 1.303 eV with a 4.2 meV splitting where the two components have FWHMs of 2.1 meV. These coupled peaks are accompanied by broader ($\text{FWHM} \approx 3.5 \text{ meV}$) less intense peaks at separations of 26 \div 31 meV on either side. At a different point on the sample surface, the spectrum, shown in Figure 2.26(c), is dominated by a complex structure with a main peak at 1.257 eV of FWHM of 2 meV accompanied by a low energy structure as well as small, broad peaks on the high energy side, at 1.300 eV and 1.356 eV. A striking aspect of this spectrum with respect to previous ones in Figure 2.26(a) and Figure 2.26(b) is the four-fold increase in photon intensity. It is instructive to compare the TCIL spectra with the photoluminescence (PL) spectrum of the sample. The PL spectra, measured by exciting by a HeNe laser, 30 mW power, is shown in Figure 2.27. The QD PL emission is centered at 1.22 eV, with a FWHM of 32 meV, the 1.29 \div 1.34 eV region corresponds to the emission from the smaller QDs and the peak centered at 1.37 eV is due to quantum well-like emission from the wetting layer (WL). By this comparison, it is observed that the TCIL peaks observed in Figs. 2.26(a) and 2.26(b) do not lie strictly in the energy region of the main QD PL emission. Such a result can be easily explained. Following Renaud and Alvarado [Renaud and Alvarado (1991)], the TCIL consists of a series of processes: (i) tunneling out of (and therefore injecting holes into) the GaAs cap region, (ii) transport of ballistic holes across cap layer, which are captured by WL and QD states and followed by, (iii), radiative recombination. The hole injection is characterized by a cone of diffusion, which defines the spatial resolution of the technique. Such a cone-angle is not well-defined and it is dependent on various parameters such as the tip dimensions, shape, the surface morphology and composition [Dahne-Prietsch and Kalka (2000)].

The influence of these extraneous factors was observed in the TCIL spectra measured using different tips (not reported here) where, due to the poor quality of the tip, broad TCIL spectra, which are averaging over a wide area, were commonly observed. The spectra reported here exhibit the narrowest TCIL peaks observed, $\approx 1.5 \div 2.0$ meV, and thus, it is proposed, exhibit high spatial resolution. Since the gap voltage is -1.5 V, energetic holes in the barrier region are created. Prior to recombination at the QDs, the injected holes must therefore undergo relaxation processes to dissipate their excess kinetic energy. In the voltage range used in these experiments, it is reasonable to assume that the dominant scattering mechanism is that of longitudinal optical (LO) phonon scattering. By virtue of the high density of available states into which holes can de-excite, the probability of multiple scattering events and their further dispersion is high [Sprinzak *et al.* (1997)]. Upon hole injection in the vicinity of the smaller dots (which are of the higher proportion), capture occurs at one of these smaller dots, which have higher confinement energies and therefore lower residual barriers, and a single peak is observed at 1.294 eV [Figure 2.26(a)]. The appearance of this high energy peak, which is not in the range of the main ensemble PL signal, is counter-intuitive, and would imply that injected carriers are more inclined to relax into, and then radiatively recombine from states which are not the lowest potential states of the system. However, the spatial resolving ability of TCIL allows the almost random selection of different points of the sample, and thus the capture of holes by the smaller QDs with higher confinement energy. At a different point on the sample [Figure 2.26(b)], coupled small QDs are filled, giving rise to ground state excitonic emission of the symmetric and anti-symmetric bonding states of the coupled QD states (the broader peaks are probably due to Raman scattering of LO phonons). Finally Figure 2.26(c) corresponds to the filling of hole states of the larger QDs (the main emission at 1.257 eV), and their neighboring dots by inter-dot tunneling processes. The initial relaxation of the injected holes into the smaller QD states is evident by the emission at 1.30 eV. The calculated differences in the exciton ground state energies for the two families of dots is ≈ 45 meV. This correlates well with the observed separation between the TCIL signals which originates from the smaller and larger dots. To conclude, the tunneling current induced luminescence spectra of single, coupled and an ensemble of InGaAs QDs can be selectively analyzed, following the complex energy dependent relaxation of the holes, which results in hole capture by QDs of different sizes depending on their spatial location.

These experimental results reinforce the well known analogy between semiconductor quantum dots and isolated atoms. By virtue of their zero-dimensionality and strongly confining potential the QD energy levels are atomic-like and their occupation is governed by Hund's rules. However, unlike real atoms, QDs possess the characteristic of charge tunability over a wide range and of both positive and negative charge. The charged state of quantum dots, that is the capture of excess charge, an unbalanced number of either electrons or holes, manifests itself in optical spectra by the reduction or increase in the excitonic recombination energy. The "spectator" excitons giving rise to the luminescent emission through their recombination are sensitive to the changes in the confining potential due to the excess charge. And so accordingly the emission energies of the radiative excitonic recombination exhibit shifts with respect to the neutral exciton, a red-shift for excess electrons and a blue-shift for excess holes. In this respect the analogy with atomic physics is increasingly valid. Just as the binding energy of valence electron to the atomic core decreases (increases) with the increase (decrease) of number of electrons in the outer shell, due to electron-electron repulsion, so the Coulomb interaction between the electrostatically stored charge and exciton electron-hole pair is the dominate contribution to the exciton recombination energy.

Electron charging of QDs has been reported by capacitance, inter-band spectroscopy and conductance measurements. Negatively charged excitons have been observed where the number of captured electrons are controlled by photo-depletion and a gated device as well as by optical charging.

The excitonic emission following the controlled hole carrier injection into a single pair of laterally coupled QDs was observed. By virtue of the high spatial resolution afforded by using an STM tip for carrier injection and the high capture rate of the QDs, luminescence spectra were collected which exhibit state-filling characteristics typical of quantum mechanically coupled QDs and energy position shifts resulting from the excess hole carriers.

By controlling growth conditions, a bimodal distribution of dot size and separation was achieved. This results in the tendency to form laterally coupled QDs. When the distance separating the QDs is sufficiently small molecule formation through pseudo covalent bonding occurs, where delocalized carrier wavefunction over the QD molecule results in an energy level scheme comprising bonding and anti-bonding states.

A prerequisite for TCIL is the presence of free carriers in the sample, due in this case to sample doping. So upon the injection of minority carriers by the STM tip, there is current flow through the sample which results in

carrier capture by the QDs, followed by radiative recombination resulting in the observed luminescent signal.

In Figure 2.28 the evolution of luminescence spectra with increasing tunneling current, measured when in tunneling contact at a single point on the GaAs capping layer using a gap voltage of -1.5 V, is shown. Each of the spectra consists of sets of major (*A* and *B*) and minor (*C* and *D*) peaks. Considering first the major peaks (*A* and *B*), for a tunneling current of 5 nA, an asymmetric doublet is observed with a 4.2 meV splitting. The lower energy component of the doublet is of a higher relative intensity. Upon increasing tunneling current a reversal in the relative intensities is observed and the higher photon energy component intensity increases. This saturation of the lower energy component signal with increasing tunneling current suggests a state filling process. Emission from the lower energy state of the system diminishes due to the filling of the excited state hole and electron state upon the injection of higher carrier densities. With increasing tunneling current there is a shift to higher photon energy of the peaks *A*, *B* and *D* (as shown in Figure 2.29).

The large FWHM of peak *A* tends to suggest that this peak is a composite of perhaps several components. The point to note is that the center of mass of this peak exhibits shifts towards higher photon energy with increasing tunneling current. So therefore it comprises mostly of components due to positively charged excitonic emission. The lower energy peak of the minor peaks, *C*, appears impervious to changes in the tunneling current intensity, in both the energy position and intensity.

From TEM measurements a statistical correlation between dot diameter and the inter dot distance has been drawn. There appears to be a direct relationship of dot size and the distance to its nearest neighbor. On the basis of this, the inter-dot distance of a diameter of 12 nm is approximately 12 nm.

The doublet (*A* and *B*) shown in Figure 2.28 is typical of excitonic recombination at a pair of laterally coupled quantum dots.

The high spatial resolution of the hole injection and the high capture efficiency of the QDs is apparent by the observation of highly narrow luminescence peaks due to excitonic recombination at a single pair (since the dot size distribution is large it is proposed that it is unlikely that more than two dots of the same size are being filled) of coupled QDs.

Formation of the QD molecule causes the lifting of the degeneracy of the *S* and *P* shell states. In the case of the *P*-shell this is accompanied by dramatic loss in oscillator strength as observed in the relatively weak

C and *D* emission. The observation of incremental blue-shifts in the excitonic recombination of QD emission, arises as a direct consequence of the localization of carrier wave functions within the QDs.

2.7 Conclusions

In this chapter we reported an overview of our experimental investigations concerning the viability of using semiconductor quantum dots as the building blocks of quantum information processing. Direct evidence of the discrete, atom-like density of states of single quantum dots has been observed in spatially resolved photoluminescence spectra, together with nonlinearities in the optical spectra which appear to be dominated by charge excitonic emission. On an equally fundamental level the charge density associated with the localized electronic states of single quantum dots have been studied.

Acknowledgments

This work has been supported by EEC project IST-1999-11311 SQID. We would like to acknowledge all the collaborators to this research within the SQID team, namely T. K. Johal, M. DeGiorgi, S. De Rinaldis, A. Passaseo, M. De Vittorio, A. Vergine, G. Pagliara, R. Cingolani, M. Lomascolo, A. Taurino, M. Catalano, F. Troiani, E. Molinari, A. Vasanelli, R. Ferreira, G. Bastard, E. Biolatti and F. Rossi. We thank all the SQID partners for the stimulating discussions and interactions during the three years of the project.

We would also thank S. Patanè, M. Labardi, M. Allegrini for the active collaboration in building the low temperature NSOM system. D. Cannella, A. Melcarne and D. Mangiullo are thanked for technical assistance.

Bibliography

- Alperson, B., Cohen, S., Rubinstein, I., Hodes, G., (1995). Room-temperature conductance spectroscopy of CdSe quantum dots using a modified scanning force microscope, *Phys. Rev. B* **52**: 17017.
- Alperson, B., Rubinstein, I., Hodes, G., Porath, D., Millo, O., (1999). Energy level tunneling spectroscopy and single electron charging in individual CdSe quantum dots, *Appl. Phys. Lett.* **75**: 1751.

- Ashoori,R.C.,(1996). Electrons in artificial atoms, *Nature* **379**: 413.
- Averin, D.V., (1998). Adiabatic quantum computation with Cooper pairs, *Solid State Commun.* **105**: 659.
- Bacher, G., Weigand, R., Seufert, J., Kulakovskii, V.D., Gippius, N.A., Forchel, A., Leonardi, K. and Hommel, D. (1999). Biexciton versus exciton lifetime in a single semiconductor quantum dot, *Phys. Rev. Lett.* **83**: 4417.
- Banin, U., Cao, Y.W., Katz, D. and Millo, O., (1999). Identification of atomic-like electronic states in indium arsenide nanocrystal quantum dots, *Nature* **400**: 542.
- Bayer, M., Stern, O., Hawrylak, P., Fafard, S. and Forchel, A. (2000). Hidden symmetries in the energy levels of excitonic artificial atoms, *Nature* **405**: 923.
- Beaumont, S.P. (1991). *Low-Dimensional Structures in Semiconductors*, NATO Asi Series. Series B, Physics, **281**.
- Betzig, E., Trautman, J.K., Harris, T.D., Weiner, J.S. and Kostelak, R.L., (1991). Breaking the Diffraction Barrier - Optical Microscopy on a Nanometric Scale, *Science* **251**: 1468.
- Bimberg, D., Grundmann, M. and Ledentsov, N.D. (1999). In *Quantum Dot Heterostructures*, Wiley, New York.
- Biolatti, E., Iotti, R.C., Zanardi, P. and Rossi, F. (2000). Quantum information processing with semiconductor macroatoms, *Phys. Rev. Lett.* **85**: 5647.
- Brasken, M., Lindberg, M., Sundholm, D. and Olsen, J. (2001). Spatial carrier-carrier correlations in strain-induced quantum dots, *Phys. Rev. B* **64**: 353121.
- Burkard, G., Loss, D. and DiVincenzo, D.P. (1999). Coupled quantum dots as quantum gates, *Phys. Rev. B* **59**: 2070.
- Cirac, J.I. and Zoller, P. (1995). Quantum Computations with Cold Trapped Ions, *Phys. Rev. Lett.* **74**: 4091.
- Cusack, M.A., Briddon, P.R. and Jaros, M. (1996). Electronic structure of InAs/GaAs self-assembled quantum dots, *Phys. Rev. B* **54**: 2300.
- Dahne-Prietsch, M. and Kalka, T. (2000). Hot-electron transport processes in ballistic-electron emission microscopy at Au-Si interfaces, *J. Elect. Spectr. and Related Phenom.* **109**: 211.
- De Giorgi, M., Vasanelli, A., Rinaldi, R., Anni, M., Lomascolo, M., Antonaci, S., Passaseo, A., Cingolani, R., Taurino, A., Catalano, M. and Di Fabrizio, E. (2000). Correlation between shape and electronic states in nanostructures, *Micron* **31**: 245.
- De Giorgi, M., Taurino, T., Passaseo, A., Catalano, M. and Cingolani, R. (2001). Interpretation of phase and strain contrast of TEM images of $In_xGa_{1-x}As/GaAs$ quantum dots, *Phys. Rev. B* **63**: 245302.
- De Giorgi, M., Rinaldi, R., Johal, T., Pagliara, G., Passaseo, A., De Vittorio, M., Lomascolo, M., Cingolani, R., Vasanelli, A., Ferreira, R. and Bastard, G. (2003). *Advanced Semiconductor and Organic Nano-techniques*(Part II), ed. by H. Morkoc, Elsevier.
- De la Broise, X., Delerue, C., Lannoo, M., Grandidier, B. and Stievenard, D. (2000). Theory of scanning tunneling microscopy of defects on semiconduc-

- tor surfaces, *Phys. Rev. B* **61**: 2138.
- Dekel, E., Ghersoni, D., Ehrenfreund, E., Garcia, J.M. and Petroff, P.M., (2000). Carrier-carrier correlations in an optically excited single semiconductor quantum dot, *Phys. Rev. B* **61**: 11009.
- Dekel, E., Regelman, D.V, Gershoni, D., Ehrenfreund, E., Schoenfeld, W.V. and Petroff, P.M. (2000). Cascade evolution and radiative recombination of quantum dot multiexcitons studied by time-resolved spectroscopy, *Phys. Rev. B* **62**: 11038.
- Dekel, E., Gershoni, D., Ehrenfreund, E., Spektor, D., Garcia, J.M. and Petroff, P.M., (1998). Optical spectroscopy of single quantum dots at tunable positive, neutral, and negative charge states, *Phys. Rev. Lett.* **80**: 4991.
- DiVincenzo, D.P., (1995). Quantum computation, *Science* **270**: 255.
- Duke, C.B., *Tunneling in Solids* (1969). Academic Press, New York.
- Empedocles, S.A., Norris,D.J. and Bawendi, M.G.(1996). Photoluminescence spectroscopy of single CdSe nanocrystallite quantum dots, *Phys. Rev. Lett.* **77**: 3873.
- Ferreira, R. and Bastard, G. (1999). Phonon-assisted capture and intradot Auger relaxation in quantum dots, *Appl. Phys. Lett.* **74**: 2818.
- Fertig, H.A. (1993). Path Decomposition and the Traversal-Time Distribution in Quantum Tunneling, *Phys. Rev. B* **47**: 1346.
- Finley, J.J., Fry, P.W., Ashmore, A.D., Lemaitre, A., Tartakovskii, A.I., Oulton, R., Mowbray, D.J., Skolnick, M.S., Hopkinson, M., Buckle, P.D. and Maksym, P.A.(2001). Observation of multicharged excitons and biexcitons in a single InGaAs quantum dot, *Phys. Rev. B* **63**: 161305.
- Finley, J. J., Ashmore, A. D., Lemaitre, A., Mowbray, D. J., Skolnick, M. S., Itskevich, I. E., Maksym, P. A., Hopkinson, M. and Krauss, T. F. 2001). Charged and neutral exciton complexes in individual self- assembled In(Ga)As quantum dots, *Phys. Rev. B* **63**: 073307.
- Fonseca, L.R.C., Jimenez, J.L., Leburton, J.P. and Martin, R.M. (1998). Self-consistent calculation of the electronic structure and electron-electron interaction in self-assembled InAs-GaAs quantum dot structures, *Phys. Rev. B* **57**: 4017.
- Franceschetti, A. and Zunger, A. (2000). Pseudopotential calculations of electron and hole addition spectra of InAs, InP, and Si quantum dots, *Phys. Rev. B* **62**: 2614.
- Fujita, S., Maruno, S., Watanabe, H., Kusumi, Y. and Ichikawa, M. (1995). Periodical Nanostructure Fabrication Using Electron Interference-Fringes Produced by Scanning Interference Electron-Microscope, *Appl. Phys. Lett.* **66**: 2754.
- Gammon, D. (1996).Fine structure splitting in the optical spectra of single GaAs quantum dots, *Phys. Rev. Lett.* **76**: 3005.
- Gammon, D., Snow, E.S. and Katzer, D.S. (1995). Excited-State Spectroscopy of Excitons in Single Quantum Dots, *Appl. Phys. Lett.* **67**: 2391.
- Gammon, D., Bonadeo, N.H., Gang Chen, Erland, J. and Steel, D.G. (2001). Optically probing and controlling single quantum dots, *Physica E* **9**: 99.
- Gammon, D. (2000). Semiconductor physics - Electrons in artificial atoms, *Nature*

- 405: 899.
- Georgsson, K., Carlsson, N., Samuelson, L., Seifert, W. and Wallenberg, L.R. (1995). Transmission Electron-Microscopy Investigation of the Morphology of InP Stranski-Krastanow Islands Grown by Metalorganic Chemical-Vapor, *Appl. Phys. Lett.* **67**: 2981.
- Gershenfeld, N.A. and Chuang, I.L. (1997). Bulk spin-resonance quantum computation, *Science* **275**: 350.
- Grandidier, B., Niquet, Y.M., Legrand, B., Nys, J.P., Priester, C., Stiévenard, D., Gerard, D.M. and Thierry-Mieg, V. (2000). Imaging the wave-function amplitudes in cleaved semiconductor quantum boxes, *Phys. Rev. Lett.* **85**: 1068.
- Grundmann, M., Stier, O. and Bimberg, D. (1995). InAs/GaAs Pyramidal Quantum Dots - Strain Distribution, Optical Phonons, and Electronic Structure, *Phys. Rev. B* **52**: 11969.
- Hameau, M., Guldner, Y., Verzelen, O., Ferreira, R., Bastard, G., Zeman, J., Lematre, A., Gérard, J.M., (1999). Strong electron-phonon coupling regime in quantum dots: Evidence for everlasting resonant polarons, *Phys. Rev. Lett.* **83**: 4152.
- Hartmann, A., Ducommun, Y., Kapon, E., Hohenester, U. and Molinari, E. (2000). Few-particle effects in semiconductor quantum dots: Observation of multicharged excitons, *Phys. Rev. Lett.* **84**: 5648.
- Hartmann, A., Loubies, L., Reinhardt, F. and Kapon, E. (1997). Self-limiting growth f quantum dot heterostructures on nonplanar 111B substrates, *Appl. Phys. Lett.* **71**: 1314.
- Heberle, A.P., Baumberg, J. J. and Kohler, K. (1995). Ultrafast Coherent Control and Destruction of Excitons in Quantum Wells, *Phys. Rev. Lett.* **75**: 2598.
- Heitz, R., Veit, M., Ledentsov, N.N., Hoffmann, A., Bimberg, D., Ustinov, V.M., Kopev, P.S. and Alferov, Zh.I. (1997). Energy relaxation by multiphonon processes in InAs/GaAs quantum dots, *Phys. Rev. B* **56**: 10435.
- Imamoglu, A., Awschalom, D.D., Burkard, G., DiVincenzo, D.P., Loss, D., Shervin, M. and Small, A. (1999). Quantum information processing using quantum dot spins and cavity QED, *Phys. Rev. Lett.* **83**: 4202.
- Jacak, L., Hawrylak, P. and Wojs, A. (1998). *Quantum Dots*, Springer, Berlin.
- Jiang, H. and Singh, J. (1997). Strain distribution and electronic spectra of InAs/GaAs self- assembled dots: An eight-band study, *Phys. Rev. B* **56**: 4696.
- Johal, T.K., Rinaldi, R., Passaseo, A., Cingolani, R., Vasanelli, A., Ferriera, R. and Bastard, G. (2002a). Imaging of the electronic states of self-assembled $In_xGa_{1-x}As$ quantum dots by scanning tunneling spectroscopy, *Phys. Rev. B* **66**: 880.
- Johal, T.K., Pagliara, G., Lomascolo, M., Taurino, A., Catalano, M., Rinaldi, R. and Cingolani, R. (2002b). Luminescence following highly localized hole carrier injection into InGaAs quantum dots, *Jap. J. Appl. Phys.* **41** No.8: 5127.
- Johal, T.K., Pagliara, G., Rinaldi, R., Passaseo, A., Cingolani, R., Lomascolo, M., Taurino, A., Catalano, M. and Phaneuf, R. (2002c). Spectroscopy of

- an ensemble of $In_{0.50}Ga_{0.50}As$ quantum dots following highly localized hole injection by a scanning tunneling microscope, *Phys. Rev. B* **66**: 155313.
- Kane, B.E. (1998). A silicon-based nuclear spin quantum computer, *Nature* **393**: 133.
- Kapteyn, C.M., Lion, M., Heitz, R., Bimberg, D., Brunkov, P.N., Volovik, B.V., Konnikov, S.G., Kovsh, A.R. and Ustinov, V.M. (2000). Hole and electron emission from InAs quantum dots, *Appl. Phys. Lett.* **76**: 1573.
- Karlsson, K.F., Moskalenko, E.S., Holtz, P.O., Monemar, B., Schoenfield, W.V., Garcia, J.M. and Petroff, P.M. (2001). Temperature influence on optical charging of self-assembled InAs/GaAs semiconductor quantum dots, *Appl. Phys. Lett.* **78**: 2952.
- Kastner, M.A. (1993). Artificial Atoms, *Phys. Today* **46**: 24.
- Landin, L., Pistol, M.E., Pryor, C., Persson, M., Samuelson, L. and Miller, M. (1999). Optical investigations of individual InAs quantum dots: Level splittings of exciton complexes, *Phys. Rev. B* **60**: 16640.
- Ledentsov, N.N. (1996). Ordered arrays of quantum dots: Formation, electronic spectra, relaxation phenomena, lasing, *Solid State Electron.* **40**: 785.
- Ledentsov, N.N., Bimberg, D., Shernyakov, Y. M., Kochnev, V. Maximov, M. V., Sakharov, A. V., Krestnikov, I. L., Egorov, A. Y., Zhukov, A. E., Tsatsulinikov, A. F., Volovik, B. V., Ustinov, V. M., Kopev, P. S., Alferov, Z. I., Kosogov, A. O. and Werner, P. (1997). Properties of strained (In,Ga,Al)As lasers with laterally modulated active region, *Appl. Phys. Lett.* **70**: 2888.
- Legrand, B., Grandidier, B., Nys, J.P., Stievenard, D., Gerard, J.M. and Thierry-Mieg, V. (1998). Scanning tunneling microscopy and scanning tunneling spectroscopy of self assembled InAs quantum dots, *Appl. Phys. Lett.* **73**: 96.
- Lelong, Ph. and Bastard, G. (1996). Binding energies of excitons and charged excitons in GaAs/Ga(In)As quantum dots, *Solid State Commun.* **98**: 819.
- Lelong, Ph., Heller, O. and Bastard, G. (1998). Coulomb interactions in small InAs quantum dots. *Solid State Electr.* **42**: 1251.
- Li, X., Wu, Y., Steel, D., Gammon, D., Stievater, T.H., Katzer, D.S., Park, D., Piermarocchi, C. and Sham, L.J. (2003). An all-optical quantum gate in a semiconductor quantum dot, *Science* **301**: 809.
- Lian, G.D., Yuan, J., Brown, L.M., Kim, G.H., Ritchie, D.A., (1998). Modification of InAs quantum dot structure by the growth of the capping layer, *Appl. Phys. Lett.* **73**: 49.
- Liao, X.Z., Zou, J., Duan, X.F., Cockayne, D.J.H., Leon, R. and Lobo, C. (1998). Transmission-electron microscopy study of the shape of buried $In_xGa_{1-x}As/GaAs$ quantum dots, *Phys. Rev. B* **58**: 4235.
- Lipsanen, H., Sopanen, M. and Ahopelto, J. (1995). Luminescence from Excited-States in Strain-Induced $In_xGa_{1-x}As$ Quantum Dots, *Phys. Rev. B* **51**: 13868.
- Lomascolo, M., Vergine, A., Rinaldi, R., Passaseo, A., Cingolani, R., Patan/'e, S., Labardi, M., Allegrini, M., Troiani, F. and Molinari, E. (2002). Dominance of charged excitons in single quantum dot photoluminescence spectra, *Phys. Rev. B* **66**: 41302.

- Loss, D. and DiVincenzo, D.P. (1998). Quantum computation with quantum dots, *Phys. Rev. A* **57**: 120.
- Marquez, J., Geelhaar, L. and Jacobi, K. (2001). Atomically resolved structure of InAs quantum dots, *Appl. Phys. Lett.* **78**: 2309.
- Martorell, J., Sprung, D.W.L., Machado, P.A. and Smith, G.C. (2001). Model of single-electron decay from a strongly isolated quantum dot, *Phys. Rev. B* **63**: 045325.
- Marzin, J.Y. and Bastard, G. (1994). Calculation of the Energy-Levels in InAs/GaAs Quantum Dots, *Solid State Commun.* **92**: 437.
- Marzin, J.Y., Gerard, J.M., Izrael, A., Barrier, D., Bastard, G., (1994). Photoluminescence of Single Inas Quantum Dots Obtained by Self- Organized Growth on Gaas, *Phys. Rev. Lett.* **73**: 716.
- Medeiros-Ribeiro, G., Garcia, J.M. and Petroff, P.M. (1997). Charging dynamics of InAs self-assembled quantum dots, *Phys. Rev. B* **56**: 3609.
- Medeiros-Ribeiro, G., Pikus, F.G., Petroff, P.M. and Efros, A.L. (1997). Single-electron charging and coulomb interaction in InAs self- assembled quantum dot arrays, *Phys. Rev. B* **55**: 1568.
- Millo, O., Katz, D., Cao, Y.W. and Banin, U. (2000). Scanning tunneling spectroscopy of InAs nanocrystal quantum dots, *Phys. Rev. B* **61**: 16773.
- Millo, O., Katz, D., Cao, Y.W. and Banin, U. (2001). Imaging and spectroscopy of artificial-atom states in core/shell nanocrystal quantum dots. *Phys. Rev. Lett.* **86**: 5751.
- Passaseo, A., Rinaldi, R., Longo, M., Antonaci, S., Convertino,A.L., Cingolani, R., Taurino, A. and Catalano, M. (2001). Structural study of InGaAs/GaAs quantum dots grown by metalorganic chemical vapor deposition for optoelectronic applications at 1.3 μm , *Journ. Appl. Phys.* **89**: 4341.
- Patel, S.R., Stewart, D.R., Marcus, C.M., Gokcedag, M., Alhassid, Y., Stone, A.D., Duruoz, C.I. and Harris, J.S. (1998). Changing the electronic spectrum of a quantum dot by adding electrons, *Phys. Rev. Lett.* **81**: 5900.
- Paul, S., Roy, J.B., Basu, P.K., (1991). Empirical Expressions for the Alloy Composition and Temperature-Dependence of the Band-Gap and Intrinsic Carrier Density, *Journ. Appl. Phys.* **69**: 827.
- Pellizzari, T., Gardiner, S.A., Cirac, J.I. and Zoller, P. (1995). Decoherence, Continuous Observation, and Quantum Computing - a Cavity Qed Model, *Phys. Rev. Lett.* **75**: 3788.
- Pryor, C. (1998). Eight-band calculations of strained InAs/GaAs quantum dots compared with one-, four-, and six-band approximations, *Phys. Rev. B* **57**: 7190.
- Quiroga, L. and Johnson, N.J. (1999). Entangled Bell and Greenberger-Horne-Zeilinger states of excitons in coupled quantum dots, *Phys. Rev. Lett.* **83**: 2270.
- Regelman, D.V., Dekel, E., Gershoni, D., Ehrenfreund, E., Williamson, A.J., Shumway, J., Zunger, A., Schoenfeld, W.V. and Petroff, P.M. (2001). Optical spectroscopy of single quantum dots at tunable positive, neutral, and negative charge states, *Phys. Rev. B* **64**: 165301.
- Renaud, P. and Alvarado, S.F. (1991). Mapping Quantum-Well Energy Profiles

- of III-V-Heterostructures by Scanning-Tunneling-Microscope-Excited Luminescence, *Phys. Rev. B* **44**: 6340.
- Rinaldi, R., DeGiorgi, M., DeVittorio, M., Melcarne, A., Visconti, P., Cingolani, R., Lipsanen, H., Sopanen, M., Drufva, T. and Tulkki, J. (2001). Longitudinal stark effect in parabolic quantum dots, *Japanese Journal of Applied Physics*, Part 1 **40**, no.3B: 2002.
- Rinaldi, R. (1998). Artificial Atoms in magnetic fields, *Int. J. Mod. Phys.* **12**: 471.
- Rontani, M., Rossi, F., Manghi, F. and Molinari, E. (1999). Coulomb correlation effects in semiconductor quantum dots: The role of dimensionality, *Phys. Rev. B* **59**: 10165.
- Ruvimov, S., Werner, P., Scheerschmidt, K., Gösele, U., Heydenreich, J., Richter, U., Ledentsov, N.N., Grundmann, M., Bimberg, D., Ustinov, V.M., Yu, A., Egorov, E., Kop'ev, P.S. and Alferov, Zh.I. (1995). Structural Characterization of (In,Ga)As Quantum Dots in a GaAs Matrix, *Phys. Rev. B* **51**: 14766.
- Salis, G., Kato, Y., Ensslin, K., Driscoll, D.C., Gossard, A.C. and Awschalom, D.D. (2001). Electrical control of spin coherence in semiconductor nanostructures, *Science* **414**: 619.
- Schedelbeck, G., Wegscheider, W., Bichler, M. and Abstreiter, G., (1997). Coupled quantum dots fabricated by cleaved edge overgrowth: From artificial atoms to molecules, *Science* **278**: 1792.
- Shnirman, A., Schön, A. and Hermon, Z. (1997). Quantum manipulations of small Josephson junctions, *Phys. Rev. Lett.* **79**: 2371.
- Sleator, T. and Weinfurter, H. (1995). Realizable Universal Quantum Logic Gates, *Phys. Rev. Lett.* **74**: 4087.
- Snow, E.S., Campbell, P.M. and Shanabrook, B.V. (1993). Fabrication of Gaas Nanostructures with a Scanning Tunneling Microscope, *Appl. Phys. Lett.* **63**: 3488.
- Solomon, G.S., Trezza, J.A., Marshall, A.F. and Harris, J.S. (1996). Vertically aligned and electronically coupled growth induced InAs islands in GaAs, *Phys. Rev. Lett.* **76**: 952.
- Sprinzak, D., Heiblum, M., Levinson, Y. and Shtrikman, H. (1997). Ballistic transport of holes and phonon replicas in lightly doped GaAs, *Phys. Rev. B* **55**: 10185.
- Steane, A. (1998). Quantum computing, *Rep. Prog. Phys.* **61**: 117.
- Stier, O., Grundmann, M. and Bimberg, D. (1999). Electronic and optical properties of strained quantum dots modeled by 8-band k-p theory, *Phys. Rev. B* **59**: 5688.
- Sugawara, M. (1995). Theory of Spontaneous-Emission Lifetime of Wannier Excitons in Mesoscopic Semiconductor Quantum Disks, *Phys. Rev. B* **51**: 10743.
- Thompson, R.M., Stevenson, R.M., Shields, A.J., Farrer, I., Lobo, C.J., Ritchie, D.A., Leadbeater, M.L. and Pepper, M. (2001). Single-photon emission from exciton complexes in individual quantum dots, *Phys. Rev. B* **64**: 201302.
- Troiani, F., Hohenester, U. and Molinari, E. (2000). Exploiting exciton-exciton

- interactions in semiconductor quantum dots for quantum-information processing, *Phys. Rev. B* **62**: 2263.
- Vasanelli, A., De Giorgi, M., Ferreira, R., Cingolani, R. and Bastard, G. (2001). Electronic structure, Stark effect and optical properties of multistacked dots, *Jpn. J. Appl. Phys.*, Part 1 **40**: 1955.
- Warburton, R.J., Miller, B.T., Durr, C.S., Bodefeld, C., Karrai, K., Kotthaus, J.P., Medeiros-Ribeiro, G., Petroff, P.M., and Huant, S. (1998). Coulomb interactions in small charge-tunable quantum dots: A simple model, *Phys. Rev. B* **58**: 16221.
- Weisbuch, C. and Vinter, G. (1991) in *Quantum Semiconductor Structures*, Academic, Boston, MA.
- Wiesendanger, R. (1998). *Scanning Probe Microscopy and Spectroscopy*, Cambridge University Press.
- Wu, W., Tucker, J.R. and Solomon, J.S. (1997). Atom-resolved scanning tunneling microscopy of vertically ordered InAs quantum dots, *Appl. Phys. Lett.* **71**: 1083.
- Xie, Q., Chen, P. and Madhukar, A. (1994). InAs Island-Induced-Strain Driven Adatom Migration During Gaas Overlayer Growth, *Appl. Phys. Lett.* **65**: 2051.
- Xie, Q., Madhukar, A., Chen, P. and Kobayashi, N.P. (1995). Vertically Self-Organized Inas Quantum Box Islands on Gaas(100), *Phys. Rev. Lett.* **75**: 2542.
- Xue, Q.-K., Hasegawa, Y. and Kiyama, H. (1999). Atomic structure of faceted planes of InAs quantum dots on GaAs(001) studied by scanning tunneling microscopy, *Jpn. J. Appl. Phys.* **38**, Part 1: 500.
- Zanardi, P. and Rossi, F. (1998). Quantum information in semiconductors: Noiseless encoding in a quantum-dot array, *Phys. Rev. Lett.* **81**: 4752.
- Zou, J., Liao, X.Z., Cockayne, D.J.H. and Leon, R. (1999). Transmission electron microscopy study of $In_xGa_{1-x}As$ quantum dots on a GaAs(001) substrate, *Phys. Rev. B* **59**: 12279.
- Zunger, A. (1998). Electronic-structure theory of semiconductor quantum dots, *MRS Bull.* **23**: 35.

Chapter 3

Ultrafast Coherent Spectroscopy of Single Semiconductor Quantum Dots

Christoph Lienau

Max-Born-Institut für Nichtlineare Optik und Kurzzeitspektroskopie

Max-Born-Strasse 2A, D-12489 Berlin, Germany

Jeremy J. Baumberg

Southampton NanoMaterials Facility

University of Southampton

Southampton, SO17 1BJ, United Kingdom

3.1 Introduction

As discussed in Chapter 7, the experimental implementation of quantum information processing (QIP) relies on identifying, coherently manipulating, coupling and detecting elementary excitations of individual quantum systems. All these operations need to be performed on a time scale much shorter than the decoherence time of the quantum system. This extremely challenging task has attracted the interest of an increasing number of experimentalists in all areas of science. Implementations of quantum logic operations are currently explored in a wide range of different quantum systems [Nielsen *et al.* (2000)], e.g., nuclear magnetic spins in liquids and solids [Gershenfeld and Chuang (1997); Vandersypen *et al.* (2001)], ions in traps [Cirac and Zoller (1995); Sorensen and Molmer (1999); Gulde *et al.* (2003); Schmidt-Kaler *et al.* (2003)], atoms in microwave resonators [Turchette *et al.* (1995)], optical lattices [Brennen *et al.* (1999)], photonic bandgap materials [Woldeyohannes and John (1999)], Josephson junctions [Makhlin *et al.* (1999);

Ioffe *et al.* (1999); Mooij *et al.* (1999); van der Wal *et al.* (2000); Yamamoto *et al.* (2003); Chiorescu *et al.* (2003)] or photons in quantum-optical systems [Franson (1997); Knill *et al.* (2001)]. The complexity of this endeavor is quite clearly demonstrated by the fact that despite the outstanding progress in this field over the last few years, the most complex quantum calculation performed to date is the factorization of the number 15 [Vandersypen *et al.* (2001)].

A particularly attractive approach for realizing all-solid-state quantum information processing relies on using charge or spin excitations of semiconductor quantum dots (QDs) as quantum bits or “qubits”. As extensively discussed in Chapter 2, in QDs, electron and hole wave functions are localized in all three spatial dimensions on a nanometer length scale due to growth-induced nanoscale variations of the semiconductor composition. This makes QDs interesting model systems for exploring the basic physics of quasi-zero-dimensional quantum confinement as well as interesting for building novel optical devices, such as low-threshold semiconductor lasers.

The optical and electronic properties of semiconductor QDs have been intensely studied during the last decade. Due to the pronounced and so far unavoidable growth-induced inhomogeneous broadening in ensembles of semiconductor QDs, the recent development of single-QD spectroscopy has provided a wealth of new information [Zrenner (2000)]. It is now understood that sufficiently confined QDs resemble in many respect atomic systems, showing atomic-like densities of states [Brunner *et al.* (1994); Hess *et al.* (1994); Gammon *et al.* (1996b)], a shell-like absorption spectrum [Hawrylak *et al.* (2000)] and at low temperatures comparatively long dephasing times of up to 1 ns [Borri *et al.* (2001); Birkedal *et al.* (2001); Bayer and Forchel (2002)]. In addition, the large extent of the electron wave function in QDs gives rise to excitonic dipole moments of 10 – 100 Debye, much larger than those of atomic systems. This strong coupling to light makes charge excitations of single quantum bits interesting for quantum information processing. Ultrafast light pulses with pulse durations in the 100 fs range allow one to generate and manipulate exciton excitations of single QDs on a sub-picosecond time scale. With such ultrafast coherent carrier control, dephasing times in the 100 ps to 1 ns range can be considered as long, allowing in principle up to 10,000 coherent manipulations before decoherence destroys the quantum information stored in excitonic quantum bits [Bayer and Forchel (2002)]. Another important consequence of the large excitonic dipole moments are comparatively strong dipolar interactions between adjacent quantum dots [Biolatti *et al.* (2000);

Biolatti *et al.* (2002)]. Those interactions give rise to a nonlocal coupling between adjacent excitonic quantum bits, an important prerequisite for implementing scalable quantum gates. Different ideas for realizations of such gates have been proposed theoretically during the last years [Biolatti *et al.* (2000); Biolatti *et al.* (2002); Chen *et al.* (2001); Piermarocchi *et al.* (2002)], and some of them will be discussed in detail in Chapter 7.

Such perspectives have triggered a world wide research effort towards coherent control of excitonic excitations in semiconductor quantum dots. First successful experiments have shown coherent control on excited state transitions in the weak-excitation regime [Bonadeo *et al.* (1998); Toda *et al.* (2000); Flissikowski *et al.* (2001)] before Rabi oscillations could be demonstrated on both ground and excited states of different quantum dot systems [Stievater *et al.* (2001); Kamada *et al.* (2001); Htoon *et al.* (2002); Zrenner *et al.* (2002); Besombes *et al.* (2003)]. All these experiments have so far revealed a finite damping of Rabi oscillations, which has been attributed either to excitation-induced dephasing due to Coulomb interactions among charge excitations [Stievater *et al.* (2001); Guenther *et al.* (2002)] or to exciton-phonon coupling [Vagov *et al.* (2002); Verzelen *et al.* (2002); Förstner *et al.* (2003)]. Most recently, an all-optical two-bit quantum logic gate has been demonstrated using the exciton and biexciton transitions of a single quantum dot [Li *et al.* (2003)].

In this chapter, we review the recent experimental work performed within the SQID project on coherent control of excitonic excitations in quantum dots. We compare experimental results obtained on two important model systems: self-assembled quantum dots (SQDs) and interface quantum dots (IQD). Specifically, we discuss different strategies for read-out of quantum information, compare experiments evidencing Rabi oscillations in both systems, demonstrate control of both amplitude and phase of the exciton polarization and discuss the role of biexciton nonlinearities in single quantum dots.

This chapter is structured as follows: in Section 2 we summarize the most important properties of the investigated samples (IQD and SQD). In Section 3 the experimental techniques are described. Results are given in Section 4. Section 5 puts our findings into perspective and gives an outlook on future experiments.

3.2 Semiconductor Quantum Dots

Two semiconductor QD systems are sufficiently well developed for us to begin to apply ideas of coherent manipulation and QIPC. These are interface quantum dots (IQDs) which are trapped at the monolayer fluctuations of narrow GaAs quantum wells, and self-assembled quantum dots (SQDs) formed by the coagulation of few monolayers of InAs on GaAs.

3.2.1 *Interface quantum dots*

An important QD model system is that of thin semiconductor quantum wells (QW). In quantum wells, local monolayer height fluctuations at the interfaces (interface roughness) and fluctuations of the alloy composition (alloy disorder) are unavoidable (Figure 3.1(a)). The resulting disordered potential leads to the localization of excitons in single “interface” quantum dots with a confinement energy of about 10 meV (Figure 3.1b). This disorder gives rise to a pronounced inhomogeneous broadening of far-field optical spectra. In experiments with high spatial and spectral resolution, however, the smooth, inhomogeneously broadened photoluminescence (PL) spectra break up into narrow emission spikes from a few localized excitons [Brunner *et al.* (1994); Hess *et al.* (1994); Gammon *et al.* (1996b); Intonti *et al.* (2001a); Intonti *et al.* (2001b); Emiliani *et al.* (2001)].

The linear optical properties of interface QDs resemble in many aspects those of atomic systems. At low temperatures, the excitonic lines display a narrow homogeneous linewidth of 30–50 μeV , in agreement with measured dephasing times of 20–30 ps. The QDs show a discrete absorption spectrum [Gammon *et al.* (1996b)] and often a fine structure splitting due to the spatial asymmetry of the monolayer islands. The temperature dependence of the exciton linewidth and the fine structure splitting has been thoroughly investigated [Gammon *et al.* (1996b); Gammon *et al.* (1996a)]. The correlation length of the disordered potential and thus also the center-of-mass wave function of localized excitons in interface quantum dots typically extends over several tens of nm, as known from near-field autocorrelation spectroscopy [Intonti *et al.* (2001b)]. This large coherence length of the excitonic wavefunction results in large QD dipole moments of 50–100 Debye and a particularly strong coupling of these excitons to light [Guest *et al.* (2002); Thränhardt *et al.* (2002)]. This makes interface quantum dots a particularly interesting model system for nonlinear spectroscopy of single quantum

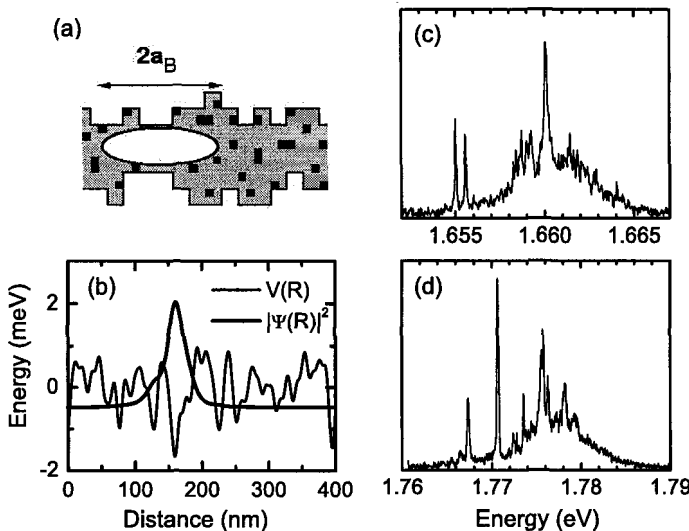


Fig. 3.1 (a) Disorder in quantum wells arises from spatial fluctuations of the local quantum well thickness (interface roughness) and of the quantum well composition (alloy disorder). (b) Schematic illustration of the effective disorder potential $V(\mathbf{R})$ and of a localized excitonic center-of-mass wave function $|\Psi(\mathbf{R})|^2$. (c,d) Representative near-field PL spectra ($T = 12\text{ K}$) of (c) a 5.1 nm thick and (d) a 3.3 nm thick (100) GaAs QW.

dots.

In this work, we investigate a sample consisting of 12 single QW layers of different thicknesses grown on a (100) GaAs substrate. The QW layers are separated by AlAs/GaAs short period superlattice barriers, each formed by nine AlAs and GaAs layers with a total thickness of 23.8 nm. Here, we investigate the top seven QWs with thicknesses of 3.3 to 7.1 nm. The layers are buried at distances between 40 and 211 nm below the surface. Growth interruptions of 10 s at each interface lead to a large correlation length of the QW disorder potential and to the formation of interface quantum dots (QD). The growth interruptions are kept short in order to avoid a monolayer splitting of the macroscopic PL spectra and to minimize the incorporation of impurities at the interfaces.

In Figure 3.1c and d representative low temperature ($T = 12\text{ K}$) near-field PL spectra are shown for the 3.3 and 5.1 nm thick (100) GaAs QW. The spectra reveal clearly the emission from excitons localized in interface quantum dots. The linewidth of the sharp resonances is limited by the spectral resolution of $100\text{ }\mu\text{eV}$. The spectra are recorded at an excitation intensity of 110 nW, corresponding to an average excitation density well below one

exciton per monolayer island. For excitation powers between 1 and 500 nW, we find a linear intensity dependence and an excitation-independent shape of the emission spectra, indicating negligible contributions from biexcitons and charged excitons.

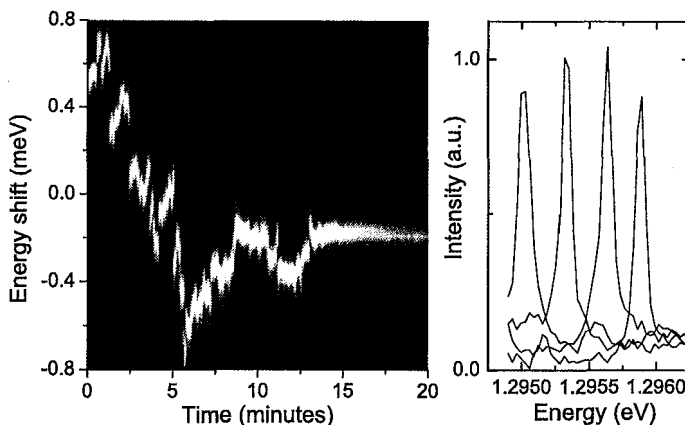


Fig. 3.2 Spectral diffusion in self-assembled quantum dots. (a) Time variation of near-field PL spectra of a single SQD on a time scale of 20 minutes. The image shows 240 spectra recorded in time intervals of 5 seconds. A HeNe laser with a power of 40 nW is used for optical excitation. (b) Individual QD PL spectra taken after 80, 125, 195 and 940 seconds (from left to right).

In addition to the sharp localized exciton emission, these spectra display at higher energies a spectrally broad background emission from more delocalized excitons in QW continuum states [Intonti *et al.* (2001a)]. This is a disadvantage for QIP applications, as it may be difficult to avoid the uncontrolled population of such delocalized exciton states when ultrashort and thus spectrally broadband pulses are used for optical excitation. Yet, we will demonstrate below that such problems can be reduced by careful spectral shaping of the excitation pulses. An important advantage of IQD over self-assembled quantum dots is the excellent interface quality of the (100)GaAs quantum wells and the strong reduction of piezoelectric and strain fields in interface quantum dots. In the investigated samples, the energetic positions of the sharp exciton emission lines remains unchanged over many hours and we observe no signs of a spectral diffusion of the exciton lines. In contrast, clear signatures of spectral diffusion of exciton emission energies were observed in InAs and InGaAs SQD samples optimized for near-field optical studies, i.e. grown in close proximity (20 – 30 nm) to the

sample surface. In such samples, we often found quite pronounced fluctuations of the QD energy (by as much as 1 meV, i.e. about 20 times larger than the spectral resolution of our PL experiment) on time scales of up to several minutes. A typical example is shown in Figure 3.2. Such spectral diffusion generally reflects DC Stark shifts of the exciton energies due to fluctuations of electrical charges, i.e. single electrons and/or holes, in the environs of the QD. We observe that these fluctuations often occur on very slow time scales of seconds to minutes. Thus it is likely that charges in deeply bound defect states are involved in these processes. These temporal changes in the charge environment of the QD may either be thermally or optically induced. In our experiments, we found evidence for both contributions, depending on the excitation conditions. Such spectral line shifts may be tolerable when luminescence-based detection schemes are used (see Section 1.3.2). In combination with absorption techniques, however, such line shifts lead to strong fluctuations of the absorption signal, making a quantitative analysis of such experiments difficult.

3.2.2 *Self-assembled quantum dots*

In contrast to interface quantum dots, both the spatial and energetic confinement of electronic wavefunctions is greatly increased in self-assembled quantum dots, with a typically of size of 10–15 nm, far below the optical wavelength inside a semiconductor ($\simeq 200\text{nm}$). This mismatch between the size of the coherent electronic wavefunction and the optical wavelength means that SQDs couple to light much more weakly than IQDs. In this respect they are closer to individual atoms. However they differ from atoms in important respects due to their physical structure and environment and thus it is important to summarize initially what is known about SQDs. We will then show spectra from a range of individual SQDs to develop a clear picture of the nanoscale system we are dealing with in comparison to a perfect two-level system.

Self-assembly of QDs refers to just one process which has been known for about 15 years [Bukowski and Simmons (2002); Petroff and Denbaars (1994)] in which a thin layer of a semiconductor grown on top of a non-lattice matched substrate can tend to break up into small islands of fairly regular size and shape. This Stranski-Krastanov growth mechanism has been extensively investigated for the InGaAs/GaAs system and it is clear that the actual structures produced are subtly controlled by many factors including growth temperature, temperature gradients and cycles, alloy

composition, capping materials, strain history and depth profile, annealing steps, and growth interruption steps. In some ways, every sample of InAs SQDs grown is different, however there are features that seem general to different samples and different groups.

A thorough review of SQD properties is not appropriate here given the huge attention focused on it in recent years, so instead we extract the salient properties [Bimberg (1999)]. Typical InAs SQDs (on which we will concentrate here as they are the most well developed for QIP applications), are truncated pyramidal in shape, with alignment along [110] and with various facets (often {110} and {111} forms). Note that the SQDs are different in shape in uncapped or cleaved samples, and hence caution is needed in using scanning probe studies to derive electronic and optoelectronic properties. Although different SQDs are electronically uncoupled due to their large spacing ($>10\text{nm}$), they sit upon a wetting layer of InAs which varies between 0-2 atoms thick and provides a very high density of quasi-localized electronic states of higher energy. A further complication is the sensitivity of SQD energy levels to the 3D strain profile due to deformation potential and piezo-electric contributions, as well as sensitivity to surrounding charge. A “good” sample will have size distributions of around 5% leading to similar inhomogeneous linewidths (Figure 3.3). However the distribution may be caused by fluctuations in any of the above parameters, including the volume, the in-plane and vertical aspect ratios, the composition, the wetting layer thickness and homogeneity, the strain, the faceting, and the surrounding charge distribution. Given these uncertainties, it is not perhaps surprising that progress has been slow in producing more homogeneous SQD samples. As we shall show below, in our experience, not just different samples, but different SQDs on the same piece of sample exhibit a high degree of variation.

In spite of this, various electronic features are common. The lowest electronic state lies about 300 meV below the wetting layer, giving good confinement at cryogenic temperatures. The electronic states are arranged in *s*-, *p*-, *d*-shells (similar to atomic spectra) which can be observed in luminescence for different pump powers (Figure 3.4). Emission lifetimes from the ground state are on the order of 1 ns and the quantum efficiency is high (up to 100%), similar to bulk III-V semiconductors, implying (perhaps surprisingly) that the interfaces between SQD and surroundings do not act as non-radiative traps. This should be contrasted with colloidal QDs grown in a solution phase in which surface traps are a major contributor to the optoelectronic properties.

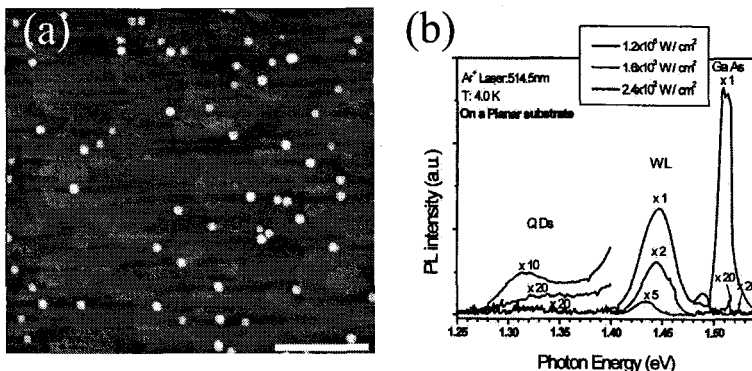


Fig. 3.3 (a) AFM of uncapped low-density SQD sample of $1 \mu\text{m} \times 1 \mu\text{m}$ area. (b) Far-field PL of cSQD sample showing emission from many QDs, wetting layer (WL) and GaAs substrate.

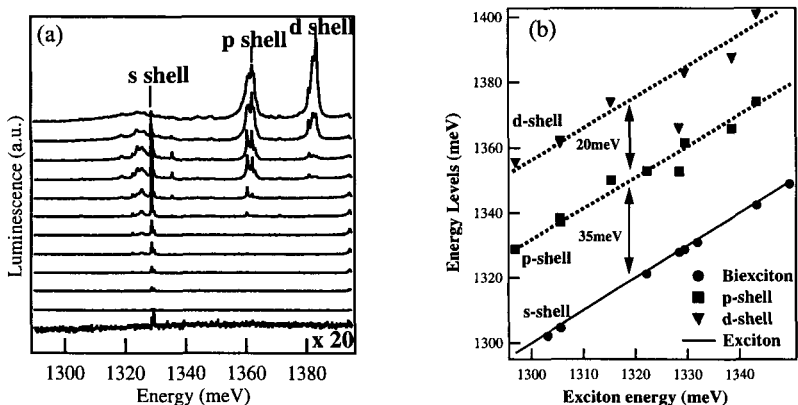


Fig. 3.4 (a) Power dependent PL of a single SQD showing the electronic shell structure (pump power increases upwards: 2, 6, 20, 60, 100, 170, 250, 365, 510, 670, 810, 930 μW , pump wavelength 532 nm). (b) Energy position of s -, p -, d - and biexciton states in 10 SQDs.

Because of this variability between different SQDs, it is absolutely necessary to look at individual SQDs experimentally. Even in optimized samples it is impossible to produce SQDs which are spaced more than 500 nm apart, hence to obtain such spectra some form of masking or near-field techniques are used. As previously discussed, although near-field techniques are ideal for spatially isolating spectra from individual SQDs, the need to grow the SQDs within $\simeq 10$ nm from the surface and the charge unavoidably present on the dielectric SNOM tip, introduce random fluctuations in the energy

of the electronic states. This makes SQD experiments, particularly for QIP applications, extremely difficult. Hence spectra on individual SQDs are isolated here using metal masks with 100-1000 nm square and circular apertures. Alternative techniques using anisotropic etching of similarly-sized mesas have proved extremely difficult for many groups, again due to fluctuating charges on the outer walls of such mesas. A typical sample has several hundred thousand such apertures, potentially giving access to a huge number of individual SQDs, however only ~ 100 are the subject of detailed study here due to the time-consuming experiments. In general, for the best samples, most apertures contain one or two SQDs (separately identified from their emission power dependence), with comparable properties (see below).

It appears that an effective simple model for the SQDs is that of a thin circular disk, in which the particular cylindrical symmetry produces a set of selection rules, and level spacings for the s , p , d states [Verzelen *et al.* (2002)]. The results in this chapter are interpreted within this basic formalism, but it should be remembered that the actual SQD is far from this situation. This can be easily seen from measurements of the vertical dipole arising from the separation of the electron and hole produced by the tapering pyramid shape of the SQD. Measurements of the photoluminescence (PL) as a function of applied vertical electric field [Fry *et al.* (2000)] unambiguously shows that the ground state hole is nearer than the electron to the base of the pyramid. In the cylindrical disk, no vertical dipole should be present, while a simple analysis of a pyramidal shape gives the reverse alignment of electron and hole.

The influence of charge in the surroundings becomes evident when PL spectra of the s -state are measured as a function of incident laser power and wavelength. Many groups have identified the exciton ($1\ s\text{-}e$, $1\ s\text{-}h$) and the ground state biexciton ($2\ s\text{-}e$, $2s\text{-}h$) by showing that the former is present as a sharp line rising linearly with power, while the latter is also a sharp emission line but ~ 1 meV lower in energy which rises quadratically with power (as seen in Figure 3.5a, b). As the biexciton appears, the exciton power dependence saturates and rolls off. In this CW experiment, there is the expected ratio between the occupation probabilities of 1 or 2 excitons in each SQD. At higher powers, further charged multi-excitons appear to the low energy side of the biexciton, and the lines broaden considerably making clear studies difficult. However such behavior is only seen for non-resonant excitation (in this case with 532 nm light).

In the case of resonant excitation at the p -states (Figure 3.5b), a dif-

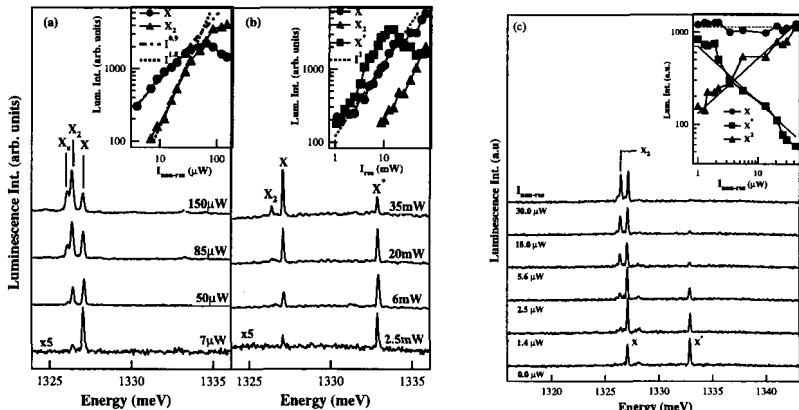


Fig. 3.5 Power dependence PL of *s*-state, pumping (a) non-resonantly (at 532 nm), (b) resonantly with the *p*-state, (c) resonantly excited at the *p*-state while simultaneously increasing additional non-resonant pump excitation. The insets show the extracted power dependence, while the different exciton lines are discussed in the text.

ferent emission spectrum is observed from the same SQD. A new PL line appears at higher energy which is stronger than the exciton line, and also rises linearly with input power. In this resonantly-pumped case, it is also interesting that the biexciton line rises only linearly with power. Because of the extremely small absorption cross-section of the SQD (which causes problems for QIPC discussed below), the powers are 10^3 times larger than when the wetting layer is excited by the pump laser.

To assign the origin of this extra sharp line (here labeled X*), we can combine the conditions of resonant and non-resonant pumping (Figure 3.5c). As the high-energy pump is slowly switched on, the X* line disappears whilst the X₂ line simultaneously increases, however the X emission is completely unaffected. This is strong evidence that the X* line is a charged exciton: when photons are directly absorbed in the charged quantum dot, they relax to the *s*-state and recombine in the presence of an extra charge. When photons are absorbed outside the charged SQD, one carrier is attracted into the QD neutralizing it, and thus emission is from both the uncharged X and X₂. No emission is possible from a charged X₂ due to Pauli exclusion. The blue shift of the X* line found in every SQD that we have looked at in these samples implies that it originates from an extra hole in the SQD. Other groups have found extra emission lines on both the red and the blue side of the exciton, corresponding to extra electrons or holes respectively. The assignment depends on the relative size of the electron and

hole s -states in the SQD: because the hole is more confined, its overlap with the photojected s -electron is smaller than its overlap with the s -hole, so that the repulsion between the two holes is stronger than the attraction of the electron and hole, leading to a net increase in exciton energy. Further evidence for background hole doping of the SQDs is provided by the temperature dependence of the X^* line whose PL intensity decreases rapidly as the temperature is raised to 20 K, though with a different dependence in each SQD. These samples allow one to explore the excited states of both charged and uncharged SQDs, helping to understand the nature of the SQD confinement.

It is extremely important to not just observe the s -states in the SQDs, but to map the higher lying energy levels, to allow quantum optical manipulation. To do this we use photoluminescence excitation spectroscopy (PLE) which convolutes the absorption spectrum with the rate of relaxation to the s -state and subsequent photon emission. Other groups have correspondingly used photocurrent spectroscopy to try and map the higher lying states, though necessitating a substantial vertical electrical field which ionizes these higher energy states, potentially broadening the absorption lines. We collect PL spectra around the s -state while exciting with a tunable CW laser, and then extract the PLE for both the X and the X^* transitions. Representative examples for three different SQDs are shown in Figure 3.6 for comparison. The most important feature is that the absorption lines are seen clearly and are rather sharp compared to the few spectra reported in the literature. We attribute these excellent features to the metal masking which reduces stray fluctuating charge, and a low-temperature-grown GaAs cap layer which is grown around the SQD as a diffusion barrier and a charge-trap, before the sample is further capped with high-quality GaAs. The sharp peaks are seen on a rising continuum background absorption known to arise from indirect transitions into the SQD from the surrounding wetting layer [Kammerer *et al.* (2001); Oulton *et al.* (2003)]. These are impossible to remove, without growing SQDs with a deeper confinement potential, which however shifts them to longer wavelengths that makes high efficiency multi-channel silicon detectors unusable. The wetting layer is thus one of the major problems for QIPC in semiconductor SQDs since there is always background absorption by unwanted states when one is acting on the target quantum state. Removal of this wetting layer constitutes one of the major tasks for SQD research.

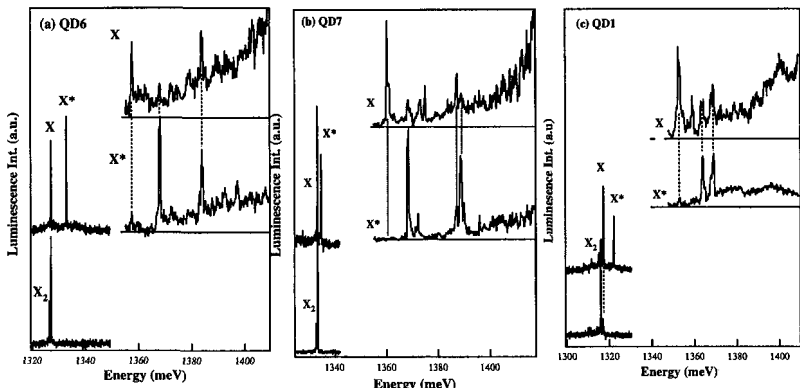


Fig. 3.6 Left: PL around the *s*-state for resonant excitation (top) and non-resonant (bottom); Right: PLE spectra of *p*-states for detection on *X* and *X** transitions, for 3 different SQDs (a-c).

In addition to this, it is clear that in these SQDs while the X_2 - X splitting is relatively constant, the Coulomb shift between uncharged and charged *s*-excitons varies considerably, from 1-10 meV in different SQDs. The separation between the *s*- X and the first *p*- X state is more consistent, around 40 meV (close to the LO-phonon energy). However the separation between the *p*- X^* and the *p*- X line also varies considerably, but is always around twice the separation of the *s*- X^* and the *s*- X lines. This suggests that the overlap between the *p* and *s* holes is greater than the overlap between two *s*-holes, which is a rather counter-intuitive result. Finally in each SQD, there are more absorption lines at higher energy, sometimes seen in both the charged and uncharged SQD spectra. This suggests that uncharged SQDs absorb resonantly into *p*-states which can then eject an electron to give positively-charged excitons (though other more unlikely possibilities could account for the same feature).

To summarize these results in the context of QIPC, they imply that each SQD may have similar confinement energies and emission energies but may have quite different shapes, aspect ratios, alloy composition or strain, leading to distorted wavefunctions and different wavefunction overlaps that control the different observed Coulomb energy shifts. On the other hand, most of the SQDs show similar spectral features, efficient emission, consistent and repeatable behavior (over many months) and sharp absorption and emission lines.

There is however one significant advantage that SQDs have over IQDs their proximity can be quite carefully controlled and there have even been some promising attempts to grow SQDs in specific locations using pre-patterning of the substrate. Vertical stacks of SQDs can be grown because the strain field of one SQD will cause the nucleation of a further SQD a few nm above it. In this way, the electronic coupling between different SQDs can be attempted. However, given the variability we have discussed above, it is extremely difficult to ensure that the two ground states are degenerate. This reduces the likelihood of success of QIPC schemes that rely on direct electronic coupling between SQDs, but makes it important to use schemes in which there is dipole Coulomb coupling between the SQDs, already shown above to be significant within a single SQD.

3.3 Experimental Techniques

The coherent quantum manipulation of semiconductor quantum dots can be most simply achieved through application of applied electric fields. These can be quasi-dc (for instance in short electrical bias pulses which can mix different electronic states inside the quantum dot), or ac electric fields, for instance microwaves (for spin precession or mixing), or optical fields (for bandgap excitation into confined electronic states). Currently all these schemes are under investigation, and they rely on the electronic states within the QD discussed above. However they then exploit different coherences within the QD, and in some cases a combination of these fields is used simultaneously.

The experiments discussed here make use primarily of optical excitation of electrons and holes within QDs. The advantages of using optical pulses is that the excitation sequences can be extremely fast (< 100 fs), whereas the dephasing time of carriers in the ground state of the highly confined QDs is supposed to be on the order of up to 1ns, similar to the radiative lifetime. In addition, resonantly tuned optical pulses should be selective, able to address only a single state in a single QD when needed. This allows for many of the necessary unitary transformations for QIPC. To entangle coherent superpositions of states, the Coulomb interaction between electrons and holes in neighboring QDs is employed, as discussed in elsewhere in this book. Thus requires more sophisticated coherent manipulation using coherently controlled optical pulse sequences [Baumberg (1998)].

3.3.1 Coherent spectroscopy on interface quantum dots

In the experiments on interface quantum dots (IQD), we read out quantum information from single interface quantum dots by directly probing the transient nonlinear optical spectrum of ground-state exciton transitions of a single quantum dot with sub-picosecond time resolution. In this section, we describe the near-field pump-probe spectrometer developed for these experiments and the signal contrast in near-field pump-probe spectroscopy of single quantum dots.

Our experimental concept is outlined in Figure 3.7(a). We use spectrally broad femtosecond laser, centered around the excitonic QW absorption resonance, coupled into a near-field fiber probe to probe the optical QD nonlinearity. As a near-field probe we use an uncoated etched single mode optical fiber taper with a cone angle of about 30° [Lambelet *et al.* (1998)]. With such probes we reach in an illumination/collection geometry - a spatial resolution of about 150 nm, i.e., about $\lambda/5$ [Intonti *et al.* (2001a)]. This high spatial resolution together with their large collection efficiency makes such uncoated fiber probes particularly well suited for semiconductor nanospectroscopy. Experimentally, we find that for GaAs samples about 1% of the light coupled into the fiber is collected in this illumination/collection geometry.

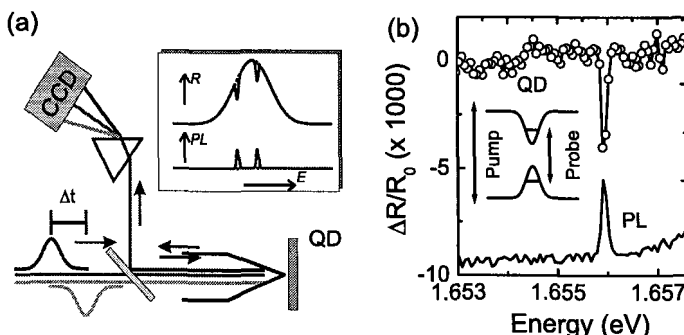


Fig. 3.7 (a) Schematic illustration of the experimental setup and of near-field PL and reflectivity spectra of the QD sample. (b) Near-field PL spectrum of a single QD (solid line) and differential reflectivity spectrum $\Delta R/R_0$ at $\Delta t = 30$ ps. PL and ΔR are recorded with identical pump pulses centered at 1.675 eV, exciting electron-hole pairs in 2D continuum states. The 100 nW probe pulses of 19 meV bandwidth are centered at 1.655 eV, around the QD absorption resonance. Inset: Schematic energy diagram.

In the pump-probe experiments, the probe laser light reflected from the QW sample is collected by the same fiber probe, dispersed in an 0.5 m

monochromator and then detected with a high sensitivity liquid-nitrogen cooled CCD camera. This steady-state reflectivity spectrum $R_0(\omega_{det})$ contains weak spectrally narrow resonances from single QD transitions (Figure 3.7(a)).

The presence of a second pump laser now affects the QD spectrum and thus gives rise to a modified probe reflectivity $R(\omega_{det})$. Differential probe reflectivity spectra $\Delta R(\omega_{det}, \Delta t)/R_0 = [R(\omega_{det}, \Delta t) - R_0(\omega_{det})]/R_0(\omega_{det})$ are recorded at a fixed spatial position of the near-field tip as a function of the time delay Δt between pump and probe pulses. To probe the nonlinear optical response from single quantum dots, the high spatial resolution of the near-field technique is needed for two reasons. First, the combined spatial and spectral resolution allows us to isolate single QD resonances (Figure 3.1). Second, the relative amplitude of the QD resonance in $R_0(\omega_{det})$ scales, in first approximation, inversely proportional to the square of the spatial resolution.

We assume for simplicity that the QD absorption spectrum can be modeled as that of an ideal two-level system (TLS) and that the incident laser power is homogeneously distributed over an area A (the areal resolution of the microscope). Then the incident power is $P = I_0 A$ and the absorbed power is $P_{QD} = I_0 \sigma_{QD}$, with I_0 being the incident intensity and σ_{QD} the QD absorption cross section. For an ideal TLS,

$$\sigma_{QD}(\omega) = \frac{\omega \mu_{QD}^2}{n c \epsilon_0 \hbar} \frac{\gamma}{\gamma^2 + (\omega - \omega_{QD}^2)}, \quad (3.1)$$

where $\omega_{QD} = 2\pi c/\lambda_{QD}$ denotes QD resonance frequency, ω the laser frequency, μ_{QD} the QD dipole moment, n the refractive index and $\gamma = 1/T_2$ the dephasing rate of the QD polarization. Thus improving the resolution from 1 μm to 100 nm increases the weak nonlinear QD signal by two orders of magnitude. For values typical for our experiments, $A = (250 \text{ nm})^2$, $\mu_{QD} = 60 \text{ D}$, $\gamma = (30 \text{ ps}^{-1})$, $n = 3.5$, $\lambda_{QD} = 750 \text{ nm}$, we estimate $\sigma_{QD}/A \simeq 0.04$, well measurable with the sensitivity of our setup. For self-assembled quantum dots, however, the dipole moment is typically 5 times smaller than for IQD, reducing the signal from a single QD to $\sigma_{QD}/A \simeq 10^{-3}$ if a monochromator with the same spectral resolution is used.

The near-field PL and differential reflectivity ΔR spectrum of a single QD are compared in Figure 3.7b. To record the ΔR spectrum we use 100 fs pump pulses derived from a 80 MHz repetition rate Ti:sapphire laser. The pump pulses in this experiment are centered at 1.675 eV and have an

energy of 1.5 fJ. They create less than five electron-hole pairs in QW states, corresponding to an excitation density of $5 \cdot 10^9 \text{ cm}^{-2}$. Relaxation of these extra carriers into the QD bleaches the QD absorption and this bleaching is probed with 1 fJ probe pulses of 18 meV bandwidth centered at 1.655 eV, around the QW absorption resonance. Figure 3.7b depicts a differential reflectivity spectrum $\Delta R(E_{det})$ at a time delay of 30 ps in the low energy region of the 5.1 nm QW absorption spectrum. It displays a single spectrally sharp resonance at exactly the same spectral position E_{QD} as the simultaneously recorded near-field PL spectrum. The large amplitude of the signal of $5 \cdot 10^{-3}$ is consistent with a spatial resolution of the experiment of 200–250 nm. Two-dimensional spatial scans indicate a resolution of 230 nm, limited by the QW-to-surface distance.

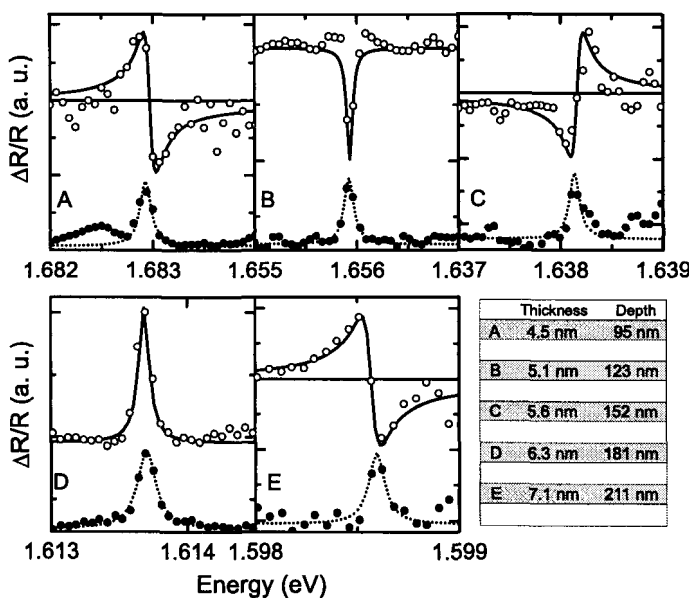


Fig. 3.8 Differential reflectivity spectra (open circles) of five interface QDs located at different depths of 95 to 210 nm below the sample surface (see inset). The differential reflectivity spectra are compared to simultaneously recorded PL spectra. Note the transition between dispersive and absorptive line shapes.

To better understand the image contrast in these pump-probe experiments, we compare in Figure 3.8 differential reflectivity $\Delta R(E_{det})$ and PL spectra recorded under similar excitation conditions for single localized excitons in five different QWs buried at distances of 95 nm to 211 nm below

the surface. We very clearly observe a transition between a dispersion-like and an absorption-like line shape as the QW-to-surface distance is varied. This behavior of the QD line shape can be understood in the framework a local oscillator model as caused by the interference between the electric probe laser field $E_R(t)$ reflected from the sample surface and the field $E_{QD}(t)$ emitted from the QD in back direction. Our experiment works in the following way (Figure 3.9). A fraction $E_R(t)$ of the probe laser transmitted through the near-field probe is reflected from the sample surface and coupled back into the near-field fiber probe. The probe field $E_T(t)$, transmitted into the semiconductor, induces a polarization $P_{QD}(t) = \int dt' \chi_{QD}(t') E_T(t-t')$ of the QD located at a distance d below the sample surface. Here, $E_T(t)$ and χ_{QD} denote the probe field interacting with the QD and the QD susceptibility, respectively. The QD polarization re-emits an electric field and a fraction of this field, $E_{QD}(t)$ is locally collected by the near-field probe where it interferes with $E_R(t)$.

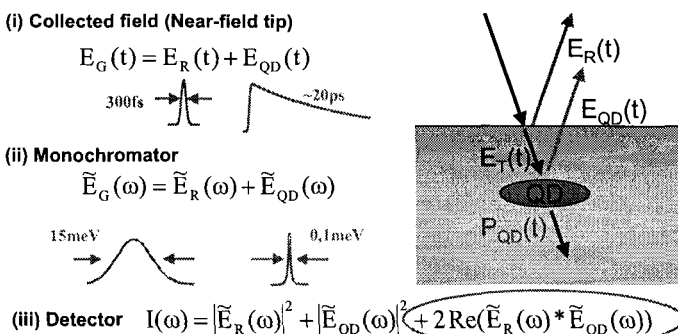


Fig. 3.9 Heterodyne detection of coherent QD polarizations. An fs probe laser is coupled through a near-field fiber probe. A large fraction E_R of the probe laser is directly reflected the sample surface into the fiber probe. The transmitted probe light E_T is induces a QD dot polarization P_{QD} and the fraction E_{QD} of the electric field re-emitted from the QD is collected by the near-field probe. E_R and E_{QD} are spectrally dispersed in a monochromator and interfere on the CCD detector. This heterodyne detection scheme greatly enhances the weak QD field.

The time-integrated reflectivity $R(\omega)$ detected behind the monochromator is proportional to $|\tilde{E}_{QD}(\omega) + \tilde{E}_R(\omega)|^2 \simeq |\tilde{E}_R(\omega)|^2 + 2\text{Re}[\tilde{E}_R^*(\omega)\tilde{E}_{QD}(\omega)]$, where $\tilde{E}(\omega)$ denotes the Fourier transform of the field $E(t)$. Here, the finite monochromator resolution and the weak contribution from $|\tilde{E}_{QD}|^2$ has been neglected. Excitation by the pump laser affects the QD polarization and thus results in a change of the QD reflectivity. The differential reflectivity

$\Delta R(\omega, \Delta t)$ represents the spectral interferogram of \tilde{E}_R and \tilde{E}_{QD} :

$$\Delta R(\omega, \Delta t) \propto \text{Re}\{\tilde{E}_R^*(\omega)[\tilde{E}_{QD}(\omega, \Delta t) - \tilde{E}_{QD,0}(\omega)]\}. \quad (3.2)$$

The spectral shape of this interferogram evidently depends on the QD polarization dynamics and on the phase delay between $E_{QD}(t)$ and $E_R(t)$. Treating the QD for simplicity as a point dipole and the near-field tip as a point-like emitter, the phase delay and thus the spectral shape of this interferogram depends on the distance between quantum dot and near-field tip. This interference effect is nicely seen in Figure 3.8 and explains the transition between absorptive and dispersive line shapes. Since the QDs are buried more than 50 nm below the surface, the near-field terms of the QD dipole emission can be neglected since they decay on a typical length scale of $\lambda/(2\pi n) \simeq 35$ nm ($n \simeq 3.5$ - refractive index). Based on an optical path of $4\pi nd/\lambda$, we estimate a phase change of $\pi/2$ for a change in QD-sample distance of 28 nm. This is in quite good agreement with the results of Figure 3.8. We consider this convincing evidence for the validity of the phenomenological local oscillator model described above. Clearly a detailed analysis of these data, using, e.g., a Green function solution of Maxwell's equations for a realistic experimental geometry is desirable for a quantitative comparison between experiment and theory.

The nice agreement between experiment and local oscillator model shows that this spectral-domain heterodyne detection scheme allows us to quantitatively measure the coherent polarization dynamics of single interface quantum dots. Different experiments using this novel experimental technique will be described below.

3.3.2 Coherent spectroscopy on self-assembled quantum dots

The main difference between SQDs and IQDs is the former's reduced size and hence increased confinement energy and smaller oscillator strength. This means that the experimental techniques presented above using direct probing of the SQD *s*-ground state are much more difficult because the signal is at least 1 to 2 orders of magnitude smaller. Recently the ground state has been resolved using electric-field modulation CW spectroscopy [Alen *et al.* (2003)]. In fact, there are no existent reports of direct time-resolved pump-probe spectroscopy on the ground state of a single SQD. Unfortunately, measurement of the *s*-state occupation are exactly what is required for QIPC experiments after a suitable multi-pulse excitation and

manipulation sequence. Everything so far thus falls short of this desired measurement. Instead most groups use *s*-state PL as a probe of the final occupation, with the consequence that *s*-excitation cannot be used because it is impossible to separate the strong exciting laser (needed due to the weak absorption) from the weak *s*-PL. Up-converting the PL from a single SQD is difficult due to the long PL lifetime and hence almost complete lack of photons at any particular time. The alternative using photocurrent from *s*-state carriers tunneling from the SQD has been successfully applied in simple cases [Zrenner *et al.* (2002)], and may prove suitable though is hard to perform at the single-shot level.

In the work presented here on SQDs, detection on the *s*-state is combined with excitation at the higher energy *p*-states described above. Although measurements on QD ensembles have shown long decoherence times of the *s*-state (hence their suitability for QIPC), the *p*-state is less studied [Kamada *et al.* (1998); Kako *et al.* (2002); Kamada *et al.* (2001)]. Much discussion exists in the literature about a phonon-bottleneck which prevents relaxation of the *p*-carriers to the ground state. However this says nothing about the phase decoherence properties. Two techniques are employed to explore the response, using either single ultrafast pulse of variable intensity (Rabi oscillations), or two phase-coherent pulses separated by a variable time-delay (coherent control).

The SQDs are grown on a GaAs substrate which is back-polished to allow excitation from the underside using a x50 microscope objective. Emission from the front surface is collected through 200 nm diameter apertures in a 100 nm thick Al film, 100 nm above the SQD layer. The PL is collimated by a x50 focal length lens before focusing through a 50 micron confocal aperture which ensures only light from the desired region is recorded. It is then focused into a 0.5 m grating monochromator and detected on a cooled-CCD. The sample is held in a cold-finger continuous-flow cryostat and remains at 4 K. Appropriate pulses of light are derived from a wavelength tunable ps or fs Ti:S laser.

For the Rabi oscillation experiments, a 1 ps pulse is used, directly produced by the laser, and tuned to the *p*-state of the desired SQD (Figure 3.10(a)). Its intensity is controlled using liquid-crystal polarization modulators which are able to rotate the polarization of the beam without displacing it on the sample (which all mechanical adjustments inevitably do). Ground state PL is recorded as the resonant pump intensity is varied.

For the coherent control experiments, the same 1 ps pulses are split into two beams, separately time-delayed on long ($1 \text{ ns} \pm 6 \text{ fs}$) and short ($20 \text{ fs} \pm$

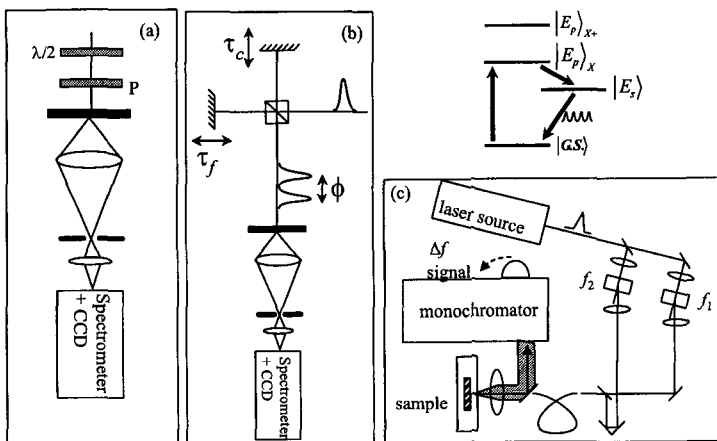


Fig. 3.10 Experimental configurations: (a) for single pulse Rabi oscillations, using a computer controlled birefringent waveplate to avoid any disturbance of the beam position with laser power and detecting *s*-PL, (b) coherent double pulse sequences generating *s*-PL depending on their relative phase, (c) ground state single QD probe using heterodyne double pulse technique where the relative phase shift in (b) varies at 70 kHz.

10 as) delay stages, and recombined at a beamsplitter before being focused into a single-mode fiber which exactly matches their spatial phase fronts. When they are focused on the sample, the first pulse excites the *p*-state resonantly, while the second time-delayed pulse interferes with the quantum state remaining from the 1st pulse. If in-phase, it excites increased occupation (stimulated absorption) while if out-of-phase it stimulates emission reducing the *p*-state occupation. The total occupation after the double pulse sequence is given by

$$N_p \propto |E_1 + E_2 e^{i\omega_p \tau_{12}} e^{-t/T_2}|^2, \quad (3.3)$$

where τ_{12} is the temporal separation of the pulses (producing fringes which oscillate at $2\pi/\omega_p$) and T_2 is the phase decoherence time of the *p*-state. Measurements of the visibility of the fringe contrast as a function of delay time allow the decoherence in a single-SQD to be measured.

In all these experiments it is important to spectrally filter the PL to remove the laser spectrum (which is much more difficult with near-resonant femtosecond pulses), as well as spatially filter the PL to remove any background from impurity/wetting layer states.

Finally, techniques to measure coherently the ground state occupation have been developed and tested. The idea is to measure the extremely weak absorption of the SQD s -state in the time domain rather than the spectral domain where it sits on a strong background transmission. Two pulses are again used, however this time they are separately diffracted from AO modulators with carrier frequencies which are 80 MHz and 80.2 MHz, before being recombined at a beamsplitter and spatially superimposed in a single-mode fiber. When they are resonantly-tuned to the s -state, the first pulse is partially absorbed, and the second pulse consequently amplified or deamplified on passage through the SQD depending on the relative phase of the evolving initial polarization. If the second pulse is in phase with the polarization excited by the first pulse, then energy is extracted from the pulses, and not all of this is remitted in PL that is collected. If the second pulse is out of phase, it re-stimulates energy absorbed from the first pulse, hence minimizing energy extracted from the pulses. Due to the continually increasing relative phase of the pulses (increasing linearly at 200 kHz), the total transmitted power should oscillate at the same frequency. Since this absorption only occurs in a narrow wavelength band, the transmitted beam is passed through a high-resolution 2 m grating spectrometer, detected on a Si avalanche photodiode, and subject to phase-sensitive lock-in detection. When the pulses are sufficiently far apart in time, only quantum states with a long decoherence time should give an observable signal, allowing extraction of the weak absorption from the background. So far however, this arrangement has failed to give an observable signal.

A similar experiment uses the fact that a pump pulse should be able to saturate the ground-state absorption (similar to the technique utilized for IQDs above). A p -state resonantly-tuned ps pulse is produced by sending a s -tuned 100fs laser pulse through a single-mode optical fiber to broaden its spectrum through nonlinear optical processes. This probe pulse is then filtered around the desired wavelength using a dispersion-neutral grating setup. The probe transmission around the s -state is monitored via lock-in detection in the presence and absence of the pump pulse (whose intensity is set to exactly inject a single $e - h$ pair). A balanced detection arrangement is used, however in order to derive the reference probe pulse, a pulse going through the same mask aperture on the sample has to be used to remove the effect of sample vibrations which change the probe transmission on a slow (kHz-Hz) time scale. An orthogonally-polarized pre-pulse is used to achieve this, which is recovered after the spectral filtering in the detection monochromator using a polarization beam-splitter mounted before identi-

cal APD detectors, and the two photocurrents are subtracted before the lock-in amplifier. However, once again, no signal is yet obtained with this arrangement, though it gives excellent test response using InGaAs quantum well samples, to transient detection sensitivities of 10^{-6} . The current interpretation is that the absorption of each SQD is just below the attainable detection sensitivity.

Thus while the experimental arrangements above give excellent absorption and decoherence data for the *p*- and *d*-states of a single SQD, they are as yet unable to interrogate the most interesting *s*-state response needed for many QIPC applications.

3.4 Results

3.4.1 Coherent control in single interface quantum dots

In this section, we describe experiments probing the coherent polarization dynamics of a single interface quantum dot induced by impulsive excitation with ultrafast light pulses. Specifically, three different topics are addressed. First, we ask the fundamental question regarding to what extent the ultrafast nonlinear optical response of a single IQD resembles that of an atomic system and how many-body Coulomb interactions often governing optical nonlinearities of higher-dimensional systems such as quantum wells and wires affect the QD polarization dynamics. Then we demonstrate coherent control of the phase of the QD polarization by probing the optical Stark effect in a single QD and coherent control of the polarization amplitude by probing Rabi oscillations in a single QD.

3.4.1.1 Ultrafast optical nonlinearities of single interface quantum dots

To study the effects of many-body interactions on the QD nonlinearities, we perform a quasi-two-color pump-probe experiment, exciting the QD sample in the QW absorption continuum with 100 fs pump-pulses at 1.675 eV with a pulse energy of 1.5 fJ. These pulses create carriers in QW states and the resulting change in the QD spectrum is probed with 1 fJ probe pulses of 18 meV bandwidth centered at 1.655 eV, around the QD resonance. The dynamics of the spectrally resolved reflectivity change measured on different QD resonances is shown in Figure 3.11. After a picosecond rise of the signal at negative delay times (probe precedes pump) one finds a partial decay with a time constant of about 6 ps, followed by a much slower decay with

time constants of 50 to 150 ps, depending on the specific QD resonance investigated.

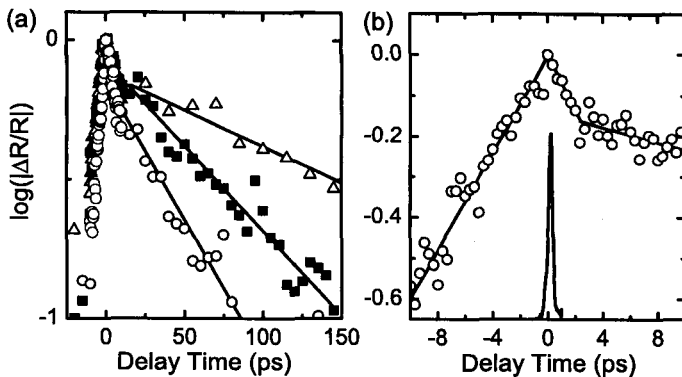


Fig. 3.11 (a) Temporal dynamics of $\Delta R/R$ for three different QD resonances (logarithmic ordinate scale). All decays are biexponential with a slow decay time varying between 30 and 150 ps. (b) Early time $\Delta R/R_0$ dynamics of a single QD resonance. A slow rise of $\Delta R/R_0$ is observed at negative time delays. The time resolution of the experiment is 150 fs, as indicated by the cross-correlation measurement (solid line around $\Delta t=0$).

The nonlinearities observed at sufficiently long positive Δt are easily understood on the basis of a simple two-level model for the QD nonlinearity. The pump laser creates a non-equilibrium distribution of electron-hole pairs in QW continuum states. Subsequent trapping of these carriers gives rise to a bleaching of the QD absorption and a concomitant decrease of the QD absorption. Hence, the decay time of ΔR reflects the lifetime of the individual exciton state probed. Following an earlier conjecture [Gammon *et al.* (1996b)], the QD population decay is mainly dominated by radiative recombination, i.e. $\tau_{rad} \simeq \tau_{QD}$. We can then estimate the dipole moment of the individual QDs using [Andreani *et al.* (1999); Thränhardt *et al.* (2002)]:

$$\frac{1}{\tau_{rad}} = n \frac{\omega^3 \cdot \mu_{QD}^2}{3\pi\epsilon_0\hbar c^3}. \quad (3.4)$$

We estimate dipole moments μ_{QD} of 50 to 85 Debye for τ_{rad} between 150 and 50 ps. These values are in rather good agreement with previous estimates [Stievater *et al.* (2001); Andreani *et al.* (1999)]. They exceed those of atomic systems by more than an order of magnitude and reflect the large spatial extension of the exciton center-of-mass wave function in these QDs. Near-field autocorrelation spectra indicate an exciton localization length of

about 40–50 nm. Due to the statistical nature of the disorder potential, the exciton localization length and thus the dipole moment and radiative recombination rate varies quite strongly from QD to QD, as seen in Figure 3.11b. Theoretical models of localized excitons in disordered quantum wells [Savona *et al.* (2002)] yield comparable results.

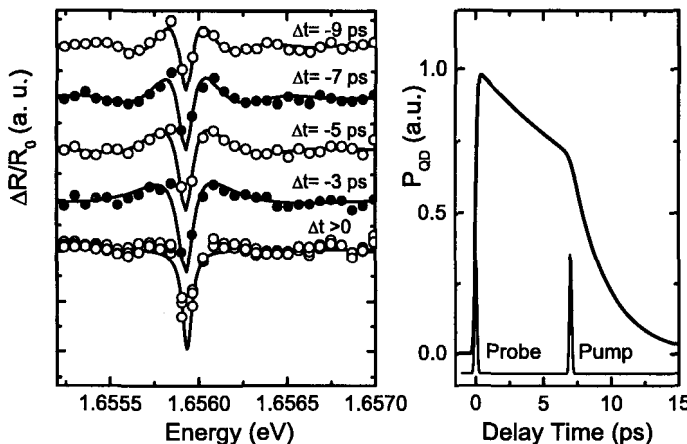


Fig. 3.12 (a) Near-field $\Delta R/R_0$ spectra (circles) at different delay times Δt . The spectra at $\Delta t < 0$ display pronounced spectral oscillations around the excitonic resonance. The solid lines show simulated spectra for the perturbed free induction decay of the coherent QD polarization assuming $T_2=15$ ps. (b) Dynamics of $P_{QD}(t)$ extracted from the time-dependent near-field $\Delta R/R_0$ spectra.

The dynamics of the QD reflectivity on a time scale of less than 10 ps, however, are quite different from what is expected for an ideal atomic system. The time evolution of $\Delta R(E_{QD}, \Delta t)$ shows an 8-ps rise at negative delay times, much slower than the 150-fs cross correlation of pump and probe pulses. A biexponential decay is found at positive delays, where the slow component reflects the exciton lifetime as discussed above. The fast decay time of about 6 ps is similar for all different QDs. The spectral characteristics of the differential reflectivity are markedly different at positive and negative delays. At negative delays, pronounced spectrally symmetric oscillations around the excitonic resonance are observed in Figure 3.12. Their oscillation period decreases with increasing negative time delay. At large positive delays, the spectra show a bleaching of the QD resonance [Guenther *et al.* (2002)].

This complex behavior reflects directly the coherent polarization dynamics of the excitonic QD excitation. To account for this behavior, one

has to consistently describe the dynamics of the field $E_{QD}(t)$ radiated from the coherent QD polarization $P_{QD}(t)$. We phenomenologically describe the QD as an effective two-level system with a ground, no-exciton state $|0\rangle$, and an excited one-exciton state $|1\rangle$. Then the quantum state of the TLS is given as a coherent superposition $|\psi(t)\rangle = c_0(t)|0\rangle + c_1(t)|1\rangle$. Within the density matrix formalism, $P_{QD}(t)$ is given as $P_{QD}(t) = \mu_{QD}^* \rho_{01} + c.c.$, where the microscopic QD polarization $\rho_{01} = \langle c_0^* c_1 \rangle$, μ_{QD} denotes the QD dipole moment and $\langle \dots \rangle$ the ensemble average [Haug and Koch (1994)]. Then, the well known Bloch equations hold and ρ_{01} obeys the equation of motion

$$\frac{\partial}{\partial t} \rho_{01}(t) = -i\omega_{QD} \rho_{01}(t) + i(1 - 2n_{QD})\omega_R - \gamma \rho_{01}(t), \quad (3.5)$$

with exciton energy ω_{QD} , dephasing rate γ , exciton population n_{QD} and generalized Rabi frequency ω_R .

In the absence of a pump laser, the resonant probe laser impulsively excites a coherent QD polarization which then decays with the dephasing rate γ (free induction decay). The re-emitted field interferes with the reflected probe laser field, giving rise to a Lorentzian QD line shape in $R_0(\omega)$ (Figure 3.2). The fact that we observe a linewidth that is limited by our monochromator resolution of about 60 μeV gives a lower limit for the QD dephasing time of $T_2 = 1/\gamma > 15$ ps.

The transient spectral oscillations around the QD exciton resonance at negative time delays indicate that this free induction decay of the $P_{QD}(t)$ is perturbed by the presence of the pump laser. In semiconductors, such oscillations have so far only been observed for higher dimensional system, e.g., studies of transient QW nonlinearities [Fluegel *et al.* (1987); Sokoloff *et al.* (1988)]. In our experiments, the off-resonant pump does not directly interact with the QD dipole but creates electron-hole pairs (density n_{QW}) in the QW continuum. Thus many-body interactions perturb the free induction decay of $P_{QD}(t)$.

The spectra at $\Delta t < 0$ are quantitatively described by assuming that an excitation-induced dephasing [Wang *et al.* (1993)], i.e., an increase in γ due to the interaction between ρ_{01} and n_{QW} is the leading contribution to the QD nonlinearity at early times. Coulomb scattering between the QD dipole and the initial nonequilibrium carrier distribution in the QW causes this additional fast damping of ρ_{01} . In the frequency domain, this excitation-induced dephasing leads to oscillatory structures in the spectrum with a period determined by the time delay between probe and pump. The solid lines in Figure 3.12a are calculated from Eq. (3.5) by assuming that

the probe-induced QD polarization $P_{QD}(t)$ decays initially with an effective dephasing time $T_2 = 15$ ps, decreasing to $T_{EID} = 3$ ps after the arrival of the pump laser (Figure 3.12b). Such an excitation-induced dephasing model accounts quantitatively for the the transient oscillations and this analysis allows to extract the QD polarization dynamics.

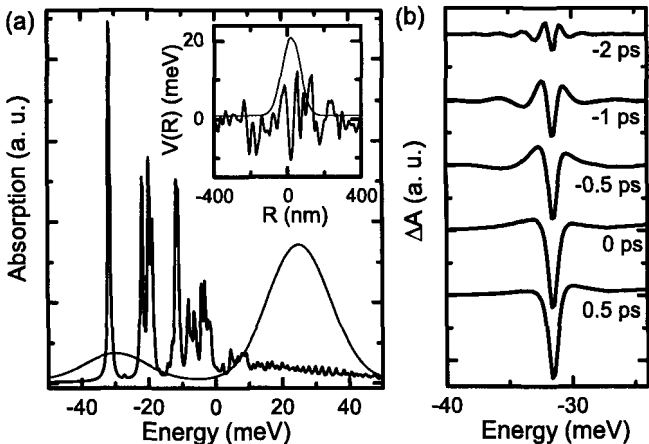


Fig. 3.13 (a) Spatially resolved linear absorption spectra of a QD ensemble calculated from the semiconductor Bloch equations. A Gaussian-correlated one-dimensional disorder potential is assumed (disorder potential and a resulting localized exciton wavefunction are shown in the inset). Dashed lines: Spectra of pump (centered at 25 meV) and probe pulses (at -30 meV). (b) Nonlinear absorption spectra for different pump-probe delays showing the perturbed free induction decay on the lowest resonance of (a).

A detailed theoretical analysis of the data was performed on the basis of the semiconductor Bloch equations in the mean-field approximation [Guenther *et al.* (2002)]. To first approximation, the excitation-induced dephasing rate should increase linearly with the pump-induced nonequilibrium carrier concentration n_{QW} in QW continuum states. Such a phenomenological model for the dephasing rate $\gamma = 1/T_2 + \gamma_1 \cdot n_{QW}$ was included in the simulations and good agreement between experiment and theoretical simulation was obtained (Figure 3.13). The theoretical calculations give strong support that excitation-induced dephasing dominates the perturbed free induction decay.

The assumption of a density-dependent dephasing rate can also explain the fast decay of the differential reflectivity at early positive delay times (Figure 3.11b). We have to assume that n_{QW} decays on a time scale of about 3 ps. This decay is most likely due to carrier trapping into QD

states. Then, the initial fast differential reflectivity decay reflects the transition from a QD nonlinearity dominated by excitation-induced dephasing to a nonlinearity dominated by exciton bleaching due to the population relaxation into the QD.

This model for the QD nonlinearity allows us to quantitatively describe the dynamics of the differential reflectivity at both positive and negative delay times [Guenther *et al.* (2003)]. It accounts for the transient spectral oscillations at negative delay times and reproduces the biexponential decay at positive delay times.

These results highlight two important features of interface quantum dots. First, the coherence of the ground state excitonic QD polarization persists for more than 10 ps even after resonant excitation with spectrally broad-band femtosecond pulses. This decoherence time is two orders of magnitude larger than the duration of the excitation pulses. On the other hand Coulomb many-body interactions may contribute significantly to their optical nonlinearities on ultrashort time scales if an additional exciton population in quantum well continuum states is created during the optical excitation process. Such many-body interactions have to be taken into account as important additional dephasing mechanisms.

3.4.1.2 Optical Stark effect and Rabi oscillations in a quantum dot: ultrafast control of single exciton polarizations

In the previous sub-section we have shown how to optically excite and read out coherent exciton polarizations of a single quantum dot using ultrafast near-field pump-probe spectroscopy. Here we now demonstrate coherent control of both the amplitude and phase of the coherent QD polarization on an ultrafast time scale. Coherent control of the population of a generic two-level system with finite electronic dipole moment μ can be achieved by resonant impulsive excitation with light pulses much shorter in duration than the decoherence time of the microscopic polarization ρ_{01} . Neglecting for simplicity the finite decoherence time of this TLS, the excited state population after the interaction with the excitation laser is given as $n_1 = \sin^2(\theta/2)$, with θ being the pulse area

$$\theta = \frac{\mu \cdot \hat{\varepsilon}}{\hbar} \int_{-\infty}^{\infty} E(t) dt, \quad (3.6)$$

where $E(t)$ denotes the time-dependent electric field profile of the excitation laser and $\hat{\varepsilon}$ its polarization direction. Thus, for weak excitation pulses

the excited state population first increases linearly with increasing pulse intensity until it reaches a value of $n = 1$ for $\theta = \pi$, i.e. until the two-level-system is fully inverted. Further increase in the pulse intensity induces stimulated emission from the excited state back to ground state and thus a decrease of excited state population. After interaction with a light pulse of area $\theta = 2\pi$ the excited state population reaches again $n = 0$, i.e. the system is back in its original state. For higher excitation, the population shows the well known Rabi oscillations. Of course this simplified picture only holds for resonant excitation and negligible decoherence and thus the study of Rabi oscillations should generally give insight into the decoherence of quantum systems in the strong excitation regime.

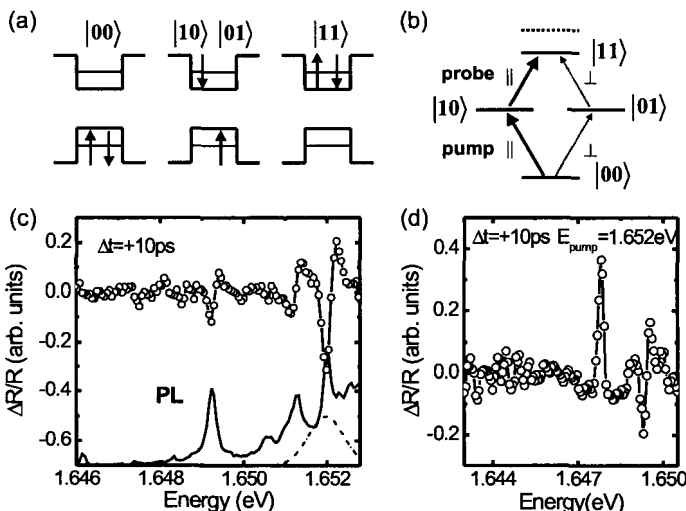


Fig. 3.14 (a) Schematics of exciton ground ($|00\rangle$), one-exciton ($|10\rangle$, and $|01\rangle$), and biexciton states $|11\rangle$ in a QD. (b) Excitation-level diagram in an interface QD and optical selection rules for pump and probe laser. (c) PL and ΔR for above bandgap excitation. In the studies of biexciton nonlinearities, the pump laser (dashed line) is tuned to the exciton resonance at 1.652 eV. (d) Pump-induced biexciton nonlinearity. The time delay between pump (at 1.652 eV) and probe laser is $\Delta t = 10$ ps.

For resonant excitation of only a single excitonic transition, we use spectrally tailored optical pulses with a spectral width of about 1 meV and a pulse duration of about 1.5 ps. We tune these pump pulses to a specific quantum dot resonance and probe the induced optical nonlinearity with collinearly polarized 15 meV broad of 200 fs duration. The idea of the experiment is to read-out the exciton population after the QD interaction

with the pump pulse by probing the induced absorption on the exciton biexciton transition. Since each confined electron state in the QD can be occupied with two electrons of opposite spin orientation, two distinguishable single exciton states with orthogonal polarization can be optically excited. Simultaneous excitation of both exciton states results in a transient population of the bound biexciton state [Figure 3.14a]. In IQDs, the biexciton energy is normally slightly smaller (1-4 meV) than the sum of the two exciton energies due to the Coulombic interaction between the two excitons. Since the monolayer islands in interface quantum dots are slightly elongated along the [-110] direction [Gammon *et al.* (1996b)], the energetic degeneracy of the two single-exciton states is slightly lifted (by typically less than 100 μ eV) [Gammon *et al.* (1996b)] and one finds linear polarization selection rules for the exciton and biexciton transitions [Gammon *et al.* (1996b); Kulakovskii *et al.* (1999); Bertoni *et al.* (2000)]. The energy level structure of the QD states and the polarization selection rules can be summarized in a four-level system for the no-exciton crystal ground state $|00\rangle$, two exciton states with orthogonal polarization $|10\rangle$ and $|01\rangle$ and the biexciton state $|11\rangle$ [Figure 3.14b]. Optical excitation of the $|00\rangle \rightarrow |10\rangle$ single exciton transition gives rise to excited state absorption on the $|10\rangle \rightarrow |11\rangle$ transition. This excited state absorption is not present in the absence of single exciton excitation. Experimentally we observe indeed, after single exciton excitation at 1.652 eV [Figure 3.14c] a new transition resonance red shifted by 1.648 eV, red-shifted by 4 meV from the single exciton transition which is assigned to the exciton-biexciton $X \rightarrow XX$ transition [Figure 3.14d]. Also the dynamics of the pump-probe signal on the $X \rightarrow XX$ is consistent with this assignment [Figure 3.15a]. We observe no biexciton nonlinearity at negative delay times (probe precedes pump), i.e. in the absence of $|10\rangle$ exciton excitation. Around time zero the $X \rightarrow XX$ rises within the time resolution of the experiment and then decays exponentially on a 40 ps time scale, i.e., with the radiative single exciton lifetime. This means that the induced $X \rightarrow XX$ is a direct measure of the transient $|10\rangle$ exciton population generated by the pump pulse. We study the effect of the pump power on this biexciton nonlinearity. The experimental results at a delay time of $\Delta t = 10$ ps are shown in Figure 3.15b. The magnitude of the differential biexciton nonlinearity ΔR_{XX} displays pronounced oscillations when varying the power of the pump laser P_{pu} . In Figure 3.15b ΔR_{XX} is plotted vs. the maximum field strength $E_{pu} \propto \sqrt{P_{pu}}$ of the pump laser. These oscillations give clear evidence for Rabi oscillations on a single ground-state exciton transition in a single interface quantum dot. Despite

the clarity of these oscillations, the experiment also shows that interface quantum dots are not an ideal two-level system. The biexcitonic nonlinearity at the second maximum, corresponding to a 3π excitation pulse, is about 1/3 smaller than that at the first maximum corresponding to a π excitation. This unwanted damping of the Rabi oscillations is caused again by excitation-induced dephasing as an additional source of decoherence. The field dependence of the biexciton nonlinearity, $\Delta R_{XX}(E_{pu})$, can well be reproduced within the framework of Optical Bloch Equations of a two-level system with an intensity-dependent dephasing rate $\gamma = 1/T_2 + \gamma_1 \cdot E_{pu}^2$ [Figure 3.15b]. Good agreement between experiment and model is achieved by assuming a dipole moment of 60 D, similar to those previously measured. The microscopic physics underlying this excitation-induced dephasing is similar to that reported for above-bandgap excitation of QW continuum states in Section 1.4.1.1. Excitation by the ps-pump pulse not only drives the desired single exciton transition but also creates coherent polarizations and incoherent populations in the QD environment. Since our pump-probe signals are accumulated over a large number of typically 10^8 laser pulses, these unwanted excitations effectively give rise to a fluctuating QD environment and, thus, to decoherence of the ensemble-averaged QD polarization. Our experimental results are well reproduced by assuming that the QD dephasing rate increases from less than $(15 \text{ ps})^{-1}$ (an upper limit given by our finite monochromator resolution) to about $(6 \text{ ps})^{-1}$ for a pulse area of 3π . In summary, this experiments evidence coherent control of the population of a single QD exciton by demonstration of Rabi oscillations.

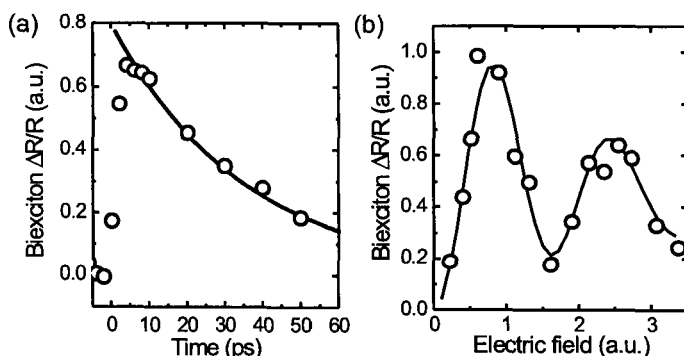


Fig. 3.15 (a) Temporal dynamics of the biexciton nonlinearity at 1.648 eV. The excitation conditions are as shown in Figure 3.14. The 30 ps decay at $\Delta t > 0$ reflects the exciton lifetime. (b) Rabi oscillation in a single IQD. Magnitude of the biexciton nonlinearity as function field amplitude of the pump laser at $\Delta t = 10 \text{ ps}$.

Full coherent control over the single exciton excitation, however, requires not only control over the exciton population or more precisely the amplitude of the microscopic polarization ρ_{01} but also control over the polarization phase $\phi = \arctan(\text{Im}(\rho_{01})/\text{Re}(\rho_{01}))$. In a Bloch sphere representation, often used to visualize the quantum dynamics of quasi-two-level systems, the momentary polarization ρ_{01} is represented as a three-dimensional vector $\rho_B = [\text{Re}(\rho_{01}), \text{Im}(\rho_{01}), 1/2(n_1 - n_0)]$, with $n_i = \langle c_i^* c_i \rangle$ describing the population of state $|i\rangle$. In this representation, polarization control thus means controlling the azimuthal angle ϕ in the $[\text{Re}(\rho_{01}), \text{Im}(\rho_{01})]$ -plane. Simultaneous control over amplitude and phase of the polarization thus gives full control over both degrees of freedom on the Bloch sphere.

Here we demonstrate control of the relative phase between the driving laser and the excitonic polarization by making use of the optical Stark effect (OSE). The OSE is one of the fundamental coherent light-matter interactions describing the light-induced shift (“dressing”) of energy levels in the presence of non-resonant laser fields. In atomic systems the OSE is well known and, for weak excitation, well described by optical Bloch equations for independent two-level systems [Mollow (1972); Häffner *et al.* (2003)]. In higher-dimensional semiconductors, e.g. quantum wells, however, the polarization dynamics induced by non-resonant light fields is much more complex than in atomic systems and often dominated by Coulomb-mediated many-body interactions [Mysyrowicz *et al.* (1986); Knox *et al.* (1989); Sieh *et al.* (1999); Saba *et al.* (2000)]. Effects such as exciton-exciton interaction, biexciton formation or higher-order Coulomb correlations may affect the magnitude of the energy shift, the exciton oscillator strength and may even reverse the sign of the shift [Sieh *et al.* (1999); Schmitt-Rink and Chemla (1986); Combescot and Combescot (1988); Ell *et al.* (1989)]. Here, we report the first experimental study of the OSE in a quasi-zero-dimensional semiconductor [Unold *et al.* (2004)].

Figure 3.16 compares the PL (solid line) from a single QD and the $\Delta R(\omega, \Delta t = 50 \text{ ps})/R_0$ spectrum for above-bandgap excitation of QW continuum states (solid circles). The absorptive ΔR spectrum reflects the bleaching of the QD resonance as described above. For below-bandgap excitation with 2 ps pump pulses tuned 3 meV below the QD resonance, however, we observe for weak excitation ($P_p \lesssim 0.2 \mu\text{W}$) and negative delay times, here $\Delta t = -4 \text{ ps}$ (probe precedes pump) a dispersive line shape centered around ω_{QD} . With increasing excitation power, we find a drastic change in the line shape of $\Delta R(\omega)$ [Figure 3.17a]: for strong excitation, the signal maximum shifts slightly towards higher energies and an increasing

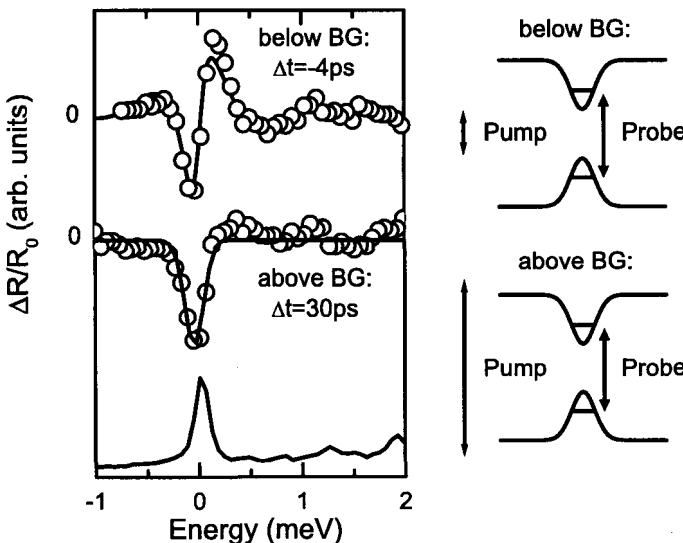


Fig. 3.16 (left) PL spectrum of a single QD resonance $\omega_{QD} = 1.6503$ eV and differential reflectivity $\Delta R(\omega)/R_0$ for above bandgap excitation at $\Delta t = 50$ ps and for below bandgap excitation at $\Delta t = -4$ ps with 2 ps pulses at 1.647 eV (bandwidth $\sigma = 0.8$ meV) in the weak excitation limit ($P_p u = 0.12 \mu\text{W}$). Solid lines: Bloch equation model. (right) Schematic excitation diagram.

number of spectral oscillations is observed, in particular on the high energy side of the QD resonance. This change in line shape occurs together with a saturation of the strength of the nonlinear signal ΔR_m , taken as the difference between minimum and maximum of $\Delta R(\omega)$ [Figure 3.17b]. As we will show below, this characteristic change in line shape allows us to extract the phase shift $\Delta\phi$ of the QD polarization due to the interaction with the off-resonant pump laser from a Bloch equation simulation. The extracted phase shift $\Delta\phi$ is plotted as a function of excitation power in Figure 3.17c.

To ensure that we are indeed probing only a light-induced shift of the exciton resonance, we also plot the time evolution of the QD nonlinearity $\Delta R_m(\Delta t)/R_0$ [Figure 3.18]. In these measurements we have used 200-fs excitation pulses tuned 14 meV below the QD resonance at 1.654 eV. It is important that the signal vanishes completely for positive delay times $\Delta t > 0$ (pump precedes probe) and rises around $\Delta t = 0$ within the time resolution of our experiment of 250 fs. For $\Delta t < 0$, $\Delta R_m(\Delta t)$ decays with a time constant of $\tau_d = 8$ ps.

The dispersive ΔR line shape observed in Figure 3.16a for below bandgap excitation and small time delays is the signature of the OSE in

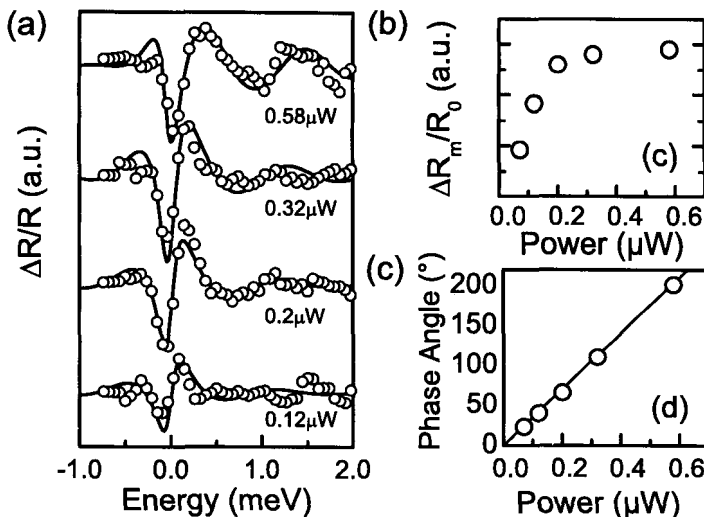


Fig. 3.17 (a) Optical Stark Effect in a single QD. Differential reflectivity spectra $\Delta R(\omega)/R_0$ for below bandgap excitation at $\Delta t = -4$ ps with 2 ps pulses at 1.647 eV (bandwidth $\sigma = 0.8$ meV) for excitation powers between 0.12 and 0.58 μW . Solid lines: Bloch equation model. (b) Variation of the signal magnitude $\Delta R_m(\omega_{QD})/R_0$ with pump power. (c) Phase shift of the QD polarization vs. pump power.

the *weak excitation limit* [Mysyrowicz *et al.* (1986)]. It reflects a transient light-induced blue shift QD exciton resonance. In the presence of an AC electric field of frequency ω_p , the transition frequency of a two-level system shifts by $\Delta\omega_0(t) = \sqrt{[(\omega_0 - \omega_p)^2 + \Omega_R(t)^2]} + \omega_p - \omega_0$. Here, ω_0 is the transition frequency without external field, $\Omega_R(t) = \mu \cdot E_p(t)/\hbar$ is the Rabi frequency, μ the transition dipole moment and $E_p(t) \cdot \cos(\omega_p t)$ the (pump) AC electric field. The blue shift $\Delta\omega_0(t)$ of the QD absorption resonance results in a dispersive $\Delta R(\omega)/R_0$ line shape, which can be approximated as $\Delta R(\omega)/R_0 \propto \Delta\omega_{0,max} \cdot \partial\alpha(\omega)/\partial\omega$, where $\alpha(\omega)$ is the QD absorption spectrum and $\Delta\omega_{0,max}$ is the maximum blue shift. Thus, in the weak excitation limit, the amplitude of the $\Delta R(\omega)/R$ signal is expected to increase linearly with increasing pump power, without change of the line shape. The spectra of Figure 3.17a taken with pump powers $\leq 0.2 \mu\text{W}$ exactly display this behavior. For such pump powers, the Rabi frequency has a maximum value of $\Omega_{R,max} = 1.75 \text{ meV} \approx 5\Delta\omega_{0,max}$.

The origin of this transient blue shift becomes clear from an analysis of the optical Bloch equations. We describe the QD as a two-level system with a radiative lifetime of $T_1 = 100$ ps corresponding to a dipole moment

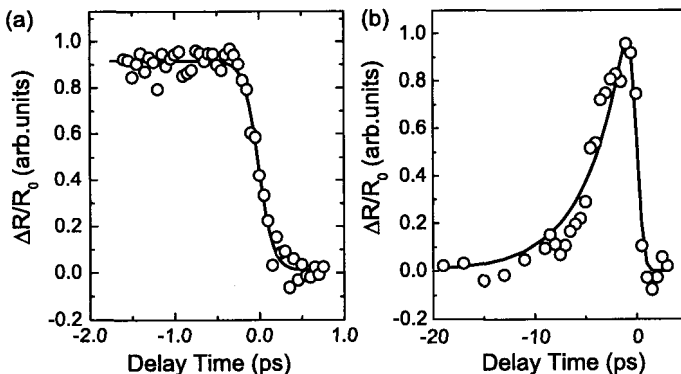


Fig. 3.18 Time evolution of $\Delta R_m(\Delta t)/R_0$ for a single QD at $\omega_{QD} = 1.6544$ eV. Here 200-fs pump pulses with a power of $58 \mu\text{W}$ were centered at 1.640 eV. $\Delta R_m(\Delta t > 0)$ vanishes and the signal for $\Delta t < 0$ decays on a ps time scale. (a) 3 ps time scale. (b) 25 ps time scale.

$\mu = 50$ Debye [Guest *et al.* (2002); Guenther *et al.* (2002); Thränhardt *et al.* (2002)]. A dephasing time of $T_2 = 8$ ps is assumed to account for our finite monochromator resolution. It is important to stress that since we know both power and duration τ_p of the pump pulses and the spatial resolution of about 250 nm, the electric field of the pump laser is estimated to within a factor of 2 and no free parameters enter the simulation.

The calculated dynamics of the QD polarization in the weak excitation limit are displayed in the rotating frame in Figure 3.19a. The probe field resonant to the exciton line changes the QD population and drives a coherent polarization oscillating at the QD resonance frequency ω_{QD} . This polarization is 90° phase-shifted with respect to the probe field ($\text{Re}[P_{QD}] = 0$). During the presence of the pump pulse, the polarization is externally driven, leading to oscillations at the detuning frequency $\omega_{det} = \omega_0 - \omega_p$. After the interaction, the polarization is phase-shifted by $\Delta\phi \approx \int \Delta\omega_0(t)dt$. It is this shift $\Delta\phi$ of the QD polarization which changes the product $E_{pr}(\omega) \cdot E_{QD}(\omega)$ of the complex electric fields and therefore the line shape. Fourier-transformation of the polarization dynamics gives directly the dispersive line shape of the $\Delta R(\omega)$ spectrum in the weak excitation limit, $\Delta\phi \lesssim 40^\circ$, at early delay times (Figure 3.16, inset in Figure 3.19a). The simulation also reproduces the time-dependent data shown in Figure 3.18. Evidently, a vanishing nonlinearity at positive time delays is predicted by the Bloch model, since then the pump laser interacts with the sample before the excitonic polarization is created. At negative delays, the OSE nonlin-

earity is expected to decay with the dephasing time of the polarization. The fact that we reproduce both predictions of this simple model experimentally is quite striking. In particular, we find within our signal-to-noise ratio, no measurable nonlinearity at $\Delta t > 0$. This indicates that we are indeed probing a pure light-induced shift of the resonance and that nonlinearities induced by real carriers generated by one- or two-photon absorption in the surrounding of the QD obviously play a negligible role [Unold *et al.* (2004)]. This conclusion is strongly supported by recording transient nonlinear spectra at different negative delay times between 0 and -10 ps. Here, pronounced spectral oscillations are observed which are quantitatively fit by the Bloch equation. Thus, even under femtosecond excitation, the nonlinear response of the IQD for below bandgap excitation is very close to that of an isolated atomic system and it appears that the excitonic QD excitation is only very weakly influenced by the complex solid state environment. To be precise, one should note that from our experiments one cannot directly tell whether the 8 ps decay at negative delay times reflects the polarization dephasing time. We are spectrally resolving the QD nonlinearity with a monochromator with about 100 μeV resolution and this finite resolution puts an upper limit of slightly less than 10 ps to the measurable decay. Thus the 8 ps decay is close to our instrument resolution and only gives a lower limit for the excitonic decoherence rate.

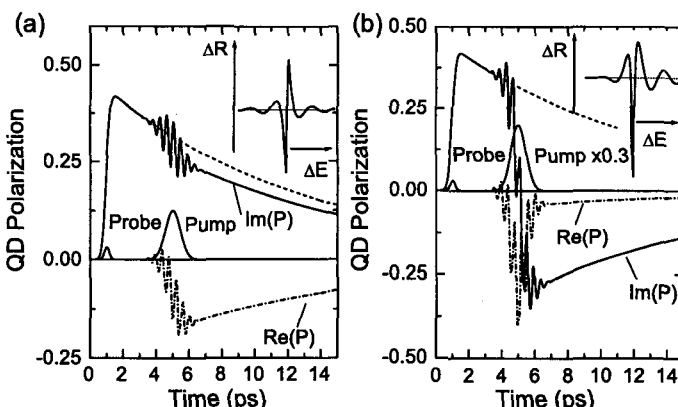


Fig. 3.19 Bloch equation simulation of the single QD optical Stark effect. Shown is the time-dependent QD polarization P_{QD} in the rotating frame with (solid line) and without (dashed line) pump laser. Nonlinear ΔR spectra are given in the inset. (a) Weak excitation limit. (b) Strong excitation limit. The chosen pump power corresponds to a phase shift $\Delta\phi = 172^\circ$.

For higher electric fields of the pump pulse, the weak excitation limit of the OSE nonlinearity is no longer valid. Experimentally one finds additional features in the transient reflectivity spectra (Figure 3.17a, traces for pump intensities of 0.32 and 0.58 μW). These spectral oscillations are a direct consequence of the interaction of the QD polarization with the strong pump field. The pump laser induces pronounced large amplitude oscillations of QD polarization at the detuning frequency during the presence of the pump laser. This is illustrated in Figure 3.19b showing the solution of Bloch equations for strong excitation with $\Omega_R = 6 \text{ meV}$ ($\omega_{det} = -10 \text{ meV}$). A large phase shift $\Delta\phi$ of 172° of the QD polarization results from this interaction and the nonlinear ΔR spectrum shows additional oscillatory structures on the high energy side, as found in the experiment. This large amplitude phase rotation corresponds to the observation of *gain* on the resonance of a single QD. In the Bloch sphere representation this phase rotation basically reflects a nutation-like motion of the Bloch vector, resulting in change in azimuthal angle after the interaction. A comparison between experimental spectra and simulation (solid lines in Figure 3.17a) allows us to quantify the phase shift $\Delta\phi$ experienced by the QD polarization. In Figure 3.17c we plot $\Delta\phi$ obtained from the simulation of the data in Figure 3.17a as a function of the pump power P_p . We find a linear increase in $\Delta\phi$ with P_p . This means that the light shift also increases linearly in our experiment, despite the saturation of ΔR_m . This linear increase in the polarization phase $\Delta\phi$ is somewhat analogous to the pulse area theorem for Rabi oscillations of the population of a two-level system when driven with a resonant pulse. Currently, we can quantitatively measure the phase shift with an accuracy of about 10° and achieve phase rotations of as much as 200° . Control of the exciton density, on the other hand, has been established above by the observation of Rabi oscillations when varying the pulse area of a resonant excitation pulse. The results show that a sequence of a resonant and an off-resonant laser pulse gives full control over both amplitude *and* phase of the coherent excitonic polarization. In particular, we can switch the QD from absorption to gain within about 1 ps.

In conclusion, we have demonstrated coherent control over amplitude and phase of the excitonic QD polarization. Rabi oscillations of up to 4π are induced and probed by ultra-fast light pulses. It appears that even in relatively weakly confined interface quantum dots, the ultrafast polarization dynamics are in many respects similar to those of an atomic system, yet with an enhanced dipole moment. Only when interacting with strong excitation pulses with an area of order 2π is excitation-induced dephasing due

to Coulomb-mediated many-body limiting the visibility of Rabi oscillations. One may expect that using quantum dots with larger confinement energies may reduce excitation-induced dephasing. Yet, so far the experiments on ground and excited state Rabi oscillations in more strongly confined self-assembled quantum dots seem to indicate that here other factors, such as enhanced exciton-phonon coupling, may be important additional decoherence sources. Certainly, the microscopic origin of exciton decoherence in single quantum dots will be the topic of much additional experimental and theoretical work in the near future. Finally we note that the experimental techniques described here allow one to probe transient optical nonlinearities in a broad spectral range and thus are particularly well suited to study excitonic couplings, e.g. by dipolar interactions, between adjacent quantum dots. Such dipolar interactions, in particular when enhanced by external electric fields, may be used for realizing potentially scalable non-local quantum gates with switching of only few picoseconds [Biolatti *et al.* (2000); Biolatti *et al.* (2002)]. The experimental study of such interactions presents an important avenue for future work.

3.4.2 Coherent control in single self-assembled quantum dots

While coherent experiments on interface quantum dots are at a relatively advanced stage, those on SQDs are much more primitive due to the greatly reduced signals obtained. Ultrafast laser pulses tuned to the resonant transitions in a SQD allow us to investigate the coherent manipulation of their electronic wavefunctions. In particular, in the SQDs discussed previously, it is possible to look at both uncharged and positively-charged single SQDs by exciting resonantly at the *s* and *p* transitions. These experiments are the necessary precursors to manipulations which display quantum entanglement of wavefunctions within one or several SQDs. They give us confidence for the first time that it is possible to successfully invert a single transition within an SQD with reasonable accuracy, and to explore the parasitic mechanisms which will limit the reliability of QIPC in SQDs.

To measure the decoherence time of the specific *p*-states identified in PLE spectroscopy, we excite them with resonantly-tuned coherently-controlled pairs of 1 ps pulses [Besombes *et al.* (2003)]. After this pulse sequence, the final population in the *p*-state relaxes down to the *s*-state in the single SQD and recombines predominantly radiatively producing PL proportional to the *p*-state population. By changing the time delay be-

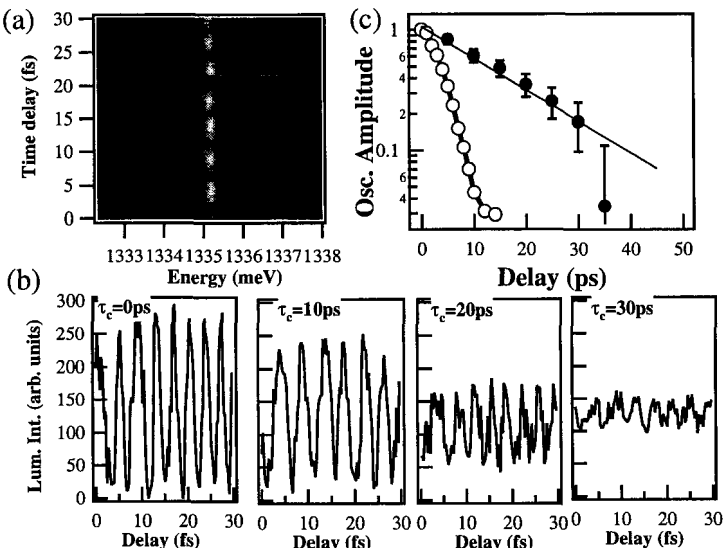


Fig. 3.20 (a) PL spectra around the *s*-state as a function of the fine time delay at a coarse delay of 15 ps. (b) PL vs. fine delay (i.e. phase) at different course time delays. (c) Dephasing and/or decay of the lowest *p*-state for the same charged (solid) and uncharged (open) SQD.

tween the pulses over a few optical cycles, the phase-dependent component to this final population is extracted for different gross separations of the two pulses (Figure 3.20). Interestingly the dephasing times extracted for charged SQDs (around 15 ps) are longer than the dephasing times for the same SQD when it is uncharged. As the intensity of the pulses is increased, the oscillations no longer remain sinusoidal (with a period corresponding to that of the *p*-state frequency), but they become strongly distorted (Figure 3.21). At the highest intensities, extra dips now appear at the positions of constructive interference between the pulses. The origin of these strong nonlinearities can be traced back to the response of a two-level system to an optical pulse. A coherently excited system will stop absorbing once it is completely inverted, and further impinging radiation will cause deexcitation.

This can be seen more clearly in the response to a single pulse. A pulse of sufficient intensity can completely invert a two-level system, and a stronger or longer pulse will act to deexcite it again. The critical parameter is the pulse area (see Eq.3.6) which is given by the Rabi frequency. The Rabi frequency is the rate at which the two-level system can be inverted

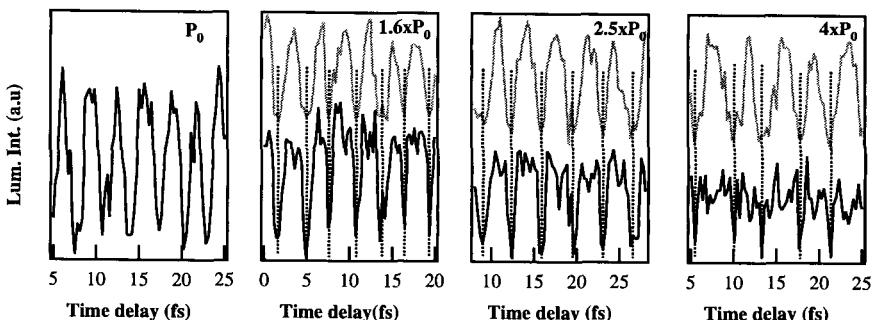


Fig. 3.21 *s*-state PL as a function of the relative phase of the *p*-state excitation pulses, of different power. At high powers, the response is higher nonlinear (black) compared to the sinusoidal relative phase of the laser pulses (gray).

and de-inverted, and thus is one of the key parameters for QIPC operations. Increasing either the pulse intensity or the pulse length increases the Rabi frequency, however it is not completely trivial to make optical pulses which are square in time, with a variable length. Instead we modify the intensity using liquid crystal modulators, and record the ground state PL as a function of the square root of the intensity (i.e. $\propto \theta$). When the incident 1ps pulse is resonantly tuned to the *p*-state, the total PL oscillates with θ [Figure 3.22a] showing that the *p*-exciton can be completely inverted and then de-excited coherently. These “Rabi oscillations” should be contrasted with other semiconductor systems such as quantum wells, in which attempts to invert the exciton lead to strong Coulomb-interactions between many excitons, screening out the exciton and suppressing any possibility of exciton inversion (i.e. excitation-induced dephasing). The selectivity of resonant excitation in a SQD suppresses Coulomb interactions, and restricts the number of excitons present. When the laser pulse is tuned slightly to either side of the wavelength of the *p*-state, a power dependent PL from the ground state is still seen (Figure 3.22b) this is absorption in the background wetting layer states mentioned previously. For resonant excitation, the Rabi oscillations are superimposed on this background absorption contribution.

The Rabi oscillations allow determination of the power in a pulse needed to completely invert each particular SQD from the intensity giving the peak PL (I_π). From estimates of the optical field strength at the sample, this allows us to calculate the dipole matrix strength of the SQDs, which are around 10 Debye. We also clearly see a large range in values of the dipole matrix element for different SQDs, varying by a factor of around two, implicating the shape and strain fields in modifying the coupling to light.

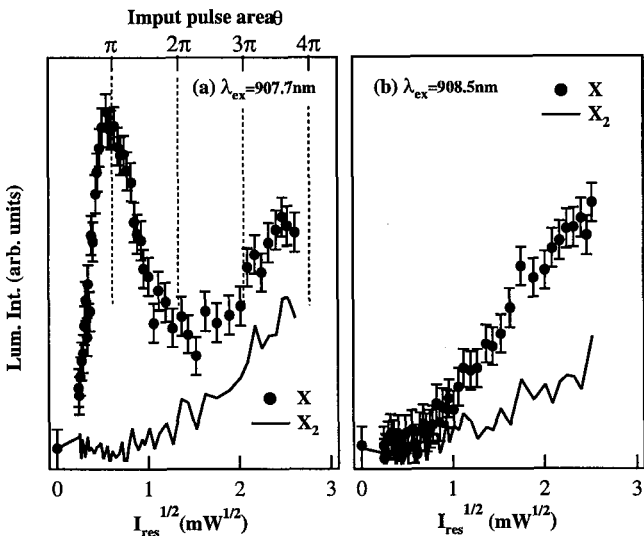


Fig. 3.22 Ground state PL as a function of the square root of the power of the excitation pulses, for resonant p -state (left) and off-resonant (right) tuning. Both exciton and biexciton s -state emission is shown, as well as the input pulse area.

We can also measure the Rabi oscillations in the same SQD when it is uncharged, and positively-charged (Figure 3.23) [Besombes *et al.* (2003)]. This implies that the p -state for the charged exciton has at least twice the oscillator strength than that for the uncharged p -state, suggesting significant differences in the size of the wavefunction overlaps in the different cases.

It is also clear that the number of Rabi oscillations we observe is limited to two. One possible cause can be seen in the simultaneous nonlinear increase in the biexciton emission, which turns on as soon as inversion is reached, and shows no sign of oscillations. Once again this implicates the role of background absorption in allowing multiple excitons to be excited within the same SQD, suggesting that extra excitons act to increase dephasing of the electronic states. One can try to increase the speed of Rabi-like excitation using shorter pulses with similar pulse areas. However, comparison of experimental results using 1 ps and 100 fs pulses show us that the wider spectral content of the latter pulses increases the background contribution from the wetting layer, and thus strongly reduces the visibility of the Rabi oscillations. Longer pulses matched to the spectral width of the transitions are thus optimal. The decrease in visibility of the Rabi oscillations of a single SQD at higher pulse powers implies that multi-photon

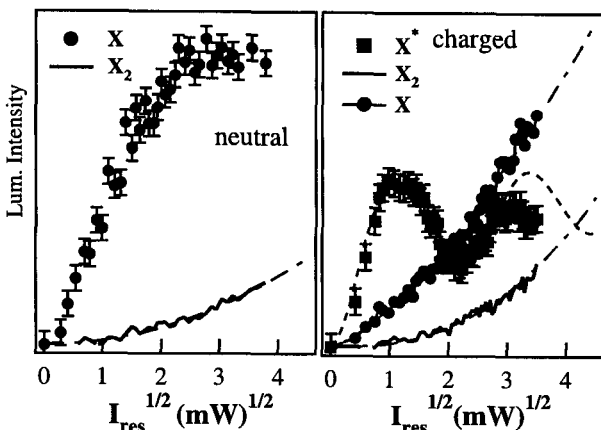


Fig. 3.23 Ground state PL as a function of the square root of the power of the excitation pulses, for the same SQD when neutral (left) and charged (right). This shows the different oscillator strength of the neutral and charged configuration, as well as biexciton and uncharged exciton contributions.

transitions or wetting layer transitions increase the decoherence rate. The current limit on Rabi oscillations is not understood within the framework of SQDs, and is clearly an important effect to be unraveled.

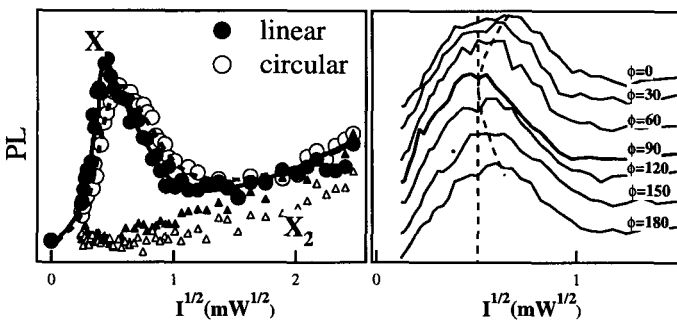


Fig. 3.24 (a) Rabi oscillations for linear- (solid) and circular- (open) polarized excitation. The Rabi oscillation peak on the s -exciton for linear polarization is at lower power, thus it has a larger oscillator strength. (b) Rabi oscillations for different orientations of the linear polarization, where $\phi=90$ is along the [110] direction.

Finally, by varying the pulse optical polarization it is possible to find the selection rules and optical axes of each SQD [Besombes *et al.* (2004)]. Typical data is shown in Figure 3.24, using both linear and circular input polarization. The observation that the linear polarization exhibits a smaller

I_π , implies the light is coupling directly to a single electronic state within the SQD. In contrast, circular polarization only inverts at higher intensity because two electronic states are being pumped (with orthogonal linear axes), thus taking more pulse area to invert. Similarly rotating the input linear polarization confirms that the anisotropy is along the [110] direction, with one axis giving larger Rabi frequency than the orthogonal axis.

Hence time-resolved ultrafast coherent experiments on single SQDs are clearly invaluable in trying to understand the decoherence properties of these two-level-like systems. It also highlights the issues for QIPC in these nanomaterials, namely the inhomogeneity of all SQD parameters.

3.5 Outlook

Key issues remain to be resolved in producing robust solid-state quantum dot systems for qubits. For the semiconductor QDs discussed in this chapter, issues of homogeneity and connectivity need to be addressed. Realistic implementations of SQD quantum logic inevitably require an approach in which each element is significantly more consistent and predictable than currently found in interface or self-assembled quantum dots. Although it is likely that effective coupling between SQDs will soon be achieved (for instance vertically-stacked) and so permit various quantum logic gate operations, a focus on improved control of the material nanostructures is inevitably required. Significant efforts are underway in many groups worldwide, and it is likely that some of the unusual new routes to assembling semiconductor nanostructures will ultimately bear fruit.

On the other hand, the QD systems currently available clearly allow a great exploration of the possibilities inherent in coherently manipulating solid-state optically-addressable qubits. With the consistent improvement in experimental techniques for studying individual QDs, more sophisticated coherent control can be realized, allowing us to study some of the theoretical ideas developed to alleviate decoherence and enhance entanglement. Particularly promising are schemes to independently address electrically as well as optically individual QDs, and to gate couplings between QDs. It is likely that the next 5 years will see significant progress in the control and manipulation of quantum coherence in small numbers of semiconductor QDs. An ambitious challenge for the further future is to create selective entanglements between QD pairs across larger QD ensembles. Attempting to define “flying qubits” which specifically transmit quantum information

through a QD ensemble using electronic spin, cavity photons, metal plasmons or another excitation, is the initial part of this challenge.

Acknowledgments

The author (CL) wishes to thank Tobias Guenther, Valentina Emiliani, Francesca Intonti, Kerstin Mueller, Roland Mueller and Thomas Unold for their invaluable contributions to this project. The experiments on IQDs reported in this chapter were performed by Tobias Guenther, Kerstin Mueller and Thomas Unold at the Max-Born-Institut in Berlin. Particular thanks are due to Thomas Elsaesser for continuous support and fruitful discussions. High-quality semiconductor samples have been provided by Soheyla Eshlaghi and Andreas D. Wieck (Ruhr-Universität Bochum). Theoretical support by Markus Glaneman, Vollrath Martin Axt and Tilmann Kuhn (Universität Münster) is gratefully acknowledged.

The author (JJB) wishes to thank Lucien Besombes, Junichi Motohisa and David Smith for their invaluable contributions. The experiments on SQDs reported in this chapter were all performed by Lucien Besombes at the University of Southampton, while the samples giving optimal results and shown here were grown by Junichi Motohisa at the University of Hokkaido in Japan.

This project has been financially supported by the Deutsche Forschungsgemeinschaft (SFB 296) and the European Union through the EFRE and SQID programs.

Bibliography

- Andreani, L. C., Panzarini, G., and Gerard, J. M. (1999). Strong-coupling regime for quantum boxes in pillar microcavities: Theory. *Phys. Rev. B* **60**: 13276.
- Alen B., Bickel F., Karrai K., Warburton R.J., Petroff P.M., Stark-shift modulation absorption spectroscopy of single quantum dots (2003). *Appl. Phys. Lett.* **83**: 2235.
- Baumberg J.J. (1998). Optical coherence in semiconductor quantum structures, *Curr Opin Solid St M* **3**: 181.
- Bayer, M. and Forchel, A. (2002). Temperature dependence of the exciton homogeneous linewidth in In_{0.60}Ga_{0.40}As/GaAs self-assembled quantum dots. *Phys. Rev. B* **65**: 041308.
- Bertoni, A., Bordone, P., Brunetti, R., Jacoboni, C., and Reggiani, S. (2000). Quantum Logic Gates based on Coherent Electron Transport in Quantum Wires. *Phys. Rev. Lett.* **84**: 5912.
- Besombes, L., Baumberg, J. J., and Motohisa, J. (2003). Coherent Spectroscopy

- of Optically Gated Charged Single InGaAs Quantum Dots. *Phys. Rev. Lett.* **90**: 257402.
- Besombes L., Baumberg J.J., Motohisa J., (2004). Polarization-dependent Ultra-fast Rabi Oscillations in Single InGaAs Quantum Dots, *Semi.Sci. Tech* **19**: 148.
- Bimberg, D. (1999). Quantum Dot Heterostructures Chichester, UK: Wiley.
- Biolatti, E., D'Amico, I., Zanardi, P., and Rossi, F. (2002). Electro-optical properties of semiconductor quantum dots: Application to quantum information processing. *Phys. Rev. B* **65**: 075306.
- Biolatti, E., Iotti, R., Zanardi, P., and Rossi, F. (2000). Quantum Information Processing with Semiconductor Macroatoms. *Phys. Rev. Lett.* **85**: 5647.
- Birkedal, D., Leosson, K., and Hvam, J. M. (2001). Long Lived Coherence in Self-Assembled Quantum Dots. *Phys. Rev. Lett.* **87**: 227401.
- Bonadeo, N. H., Chen, G., Gammon, D., Katzer, D. S., Park, D., and Steel, D. G. (1998). Nonlinear Nano-Optics: Probing One Exciton at a Time. *Phys. Rev. Lett.* **81**: 2759.
- Borri, P., Langbein, W., Schneider, S., Woggon, U., Sellin, R. L., Ouyang, D., and Bimberg, D. (2001). Ultralong Dephasing Time in InGaAs Quantum Dots. *Phys. Rev. Lett.* **87**: 157401.
- Brennen, G. K., Caves, C. M., and Deutsch, I. H. (1999). Quantum Logic Gates in Optical Lattices. *Phys. Rev. Lett.* **82**: 1060.
- Brunner, K., Abstreiter, G., Böhm, G., Tränkle, G., and Weimann, G. (1994). Sharp-Line Photoluminescence and Two-Photon Absorption of Zero-Dimensional Biexcitons in a GaAs/AlGaAs Structure. *Phys. Rev. Lett.* **73**: 1138.
- Bukowski T.J., Simmons J.H. (2002). Quantum dot research: Current state and future prospects *Crit Rev Solid State* **27**: 119.
- Chen, P., Piermarocchi, C., and Sham, L. J. (2001). Control of Exciton Dynamics in Nanodots for Quantum Operations. *Phys. Rev. Lett.* **87**: 067401.
- Chiorescu, I., Nakamura, Y., Harmans, C. J. P. M., and Mooij, J. E. (2003). Coherent Quantum Dynamics of a Superconducting Flux Qubit. *Science* **299**: 1869.
- Cirac, J. C. and Zoller, P. (1995). Quantum Computations with Cold Trapped Ions. *Phys. Rev. Lett.* **74**: 4091.
- Combescot, M. and Combescot, R. (1988). Excitonic Stark Shift: A Coupling to "Semivirtual" Biexcitons. *Phys. Rev. Lett.* **61**: 117.
- Ell, C., Müller, J. F., Sayed, K. E., and Haug, H. (1989). Influence of Many-Body Interactions on the Excitonic Optical Stark Effect. *Phys. Rev. Lett.* **62**: 304.
- Emiliani, V., Intonti, F., Lienau, C., Elsaesser, T., Nötzel, R., and Ploog, K. H. (2001). Near-field optical imaging and spectroscopy of a coupled quantum wire-dot structure. *Phys. Rev. B* **64**: 155316.
- Flissikowski, T., Hundt, A., Lowisch, M., Rabe, M., and Henneberger, F. (2001). Photon Beats from a Single Semiconductor Quantum Dot. *Phys. Rev. Lett.* **86**: 3172.
- Fluegel, B., Peyghambarian, N., Olbright, G., Lindberg, M., Koch, S. W., Joffre,

- M., Hulin, D., Migus, A., and Antonetti, A. (1987). Femtosecond Studies of Coherent Transients in Semiconductors. *Phys. Rev. Lett.* **59**: 2588.
- Förstner, J., Weber, C., Danckwerts, J., and Knorr, A. (2003). Phonon-Assisted Damping of Rabi Oscillations in Semiconductor Quantum Dots. *Phys. Rev. Lett.* **91**: 127401.
- Franson, J. D. (1997). Cooperative Enhancement of Optical Quantum Gates. *Phys. Rev. Lett.* **78**: 3852.
- Fry P.W., Itskevich I.E., Mowbray D.J., et al. (2000). Inverted electron-hole alignment in InAs-GaAs self-assembled quantum dots *Phys Rev Lett* **84**: 733.
- Gammon, D., Snow, E. S., Shanabrook, B. V., Katzer, D. S., and Park, D. (1996a). Homogeneous linewidths in the optical spectrum of a single gallium arsenide quantum dot. *Science* **273**: 87.
- Gammon, D., Snow, E. S., Shanabrook, B. V., Katzer, D. S., and Park, D. (1996b). Fine Structure Splitting in the Optical Spectra of Single GaAs Quantum Dots. *Phys. Rev. Lett.* **76**: 3005.
- Gershenfeld, N. and Chuang, I. L. (1997). Bulk Spin-Resonance Quantum Computation. *Science* **275**: 350.
- Guenther, T., Lienau, C., Elsaesser, T., Glanemann, M., Axt, V. M., Kuhn, T., Eshlaghi, S., and Wieck, A. D. (2002a). Coherent Nonlinear Optical Response of Single Quantum Dots Studied by Ultrafast Near-Field Spectroscopy. *Phys. Rev. Lett.* **89**: 057401.
- Guenther, T., Lienau, C., Elsaesser, T., Glanemann, M., Axt, V. M., and Kuhn, T. (2002b). Guenther et al. Reply: *Phys. Rev. Lett.* **90**: 139702.
- Guest, J. R., Stievater, T. H., Li, X., Cheng, J., Steel, D. G., Gammon, D., Katzer, D. S., Park, D., Ell, C., Thränhardt, A., Khitrova, G., and Gibbs, H. M. (2002). Measurement of optical absorption by a single quantum dot exciton. *Phys. Rev. B* **65**: 241310.
- Gulde, S., Riebe, M., Lancaster, G. P. T., Becher, C., Eschner, J., Häffner, H., Schmidt-Kaler, F., Chuang, I. L., and Blatt, R. (2003). Implementation of the Deutsch-Jozsa algorithm on an ion-trap quantum computer. *Nature* **421**: 48.
- Häffner, H., Gulde, S., Riebe, M., Lancaster, G., Becher, C., Eschner, J., Schmidt-Kaler, F., and Blatt, R. (2003). Precision Measurement and Compensation of Optical Stark Shifts for an Ion-Trap Quantum Processor. *Phys. Rev. Lett.* **90**: 143602.
- Haug, H. and Koch, S. W. (1994). *Quantum theory of the optical and electronic properties of semiconductors*. Singapore: World Scientific, 2 edition.
- Hawrylak, P., Narvaez, G. A., Bayer, M., and Forchel, A. (2000). Excitonic Absorption in a Quantum Dot. *Phys. Rev. Lett.* **85**: 389.
- Hess, H. F., Betzig, E., Harris, T. D., Pfeiffer, L. N., and West, K. W. (1994). Near-field spectroscopy of the quantum constituents of a luminescent system. *Science* **264**: 1740.
- Htoon, H., Takagahara, T., Kulik, D., Baklenov, O., Holmes, A. L., Jr., and Shih, C. K. (2002). Interplay of Rabi Oscillations and Quantum Interference in Semiconductor Quantum Dots. *Phys. Rev. Lett.* **88**: 087401.
- Intonti, F., Emiliani, V., Lienau, C., Elsaesser, T., Nötzel, R., and Ploog, K. H.

- (2001a). Near-field optical spectroscopy of localized and delocalized excitons in a single GaAs quantum wire. *Phys. Rev. B* **63**: 075313.
- Intonti, F., Emiliani, V., Lienau, C., Elsaesser, T., Savona, V., Runge, E., Zimermann, R., Nötzel, R., and Ploog, K. H. (2001b). Quantum Mechanical Repulsion of Exciton Levels in a Disordered Quantum Well. *Phys. Rev. Lett.* **87**: 076801.
- Ioffe, L. B., Geshkenbeim, V. B., Feigel'man, M. V., Fauchère, A. L., and Blatter, G. (1999). Environmentally decoupled sds -wave Josephson junctions for quantum computing. *Nature* **398**: 679.
- Kako S., Sugimoto T., Toda Y., Ishida S., Nishioka M., Arakawa Y. (2002). Observation of dip structures in PLE spectra of a highly excited single self-assembled quantum dot, *Physica E* **13**: 151.
- Kamada H., Ando H., Temmyo J., Tamamura T. (1998). Excited-state optical transitions of excitons and biexcitons in a single InGaAs quantum disk, *Phys Rev B* **58**: 16243.
- Kamada, H., Gotoh, H., Temmyo, J., Takagahara, T., and Ando, H. (2001). Exciton Rabi Oscillation in a Single Quantum Dot. *Phys. Rev. Lett.* **87**: 246401.
- Kammerer C., Cassabois G., Voisin C., Delalande C., Roussignol P., Gerard J.M. (2001). Photoluminescence up-conversion in single self-assembled InAs/GaAs quantum dots, *Phys. Rev. Lett.* **87**: 207401.
- Knill, E., Laflamme, R., and Milburn, G. J. (2001). A scheme for efficient quantum computation with linear optics. *Nature* **409**: 46.
- Knox, W. H., Chemla, D. S., Miller, D. A. B., Stark, J. B., and Schmitt-Rink, S. (1989). Femtosecond ac Stark effect in semiconductor quantum wells: Extreme low- and high-intensity limits. *Phys. Rev. Lett.* **62**: 1189.
- Kulakovskii, V. D., Bacher, G., Weigand, R., Kümmell, T., and Forchel, A. (1999). Fine Structure of Biexciton Emission in Symmetric and Asymmetric CdSe/ZnSe Single Quantum Dots. *Phys. Rev. Lett.* **82**: 1780.
- Lambelet, P., Sayah, A., Pfeffer, M., Philipona, C., and Marquis-Weible, F. (1998). Chemically etched fiber tips for near-field optical microscopy: a process for smoother tips. *Appl. Optics* **37**: 7289.
- Li, X., Wu, Y., Steel, D., Gammon, D., Stievater, T. H., Katzer, D. S., Park, D., Piermarocchi, C., and Sham, L. J. (2003). An All-Optical Quantum Gate in a Semiconductor Quantum Dot. *Science* **301**: 809.
- Makhlin, Y., Schön, G., and Shnirman, A. (1999). Josephson-junction qubits with controlled couplings. *Nature* **398**: 305.
- Mollow, B. R. (1972). Stimulated Emission and Absorption near Resonance for Driven Systems. *Phys. Rev. A* **5**: 2217.
- Mooij, J. E., Orlando, T. P., Levitov, L., Tian, L., van der Wal, C. H., and Lloyd, S. (1999). Josephson Persistent-Current Qubit. *Science* **285**: 1036.
- Mysyrowicz, A., Hulin, D., Antonetti, A., Migus, A., Masselink, W. T., and Morkoç, H. (1986). "Dressed Excitons" in a Multiple-Quantum-Well Structure: Evidence for an Optical Stark Effect with Femtosecond Response Time. *Phys. Rev. Lett.* **56**: 2478.
- Nielsen, M. A., and Chuang, I. L. (2000). *Quantum Computation and Quantum Information*.

- Information.* Cambridge: Cambridge University Press.
- Oulton R., Finley J.J., Tartakovskii A.I., et al. (2003). Continuum transitions and phonon coupling in single self-assembled Stranski-Krastanow quantum dots *Phys Rev B* **68**: 235301.
- Petroff P.M., Denbaars S.P., (1994). MBE And MOVCD Growth And Properties Of Self-Assembling Quantum-Dot Arrays in III-V Semiconductor Structures, *Superlattices And Microstructures* **15**: 15.
- Piermarocchi, C., Chen, P., Dale, Y. S., and Sham, L. J. (2002). Theory of fast quantum control of exciton dynamics in semiconductor quantum dots. *Phys. Rev. B* **65**: 075307.
- Saba, M., Quochi, F., Ciuti, C., Martin, D., Staehli, J.-L., Deveaud, B., Mura, A., and Bongiovanni, G. (2000). Direct observation of the excitonic ac Stark splitting in a quantum well. *Phys. Rev. B* **62**: 16322.
- Savona, V., Runge, E., Zimmermann, R., Intonti, F., Emiliani, V., Lienau, C., and Elsaesser, T. (2002). Level Repulsion of Localized Excitons in Disordered Quantum Wells. *phys. stat. sol. (a)* **190**: 625.
- Schmidt-Kaler, F., Häffner, H., Riebe, M., Gulde, S., Lancaster, G. P. T., Deuschle, T., Becher, C., Roos, C. F., Eschner, J., and Blatt, R. (2003). Realization of the Cirac-Zoller controlled-NOT quantum gate. *Nature* **422**: 408.
- Schmitt-Rink, S. and Chemla, D. S. (1986). Collective Excitations and the Dynamical Stark Effect in a Coherently Driven Exciton System. *Phys. Rev. Lett.* **57**: 2752.
- Sieh, C., Meier, T., Jahnke, F., Knorr, A., Koch, S. W., Brick, P., Hübner, M., Ell, C., Princeas, J., Khitrova, G., and Gibbs, H. M. (1999). Coulomb Memory Signatures in the Excitonic Optical Stark Effect. *Phys. Rev. Lett.* **82**: 3112.
- Sokoloff, J. P., Joffre, M., Fluegel, B., Hulin, D., Lindberg, M., Koch, S. W., Migus, A., Antonetti, A., and Peyghambarian, N. (1988). Transient oscillations in the vicinity of excitons and in the band of semiconductors. *Phys. Rev. B* **38**: 7615.
- Sorensen, A. and Molmer, K. (1999). Quantum Computation with Ions in Thermal Motion. *Phys. Rev. Lett.* **82**: 1971.
- Stievater, T. H., Li, X., Steel, D. G., Gammon, D., Katzer, D. S., Park, D., Piermarocchi, C., and Sham, L. J. (2001). Rabi Oscillations of Excitons in Single Quantum Dots. *Phys. Rev. Lett.* **81**: 2759.
- Thränhardt, A., Ell, C., Khitrova, G., and Gibbs, H. M. (2002). Relation between dipole moment and radiative lifetime in interface quantum dots. *Phys. Rev. B* **65**: 035327.
- Toda, Y., Sugimoto, T., Nishioka, M., and Arakawa, Y. (2000). Near-field coherent excitation spectroscopy of InGaAs/GaAs self-assembled quantum dots. *Appl. Phys. Lett.* **76**: 3887.
- Turchette, Q. A., Hood, C. J., Lange, W., Mabuchi, H., and Kimble, H. J. (1995). Measurement of Conditional Phase Shifts for Quantum Logic. *Phys. Rev. Lett.* **75**: 4710.
- Unold, T., Mueller, K., C. Lienau, T. Elsaesser, and Wieck, A. D. (2004). Op-

- tical Stark Effect in a Quantum Dot: Ultrafast Control of Single Exciton Polarizations. *Phys. Rev. Lett.* **92**: 157401.
- Vagov, A., Axt, V. M., and Kuhn, T. (2002). Electron-phonon dynamics in optically excited quantum dots: Exact solution for multiple ultrashort laser pulses. *Phys. Rev. B* **66**: 165312.
- van der Wal, C. H., ter Haar, A. C. J., Wilhelm, F. K., Schouten, R. N., Harmans, C. J. P. M., Orlando, T. P., Lloyd, S., and Mooij, J. E. (2000). Quantum Superposition of Macroscopic Persistent-Current States. *Science* **290**: 773.
- Vandersypen, L. M. K., Steffen, M., Breyta, G., Yannoni, C. S., Sherwood, M. H., and Chuang, I. L. (2001). Experimental realization of Shor's quantum factoring algorithm using nuclear magnetic resonance. *Nature* **414**: 883.
- Verzelen O., Bastard G., Ferreira R. (2002). Energy relaxation in quantum dots *Phys Rev B* **66**: 081308.
- Verzelen, O., Ferreira, R., and Bastard, G. (2002). Excitonic Polarons in Semiconductor Quantum Dots. *Phys. Rev. Lett.* **88**: 146803.
- Wang, H., Ferrio, K., Steel, D. G., Hu, Y. Z., Binder, R., and Koch, S. W. (1993). Transient nonlinear optical response from excitation induced dephasing in GaAs. *Phys. Rev. Lett.* **71**: 1261.
- Woldeyohannes, M. and John, S. (1999). Coherent control of spontaneous emission near a photonic band edge: A qubit for quantum computation. *Phys. Rev. A* **60**: 5046.
- Yamamoto, T., Pashkin, Y. A., Astafiev, O., Nakamura, Y., and Tsai, J. S. (2003). Demonstration of conditional gate operation using superconducting charge qubits. *Nature* **425**: 941.
- Zrenner, A. (2000). A close look on single quantum dots. *J. Chem. Phys.* **112**: 7790.
- Zrenner, A., Beham, E., Stuffer, S., Findeis, F., Bichler, M., and Abstreiter, G. (2002). Coherent properties of a two-level system based on a quantum-dot photodiode. *Nature* **418**: 612.

This page intentionally left blank

Chapter 4

Few-Particle Effects in Semiconductor Macroatoms/Molecules

F. Troiani, U. Hohenester¹ and E. Molinari

INFM Center on NanoStructures and BioSystems at Surfaces (S3)

Dipartimento di Fisica, Università di Modena e Reggio Emilia

Via Campi 213/A, 41100 Modena, Italy

4.1 Introduction

As anticipated in Chapter 1, one of the most appealing features of semiconductor quantum dots (QDs) consists in the possibility they offer to experimentally control the number of confined carriers. Besides, the 3D-spatial confinement enhances the Coulomb interactions and the resulting effects, namely the energy renormalizations of the inter-band transitions due to the presence of additional (“spectator”) carriers and the spatial correlations between electrons and holes. The main focus of the present chapter is precisely on these few-particle effects, as well as on their interplay with single-particle ones, such as the tunneling-induced inter-dot coupling. The fundamental role of the electric field as a flexible tool for tuning such interplay and engineering the optical response of the “artificial molecules” is finally discussed.

¹present affiliation: Institut für Theoretische Physik, Karl-Franzens-Universität Graz,
Universitätsplatz 5, 8010 Graz, Austria

4.2 Excitons

4.2.1 Semiconductors of higher dimension

We first consider one electron-hole pair inside a bulk semiconductor. If the Coulomb attraction between the two carriers is sufficiently weak, one can employ the usual envelope-function and effective-mass approximations: the first approximation assumes that the electron-hole wavefunction approximately consists of atomic-like wavefunctions modulated by an envelope function, and the latter one assumes parabolic dispersions for electrons and holes near the band minima, which are characterized by the effective electron and hole masses m_e and m_h , respectively. Then,

$$H = - \sum_{i=e,h} \frac{\nabla_{\mathbf{r}_i}^2}{2m_i} - \frac{e^2}{\kappa|\mathbf{r}_e - \mathbf{r}_h|} \quad (4.1)$$

describes the interacting electron-hole system, with κ the static dielectric constant of the bulk semiconductor. In the solution of Eq. (4.1) one usually introduces the center-of-mass and relative coordinates $\mathbf{R} = (m_e \mathbf{r}_e + m_h \mathbf{r}_h)/M$ and $\rho = \mathbf{r}_e - \mathbf{r}_h$, respectively, and decomposes $H = H_{\mathbf{R}} + H_{\rho}$ into the parts

$$H_{\mathbf{R}} = -\frac{\nabla_{\mathbf{R}}^2}{2M}, \quad H_{\rho} = -\frac{\nabla_{\rho}^2}{2\mu} - \frac{e^2}{\kappa|\rho|}, \quad (4.2)$$

with $M = m_e + m_h$ and $\mu = m_e m_h / M$. Correspondingly, the total wavefunction can be decomposed into parts $\Psi^x(\mathbf{R})$ and $\phi^n(\rho)$ associated to the center-of-mass and relative motion, respectively, whose solutions are provided by the Schrödinger equations

$$H_{\mathbf{R}} \Psi^x(\mathbf{R}) = E_x \Psi^x(\mathbf{R}), \quad H_{\rho} \phi^n(\rho) = \epsilon_n \phi^n(\rho). \quad (4.3)$$

Here, the first equation describes the motion of a free particle with mass M , and the second one the motion of a particle with mass μ subject to the potential $-e^2/\kappa|\rho|$, whose solutions are provided by those of the hydrogen atom but for the modified Bohr radius $a_o = \kappa/\mu e^2$ and Rydberg energy $R_o = e^2/(2\kappa a_o)$ (with typical values $a_o \sim 10$ nm and $R_o \sim 5$ meV for GaAs). In the field of semiconductor physics the Coulomb-bound electron-hole pair is usually referred to as an *exciton*.

Similar results also apply to the lower-dimensional quantum wells and quantum wires, provided that $\phi^n(\rho)$ is replaced by the corresponding two-

and one-dimensional wavefunctions, respectively. For instance,

$$\phi_o(\rho) = \frac{4}{a_o} \exp\left(-\frac{2\rho}{a_o}\right), \quad \epsilon_o = -4R_o \quad (4.4)$$

is the wavefunction of the ground state exciton in two dimensions, and ϵ_o the corresponding energy.

4.2.2 Semiconductor quantum dots

How are the results of the previous section modified in the presence of additional quantum confinements $U_e(\mathbf{r}_e)$ and $U_h(\mathbf{r}_h)$ for electrons and holes? In analogy to Eq. (4.1) we employ the envelope-function and effective-mass approximations, and describe the interacting electron and hole subject to the quantum-dot confinement through the Hamiltonian

$$H = \sum_{i=e,h} \left[-\frac{\nabla_{\mathbf{r}_i}^2}{2m_i} + U_i(\mathbf{r}_i) \right] - \frac{e^2}{\kappa|\mathbf{r}_e - \mathbf{r}_h|}. \quad (4.5)$$

Apparently, a separation into center-of-mass and relative motion is no longer possible because of the additional terms $U_i(\mathbf{r}_i)$.

Quite generally, the first term on the right-hand side of Eq. (4.5) accounts for the motion of the carriers in presence of U_i . Provided that the potential is sufficiently strong, the carrier motion becomes confined in all three spatial directions. Suppose that L is a characteristic confinement length. Then two limiting cases can be readily identified in Eq. (4.5): in case of *weak confinement*, i.e. for $L \gg a_o$, the dynamics of the electron-hole pair is dominated by the Coulomb attraction and the confinement potentials $U_i(\mathbf{r}_i)$ only provide a weak perturbation; in the opposite case of *strong confinement*, i.e. for $L \ll a_o$, confinement effects dominate and the Coulomb part of Eq. (4.5) can be treated perturbatively. In the following we shall discuss both cases in slightly more detail.

4.2.2.1 Weak confinement regime

We first consider the weak confinement regime. A typical example is provided by monolayer interface fluctuations in semiconductor quantum wells, present even in the samples of highest quality, which result in terraces with spatial dimensions of several tens to hundreds of nanometers [Guest *et al.* (2001); Matsuda *et al.* (2003)]. Under appropriate conditions the electron-hole pair becomes confined within the region of increased quantum-well

thickness. If the resulting confinement length L is much larger than the Bohr radius a_o , the correlated electron-hole wavefunction factorizes into a center-of-mass and relative part, where, to a good degree of approximation, $\phi_o(\mathbf{r})$ is given by the wavefunction (4.4) of the ideal quantum well (“rigid-exciton approximation” [Zimmermann *et al.* (1997)]). It then becomes possible to integrate over ρ and to recover an effective Schrödinger equation for the exciton center-of-mass motion

$$\left[-\frac{\nabla_{\mathbf{R}}^2}{2M} + \bar{U}(\mathbf{R}) \right] \Psi^x(\mathbf{R}) = E_x \Psi^x(\mathbf{R}), \quad (4.6)$$

where $\bar{U}(\mathbf{R})$ is a potential obtained through convolution of $U_e(\mathbf{r}_e)$ and $U_h(\mathbf{r}_h)$ with the two-dimensional exciton wavefunction (4.4) [Zimmermann *et al.* (1997)]. Figure 4.1 shows for a prototypical square-like confinement the corresponding $\bar{U}(\mathbf{R})$, which only depicts small deviations from the rectangular shape.

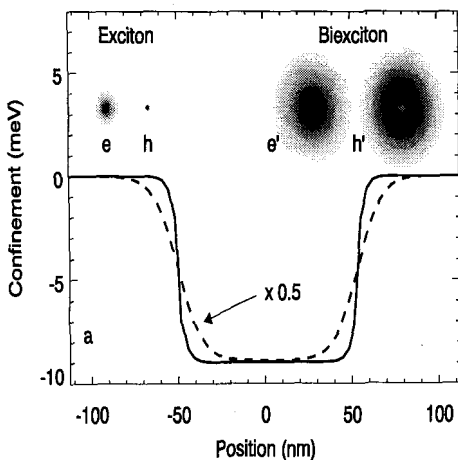


Fig. 4.1 Exciton: weak confinement

4.2.2.2 Strong confinement regime

Let us next consider the case of strong confinement where the confinement length is smaller than the excitonic Bohr radius a_o . This situation approximately corresponds to that of most types of self-assembled quantum dots [Bimberg *et al.* (1998); Jacak *et al.* (1998)], where carriers are confined in

a region of typical size $10 \times 10 \times 5 \text{ nm}^3$ and the band offsets between dot and surrounding material are of the order of several hundreds of meV.

Let $\phi_i^\lambda(\mathbf{r}_i)$ denote the solutions of the single-particle Schrödinger equations

$$\left[-\frac{\nabla_{\mathbf{r}_i}^2}{2m_i} + U_i(\mathbf{r}_i) \right] \phi_i^\lambda(\mathbf{r}_i) = \epsilon_i^\lambda \phi_i^\lambda(\mathbf{r}_i). \quad (4.7)$$

To the lowest order of approximation, the ground state Ψ^X of the interacting electron-hole system is simply given by the product of electron and hole single-particle states of lowest energy

$$\Psi^X(\mathbf{r}_e, \mathbf{r}_h) \sim \phi_e^o(\mathbf{r}_e) \phi_h^o(\mathbf{r}_h), \quad (4.8)$$

$$E_X \sim \epsilon_e^o + \epsilon_h^o - \int d\mathbf{r}_e d\mathbf{r}_h \frac{|\phi_e^o(\mathbf{r}_e)|^2 |\phi_h^o(\mathbf{r}_h)|^2}{\kappa |\mathbf{r}_e - \mathbf{r}_h|}. \quad (4.9)$$

Here, the ground state energy E_X is the sum of the electron and hole single-particle energies reduced by the Coulomb attraction between the two carriers. Excited electron-hole states can be obtained in a similar manner by promoting the carriers to excited single-particle states.

We emphasize that the viewpoints of the weak and strong confinement regime are entirely opposite: in the first case, Eq. (4.6), the system is dominated by the attractive electron-hole Coulomb interaction which gives rise to a Coulomb-bound electron-hole pair propagating in an effective confinement potential; in the latter case, Eq. (4.8), the system is dominated by the single-particle properties induced by the strong quantum confinement and the Coulomb interaction only gives rise to small energy renormalizations.

In many cases the wavefunction ansatz of Eq. (4.8) is oversimplified. In particular, when the confinement length is comparable to the exciton Bohr radius a_o , the electron-hole wavefunction can no longer be written as a product (4.8) of only two single-particle states. An improved description can be obtained by expanding in Eq. (4.8) the electron-hole wavefunction and the Hamiltonian in the single-particle bases (4.7), with a typical number of ten electron and hole states, and to obtain the correlated electron-hole wavefunction through diagonalization of the resulting Hamiltonian matrix.

4.2.3 Spin structure

Besides the orbital degrees of freedom described by the envelope part of the wavefunction, the atomic part additionally introduces spin degrees of

freedom. For $III-V$ semiconductors an exhaustive description of the band structure near the Γ point is provided by an eight-band model [Haug and Koch (1993)] containing the s -like conduction band states $|s, \pm \frac{1}{2}\rangle$, the p -like valence band states $|\frac{3}{2}, \pm \frac{3}{2}\rangle$ and $|\frac{3}{2}, \pm \frac{1}{2}\rangle$ associated to heavy and light holes, respectively, and the spin-orbit split-off band $|\frac{1}{2}, \pm \frac{1}{2}\rangle$. To a good approximation light-hole and split-off states can be neglected because of the strong confinement along growth direction and the large energy separation of the split-off bands, and we are left with the conduction-band and heavy-hole states.

It turns out to be convenient to introduce the exciton basis $|\pm 1\rangle$ and $|\pm 2\rangle$ of bright and dark excitons [Bayer *et al.* (2002)]. These states are split by a small amount $\delta_o \sim 10-100 \mu\text{eV}$ because of the electron-hole exchange interaction H_x , and the eigenstates are obtained from the Hamiltonian matrix

$$H_x = \frac{1}{2} \begin{pmatrix} \delta_o & \delta' & 0 & 0 \\ \delta' & \delta_o & 0 & 0 \\ 0 & 0 & -\delta_o & \delta'' \\ 0 & 0 & \delta'' & -\delta_o \end{pmatrix}. \quad (4.10)$$

Here, δ' and δ'' are small constants which are nonzero only for asymmetric quantum dots. Depending on such symmetry breaking, the single-exciton states exhibit circular or linear polarization selection rules [Bayer *et al.* (2002)].

If a magnetic field is applied along the growth direction z , the two bright exciton states become energetically split and can be distinguished in optical experiments. Alternatively, in the Voigt geometry a magnetic field B_x is applied along x and leads to a mixing of exciton states approximately described by the Hamiltonian

$$\frac{\mu_B B_x}{2} \begin{pmatrix} 0 & 0 & g_e & g_h \\ 0 & 0 & g_h & g_e \\ g_e & g_h & 0 & 0 \\ g_h & g_e & 0 & 0 \end{pmatrix}, \quad (4.11)$$

with μ_B the Bohr magneton and g_e and g_h the g -factor for electrons and holes, respectively. We will return to Eq. (4.11) later in the discussion of possible exciton-based quantum computation schemes.

4.3 Biexcitons

In semiconductors of higher dimension a few higher-order electron-hole complexes have been observed experimentally: for instance, the negatively charged exciton, which consists of one hole and two electrons with opposite spin orientations, and the biexciton, which consists of two electron-hole pairs with opposite spin orientations. In both cases the binding energy is of the order of a few meV and is attributed to genuine Coulomb correlations: in the negatively charged exciton the carriers are arranged such that the hole is preferentially located in-between the two electrons and thus effectively screens the repulsive electron-electron interaction; similarly, in the biexciton the four carriers arrange in a configuration reminiscent of the H_2 molecule, where the two heavier particles — the holes — are located at a fixed distance, and the lighter electrons are delocalized over the whole few-particle complex and are responsible for the binding (see inset of Figure 4.1). In the literature a number of variational wavefunction *ansätze* are known for the biexciton description, e.g. that of Kleinman [Kleinman (1983)]:

$$\Psi(\mathbf{r}_e, \mathbf{r}_h, \mathbf{r}_{e'}, \mathbf{r}_{h'}) = \exp[-(s_1 + s_2)/2] \cosh[\beta(t_1 - t_2)] \chi(r_{hh'}), \quad (4.12)$$

with $s_1 = r_{eh} + r_{eh'}$, $s_2 = r_{e'h} + r_{e'h'}$, $t_1 = r_{eh} - r_{eh'}$, $t_2 = r_{e'h} - r_{e'h'}$, and r_{ij} the distance between particles i and j . Here, the first two terms on the right-hand side account for the attractive electron-hole interactions, and $\chi(r_{hh'})$ for the repulsive hole-hole one (β is a variational parameter). In the inset of Figure 4.1 we plot the probability distribution for the electron and hole as computed from Eq. (4.12): as apparent from the figure, in comparison to the exciton the biexciton is much more delocalized and correspondingly the biexciton binding is much weaker.

4.3.1 Weak confinement regime

Suppose that the biexciton is subject to an additional quantum confinement, e.g. induced by interface fluctuations. If the characteristic confinement length L is larger than the excitonic Bohr radius a_o and the extension of the biexciton, one can, in analogy to excitons, introduce a “rigid-biexciton” approximation: here, the biexciton wavefunction (4.12) of the ideal quantum well is modulated by an envelope function which depends on the center-of-mass coordinate of the biexciton. An effective confinement for the biexciton can be obtained through appropriate convolution of $U_i(\mathbf{r}_i)$,

which is shown in Figure 4.1 for a representative interface fluctuation potential: because of the larger extension of the biexciton wavefunction, the effective potential exhibits a larger degree of confinement and correspondingly the biexciton wavefunction is more localized.

Excitons and biexcitons in weakly confined quantum systems have recently attracted much interest since, for reasons to be explained below, the light coupling is strongly enhanced as compared to the strong confinement regime. Indeed, a number of spectacular experiments has been reported in the literature, such as coherent-carrier control [Bonadeo *et al.* (1998)], optically induced entanglement creation [Chen *et al.* (2000)], or all-optical quantum gates [Li *et al.* (2003)]. However, a word of caution regarding the nature of biexcitons is appropriate. In absence of Coulomb correlations, the exciton ground state would consist of one electron and hole in the respective state of lowest energy, and the biexciton ground state of two such uncorrelated excitons with opposite spin orientations. In the language of qubits, the two spin-degenerate exciton states could be denoted with $|1\rangle \otimes |0\rangle$ and $|0\rangle \otimes |1\rangle$, and accordingly the uncorrelated biexciton state would be the $|1\rangle \otimes |1\rangle$ one. How is this qubit notation modified when additionally Coulomb correlations are considered? Completely! While in an uncorrelated biexciton state the two excitons are delocalized over the whole structure, in the correlated state — e.g. that of Eq. (4.12) — electrons and holes stay together throughout because of Coulomb correlations. For that reason the correlated biexciton has almost no overlap with the $|1\rangle \otimes |1\rangle$ state.

4.3.2 Strong confinement regime

In the strong-confinement regime the “binding” of few-particle complexes is not due to Coulomb correlations but to the quantum confinement, whereas Coulomb interactions only introduce minor energy renormalizations. It thus becomes possible to confine various few-particle electron-hole complexes which are unstable in semiconductors of higher dimension.

We start our discussion with the few-particle complex consisting of two electrons and holes. In analogy to higher-dimensional semiconductors, we shall refer to this complex as a *biexciton* keeping in mind that the binding is due to the strong quantum confinement rather than Coulomb correlations. To the lowest order of approximation, the biexciton ground state Ψ^{XX} in the strong confinement regime is given by the product of two excitons (4.8) with opposite spin orientations

$$\Psi^{XX}(\mathbf{r}_e, \mathbf{r}_h, \mathbf{r}_{e'}, \mathbf{r}_{h'}) \sim \mathcal{A}_{eh} \Psi^X(\mathbf{r}_e, \mathbf{r}_h) \Psi^X(\mathbf{r}_{e'}, \mathbf{r}_{h'}) \quad (4.13)$$

$$E_{XX} \sim 2 E_X + \langle H_{ee'} + H_{hh'} + H_{eh'} + H_{e'h} \rangle, \quad (4.14)$$

where \mathcal{A}_{eh} accounts for the proper anti-symmetrization of the wavefunction. The second term on the right-hand side of Eq. (4.14) accounts for the repulsive and attractive Coulomb interactions not included in E_X . If electron and hole single-particle states have the same spatial extension, the repulsive contributions $H_{ee'}$ and $H_{hh'}$ are exactly canceled by the attractive contributions $H_{eh'}$ and $H_{e'h}$ and the biexciton energy is just twice the exciton energy, i.e. there is no binding energy for the two neutral excitons.

In general, this description is too simplified. If the electrons and holes arrange in a more favorable configuration, such as the H_2 one in the weak confinement regime, the Coulomb energy can be reduced. Within the framework of perturbation theory, such correlation effects imply that the biexciton wavefunction no longer is a single product of two states but acquires additional components from excited states. A rough estimate for the magnitude of such correlation effects is given in first order perturbation theory by $\langle H \rangle^2 / (\Delta\epsilon)$, with $\langle H \rangle$ the average gain of Coulomb energy (typically a few meV) and $\Delta\epsilon$ the splitting of single-particle states (typically a few tens of meV). In general, it turns out to be convenient to parametrize the biexciton energy through

$$E_{XX} = 2 E_X - \Delta, \quad (4.15)$$

where Δ is the biexciton binding energy. Its value is usually positive and somewhat smaller than the corresponding quantum-well value, but can sometimes even acquire negative values (“biexciton anti-binding” [Rodt *et al.* (2003)]).

4.4 Few-Particle States

Besides the exciton and biexciton states, quantum dots in the strong confinement regime can host a number of other few-particle complexes. Depending on whether they are neutral, i.e. consist of an equal number of electrons and holes, or charged, we shall refer to them as *multi excitons* or *multi-charged excitons*. In this section we shall briefly discuss for such electron-hole aggregates the nature of the respective ground states.

4.4.1 Multi excitons

Since electron-hole pairs are neutral objects, quantum dots can be populated by a relatively large number of pairs ranging from six [Bayer *et al.* (2000)] to several tens [Rinaldi *et al.* (2000)] dependent on the dot confinement. Reminiscent of the periodic table, the main aufbau principle is given by the successive filling of single-particle shells. Owing to the approximate cylinder symmetry of artificial atoms — electron and hole wavefunctions are typically much stronger confined in growth direction —, the lowest electron (hole) shell can host two carriers with opposite spin orientations, the next one four, and so on and forth. In the following we shall adopt the usual notation to label shells with $1s, 1p, \dots$, where the number indicates the radial quantum number and the letter the angular momentum [Jacak *et al.* (1998)].

X .—The exciton ground state discussed in Section 4.2 consists of one electron and hole in the respective $1s$ shells. Its energy is given by the sum of single-particle energies reduced by the attractive Coulomb interaction $\langle H_{eh} \rangle \sim 10$ meV.

XX .—The biexciton ground state discussed in Section 4.3 consists of two electron-hole pairs with opposite spin orientations which fully occupy the $1s$ shells. Its energy is $2E_X$ diminished by the biexciton binding $\Delta \sim 1$ meV due to non-compensating contributions $\langle H_{ee} + H_{hh} + 2H_{eh} \rangle$ in Eq. (4.14) and genuine Coulomb correlations.

$3X$.—When a further electron-hole pair is added to the system, the additional carriers must be placed in the higher $1p$ single-particle shells. Correspondingly, the triexciton energy $E_{3X} \sim 3E_X + \Delta\epsilon^e + \Delta\epsilon^h$ is increased by the single-particle level splittings. As regarding Coulomb effects, the main additional contribution is due to exchange interactions: in the triexciton state two electrons (holes) have parallel spin orientations, which gives rise to a Coulomb hole and an energy reduction of typically ~ 10 meV. The triexciton electron-hole configuration is sketched in Figure 4.2.

$4X$.—The next electron-hole pair has to be placed again in the $1p$ shell. In analogy to Hund's rule which favours parallel-spin configurations for open shell atoms, the two electrons (holes) in the $1p$ shell have the same spin orientations.

With increasing number of electron-hole pairs the $1p$ shell becomes filled, and, similarly to the above discussion, the energies can be decomposed into single-particle, Hartree-type — i.e., electrostatic repulsion or attraction of the form (4.9) —, exchange, and correlation effects. The reader is referred

to the literature for details [Hawrylak (1999)].

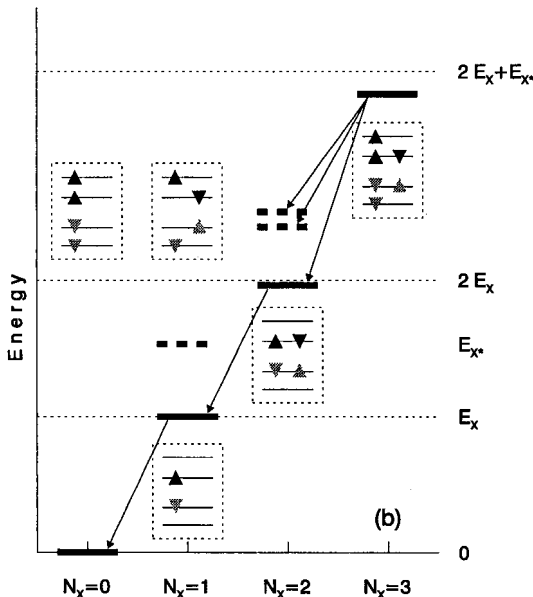


Fig. 4.2 Schematic multi exciton energy levels.

4.4.2 Multi-charged excitons

Similar conclusions apply for multi-charged excitons. Because of the dominant single-particle character the aufbau principle for negatively and positively charged excitons is dominated by successive filling of single-particle states, whereas Coulomb interactions only give rise to minor energy renormalizations. The only marked difference in comparison to multi excitons is the additional Coulomb repulsion due to the imbalance of electrons and holes, which manifests itself in the carrier-capture characteristics [Hartmann *et al.* (2000)] and in the instability of highly charged carrier complexes [Warburton *et al.* (2000); Findeis *et al.* (2001)].

4.4.3 Configuration interactions

Despite the widespread success of the strong-confinement picture advocated in this section, it is sometimes oversimplified and not able to give quantita-

tive agreement with experiment. This holds in particular true for excited multi exciton and multi-charged exciton states, which, as will be discussed below, strongly influence the optical spectra. It is thus often imperative to rely on more refined theoretical description models. A particularly successful approach is provided by the method of *configuration interactions*, which we shall briefly discuss in the following.

Consider a few-particle system with N_e electrons and N_h holes, whose wavefunction is of the form

$$\left[\mathcal{A}_e \prod_{i=1}^{N_e} \phi_e^{\lambda_e^i}(\mathbf{r}_i) \right] \left[\mathcal{A}_h \prod_{j=1}^{N_h} \phi_h^{\lambda_h^j}(\mathbf{r}_j) \right], \quad (4.16)$$

where the operator \mathcal{A}_i accounts for a proper anti-symmetrization of the wavefunction. In the uncorrelated ground state only the N_e single-electron states and N_h single-hole states of lowest energy would be populated. Let us denote the corresponding state with $|\Lambda_o\rangle$.

We can now construct a sequence of excited states $|\Lambda_\mu\rangle$ by promoting electrons and holes to excited single-particle states. To keep the number of excited states small (typically a few thousand) an appropriate truncation procedure has to be introduced, conveniently based on a restricted basis set for single-particle states and an energy cutoff for $\sum_{i=1}^{N_e} \epsilon_e^{\lambda_e^i}$ and $\sum_{j=1}^{N_h} \epsilon_h^{\lambda_h^j}$. One finally expands the Hamiltonian H in the Λ -basis, i.e. $H_{\mu\nu} = \langle \Lambda_\mu | H | \Lambda_\nu \rangle$, and obtains the eigenfunctions and energies of the Coulomb correlated system through direct diagonalization of $H_{\mu\nu}$. Results of such configuration-interaction calculations will be shown in the following section.

4.5 Optical Spectroscopy

In spite of the continuing progress in dot fabrication, all the available approaches still suffer from the effects of inhomogeneity and dispersion in the dot size, which leads to large linewidths when optical experiments are performed on large dot ensembles. A major advancement in the field has come from different types of local optical experiments, that allow the investigation of individual quantum dots thus avoiding inhomogeneous broadening [Zrenner (2000)], e.g. mesa-type structures, shadow masks, or near-field optical microscopy.

Quite generally, light-matter coupling is described by the interaction

Hamiltonian $-\mathcal{EP}$ [Haug and Koch (1993)], with \mathcal{E} the electric field of the light and \mathcal{P} the material polarization. Within the usual rotating-wave and dipole approximations [Haug and Koch (1993); Scully and Zubairy (1997)] the interaction Hamiltonian reads

$$H_{op} = -\frac{1}{2} \int d\mathbf{r} \left[\mu \mathcal{E}^{(-)} \hat{\psi}_h(\mathbf{r}) \hat{\psi}_e(\mathbf{r}) + \text{h.c.} \right], \quad (4.17)$$

with μ the dipole moment of the bulk material, $\mathcal{E}^{(\pm)}$ the electric field component of the light evolving with positive or negative frequency components [Scully and Zubairy (1997)], $\hat{\psi}_{e,h}^\dagger(\mathbf{r})$ the fermionic field operators creating an electron or hole at position \mathbf{r} , and h.c. denoting the hermitian conjugate of the preceding term. Equation (4.17) allows one to compute both absorption and luminescence: in the first case \mathcal{E} is treated classically, in the latter one \mathcal{E} is expanded in a photon basis. In single-dot spectroscopy one usually does not directly measure absorption but uses the technique of photoluminescence excitation spectroscopy instead: here, a transition to an excited few-particle state is induced by an external laser; consecutively the system relaxes through environment couplings, e.g. phonon scatterings, to the respective few-particle ground state, and finally decays through photon emissions which are detected. Photoluminescence and photoluminescence excitation spectroscopy provide similar — although complementary — information (ground state versus excited state properties), and will be discussed in the following in parallel.

4.5.1 *Excitons and biexcitons*

4.5.1.1 *Weak confinement regime*

As is apparent from Eq. (4.17), optical spectroscopy is sensitive to that part of the wavefunction where the electron and hole are at the same position. In the rigid-exciton approximation the probability of finding the electron and hole at the same position is given by the squared modulus of $\Psi^x(\mathbf{R})\phi^o(\mathbf{0})$. Then, the optical absorption $\alpha(\omega)$ at a given photon energy ω is proportional to

$$\alpha(\omega) \propto \left| \int d\mathbf{R} \Psi^x(\mathbf{R}) \right|^2 \pi \delta(\omega - E_x), \quad (4.18)$$

i.e. absorption only occurs at photon energies corresponding to an excitonic transition energy E_x . In general, the lineshape of the absorption peaks is not exactly δ -like but is broadened because of environment interactions such

as photon emission or phonon-assisted dephasing. The strength of the absorption peaks in Eq. (4.18), often referred to as the oscillator strength, is determined by the average of the wavefunction. For wavefunctions depicted in Figure 4.1 this average is nonzero for the ground state and zero for the excited states with one node along x or y . Most importantly, the oscillator strength increases with increasing delocalization of the exciton envelope function $\Psi^x(\mathbf{R})$, and is responsible for the large light-matter coupling of optical excitations in weakly confined quantum dots.

If the exciton is excited in scanning near-field optical spectroscopy by an inhomogeneous field distribution $\mathcal{E}(\mathbf{r})$ it becomes possible to directly probe the excitonic wavefunction $\Psi^x(\mathbf{R})$. Indeed, in [Matsuda *et al.* (2003)] the authors were able to directly map the exciton and biexciton wavefunction of lowest energy, and found in agreement to the results depicted in Figure 4.1 a stronger degree of localization of the biexciton. In principle, such experiment would also allow to map excitonic states which are far-field forbidden because of symmetry reasons.

4.5.1.2 Strong confinement regime

In the strong confinement regime the optical response is strongly governed by the single-particle properties. However, as we shall discuss in the following Coulomb interactions are responsible for pronounced renormalization effects which leave a clear fingerprint in the optical response. In the context of quantum dot based quantum computation schemes it is precisely this fingerprint that allows the optical manipulation of individual few-particle states.

Similarly to the absorption (4.18) in the weak-confinement regime, the optical absorption of the exciton state (4.8) becomes

$$\alpha(\omega) \propto \left| \int d\mathbf{r} \Psi^X(\mathbf{r}, \mathbf{r}) \right|^2 \pi \delta(\omega - E_X). \quad (4.19)$$

Since to a good approximation electron and hole are uncorrelated and the exciton is confined within a small space region, the oscillator strength is much smaller as compared to the weak confinement regime. The approximately product-type structure (4.8) of the exciton wavefunction and the similar shape of electron and hole wavefunctions gives rise to optical selection rules where only transitions between electron and hole states with corresponding quantum numbers, e.g. $1s-1s$ or $1p-1p$, are allowed.

We next consider optical excitation of a biexciton state. Since the light-

matter coupling of Eq. (4.17) only adds or removes electrons and holes in single pairs, in absorption the biexciton is conveniently created through intermediate excitation of one exciton, i.e. through the process $0 \rightarrow X \rightarrow XX$ where 0 corresponds to the dot vacuum with no electron-hole pairs present. Alternatively, in a luminescence experiment one monitors the transition $XX \rightarrow X$ (see Figure 4.2). The cross section for the transition from the exciton state (4.8) to the biexciton state (4.13) is given by

$$\alpha(\omega) \propto \left| \int d\tau \Psi^{XX}(\mathbf{r}, \mathbf{r}, \mathbf{r}_e, \mathbf{r}_h) \Psi^X(\mathbf{r}_e, \mathbf{r}_h) \right|^2 \pi \delta(\omega + E_X - E_{XX}), \quad (4.20)$$

where $d\tau$ denotes the integration over \mathbf{r}_e , \mathbf{r}_h , and \mathbf{r} . The oscillator strength depends on the overlap between the exciton and biexciton state, which for optically allowed transitions is approximately one, and the transition occurs according to Eq. (4.15) at photon energy $\omega = E_X - \Delta$.

4.5.2 Multi excitons

What happens if the dot becomes populated by an even larger number of electron-hole pairs? Experimentally, such multi-exciton occupancies are usually achieved as follows: a strong pump laser creates electron-hole pairs in continuum states — e.g. the wetting layer [Bimberg *et al.* (1998)] — in the vicinity of the quantum dot, and some of the carriers become captured in the dot; owing to the fast subsequent carrier relaxation the few-particle system relaxes to the respective state of lowest energy, and finally one electron and hole in the dot recombine by emitting a photon. Information about the few-particle carrier states can thus be obtained in steady-state experiments by varying the pump intensity and monitoring the dot luminescence.

To grasp the essential features of such multi-exciton spectroscopy, let us discuss the decay of the triexciton state consisting of two electrons with opposite spin orientations in the in the $1s$ shell, one electron in the $1p$ shell, and a corresponding configuration for holes (see Figure 4.2). Because of wavefunction symmetry only electrons and holes with corresponding quantum numbers can decay through photon emission. If the electron and hole in the respective $1p$ shells recombine through the $3X \rightarrow XX$ channel, the energy of the emitted photon is of the order $E_X + \Delta\epsilon_e + \Delta\epsilon_h$, i.e. its energy is typically a few tens of meV larger than those of the $XX \rightarrow X$ and $X \rightarrow 0$ decays. On the other hand, if one electron and hole in the respective $1s$ shells recombine, the system ends up in an excited biexciton

state XX^* with one electron-hole pair in the $1s$ and one in the $1p$ one. As mentioned above, such excited states are subject to pronounced Coulomb renormalizations which can be directly monitored through the photon energy $\omega = E_{3X} - E_{XX^*}$.

Figure 4.3 shows for a prototypical dot confinement the luminescence spectra calculated within a configuration interaction approach for the decay of various multi exciton states. Although the detailed evolution of the spectra is intuitively not easy to understand [Hawrylak (1999); Bayer *et al.* (2000)], two main features can be readily observed: first, luminescence spectra for triexcitons or complexes involving more than three electron-hole pairs exhibit peaks at photon frequencies corresponding to transitions from different single-particle shells; second, because of Coulomb correlations each few-particle state has its own spectroscopic fingerprint and can be unambiguously identified in experiment.

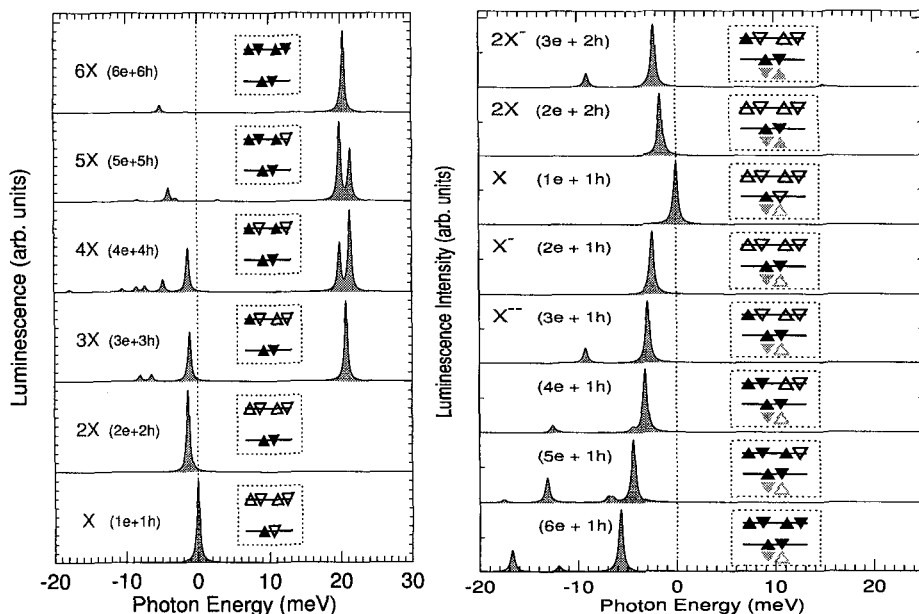


Fig. 4.3 Multiexcitons and multi-charged excitons

4.5.3 Multi-charged excitons

Coulomb interactions not only lead to renormalizations of multi-exciton states but also of multi-charged excitons. Experimental realization of such carrier complexes can be found, e.g., in [Hartmann *et al.* (2000)], where GaAs-based quantum dots are remote-doped with electrons from donors located in the vicinity of the dot. Employing the mechanism of photo-depletion of the quantum dot together with the slow hopping transport of impurity-bound electrons back to the dot, it is possible to efficiently control the number of surplus electrons in the dot from one to approximately six. Other possibilities of remote doping are to place dots within a $n-i$ field-effect structure [Warburton *et al.* (2000); Findeis *et al.* (2001)] and to apply an external gate voltage to control the number of surplus electrons. Typical multi-charged exciton spectra are shown in Figure 4.3b. Quite generally, with increasing doping the spectral changes are similar to those presented for multi-exciton states. More specifically, for negatively charged dots the main peaks red-shift because of exchange and correlation effects, and each few-particle state leads to a specific fingerprint in the optical response. Conversely, when the dot becomes positively charged the emission-peaks preferentially shift to the blue [Regelman *et al.* (2001)]. This unique assignment of peaks or peak multiplets to given few-particle configurations allows to unambiguously determine the detailed few-particle configuration of carriers in quantum dots in optical experiments.

4.6 Inter-dot Coupling: Tunneling *vs.* Coulomb Correlations

The coherent coupling between neighbouring QDs is an issue of crucial importance: on the one hand, it is essential to the design and the realization of quantum-information devices; on the other hand, the coupling of such artificial molecules can be tuned to regimes beyond those accessible to “natural” molecules, therefore allowing the investigation of novel physical phenomena, which are typically related to the highly correlated nature of the few-particle states. In the following we consider the width d of the inter-dot barrier as an ideal control of such coupling regime, of the related (inter-dot) spatial correlations and of the resulting (effective) Hilbert-space structure characterizing the biexciton states [Troiani *et al.* (2002); Rontani *et al.* (2001)].

Let us first analyze the single-particle (SP) ingredients of our many-body calculations. We consider a prototypical confinement potential for the artificial molecule, which is double-well like in the growth (z) direction and $2D$ -parabolic in the (xy) plane: $V_{(e,h)}(\mathbf{r}) = \frac{1}{2}m\omega_{(e,h)}^2(x^2+y^2) + V_0^{(e,h)}[\theta(d/2 - |z|) + \theta(|z| - l - d/2)] \equiv V_{2DP}^{(e,h)}(x, y) + V_{DW}^{(e,h)}(z)$. Being the SP Hamiltonian separable into the sum of a z -dependent and of an xy -dependent part, the wavefunctions are correspondingly factorized: $\phi(\mathbf{r}) = \varphi(x, y)\chi(z)$. Figure 4.4 shows the energies for the “bonding” (solid line) and “antibonding” (dashed line) states of lowest energy for electrons (left axis) and holes (right axis), respectively; the insets display the corresponding wavefunctions, $\chi_B(z)$ and $\chi_{AB}(z)$, for two selected values of the inter-dot distance d . Because of the heavier hole mass the tunneling of holes is suppressed at smaller inter-dot distances d than that of electrons; this is also reflected in the faster decrease of the bonding-antibonding splitting $2t_{e,h}$ with increasing d .

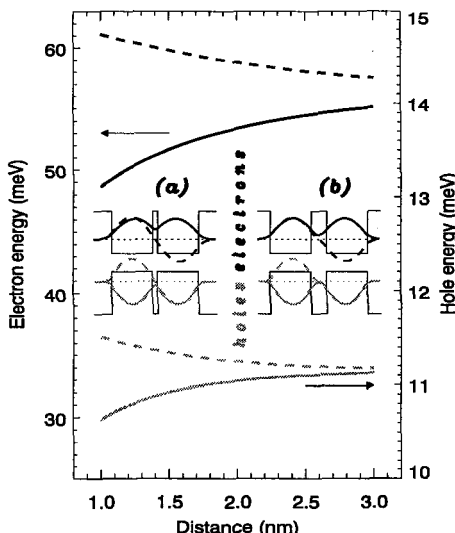


Fig. 4.4 Contribution to the single-particle energy for electrons (upper part, left axis) and holes (lower part, right axis) arising from the z -dependent part of the Hamiltonian: the solid [dashed] lines correspond to the [anti-] bonding states. The same convention is adopted for the plots of the wavefunctions $\varphi_{B,AB}(z)$ at $d = 1.2$ nm (a) and $d = 2.8$ nm (b). At each fixed inter-dot distance, the electrons are seen to tunnel in the barrier more than holes do; correspondingly, they show a larger splitting $2t$ between the antibonding and the bonding states.

In a SP picture, i.e. neglecting the Coulomb interactions, the electron-hole ground state is simply obtained by progressively filling single-particle states of increasing energy: it therefore coincides with the Slater determinant ("configuration") of lowest SP energy. If the Coulomb interactions are taken into account, each few-particle eigenstate results from the mixing of different configurations and from the population of higher orbitals. With respect to the excitations in the z direction, the gain in Coulomb energy arising from the inter-dot spatial correlations is achieved at the price of populating AB orbitals. The few-particle electron-hole states thus result from the detailed interplay between these two trends, where the relative importance of SP energy and the increase of the Coulomb one arising from spatial correlations along z varies with inter-dot distance d .

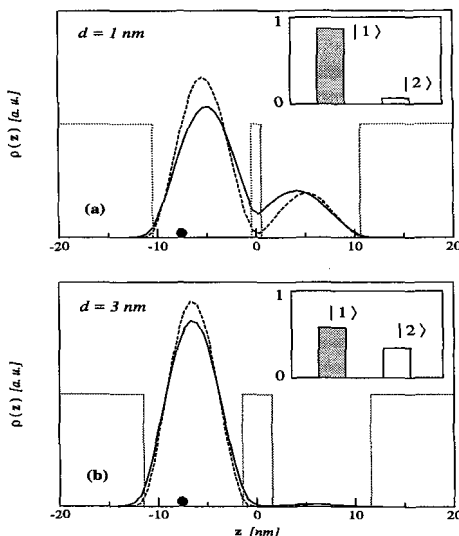


Fig. 4.5 Conditional probability distributions $\rho(z)$ for electrons (solid lines) and holes (dashed lines) in the lowest exciton state $|X_0\rangle$ at $d = 1 \text{ nm}$ (upper panel) and $d = 3 \text{ nm}$ (lower panel); the z coordinate of the fixed carrier is pointed out by the black circle; the double-box like profile of the confining potential in the growth direction is also represented. The spatial correlation between the electron and the hole is seen to increase with increasing d , together with the population transfer from the bonding (gerade) to the antibonding (ungerade) orbitals: the heights of the gray and white columns in the insets correspond to $|c_0|^2$ and $|c_1|^2$, respectively, where $|0\rangle = |\sigma_B, \uparrow; \sigma_B, \downarrow\rangle$ and $|1\rangle = |\sigma_{AB}, \uparrow; \sigma_A B, \downarrow\rangle$.

We next consider systems of interacting carriers composed of an equal number of electrons (N_e) and holes (N_h). Let us start by considering the simplest case, namely that of a single electron-hole pair, and the way in which its ground state depends on the width of the barrier. In Figure 4.5 we plot the spatial distributions of the electron [hole] corresponding to given positions of the hole [electron], at inter-dot distances of $d = 1$ nm (a) and $d = 3$ nm (b); the two insets represent the contributions to the electron-hole ground states of $|1\rangle \equiv |\sigma_B^{(e)} \uparrow, \sigma_B^{(h)} \uparrow\rangle$ and $|2\rangle \equiv |\sigma_{AB}^{(e)} \uparrow, \sigma_{AB}^{(h)} \uparrow\rangle$, where σ denotes the lowest eigenstate of h_{xy} . Apparently, the decreasing of the tunneling comes with an increasing spatial correlation (electron more localized around the hole and vice versa) and an increasing contribution from the $|2\rangle$ state. The slight difference between the plots associated to electrons and holes at each inter-dot distance are due to the differences in the barrier heights (400 meV for electrons and 215 meV for holes) and in the effective masses ($m_e^* = 0.067 m_0$ and $m_h^* = 0.38 m_0$) of the two carriers: as a consequence electrons tunnel in the AlGaAs barrier more than holes and tend to be less localized in the dots. It is worth noticing that at $d = 3$ nm the electronic tunneling still induces a pronounced splitting between the two delocalized bonding and anti-bonding single-particle states ($\epsilon_B = 35.11$ meV and $\epsilon_{AB} = 37.52$ meV). In spite of this, due to Coulomb correlation, the energetic value and the spatial distribution of the excitonic ground state closely resembles that of an exciton in a single QD; besides, the splitting between the ground and the first excited states is negligible. In other words the “excitonic tunneling” is suppressed at smaller inter-dot distances than the electronic one.

If the double dot is occupied by two electrons and two holes, both attractive and repulsive interactions are present. Intuitively one would expect carriers with identical charge to avoid each other and carriers of opposite charge to be found close to each other. In Figure 4.6 we compare the inter-dot spatial correlations for two different values of the electron and hole spin quantum numbers and for $d = 1$ nm. The singlet-singlet lowest state ($S_e = 0, S_h = 0$) is characterized by a small correlation between the electrons (panel (a)) and by a more pronounced one between holes (panel (c)). Analyzing the eigenfunction associated to this state, one observes that only the electron single-particle state $\sigma_B^{(e)}$ is meaningfully (and twice) occupied, while for holes strong contributions arise from both bonding and anti-bonding orbitals. As already mentioned, this asymmetry between the two kinds of carriers depends on the fact that the same gain in Coulomb energy has a greater kinetic cost for electrons

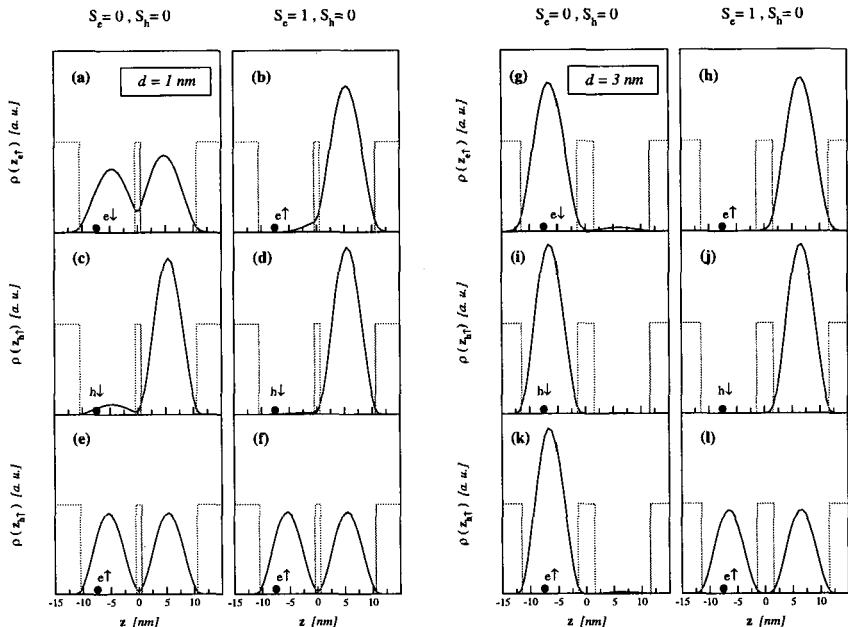


Fig. 4.6 Conditional probability distributions along z of electrons and holes in the lowest single-singlet (left side) and triplet-singlet (right side) biexciton states: $\rho(z_\alpha) = \int dx_\alpha dy_\alpha \int dr_\beta g_{\alpha,\beta}(\mathbf{r}_\alpha, \mathbf{r}_\beta)$, where $g_{\alpha,\beta}(\mathbf{r}_\alpha, \mathbf{r}_\beta) = \langle \hat{\psi}_\alpha^\dagger(\mathbf{r}_\alpha) \hat{\psi}_\beta^\dagger(\mathbf{r}_\beta) \hat{\psi}_\beta(\mathbf{r}_\beta) \hat{\psi}_\alpha(\mathbf{r}_\alpha) \rangle$ is the pair-correlation function, and $\hat{\psi}_\beta = e\uparrow, e\downarrow, h\uparrow, h\downarrow(\mathbf{r}_\beta)$ are the spin-resolved electron and hole field operators. The black circle in each panel gives the position along z of the fixed carrier. The inter-dot correlations of the singlet-singlet biexciton are strikingly different at small ($d = 1$ nm, panels (a), (c), (e)) and large ($d = 3$ nm, panels (g), (i), (k)) distances, whereas the probability distributions in the triplet-singlet case do not show a meaningful dependence on d (compare panels (b), (d), (f) with (h), (j), (l), respectively).

than for holes. Besides, the spatial distribution of holes (panel (e)) is not affected by the position of the electrons, and viceversa: the overall wavefunction can thus be approximately written in the factorized form $\psi(r_{e\uparrow}, r_{e\downarrow}, r_{h\uparrow}, r_{h\downarrow}) \simeq \psi_e(r_{e\uparrow}, r_{e\downarrow}) \times \psi_h(r_{h\uparrow}, r_{h\downarrow})$. In order to stress the role played by the spin in determining the spatial arrangement of the carriers, let us now consider the triplet-singlet state ($S_e = 1, S_h = 0$) of lowest energy. Also in this case the correlation between electrons and holes is negligible (panel (f)), while the probability of finding two electrons in the same dot is strongly suppressed by the anti-symmetric nature of $\psi_e(r_{e\uparrow}, r_{e\uparrow})$: the two electrons and the two holes can thus be thought of as independent subsys-

tems, while the biexciton essentially consists in a couple of non-interacting electron-hole pairs, each localized in a different dot.

The differences between the two spin configurations are even more dramatic at bigger inter-dot distances ($d = 3$ nm). Surprisingly enough, the singlet-singlet configuration (Figures 4.6 (g), (h), (i)) has undergone a transition to a phase in which all carriers are localized in the same QD (either of the two, due to symmetry). The pair-correlation functions clearly show that, if the position of one of the four particles is fixed in one QD, all the others are completely localized in the same one. This behavior can only be explained in terms of the in-plane correlations. In fact, in a mean field picture the strong similarity between the electron and hole wavefunctions corresponding to equal sets of quantum numbers implies a vanishing biexcitonic binding energy ΔE (which is defined as the difference between twice the energy of the excitonic ground state and that of the biexcitonic one): whether the electron-hole pairs are localized in the same dot or in different ones, the attractive and the repulsive Coulomb terms essentially cancel. When in-plane correlation comes into play, however, the localization of all particles in the same QD gives rise to a positive ΔE , which can be understood as a short-range (i.e., intradot) induced dipole-induced dipole interaction. The transition in the ground state biexciton between two such correlation regimes occurs when the energetic cost of the inter-dot spatial correlations is smaller than namely the gain in Coulomb energy that they allow. The triplet-singlet state, instead, does not undergo any such transition (Figures 4.6 (j), (k), (l)): the localization of the two electrons in the same dot is again prevented by the symmetry of $\psi_e(\vec{r}_{e\uparrow}, \vec{r}_{e\uparrow})$.

The behaviors that have been discussed so far are also reflected by the mean values of the Coulomb energies (Figure 4.7). Let us start by considering the three spin arrangements $(S_e, S_h) = (1, 1), (0, 1), (1, 0)$. As shown in panel (a), the electron-electron repulsion energy $\langle V_{ee} \rangle$ monotonically decreases with increasing d for all the three cases: the two electrons are always in different dots; in addition, the two dots get further and further apart. As already discussed above, for $S_e = 1$ the spatial separation of the two electrons is a direct consequence of the permutational symmetry of the wavefunction. The repulsion between the electrons also decreases for $(S_e, S_h) = (0, 1)$: the transition towards a maximally localized state is here prevented by the symmetry of $\psi_h(\vec{r}_{h\uparrow}, \vec{r}_{h\uparrow})$, which indirectly affects the electron distribution. Analogous behaviors are seen to occur with respect to the hole-hole interaction (c). The trends of the electron-hole Coulomb (b) interactions are hardly distinguishable one from the other: however, the

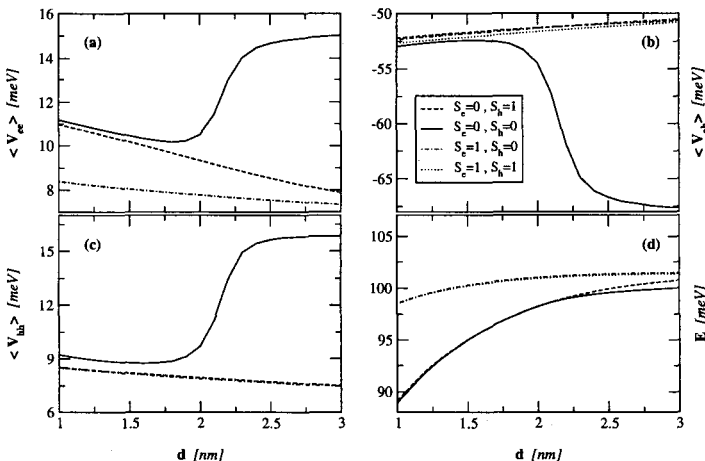


Fig. 4.7 Functional dependence of the electron-electron, electron-hole and hole-hole Coulomb interactions on the inter-dot distance d (panels (a), (b) and (c), respectively); the energy eigenvalues of the same biexciton states, namely the ones of lowest energy corresponding to each of the four spin states, are also reported (panel (d)). The monotonic trend of all the states but the singlet-singlet one reflects the localization of the two electron-hole pairs in different dots. On the contrary, the abrupt increase of all the Coulomb terms in the singlet-singlet case corresponds to the localization of the biexciton ground state in a single QD.

monotonic decrease $|\langle V_{eh} \rangle|$ reflects that of the inter-dot interaction with increasing d . Unlike all the three cases so far discussed, that of the singlet-singlet state (continuous lines) is characterized by a sharp increase in all the Coulomb interactions, occurring for $d \approx 2.25$ nm: such transitions are fully consistent with our above interpretation of the pair-correlation functions. The total energies corresponding to such four spin states are plotted in panel (d). The lowest singlet-singlet state turns out to be the system's ground state at any inter-dot distance. In the weak-coupling limit, the energies of all spin configurations but $S_e = S_h = 0$ asymptotically tend to a value which is twice the energy of the excitonic ground state in a single dot, $E_{X_0}^{SD}$ (i.e., no exciton-exciton interaction). The energy of the singlet-singlet state, instead, tends to that of the biexcitonic ground state in a single QD, $2E_{X_0}^{SD} - \Delta E$.

We next consider the possibility of experimentally revealing such transitions. In Figure 4.8 we plot the optical spectra of the artificial molecule as a function of d . The dashed line corresponds to the absorption of a photon inducing a transition from the double-QD ground state to the lowest

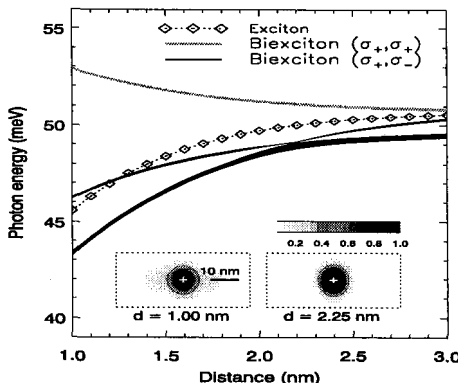


Fig. 4.8 Optical response of the artificial molecule as a function of d . The dotted line corresponds to the transition between the dot ground state and the lowest exciton one $|X_0\rangle$; the solid gray line refers to the transition between $|X_0\rangle$ and the lowest triplet-triplet biexciton; the solid black lines, which anti-cross at $d \approx 2.25 \text{ nm}$, involve the two lowest singlet-singlet biexciton, $|B_0\rangle$ and $|B_1\rangle$. The thickness of the solid lines is proportional to the transition oscillator strength. In the two insets we plot the electron-hole pair-correlation function for $|B_0\rangle$, as a function of the relative coordinates: $\bar{g}_{eh}(x, y = 0, z) = \int \int g_{eh}(x_e, y_e, z_e; x_h = x_e - x, y_h = y_e, z_h = z_e - z) dx_e$; the crosses in the plots indicate the origin $x = z = 0$.

exciton one $|X_0\rangle$: the dependence of the energy on d reflects the dominant occupation of bonding orbitals characterizing $|X_0\rangle$. The solid lines are associated to the transitions from $|X_0\rangle$ to the lowest biexciton state with ($S_e = 1, S_h = 1$) (gray line), and to the lowest two with ($S_e = 0, S_h = 0$) (black lines); the thickness of the lines is proportional to the oscillator strengths of the respective transitions. The use of circularly polarized light allows one to selectively excite (and detect) excitons with specific spin orientations: a triplet-triplet biexciton, for example, can only be created by (and relax to) two photons with the same circular polarization, denoted by (σ_+, σ_+) in the figure. The main features that are worth noticing are the following: in the transition involving the triplet-triplet biexciton, because of the Pauli exclusion principle, the “second” electron-hole pair occupies the antibonding orbitals, as reflected by the dependence of the optical transition energy on the inter-dot distance. On the contrary, the transitions from the singlet-singlet biexciton states show a “bonding”-like dependence on d . More specifically, one can see that at a critical inter-dot distance $d_c \approx 2.25 \text{ nm}$ an anti-crossing occurs between the two solid black lines, and the energetically lowest one picks up all the oscillator strength. Besides, at

the largest inter-dot distances, $d \simeq 3$ nm, two of the lines merge with the exciton energy: the corresponding biexciton states consist in two spatially separated excitons localized in the two dots, as discussed above.

The discussed behaviors, and in particular the sharp transition in the biexciton lowest state $|B_0\rangle$, depend on the detailed balance between an SP effect (the inter-dot tunneling) and a few-particle one (the Coulomb-induced spatial correlations). Further calculations that we have performed with different profiles of the confinement potential, as well as the above rationale, seem to demonstrate that these effects do not critically depend on the details of the present model. Qualitative deviations from these functional dependences might essentially arise from a strong asymmetry between the electron and hole wavefunctions (typically consisting in a stronger localizations of the holes with respect to the electrons), which would imply a prevalence of the repulsive interactions on the attractive ones: such a “mean-field effect” might result in a suppression of the strong localization of the carriers induced by the inter-dot correlations.

The main focus of the present book is on the possible implementation of QIP with semiconductors macroatoms and molecules. As discussed in Chapter 8, some of these are based on the identification of the computational degrees of freedom with specific inter-band excitations localized in the dots. The underlying physical assumption is that each dot can be thought of as a subsystem: this implies, among other things, that each exciton is strictly localized in a different dot, and allows to map the system Hamiltonian onto an (effective) Ising one. Our analysis of the biexciton states in an artificial molecule shows that such assumption is only justified if the inter-dot tunneling is suppressed, whereas, due to the inter-dot correlations, it breaks down even (and more strikingly) in the weak-coupling regime.

4.7 Inter-Dot Coupling: Role of the Electric Field

One of the appealing features of semiconductor QDs consists in the possibility they offer to engineer the single- and few-particle states, as well as the resulting spectral properties, not only by selecting their structural parameters during the growth process, but also by subsequently applying external fields. Indeed, the physical transitions occurring as a function of electric or magnetic fields can be experimentally observed within a given sample: this avoids non-trivial comparisons between quantities related to

different structures. With respect to the possible use of artificial atoms and molecules as qubits, the application of an electric field has been suggested in order to induce permanent dipoles in the excitonic states, resulting in dipole-dipole interaction between excitons (qubits) localized in neighbouring dots. The more critical aspects of a similar strategy are related to the need of spectrally resolving each single qubit within a large array, and of suppressing decohering phenomena such as the radiative recombination, typically acting on time scales of tens to hundreds of ps. In these two respects an increased tuneability of the exciton energy and of the oscillator strength (i.e., of the recombination time) might turn out to be extremely useful: in the following we discuss how this can be achieved by considering coupled rather than single QDs [Troiani (2003)].

As a preliminary step, we consider the effects of the interplay between tunneling and electric field F on the SP states, which is described by the z -dependent part of the confining potential, namely $V_0^{(e,h)}[\theta(d/2 - |z|) + \theta(|z| - l - d/2)] - q_{e,h}Fz$. The Figure 4.9 shows the distributions along z corresponding to the electron and hole SP ground states as a function of F and of the inter-dot distance d . These eigenstates result from a competition between the coherent coupling, that tends to delocalize the wavefunctions over the double dot, and the field, which instead tends to localize them in one dot or in the other: the misalignment between the energy levels of the two dots introduced by the field is approximately given by $2\Delta \equiv e(d+l)F$. The ratio $x \equiv \Delta/t$ (where $2t$ is the bonding-antibonding splitting) thus provides a good estimate of the relative strength of two such effects and of the resulting degree of localization of each carrier: this is found to increase from electrons to holes (as already mentioned, $m_e^* < m_h^*$, and thus $t_e > t_h$) and with increasing d (see Figure 4.9(a-d)). In the same range of values of F the SP eigenstates and eigenfunctions corresponding to a single dot (not reported here) are hardly affected by the field. Within the present picture, such a difference can be intuitively understood by thinking of the single QD as a double dot in the limit $d \rightarrow 0$: the values of $x \equiv \Delta/t$ corresponding to an electric field $F \leq 8$ kV/cm turn out to be very small both for electrons ($x_e \leq 0.038$) and for holes ($x_h \leq 0.18$).

The properties of the exciton states result from the interplay between the SP effects and the electron-hole Coulomb interaction. Figure 4.10 shows the Stark shifts and the oscillator strengths of the exciton ground state $|X_0\rangle$ as a function of F and d (panel (a)) and the contributions to the total energy arising from H_{SP} and H_C (Figure 4.10(b-c)); the results for the single dot are also reported for a comparison. The magnitude of the quantum

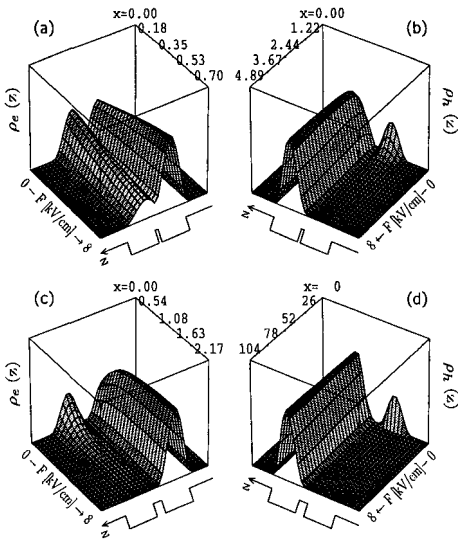


Fig. 4.9 Spatial distribution $\rho(z) = |\chi(z)|^2$ of the electron (a,c) and hole (b,d) lowest wavefunctions as a function of the electric field F , for $d = 1 \text{ nm}$ (a,b) and $d = 3 \text{ nm}$ (c,d); the double-well profile of the confinement potential in the growth direction is sketched below each of the four plots. The degree of localization of both carriers essentially depends on $x \equiv \Delta/t = e(d+l)F/2t$, with F ranging from 0 to 8 kV/cm.

confined Stark effect (QCSE) is greatly enhanced and shows a qualitatively different dependence on the field in coupled dots as compared to single ones (“anomalous Stark effect”). In fact, while in single QDs the Stark shift $\Delta E \equiv E(F) - E(0)$ typically shows a quadratic dependence on F , due to the perturbative nature of the contribution from the field, a similar behavior cannot generally be expected in artificial molecules [Sheng and Leburton (2002); Janssens (2002)]. In detail, the field induces a monotonic decrease of the single-particle energy E_{SP} , which determines the negative sign of the Stark shift, and a progressive spatial separation of the carriers, as demonstrated by the increasing Coulomb energy E_C and oscillator strengths (Figure 4.10 (a-c)).

A closer inspection of the plots reveals the occurrence of two regimes. In the strong-field region ($F \gtrsim 6 \text{ kV/cm}$) the overlap between the electron and hole distributions rapidly decreases and ΔE depends quasi linearly on F (as in the case of a field-rigid dipole interaction): both trends are enhanced at larger values of the inter-dot distance d . In the weak-field region ($F \lesssim 6 \text{ kV/cm}$) the interplay between tunneling, Coulomb interaction and electric

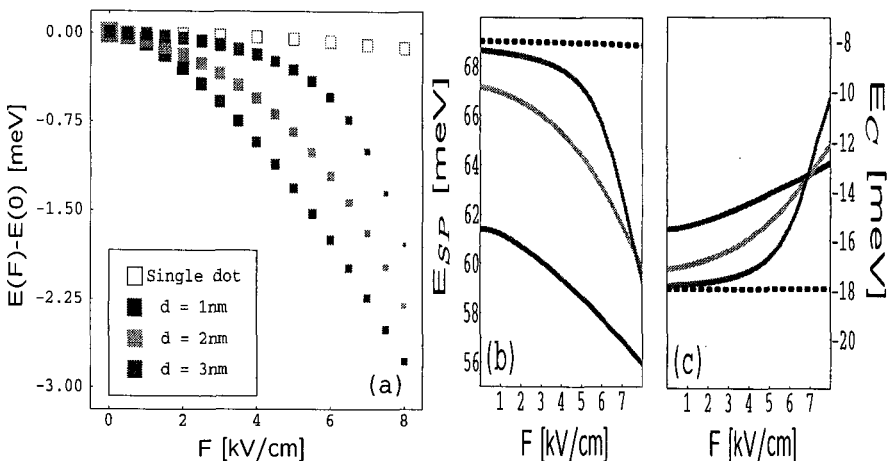


Fig. 4.10 (a) Quantum confined Stark effect as a function of the applied field for vertically-coupled QDs with inter-dot distances $d = 1, 2, 3$ nm (intermediate, light and dark gray squares, respectively). The sides of the squares are proportional to the intensities of the corresponding optical transitions. The contributions to the exciton energy arising from the SP- and from the Coulomb interaction-terms in the Hamiltonian are plotted in the (b) and (c) panels, respectively, with the same convention for the colours.

field is more balanced: rather counterintuitively, the energies E , E_{SP} and E_C get closer to the single-dot value as d is increased. As discussed in the following, this can be attributed to the fact that the strength of the inter-dot coupling determines to which extent the carrier-carrier Coulomb interaction can oppose the effects of the electric field.

The spatial distribution of the carriers provides some more physical insight in the exciton ground state $|X_0\rangle$. In Figure 4.11(a)[(b)] we plot the probability of finding the electron (hole) in the upper dot for $d = 1, 2$ and 3 nm (intermediate, light and dark gray squares, respectively), and in the upper part of the single dot (black dotted line). As expected from the previous discussion on the SP states, the hole is highly localized in the upper dot already at small values of the field and especially for large values of d . On the other hand, the behavior of the electron again reflects the existence of the two regimes. In the strong-field region the electron is seen to approach the lower dot, under the direct influence of the field; in the weak-field region the Coulomb interaction with the hole dominates and the electron tends to be localized in the upper dot. This spatial arrangement is also reflected by the small changes in this region of the oscillator strength and Coulomb

interaction (Figure 4.102(b-c)). The curves plotted in Figure 4.11(a) cross at $F \approx 7$ kV/cm: both in the weak- and in the strong-field regimes the degree of localization of the electron, in the upper or in the lower dot, respectively, is opposed by the tunneling. For $d = 1$ nm the electron is basically frozen on a delocalized bonding orbital and N_{ud}^e does not deviate significantly from 1/2 in the considered range of F values; at large inter-dot distances ($d = 3$ nm) t_e is small enough for the antibonding orbital to be also occupied in order to produce the localization of the electron in either dot, depending on the relative strength of the external- and of the hole-induced electric field.

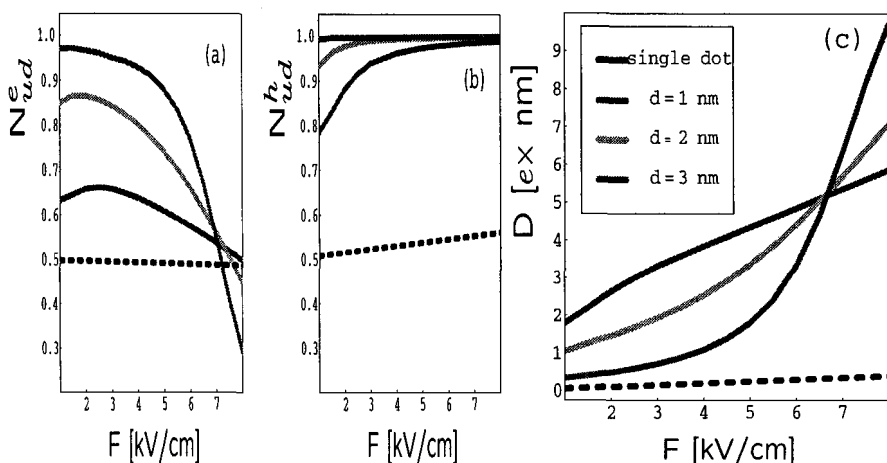


Fig. 4.11 Probability of finding (a) the electron and (b) the hole in the upper dot (UD) for $d = 1, 2$ and 3 nm (intermediate, light and dark gray, respectively), where $N_{UD}^{e,h} = \langle X_0 | \int_{UD} \hat{\psi}_{e,h}^\dagger(\mathbf{r}) \hat{\psi}_{e,h}(\mathbf{r}) d\mathbf{r} | X_0 \rangle$; the black dotted line gives the probability of finding the carriers in the upper half of the single dot. (c) Dependence on F of the induced dipole $D = \langle X_0 | \int z [\hat{n}_h(z) - \hat{n}_e(z)] d\mathbf{r} | X_0 \rangle$, where $\hat{n}_{e,h}(z) = \int \hat{\psi}_{e,h}^\dagger(\mathbf{r}) \hat{\psi}_{e,h}(\mathbf{r}) dx dy$, with the same convention for the colours.

The polarizability of the exciton ground state also reflects this behavior. While the value of D is on average greatly enhanced in coupled QDs as compared to the single one (black dotted vs. solid gray lines in Figure 4.11(c)), the sign of $\partial D / \partial d$ actually depends on the range of electric-field values of interest. For $F \lesssim 6$ kV/cm, where the electron tends to follow the hole in the upper dot, the larger degree of localization resulting from the larger values of d tends to suppress the dipole; for $F \gtrsim 6$ kV/cm, where the elec-

tron interaction with the field dominates on that with the hole, a larger degree of localization results in a larger induced dipole. Depending on the detailed balance between SP and Coulomb terms in the Hamiltonian, either the strongly or the weakly coupled QDs show the highest polarizability.

To conclude, we give an estimate of the dipole-dipole interaction that a field of 8 kV/cm can induce between two pairs of vertically coupled dots, given that $E_{int} \simeq [\vec{D}_1 \cdot \vec{D}_2 - 3(\vec{D}_1 \cdot \hat{r}_{12})(\vec{D}_2 \cdot \hat{r}_{12})]/\kappa r_{12}^3$, and with $\vec{D}_1 \parallel \vec{D}_2 \perp \vec{r}_{12}$, $|\vec{D}_{1,2}| = 10 \text{ e}\times\text{nm}$ and $r_{12} = 20 \text{ nm}$. The energy shift produced by the exciton-exciton interaction is $E_{int} \simeq 1.4 \text{ meV}$, roughly corresponding a time scale of a ps (see Chapter 8 for a discussion on the relevance of such exciton-exciton interaction).

Acknowledgments

We wish to thank Massimo Rontani and Guido Goldoni for their contributions to the research activity reviewed in this chapter.

This work has been partly supported by the European Commission through the Research Project SQID within the *Future and Emerging Technologies (FET)* programme, and by the Italian Foreign Office through the Research Project *Quantum Control of Charge and Spin State: The Next Generation Nanodevices* in the framework of the scientific cooperation protocol between Italy and Japan.

Bibliography

- Bayer, M., Stern, O., Hawrylak, P., Fafard, S. and Forchel, A. (2000). Hidden symmetries in the energy levels of excitonic ‘artificial atoms’, *Nature* **405**: 923.
- Bayer, M., Ortner, G., Stern, O., Kuther, A., Gorbunov, A.A., Forchel, A., Hawrylak, P., Fafard, S., Hinzer, K., Reinecke, T.L., Walck, S.N., Reithmaier, J.P., Klopf, F. and Schäfer, F. (2002). Fine structure of neutral and charged excitons in self-assembled In(Ga)As/(Al)GaAs quantum dots, *Phys. Rev. B* **65**: 195315.
- Bimberg, D., Grundmann, M. and Ledentsov, N. (1998). *Quantum dot heterostructures* (John Wiley, New York).
- Bonadeo, N.H., Erland, J., Gammon, D., Park, D., Katzer, D.S. and Steel, D.G. (1998). Coherent optical control of the quantum state of a single quantum dot, *Science* **282**: 1473.
- Chen, G., Bonadeo, N.H., Steel, D.G., Gammon, D., Katzer, D.S., Park, D. and

- Sham, L.J. (2000). Optically induced entanglement of excitons in a single quantum dot, *Science* **289**: 1906.
- Findeis, F., Baier, M., Zrenner, A., Bichler, M., Abstreiter, G., Hohenester, U. and Molinari, E. (2001). Optical excitations of a self-assembled artificial ion, *Phys. Rev. B* **63**: 121309.
- Guest, J.R., Stievater, T.H., Gang Chen, Tabak, E.A., Orr, B.G., Steel, D.G., Gammon, D. and Katzer, D. S. (2001). Near-field coherent spectroscopy and microscopy of a quantum dot system, *Science* **293**: 2224.
- Hartmann, A., Ducommun, Y., Kapon, E., Hohenester, U. and Molinari, E. (2000). Few-particle effects in semiconductor quantum dots: observation of multicharged excitons, *Phys. Rev. Lett.* **84**: 5648.
- Haug, H. and Koch, S.W. (1993). *Quantum theory of the optical and electronic properties of semiconductors* (World Scientific, Singapore).
- Hawrylak, P. (1999). Excitonic artificial atoms: engineering optical properties of quantum dots, *Phys. Rev. B* **60**: 5597.
- Jacak, L., Hawrylak, P. and Wojs, A. (1998). *Quantum Dots* (Springer, Berlin).
- Janssens, K.L., Partoens, B. and Peeters, F.M. (2002). Stark shift in single and vertically coupled type-I and type-II quantum dots, *Phys. Rev. B* **65**: 233301.
- Kleinman, D.A. (1983). Binding energy of biexcitons and bound excitons in quantum wells, *Phys. Rev. B* **28**: 871.
- Li, X., Wu, Y., Steel, D., Gammon, D., Stievater, T.H., Katzer, D.S., Park, D., Piermarocchi, C. and Sham, L.J. (2003). An all-optical quantum gate in a semiconductor quantum dot, *Science* **301**: 809.
- Matsuda, K., Saiki, T., Nomura, S., Miura, M., Aoyagi, Y., Nair, S. and Takagahara, T. (2003). Near-field optical mapping of exciton wave functions in a GaAs quantum dot, *Phys. Rev. Lett.* **91**: 177401.
- Regelman, D.V., Dekel, E., Gershoni, D., Ehrenfreund, E., Williamson, A.J., Shumway, J., Zunger, A., Schoenfeld, W.V. and Petroff, P.M. (2001). Optical spectroscopy of single quantum dots at tunable positive, neutral, and negative charge states, *Phys. Rev. B* **64**: 165301.
- Rinaldi, R., Antonaci, S., De Vittorio, M., Cingolani, R., Hohenester, U., Molinari, E., Lippsanen, H. and Tulkki, J. (2000). Effects of few-particle interaction on the atomiclike levels of a single strain-induced quantum dot, *Phys. Rev. B* **62**: 1592.
- Rodt, S., Heitz, R., Schliwa, A., Sellin, R.L., Guffarth, F. and Bimberg, D. (2003). Repulsive exciton-exciton interaction in quantum dots, *Phys. Rev. B* **68**: 035331.
- Rontani, M., Troiani, F., Hohenester, U. and Molinari, E. (2001). Quantum phases in artificial molecules, *Solid State Commun.* **119**: 309.
- Scully, M.O. and Zubairy, M.S. (1997). *Quantum Optics* (Cambridge University Press, Cambridge).
- Sheng, W. and Leburton, J.-P. (2002). Anomalous quantum-confined Stark effects in stacked InAs/GaAs self-assembled quantum dots, *Phys. Rev. Lett.* **88**: 167401.
- Troiani, F., Hohenester, U. and Molinari, E. (2002). Electron-hole localization in

- coupled quantum dots, *Phys. Rev. B* **65**: 161301.
- Troiani, F. (2003). Tunneling and electric-field effects on electron-hole localization in artificial molecules, *Solid State Commun.* **119**: 309.
- Warburton, R.J., Schäflein, C., Haft, D., Bickel, F., Lorke, A., Karrai, K., Garcia, J.M., Schoenfeld, W. and Petroff, P.M. (2000). Optical emission from a charge-tunable quantum ring, *Nature* **405**: 926.
- Yu, P.Y. and Cardona, M. (1996). *Fundamentals of Semiconductors* (Springer, Berlin).
- Zimmermann, R., Große, F. and Runge, E. (1997). Excitons in semiconductor nanostructures with disorder, *Pure and Appl. Chem.* **69**: 1179.
- Zrenner, A. (2000). A close look on single quantum dots, *J. Chem. Phys.* **112**: 7790.

Chapter 5

Electron-Phonon Interaction in Semiconductor Quantum Dots

R. Ferreira and G. Bastard¹

Laboratoire Pierre Aigrain

Ecole Normale Supérieure

24 rue Lhomond F75005 Paris, France

5.1 Introduction

As anticipated in the introductory part of this book (see Chapter 1), the release of excess energy by carriers is of primary importance to the operation of classical semiconductor devices [Shah (1992); Ridley (1988)]. By classical devices we mean devices whose electronic behavior can essentially be described in terms of the time dependence of the populations of the various states, the populations being the diagonal components of the electronic density matrix. On the contrary, the coherences i.e. the off diagonal components of this matrix, decay in a classical device very quickly. This is why when investigating the response of a classical device on time scales which are long compared to the coherence decay time, the rate equations which govern the time evolution of the populations are so powerful in accounting for its behavior. The Boltzmann equation is a well known rate equation for the electron population and, if correctly amended to take into account the size quantization genuine to heterostructures, it does provide a good description of the electronic behavior of the majority of bulk and heterostructure devices [Ando *et al.* (2002)], e.g. lasers, field effect tran-

¹Hong Kong University for Science and Technology, Clear Water Bay Kowloon, Hong Kong, China.

sistors. In quantum devices the knowledge of the populations is no longer enough to correctly describe their response. For instance, the behavior of the optical response of semiconductor bulk materials or heterostructures at short time is not only governed by the populations but it also depends on the coherences of these generalized two-level atoms [Rossi and Kuhn (2002)]. Quantum devices as much as classical ones need the knowledge of the mechanisms which lead to energy dissipation to understand their response.

As discussed in Chapter 7, quantum logic operations have recently been advocated as substitutes to classical operations to bypass the perilous demand of decreasing device sizes. In particular, semiconductor quantum dots (QDs) seem to be quite relevant to implement quantum logic operations because of the discrete nature of their low lying states. Quantum operations make use of entangled quantum states of the device. Nothing is more detrimental to them than the decoherence effects, i.e. those effects which make it impossible to maintain the entanglements of eigenstates but instead replace them by statistical mixtures. These changes occur because the quantum device one wants to manipulate undergoes too many uncontrollable inelastic interactions with the surrounding world, which irreversibly affect its time dependent phase. Thus, to keep the quantum entanglements as long-lived as possible, one must solve the problem of the energy dissipation in semiconductor QDs.

In the present chapter, we wish to highlight the recent experiments and calculations which have led to the conclusion that the electron-phonon interaction in QDs operates in a radically different way from that found in bulks and quantum well structures. The strongly discrete nature of the low lying electronic states is responsible for such a drastic change [Bastard and Molinari (this volume)] and we shall see that the three-dimensional electronic size quantization profoundly affects the quantum mechanical aspects of the relaxation processes. The present chapter is organized as follows. After a brief survey of our understanding of the electron-phonon interaction in semiconductors, we shall examine the conclusion one may straightforwardly draw from applying the usual description to quantum dots. This has led to the phonon bottleneck prediction (see Section 5.2). In Section 5.3, we shall present the experimental evidences of the failure of the usual approach and discuss the polaronic description in QDs. Section 5.4 will be devoted to the understanding of the energy relaxation within the polaronic picture. In Section 5.5 we review the extension of the polaronic effects to the case of inter-band excitations where electron-hole pairs are created. Fi-

nally, Section 5.6 will be devoted to a discussion of the carriers' interaction with acoustic phonons in quantum dots.

5.2 Energy Relaxation in Bulk and Quantum Well Structures

The way the electronic degrees of freedom relax their excess energy has been intensively studied in the past and numerous experiments as well as calculations have resulted in a fairly good knowledge of the energy dissipation in bulk semiconductors and quantum well devices. For III-V and II-VI semiconductors, the most efficient relaxation is, by far, the interaction with the longitudinal optical phonons, if it is energy allowed. Then comes the scattering by acoustic phonons, either via the deformation potential or the piezo-electric scattering.

The phonons are usually classified into acoustic and optical branches, a distinction which operates the best at small wavevectors [Yu and Cardona (1999)]. For the two atoms basis of the zincblende lattice the long wavelength acoustic (optical) phonons correspond to vibrations of the two basis atoms that are in phase (in phase opposition). As a result of the different atoms basis in the III-V or II-VI materials, the optical phonons carry a longitudinal oscillating electric field that couples very strongly to the electrons (Fröhlich interaction) and dominates the energy relaxation. When the emission of optical phonons is not allowed, the energy relaxation proceeds via the (less efficient) emission of less energetic acoustic phonons. In this case, the carriers are perturbed by the deformations of the lattice in the presence of sound waves (deformation potential interaction) [Shah (1992); Ridley (1988); Yu and Cardona (1999)].

Without interaction, the exact eigenstates of the electron-phonon systems can be chosen as the factorized states $|n, \vec{k}\rangle \otimes |\nu, \vec{q}\rangle$, where the first ket corresponds to the electron states while the second labels the phonon states. For simplicity, some labels are not indicated, like the electron spin quantum number or the polarization of the vibration. For these factorized states the electron and phonon energies add up. Note finally that the factorized states written above are not the exact eigenstates of the full vibration Hamiltonian because the phonons corresponds to the quantization of the harmonic vibrations. Anharmonicity is a weak effect (for temperature much lower than the melting point). It nevertheless makes the phonon interacting. This results in a finite lifetime of a given phonon

mode and also gives rise to the phonon thermalization. The lifetime of zone center optical phonons is some ≈ 10 ps at low temperature in GaAs and some ≈ 4 ps at room temperature [Vallee and Bogani (1991); Vallee (1994)]. The lifetime of the acoustic phonons is considerably longer.

The first correction to the independent electrons and phonons (in a given mode ν) can be written [Ridley (1988); Yu and Cardona (1999)]

$$H_{e-ph} = \sum_{\vec{q}} V(\vec{q}) e^{-i\vec{q}\cdot\vec{r}} b_{\vec{q}}^\dagger + V^*(\vec{q}) e^{i\vec{q}\cdot\vec{r}} b_{\vec{q}}, \quad (5.1)$$

where the mode index ν has been dropped and where $b_{\vec{q}}^\dagger$ and $b_{\vec{q}}$ are the creation and annihilation operators of one phonon with wavevector \mathbf{q} in the mode ν . The strength $V(\mathbf{q})$ depends on the particular interaction (Fröhlich, deformation potential, ...; see below) and \mathbf{r} is the electron position vector. A writing such as (5.1) immediately implies that any wavevector given to (taken from) the phonons is taken from (given to) the electrons, just because of the plane wave term. Also, the linearity in creation and annihilation means that only factorized electron-phonon (e-ph) states that differ by one phonon are coupled by the e-ph Hamiltonian. In this respect (5.1) is in close analogy with the electron-photon interaction when the electromagnetic field is weak.

Before discussing the way one usually handles (5.1) in actual calculations, let us briefly mention that phonons in heterostructures have received a considerable attention (for a recent review see [Jusserand (2002)]). There exist propagating phonon modes over the whole heterostructure, localized modes in one kind of layer and interface modes which decay on both sides of the interfaces. Each of these modes interacts with the electron by a term like (5.1) and each has a specific coupling strength V . It has been shown by Lee *et al.* [Lee *et al.* (1995)] that when summing all the contributions of the various kinds of phonons, one ends up with scattering times for the electrons which are rather close to what would be obtained if the phonons were taken as bulk modes. We shall make this simplifying approximation in the following, in particular because we shall deal with QDs where there is not much known about the phonon modes of actual structures.

Once the initial state of, say, a QW structure is given, one looks at its time evolution. Usually, the initial state is a factorized state $|n, \vec{k}\rangle \otimes |\alpha\rangle = |n\vec{k}\alpha\rangle$ where α stands for all the phonon quantum numbers. It would remain forever stable if it were not for the e-ph interaction. The latter induces transitions between the initial state $|n\vec{k}\alpha\rangle$ and the various other

factorized states. Let $P_{n\vec{k}\alpha}$ be the survival probability to find the interacting electrons and phonons in the same quantum state as at $t = 0$. Assuming H_{e-ph} to be small we find

$$\ln(P_{n\vec{k}\alpha}) \approx - \sum_{n'\vec{k}'\alpha'} \left| \langle n'\vec{k}'\alpha' | H_{e-ph} | n\vec{k}\alpha \rangle \right|^2 \times \frac{4 \sin^2 \frac{t}{2\hbar} \left(\varepsilon_\alpha + \varepsilon_n(\vec{k}) - \varepsilon_{\alpha'} - \varepsilon_{n'}(\vec{k}') \right)}{\left(\varepsilon_\alpha + \varepsilon_n(\vec{k}) - \varepsilon_{\alpha'} - \varepsilon_{n'}(\vec{k}') \right)^2}, \quad (5.2)$$

where $\varepsilon_n(\mathbf{k})$ is the two-dimensional dispersion of the n^{th} sub-band. The long time behavior of the survival probability is interesting. One finds readily

$$\ln(P_{n\vec{k}\alpha}) \approx - \frac{t}{\tau_{n\vec{k}\alpha}} \quad (5.3)$$

$$\frac{1}{\tau_{n\vec{k}\alpha}} = \frac{2\pi}{\hbar} \sum_{n'\vec{k}'\alpha'} \left| \langle n'\vec{k}'\alpha' | H_{e-ph} | n\vec{k}\alpha \rangle \right|^2 \delta \left(\varepsilon_\alpha + \varepsilon_n(\vec{k}) - \varepsilon_{\alpha'} - \varepsilon_{n'}(\vec{k}') \right), \quad (5.4)$$

that is to say the Fermi golden rule; either in the form of a constant transition rate to leave the initial state to any other factorized state of the same energy or in the form of an exponentially decaying survival probability to find the system in the same state as at $t = 0$. The origin of such an irreversible departure from the initial state is the huge size of the phase space available to the electron-phonon system. We deal here with mixed continuums: the broad electronic ones (\approx eV) and the phonon ones (\approx 5-100 meV depending on the material and the kind of phonon). Contrarily to the few levels systems (e.g. two-level systems) where the phase space to explore is very small and the system comes back to the initial state (periodically for a two-levels system), we find that the survival probability decreases very quickly with time for the macroscopic continuums of the electron-phonon systems.

Once the Fermi golden rule (also called weak coupling if one reasons in terms of the coupling between the initial factorized state and the continuum of all the final factorized states) is established, one computes the various matrix elements and integrate over all the final states with the same energy as the initial one to get the scattering time of the initial state. An example of such a calculation is shown in Figure 5.1 where the intra-sub-band and

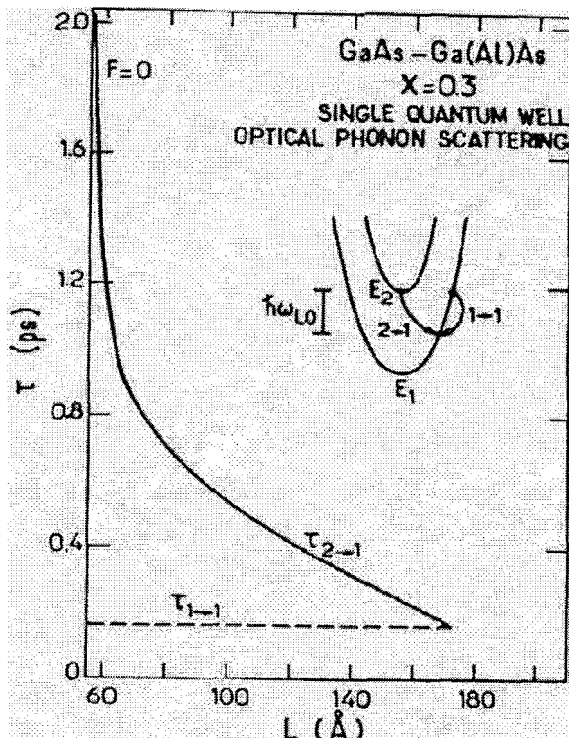


Fig. 5.1 The relaxation time of a QW electron due to the emission of LO phonons is plotted against the well width L in the case the emission of optical phonons [Ferreira and Bastard (1989)]. From [Ferreira and Bastard (1989)].

inter-sub-band electron scattering times in single quantum well structures are plotted versus the well width L in the case the emission of optical phonons [Ferreira and Bastard (1989)]. These phonons have been taken bulk-like and their dispersion has been neglected. We note that a typical scattering time (≈ 1 ps) is much shorter than the LO phonon lifetime, which *a posteriori* supports the idea of discussing of the H_{e-ph} -induced transitions between factorized states, the latter being long lived enough in spite of the anharmonicity effects on the phonons. The discussion of the electron-phonon interaction within a basis of factorized states applies equally well to the (weak) couplings with the long lived acoustic phonons.

The correctness of the weak coupling approach to handle the various electron-phonon interactions in bulk materials and QW heterostructures is very firmly established. Curves such as the energy loss rates are nicely

interpreted by this theory provided the phonon re-absorption is accounted for (see [Shah (1992)] for detailed discussions).

The weak coupling theory was applied in the early Nineties to the case of quantum dots [Bockelmann and Bastard (1990); Benisty *et al.* (1991)]. A previous chapter has given a survey of the QDs' which will not be repeated here. Striking predictions regarding the poor relaxation of the carriers in QDs were obtained from this weak coupling approach: this is the phonon bottleneck effect. In the following we consider separately the energy relaxation problem for confined electrons interacting with optical and acoustic phonons.

For optical phonons, the physical origin of the phonon bottleneck effect can be traced back to the Fermi golden rule. Since the energy of the electron-phonon system has to be conserved (see 5.3), the emission of a LO phonon by an electron in a QD is possible only if the electronic energy difference between the initial and the final state is equal to the energy of the emitted phonon. Since the LO phonons have little dispersion, an effect further enhanced by the shape in the k space of the e-ph coupling, which chops the large k phonons contributions because of decaying form factors (see below), one arrives at the conclusion that no LO phonon can be emitted because the energy of the electron-phonon system cannot be conserved. To make the argument more explicit, assume the LO phonons to be bulk-like and dispersionless (with energy $\eta\omega_{LO}$). The Fermi golden rule tells us that the relaxation time from an excited electronic state $|e\rangle$ to the ground state $|g\rangle$ due to the emission of LO phonons is given by

$$\frac{1}{\tau_e} = \frac{2\pi}{\hbar} (1 + n_{LO}) \delta(\varepsilon_e - \varepsilon_g - \hbar\omega_{LO}) \frac{1}{8\pi^3} \int d^3q |V_F(q)|^2 |\langle e| e^{-i\vec{q}\cdot\vec{r}} |g\rangle|^2 \quad (5.5)$$

where n_{LO} is the mean number of LO phonons at temperature T and V_F is the Fröhlich e-ph coupling term: $|V_F(\vec{q})|^2 \approx 1/q^2$. From (5.5) one clearly sees that the only phonons contributing significantly to the $|e\rangle \rightarrow |g\rangle$ relaxation have a wavevector q such that $q l_{dot} < \pi$ where “ l_{dot} ” stands for the various lengths which characterize the decay far from the QD of the product of the envelope functions $\psi_e^*(\mathbf{r})\psi_g(\mathbf{r})$. Since these envelopes are fairly well localized inside the QD, the l_{dot} 's are in practice comparable to the QD sizes. Note also that the delta function in (5.5) leads to a vanishing relaxation unless there is an exact matching between the energy separation $\Delta\varepsilon = \varepsilon_e - \varepsilon_g$ between the two confined electron states and the phonon energy. All of these lead to the conclusion that the most effective energy

relaxation process in III-V semiconductors is inoperative in QDs.

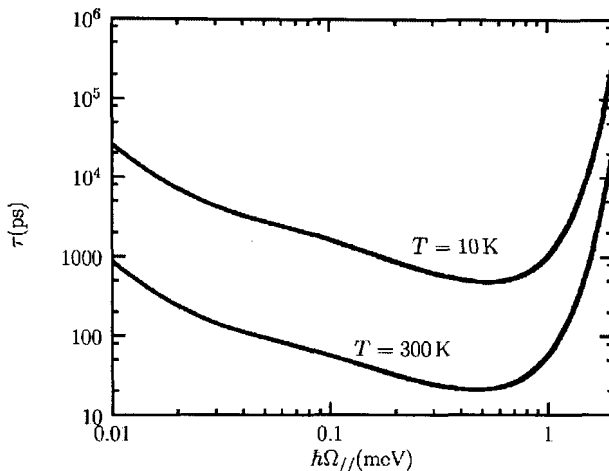


Fig. 5.2 Calculated scattering time due to the emission of acoustic phonons between the first excited and the ground QD states plotted against the in plane energy separation $\eta\Omega_{parallel}$. Harmonic confinement with a strong vertical confinement ($\eta\Omega_z = 50 \text{ meV}$). From [Verzelen *et al.* (2002)].

Acoustic phonons have a broader spectrum. However, as shown in Figure 5.2, the shape of deformation potential makes the emission of energetic acoustic phonons prohibitively long (this is again due to the decaying form factors at large wavevectors) for electronic energy separation larger than a few meVs [Verzelen *et al.* (2002)]. Assuming the e-ph interaction arises from the deformation potential and taking bulk-like isotropic longitudinal acoustic phonons ($\omega(\vec{q}) = c_s q$ where c_s is the sound velocity in the medium, taken equal to the GaAs one) one gets for the scattering time of the $|e\rangle \rightarrow |g\rangle$ relaxation:

$$\frac{1}{\tau_e} = \frac{2\pi}{\hbar} (1 + n_{ac}(q_s)) \frac{|V_{DP}(q_s)|^2 q_s^2}{8\pi^3 \hbar c_s} \iint \sin \theta d\theta d\phi |\langle e | e^{-i\vec{q}\cdot\vec{r}} | g \rangle|^2 \quad (5.6)$$

$$\hbar c_s q_s = \varepsilon_e - \varepsilon_g, \quad (5.7)$$

where θ and ϕ are the spherical angles of the wavevector \mathbf{q}_s and $V_{DP}(\mathbf{q})$ is the deformation potential coupling term: $|V_{DP}(\mathbf{q})|^2 \propto \eta c_s q$.

To summarize the weak coupling predictions for a typical InAs/GaAs QD, one finds that the emission of either optical or acoustic phonons is in practice impossible. Hence, an excited electron cannot relax in QDs by the same mechanisms that are so prevalent in bulk and QW structures. This prediction of an inhibited relaxation did not reach a good agreement with experiment, although some optical data showed an inhibited relaxation compared to what is found in QWs [Urayama *et al.* (2001); Heitz *et al.* (2001)]. Various reasons for this failure (unrelated to the validity or not of the weak coupling approach) can be put forward. Firstly, the relaxation in many devices takes place under strong excitation conditions, that is to say when there are many carriers nearby the QD. If so, the Auger effects (carrier-carrier interactions) come into play and are efficient ways to bypass the phonon bottleneck [Uskov *et al.* (1998); Müller *et al.* (2003); Bockelmann and Egeler (1992)]. Although Auger effects do not change the total energy of the electron gas, they may induce a relaxation in one subsystem (the QD electrons) while the other carriers (whose fate is not so important to the device behavior) get excited in the continuum and (efficiently) emit phonons to cool down. Secondly, multi-phonon emissions were advocated to alleviate the strict energy conservation found in Eq. (5.4) [Heitz *et al.* (1996); Heitz *et al.* (1997)]. This process turned out not to be very efficient: only one or two meVs could in practice be gained to smear the exact energy conservation [Inoshita and Sakaki (1992); Kral and Khas (1998)]. Lastly, the experiments often involved inter-band excitation, thus the creation of electron-hole pairs rather than electrons (or holes) only. This leads to the existence of the intra-dot Auger effect that is operative [Ferreira and Bastard (1999)] provided the pair excited state is closer in energy to the wetting layer continuum than to the ground state. Although there are not very many carriers (only one e-h pair bound to the dot is required), the Auger disintegration of the pair leads to the relaxation of one of the two particles while the other is ejected in the continuum. It is very efficient (Auger times of a few ps were calculated). However, these different processes were unable to explain the rather efficient relaxation observed in many optical experiments [Fafard *et al.* (1995); Oulton *et al.* (2002)], in particular the results of resonant photoluminescence excitation experiments performed on either weakly inhomogeneous ensembles of dots or on single QDs. In the later case an electron-hole pair is photocreated in a bound orbit, which is deep enough in energy to preclude the contribution of the different Auger processes. In the same way (and more importantly), recent intra-band experiments done on doped dots

(to be discussed below) clearly indicate that the energy relaxation among confined levels has to be associated to the coupling of the bound electron to phonons [Hameau *et al.* (1999); Hameau *et al.* (2002)].

It is now well established that the problem of energy relaxation in QDs cannot be tackled without a deep analysis of the coupling between confined carriers and phonons. In fact, the energy relaxation problem by phonon emission was left unsolved until magneto-absorption experiments demonstrated that the weak coupling approach to the e-ph interaction in dots, which leads to the phonon bottleneck effect, is a model that is essentially inapplicable to the QDs) [Hameau *et al.* (1999)]. We present in the following the main outcomes of magneto-optical experiments and the theoretical framework developed to properly account for the coupling between carriers confined in a QD and the vibrations of the atoms of the underlying semiconductor lattice.

5.3 Magneto-Absorption in Quantum Dots: the Evidence of Polaron

While the inter-band optical measurements related to carrier relaxation provided ambiguous answers about the correctness of the weak coupling description of the e-ph interaction, intra-band magneto-absorption experiments furnished clear cut evidences that this description was incorrect and needed to be replaced by a more complete one. This technique is a very direct one in that it probes the optically active eigenstates of the structures. The QDs are loaded by electrons by a controlled modulation (spike) doping of the GaAs barrier. Relaxation effects play a small part (in the line broadening). The magnetic field acts like a control parameter that fixes the energy distance between the ground state and the first excited electronic state. Because the zero-field size quantization is so pronounced, the magnetic field acts as a perturbation to the zero-field level scheme. This is the well known Zeeman effect of atomic physics except that one deals with flat atoms in the case of InAs/GaAs QDs instead of spherically symmetric atoms. We shall therefore deal with a ground state $|g\rangle$ (orbitally non degenerate and of S symmetry in circular dots) and an excited level $|e\rangle$ which would be twice degenerate at zero magnetic field in circular QDs.

Under the application of a strong magnetic field parallel to the growth direction, the excited states split into a $|P_+\rangle$ and a $|P_-\rangle$ component (see Figure 5.3) which are separated by the cyclotron energy $\eta\omega_c$ ($= \eta eB/m^*$).

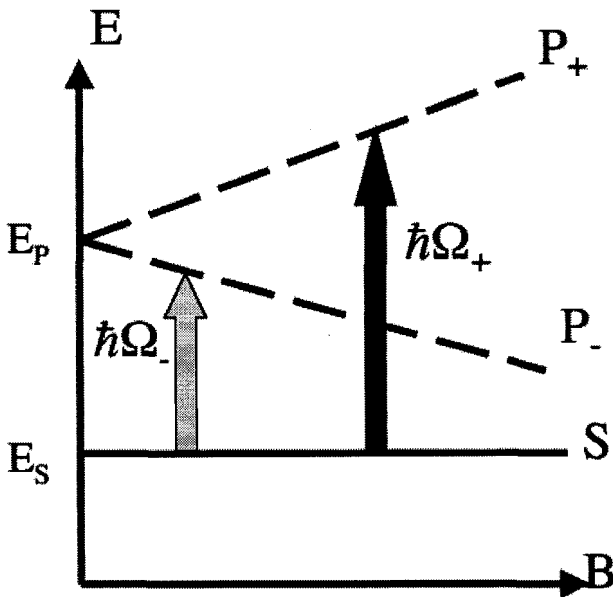


Fig. 5.3 Magnetic field dependence of the energy levels of a flat circular atom (schematic).

It is not difficult to account for a slight departure from the circularity (InAs QDs are known to be elongated along the [Shah (1992); Jusserand (2002)] crystallographic direction). One finds readily that the ground state is essentially unchanged (apart from a small diamagnetic shift) while the P_+ - P_- degeneracy is lifted even at zerofield:

$$\begin{aligned}\varepsilon_g(B) &= \varepsilon_S + \gamma_S B^2 \\ \varepsilon_{\pm}(B) &= \varepsilon_P \pm \sqrt{\left(\frac{\delta}{2}\right)^2 + \left(\frac{\hbar\omega_c}{2}\right)^2} + \gamma_P B^2,\end{aligned}\quad (5.8)$$

where δ is the zero field splitting and $\gamma_S B^2$ and $\gamma_P B^2$ are the (small) diamagnetic contributions to the S and P states respectively. Even at $B = 23\text{T}$ the diamagnetic terms are only a few meVs.

This description of the electronic levels and their fan dispersion under an applied magnetic field corresponds to the so-called “macro-atom” model. Within this model, illumination by far-infrared (FIR) light leads to transitions among different *electronic* levels coupled by the dipolar interaction

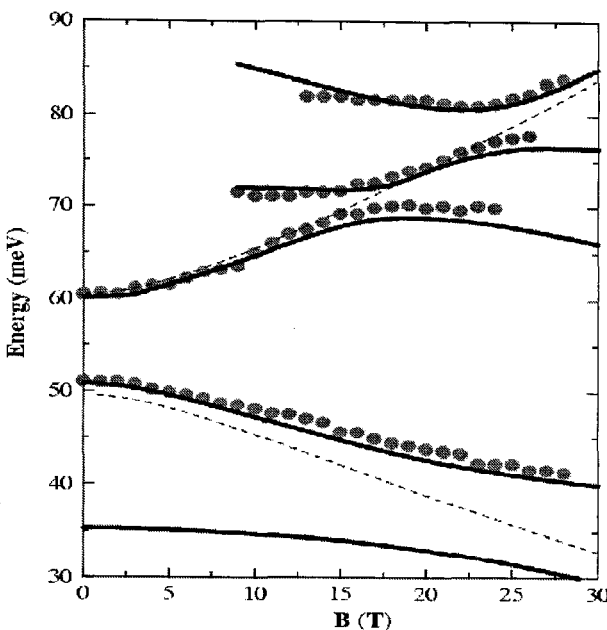


Fig. 5.4 Fan chart of the magneto-absorption experiments performed on InAs/GaAs QDs loaded by one electron on average. Dots: experiments. Solid line: polaron theory. Dashed line: purely electronic model (weak coupling between electrons and LO phonons). From [Hameau *et al.* (2002)].

irrespective of the other degrees of freedom, in particular the vibrations. In particular, intra-band magneto-absorption experiments should display two lines at the photon energies $\eta\Omega_{\pm}(B) = \varepsilon_{\pm}(B) - \varepsilon_g(B)$. Figure 5.4 shows the fan chart obtained on a modulation doped QD sample where the QDs contain one electron on the average. It is clear that the macro-atom model fails short of explaining these experimental data. In lieu of two branches Ω_{\pm} smoothly varying with B , one finds several anti-crossings superimposed on the two branches Ω_{\pm} of the macro-atom model. These anti-crossings are maximum any time one electronic level intersects the one or two LO phonon replicas of another electronic states ($\eta\omega_{LO} \approx 36$ meV in GaAs and strained InAs). This experimental fact hints that a proper interpretation of the experiments should incorporate the coupling of confined electrons with optical phonons.

We show in the following that, if we abandon the macro-atom scheme but instead focus our attention on the factorized electron-phonon states coupled by H_{e-ph} , we are able to interpret the experimental results as evidence that over a broad energy range, typically from 36 meV to about 80 meV, H_{e-ph} mixes very efficiently the factorized states which differ in their electronic quantum number and in their occupation of the LO phonon. In other words, it appears that in QDs the discrete nature of the electronic spectrum favors the creation of fairly stable entanglements of electronic and LO phonon states, the *polaron* states, and FIR absorption experiments probe such mixed levels, instead of the purely electronic ones. This striking feature is just opposite to the findings in bulk and QW structures where the electron-phonon interaction weakly couples the factorized states and, in effect, can be re-incorporated as a finite lifetime of the factorized states.

Before proceeding with the theoretical interpretation of the experimental results, let us briefly recall the main aspects of the model proposed by Verzelen *et al.* to handle the e-LO phonons coupling in self-assembled QDs [Hameau *et al.* (1999); Verzelen (2002)]. Firstly, we form a basis of factorized states, like in the bulk case. The whole Hilbert space should comprise both bound and continuum electron states and the whole set of phonon occupancies. However, since we are primarily interested in the low lying coupled states, we restrict the electron levels to the sole S-like and P-like bound ones. Moreover, at low temperature only low occupancy vibrations are necessary (up to two phonons or so). Secondly, we consider bulk phonons, as discussed previously. Thirdly, we discretize the phonons modes, by using an approximate description of the bulk dispersions. Finally, we diagonalize the Fröhlich interaction within this truncated basis. Note that both diagonal and non-diagonal couplings exist. They respectively correspond to the coupling of factorized states with the same or with different electronic states (but which differ by one-phonon occupancy in both cases).

Let us come back to the previous experimental situation. The stable entanglements evidenced in the measurements are the signature of a strong coupling between the electron and LO phonon states. The principal features of this strong coupling regime can be understood within a subset of the whole Hilbert space. More specifically, we shall study the large anti-crossing exhibited by the Ω_- branch near 23 T in Figure 5.4. To this aim, we disregard diagonal couplings and retain: (i) the discrete state: $|d\rangle = |e_-\rangle \otimes |0_{\vec{q}}\rangle$ with an energy ε_d ; and (ii) the one-phonon replica of the ground state: $|\nu_i\rangle = |g\rangle \otimes |1_{\vec{q}_i}\rangle$ with energies $\varepsilon_g + \eta\omega_{LO}(\vec{q}_i)$. The ket $|1_q\rangle$ represents the

phonon state where one LO phonon with wavevector \mathbf{q} has been excited.

The one-phonon replica forms a continuum which extends from $\varepsilon_g + \varepsilon_m$ to $\varepsilon_g + \varepsilon_M$ (where $\varepsilon_M - \varepsilon_m$ is the width of the LO phonon dispersion). The magnetic field acts as a control parameter on the system. It allows the discrete state $|d\rangle$ to be embedded into the one LO phonon continuum $|\nu_i\rangle$. Note that there exist other states which we shall discard, for instance the two-phonon continuum double replica of the ground state or the one-phonon continuum replica of $|d\rangle$. These continua are never resonant with $|d\rangle$. Their inclusion would improve the quantitative accuracy of the calculations but they won't change the qualitative conclusions we shall reach. In the actual calculations of the magneto-absorption fan chart (see [Hameau *et al.* (1999)]) all the relevant zero-phonon states and one and two-phonon replicas have been included.

In the truncated basis $\{|d\rangle, |\nu_i\rangle\}$ the stationary solutions of the complete Hamiltonian $H_e + H_{ph} + H_{e-ph}$ with an energy ε can be written

$$|\psi\rangle = a|d\rangle + \sum_{\vec{q}} \gamma(\vec{q}) |g, 1_{\vec{q}}\rangle. \quad (5.9)$$

We note that

$$\begin{aligned} \langle d | H_{e-ph} | d \rangle &= \langle \nu_i | H_{e-ph} | \nu_j \rangle = 0 \\ \langle d | H_{e-ph} | \nu_i \rangle &= V^*(\vec{q}_i) \langle e | e^{i\vec{q} \cdot \vec{r}} | g \rangle. \end{aligned} \quad (5.10)$$

The expressions (5.5), (5.6), (5.7) show that the only phonons efficiently coupled to the electrons are those with small vectors. More precisely, we know that the states bound to the dot have wavefunctions with spatial extensions of the order of the dot size. This means that the coupling matrix element between the discrete state and the continuum will involve phonons with $q < \pi / (\text{dimension of the dot})$. This cut off restricts even further the width of the continuum. The stationary solutions of our problem are the zeros of the determinant:

$$\left| \begin{array}{cccc} \varepsilon_d - \varepsilon & \langle d | H_{e-ph} | \nu_1 \rangle & \dots & \langle d | H_{e-ph} | \nu_N \rangle \\ \langle \nu_1 | H_{e-ph} | d \rangle & \varepsilon_{\nu_1} - \varepsilon & 0 & 0 \\ \dots & 0 & \dots & 0 \\ \langle \nu_N | H_{e-ph} | d \rangle & 0 & 0 & \varepsilon_{\nu_N} - \varepsilon \end{array} \right|. \quad (5.11)$$

As seen in (5.11) we have to diagonalize a $(N+1) \times (N+1)$ matrix, where N is the (macroscopic) number of phonon states which describe the one-phonon replica of the ground state.

In reality, there exist a large number of states of the complete Hamiltonian which have no projection on the discrete state. They fulfill $a = 0$ in (5.9) for any energy ε , which leads to the constraint

$$\sum_{\vec{q}_i} \langle d | H_{e-ph} | g, 1_{\vec{q}_i} \rangle \gamma(\vec{q}_i) = 0. \quad (5.12)$$

When $a \neq 0$ instead, we extract from (5.11)

$$\gamma(\vec{q}_i) = a \frac{\langle \nu_i | H_{e-ph} | d \rangle}{\varepsilon - \varepsilon_g - \hbar\omega_{LO}(\vec{q}_i)}. \quad (5.13)$$

Thus, it appears that the discrete state $|d\rangle$ couples only to the particular linear combinations of continuum states $|g, 1_{\vec{q}}\rangle$ which obey Eq. (5.13.) The eigenenergies are the ε which fulfill

$$\varepsilon - \varepsilon_d = \sum_{\vec{q}_i} \frac{|\langle d | H_{e-ph} | g, 1_{\vec{q}_i} \rangle|^2}{\varepsilon - \varepsilon_g - \hbar\omega_{LO}(\vec{q}_i)}. \quad (5.14)$$

In (5.14) one should add a small imaginary part to the quantity ε when dealing with a true continuum, whereas no such term is necessary if the continuum is discretized. For a true continuum, we finally obtain

$$\varepsilon - \varepsilon_d = R(\varepsilon) - iI(\varepsilon), \quad (5.15)$$

where

$$R(\varepsilon) = P \sum_{\vec{q}} \frac{|\langle d | H_{e-ph} | g, 1_{\vec{q}} \rangle|^2}{\varepsilon - \varepsilon_g - \hbar\omega_{LO}(\vec{q})} \quad (5.16)$$

$$I(\varepsilon) = \pi \sum_{\vec{q}} |\langle d | H_{e-ph} | g, 1_{\vec{q}} \rangle|^2 \delta(\varepsilon - \varepsilon_g - \hbar\omega_{LO}(\vec{q})). \quad (5.17)$$

The one-phonon continuum extends from $\varepsilon_g + \varepsilon_m$ to $\varepsilon_g + \varepsilon_M$. $I(\varepsilon)$ is non vanishing only in this interval and it is positive. It is peaked around $\varepsilon_g + \varepsilon_M$. It looks like a one LO phonon density of states, however distorted by the coupling efficiency to the electrons which strongly favors small \vec{q} phonons (see above). $R(\varepsilon)$ is an S-shaped curve which goes to ± 0 when $\varepsilon \rightarrow \pm\infty$ and changes sign in the segment $[\varepsilon_g + \varepsilon_m, \varepsilon_g + \varepsilon_M]$. Far away from the continuum energy ($I(\varepsilon) = 0$), we find a solution that approaches the unperturbed

discrete state energy:

$$\varepsilon - \varepsilon_d \approx R(\varepsilon_d) = \sum_{\vec{q}} \frac{|\langle d | H_{e-ph} | g, 1_{\vec{q}} \rangle|^2}{\varepsilon_d - \varepsilon_g - \hbar\omega_{LO}(\vec{q})}, \quad (5.18)$$

which is the usual second order perturbation result. We note that the perturbed solution lies above (below) the unperturbed one when the discrete state energy is larger (smaller) than the continuum one. In the strongly detuned regime $|\Delta(\vec{q})| = |\varepsilon_d - (\varepsilon_g + \eta\omega_{LO})| >> \varepsilon_M - \varepsilon_m$, the width of the continuum can be disregarded. The perturbed solution (5.18) reads $\varepsilon \approx \varepsilon_d + \lambda^2/\Delta(0)$, and the following picture applies: H_{e-ph} mixes all the one-phonon states to form one particular linear combination, such that the interaction of the discrete level with the narrow continuum can be replaced by an effective two-level problem with an effective coupling strength λ_g (see e.g. [Verzelen (2002)] and below). When the control parameter makes the discrete state approach the continuum the perturbative estimate (5.18) is insufficient and one should switch to finding numerically the solution(s) of

$$\varepsilon - \varepsilon_d = R(\varepsilon). \quad (5.19)$$

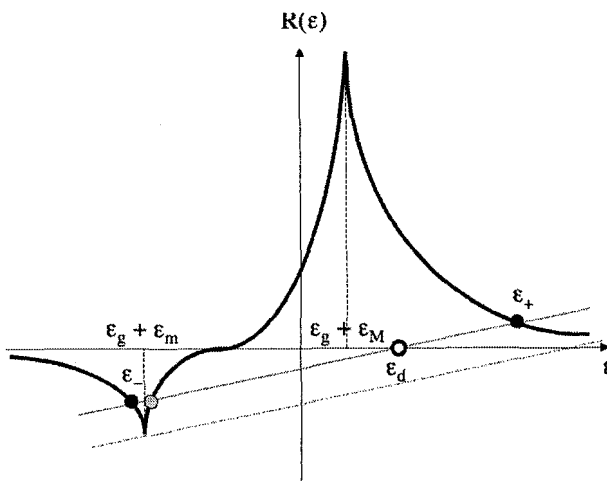


Fig. 5.5 Strong coupling between a discrete state and a continuum. Graphical solutions of Eq. (5.19). Two solutions appear outside the continuum (black dots).

A graphical discussion is possible. One should investigate two cases depending on whether the slope of the $\varepsilon - \varepsilon_d$ is small or large (an explicit criterion will be given below). Suppose for the sake of clarity that $\varepsilon_d > \varepsilon_g + \varepsilon_M$. If the slope of the line $\varepsilon - \varepsilon_d$ is small enough, this line will intersect the function $R(\varepsilon)$ for two values ε_+ and ε_- outside the continuum (see Figure 5.5). When ε_d increases from $\varepsilon_M + \varepsilon_g$ the solution ε_+ also increases and becomes closer and closer from ε_d . Far away from $\varepsilon_M + \varepsilon_g$ one recovers the perturbative estimate of (5.18).

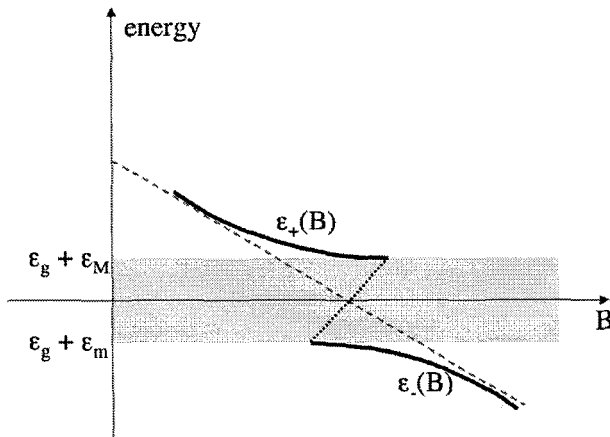


Fig. 5.6 B dependence of the two solutions of the equation (5.19) outside the continuum (solid lines). Strong coupling. Over a finite range of B , there are for each B two solutions outside the continuum. Far away from the anticrossing there is a single solution which approaches the unperturbed discrete state, as it should.

In a symmetrical fashion, when ε_d approaches $\varepsilon_g + \varepsilon_m$ from below, the solution ε_- which was very close from ε_d moves away from ε_d . The line $\varepsilon - \varepsilon_d$ intersects $R(\varepsilon)$ only once when ε_d is far enough from $\varepsilon_g + \varepsilon_m$. When ε comes close enough from $\varepsilon_g + \varepsilon_m$, a second solution shows up on the other side of the continuum (the + branch in Figure 5.6).

The two branch regime witnesses the strong coupling between the discrete state and the continuum. Over a finite range of the control parameter, there exist two solutions outside the continuum. The coupling is so strong that it prevents the discrete state from entering into the continuum. The anticrossing behavior between the + and - branches recalls that of the two-level system as a function of the detuning between the two interacting

levels. These two levels here are the discrete state on the one hand and the particular superposition of the 1 LO replicas of the ground state on the other hand.

The strong coupling regime does not always exist. Suppose the interaction term is weak enough that the graphical construction to find the bound state corresponds now to a large slope for the line $\varepsilon - \varepsilon_d$.

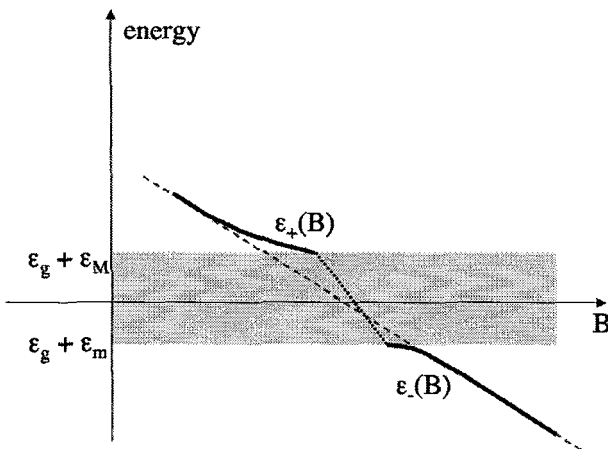


Fig. 5.7 B dependence of the solutions of Eq. (5.19) in the weak coupling situation. For each B there is at most one solution outside the continuum.

At most one solution is found for a given value of the control parameter. More importantly, there is in the weak coupling regime a finite range of the control parameter where there is no solution outside the continuum (see Figure 5.7). We cannot describe the solution in the continuum as before, since now the imaginary contribution $I(\varepsilon)$ is nonzero. One can show that one should search for complex values of the energies. Instead of displaying a true bound state the system displays a virtual bound state (a resonance) whose imaginary part of the energy corresponds to the damping of the states due to its dissolution in the continuum. Suppose we solve (5.15) in the vicinity of ε_r which is the root of $\varepsilon_r - \varepsilon_d = R(\varepsilon_r)$. We find

$$\varepsilon = \varepsilon_r + x \quad x \approx \frac{-iI(\varepsilon_r)}{1 - \frac{dR}{d\varepsilon}(\varepsilon_r) + i\frac{dI}{d\varepsilon}(\varepsilon_r)}. \quad (5.20)$$

As expected the correction to the real quantity ε_r comprises an imaginary

term. If the coupling is indeed very small the denominator in (5.20) is nearly 1 and we can identify ε_r with $\varepsilon_d + R(\varepsilon_d)$ and x with $-i\Gamma/2$ with

$$\Gamma = \frac{\hbar}{\tau} = 2\pi \sum_{\vec{q}} |\langle d | H_{e-ph} | g, 1_{\vec{q}} \rangle|^2 \delta(\varepsilon_d - \varepsilon_g - \hbar\omega_{LO}(\vec{q})), \quad (5.21)$$

which is the Fermi golden rule.

To summarize the weak coupling regime of the electron-phonon interaction, we have found that the upper branch in Figure 5.7 corresponds first to a stable bound state which, when B increases, enters into the continuum and dissolves into it to finally reappear at a still larger field as a bound state on the other side of the continuum.

The condition which ensures the transition from the weak coupling to the strong coupling can be simply derived. Suppose the solution of $\varepsilon_r = \varepsilon_d + R(\varepsilon_d)$ coincides with the ends of the upper branch, i.e. with $\varepsilon_g + \varepsilon_M$. The weak coupling means that the line $\varepsilon - \varepsilon_d$ does not intersect $R(\varepsilon)$ at an energy lower than $\varepsilon_g + \varepsilon_m$. This implies that

$$\varepsilon_g + \varepsilon_m - \varepsilon_d \leq R(\varepsilon_g + \varepsilon_m) \quad (5.22)$$

or, equivalently

$$\varepsilon_M - \varepsilon_m = \Delta \geq R(\varepsilon_M + \varepsilon_g) - R(\varepsilon_m + \varepsilon_g). \quad (5.23)$$

Note that the right hand side of (5.23) is the sum of two positive contributions which involve the modulus squared of the coupling matrix elements. We therefore find that if we increase the strength of the coupling between the discrete state and the continuum (everything kept constant elsewhere) the condition of the weak coupling (5.22, 5.23) will become violated. Symmetrically, if we keep the strength constant but decrease the width of the continuum (5.23) will become violated when Δ is smaller than a critical Δ_c .

Note the analogy between this discussion and the condition that a finite range three-dimensional potential (e.g. a spherical dot with finite barrier height) admits bound states. One knows that the well has to be sufficiently attractive or sufficiently wide to support bound states.

While the weak coupling situation (e.g. found in QWs) corresponds to an irreversible dilution of the bound state $|d\rangle$ into the $|g, 1_{\vec{q}}\rangle$ continuum, the strong coupling situation between the electrons and the LO phonons in QDs gives rise to the creation of new mixed elementary excitations between the electrons and the phonons: the polarons. These mixed modes appear as

discrete states of the coupled electron-phonon system ([Inoshita and Sakaki (1992)], [Kral and Khas (1998)], [Hameau *et al.* (1999)], [Fomin *et al.* (1998)]). The polaron wavefunction is an entanglement between different discrete electronic states and different phonon occupations. It is not, even approximately, a factorized state as found in the weak coupling theory.

In order to get a better understanding of the polaron states in QDs, we evaluate in the following a few physical quantities related to these stationary mixed states.

Firstly, let us point out that the average number of phonons $\langle n \rangle$ in the polaron is neither 0 nor 1. One can in fact compute $\langle n \rangle$ easily from (5.9) to find

$$\langle n \rangle = 1 - |a|^2. \quad (5.24)$$

At resonance when $\varepsilon_d(B) = \varepsilon_g + \varepsilon_m + \Delta/2$ one finds $\langle n \rangle \approx 1/2$. Note this value is considerably larger than found in bulk GaAs, where the average number of LO phonons is $\approx 4\%$ because GaAs is only weakly polar (see [Yu and Cardona (1999)]).

The previous model also enables us to discuss the nature of the phonon emission in QDs. In QWs, where the electron-phonon interaction is in the weak coupling regime, we know that the phonon emission is irreversible to the extent that any initial factorized state dissolves into the continuum of the factorized final states. In QDs, because of the smaller Hilbert space, we can directly compute the time evolution of the phonon population $n(t)$ carried by the polaron state. To simplify the algebra, we assume that the electron-phonon system has been prepared at $t = 0$ in the discrete factorized state $|d\rangle = |e, 0\rangle$. Thus, at $t = 0$ the electron is in the excited state $|e\rangle$ and there is no phonon present in the system. As time goes on, an energy exchange between the electron and the lattice vibrations becomes allowed, because of H_{e-ph} . At time t , we readily get the average phonon population

$$n(t) = \langle e, 0 | e^{i \frac{Ht}{\hbar}} \left(\sum_{\vec{q}} b_{\vec{q}}^\dagger b_{\vec{q}} \right) e^{-i \frac{Ht}{\hbar}} | e, 0 \rangle \quad (5.25)$$

or

$$n(t) = \sum_{\vec{q}} \left| \langle g, 1_{\vec{q}} | e^{-i \frac{Ht}{\hbar}} | e, 0 \rangle \right|^2 = 1 - \left| \langle e, 0 | e^{-i \frac{Ht}{\hbar}} | e, 0 \rangle \right|^2, \quad (5.26)$$

that is to say

$$n(t) = 1 - P_{surv}(t), \quad (5.27)$$

where $P_{surv}(t)$ is the survival probability in the initial state. For simplicity, let us focus on the resonant situation where the control parameter has embedded the discrete state in the continuum. Eq. (5.25) leads to two radically different time-evolutions for $n(t)$, depending on the strength of the e-ph coupling, as follows.

The weak coupling regime can be described in many equivalent ways. In this regime, the survival probability in the initial factorized state decreases exponentially to zero on a time scale given by the Fermi golden rule (5.21). This result characterizes a phonon emission process, since $n(t)$ starts from zero at initial time and increases to 1 when $t \rightarrow \infty$. It implies also that the exchange of energy between the electron and the lattice, triggered by H_{eph} , is irreversible: the electron scatters towards a lower energy state while the lattice vibrations gain the same amount of energy. Finally, the weak coupling is also equivalently characterized by the fact that the probability of having the *same* phonon re-absorbed by the electron (thus bringing the total system back to the *same* initial factorized state) is negligible at long time (even if we neglect the fact that the emitted phonon will subsequently decompose into two low energetic ones by the anharmonic terms, initializing a cascade process which will irreversibly redistribute the initial electron energy over many lattice modes).

In the strong coupling regime instead, two discrete states are pulled out of the continuum even though the control parameter has put the discrete state in the continuum. The survival probability shows oscillations at the Rabi frequency between these two states, which are similar to the response of a two-level system initially prepared in a linear superposition of its eigenstates. It turns out that, for a finite width phonon dispersion, the oscillations are not complete (i.e. between 0 and 1) because of the presence of a third (overdamped) solution of (5.15) in the continuum (see Figure 5.5). At long time however, when the contribution of the complex root has faded away, $n(t)$ should oscillate with time. This oscillatory phonon mean number can be interpreted as a cyclic coherent absorption/emission of phonons by the electron, which contrasts with the irreversible phonon emission of the weak coupling regime.

When the continuum width is zero (monochromatic phonons) there exist only two non-trivial (i.e., which involve admixtures of both electronic and phonon degrees of freedom) solutions ε_{\pm} to (5.15) for any value of the

control parameter or, equivalently, for any value of the detuning $\delta(B) = \varepsilon_d - \varepsilon_g - \eta\omega_{LO}$ between the discrete state and the dispersionless one-phonon replica of the ground state:

$$\varepsilon_{\pm} = \varepsilon_d - \frac{\delta(B)}{2} \pm \sqrt{\left(\frac{\delta(B)}{2}\right)^2 + U^2}, \quad (5.28)$$

where

$$U^2 = \sum_{\vec{q}} |\langle e, 0 | H_{e-ph} | g, 1_{\vec{q}} \rangle|^2. \quad (5.29)$$

The corresponding polaron eigenstates read

$$\begin{aligned} |+\rangle &= a_+ |e, 0\rangle + b_+ |g, 1_{eg}\rangle \\ |-\rangle &= a_- |e, 0\rangle + b_- |g, 1_{eg}\rangle, \end{aligned} \quad (5.30)$$

where $b_+ = (a_-)^*$, $b_- = -(a_+)^*$ and $|1_{e,g}\rangle$ is a particular linear combination of one-phonon bulk states $|1_q\rangle$:

$$|1_{eg}\rangle = \sum_{\vec{q}_i} V_{eg}(\vec{q}_i) |1_{\vec{q}_i}\rangle \quad (5.31)$$

$$V_{eg}(\vec{q}_i) = \frac{\langle e, 0 | H_{e-ph} | g, 1_{\vec{q}_i} \rangle^*}{|U|}. \quad (5.32)$$

Equation (5.32) clearly shows the entangled nature of the polarons' states. The amounts of discrete state in the polaron wavefunctions are $|a_{\pm}|^2$, where

$$|a_{\pm}| = \frac{1}{\sqrt{1 + \frac{U^2}{\left(\frac{\delta(B)}{2} \pm \sqrt{\frac{\delta^2(B)}{4} + U^2}\right)^2}}} \quad (5.33)$$

with the typical two-level system features that $|a_{\pm}| = 1/\sqrt{2}$ if $\delta(B) = 0$ while at large positive detuning $|a_+| \rightarrow 1$ and $|a_-| \rightarrow 0$. For an arbitrary detuning there is of course $|a_+|^2 + |a_-|^2 = 1$, which simply states that the total amount of discrete state percentage adds to one.

According to the previous model, only one particular phonon mode, $|1_{eg}\rangle$, couples to the discrete state for a flat phonon dispersion. This “phonon wavepacket” can be constructed because all the bulk phonons are degenerate. This means that any linear combination of propagative modes is also a phonon eigenstate with the same energy $\eta\omega_{LO}$. Of course,

any complete set of orthonormal one-phonon states (like the bulk propagative ensemble) can be used as a basis for the diagonalization of the H_{e-ph} interaction. It turns out that, by properly choosing among the infinity of possible sets, we can find one ensemble for which only one mode, when associated to $|g\rangle$, couples to the discrete level $|e\rangle$. This very particular phonon mode ($|1_{eg}\rangle$) is intimately linked to the $|e\rangle$ and $|g\rangle$ pair of electronic states, as is clear from Eqs. (5.31, 5.32).

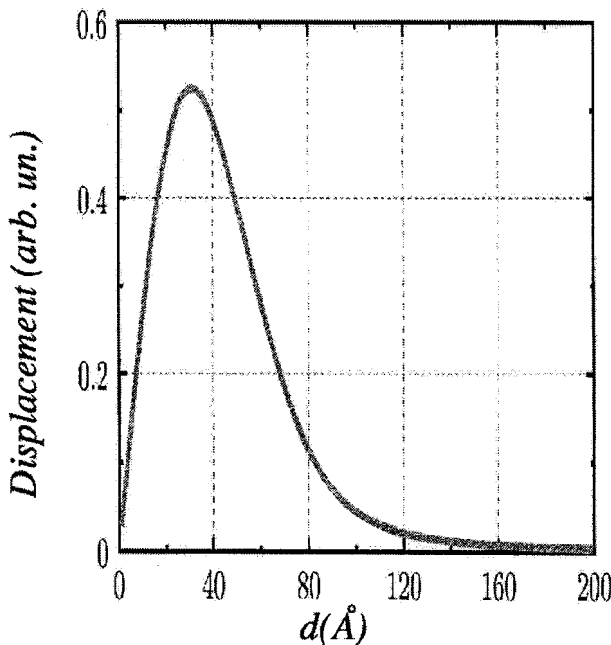


Fig. 5.8 Mean square displacements of atoms in a polaron state.

Propagative phonons involve the motion of all atoms, which at a given time display displacements which are periodic in space as a result of the translation invariance of the lattice potential [Davydov (1980)]. It is interesting to investigate the atomic displacements which correspond to the particular mode $|1_{eg}\rangle$. Without entering into details, let us point out that the mean displacements of the atoms vanish for both the $|+\rangle$ and $|-\rangle$ polaron states, like in a periodic crystal. The mean square displacements,

instead, do not vanish but, contrarily to the spatial periodicity obtained for the bulk case, they display a spatial localization. We show in Figure 5.8 the position-dependent amplitude of the vibrating atoms (square root of the average squared amplitude), along an in-plane direction at the basis of a truncated pyramid that floats on a one monolayer thick InAs wetting-layer. We see that only the atoms within the QDs have a significant amplitude. Thus, despite the fact that we have initially assumed a basis of propagative (thus delocalized) LO phonons, the coupling of the lattice atoms to localized electronic levels generate one particular phonon mode which is also somehow localized within the QD. In the same way, the electronic probability density related to the polaron states Eqs. (5.31, 5.32) are

$$P_{\pm}(\mathbf{r}) = |a_{\pm}|^2 + |\Psi_e(\mathbf{r})|^2 + |b_{\pm}|^2 + |\Psi_g(\mathbf{r})|^2. \quad (5.34)$$

This means that the electronic distribution inside the QD can be radically different from the ones related to the wavefunctions $\Psi_e(\mathbf{r})$ or $\Psi_g(\mathbf{r})$ for the states $|e\rangle$ and $|g\rangle$, respectively.

So far we have discussed the electron-optical phonon interaction. One may wonder what happens for the coupling between the electrons and the acoustic phonons in QDs. Calculations [Verzelen (2002)] have shown that there exists an irreversible dilution of $|e, 0\rangle$ into the continuum of $|g, 1_q\rangle$. This is due to a weaker H_{e-ph} and to a wider acoustic continuum. The main limitation of the deformation potential coupling is its strong dependence upon the energy of the phonons involved. Indeed, as shown in Figure 5.2, an efficient relaxation is possible only between bound electron states which are neither too close nor too far away in energy.

In conclusion, the early studies of the energy relaxation in QDs based on a lowest order perturbative treatment are essentially (but not strictly, as discussed below) correct for the deformation potential coupling in Eqs. (5.6,5.7), contrarily to the case of the Fröhlich interaction in Eq. (5.4). However, it is worth stressing that the existence of a strong coupling between factorized states involving different confined electron levels and LO phonon occupancies is not the only (although probably the most striking) effect to be assigned to the Fröhlich coupling in QDs. In the same way, different aspects of the electron-acoustic phonon coupling in quantum dots cannot be simply reduced to scattering rates between slightly energetically separated states. We point out in Sections V and VI another important effect which results from the coupling between confined carriers and phonons (acoustic or optical) and which may involve only a single confined electronic level and that goes beyond the second-order perturbation scheme.

5.4 Energy Relaxation in the Polaron Framework

We know that the weak coupling theory ran into troubles (“phonon bottleneck”) when it was used to explain the energy relaxation in QDs. The polaron description, although it accounts nicely for the optical data, faces similar difficulties in explaining the energy relaxation in QDs. Actually, once we have solved (5.15), we have found the stationary states of the interacting electron-phonon system. Thus, the system, once placed in such a state, would never evolve and in particular would never relax. If prepared into a linear superposition of polaron states, it would (Rabi) oscillate between the various states but no irreversible loss of energy would happen. One therefore ends up with an “absolute phonon bottleneck” since the very idea of relaxation becomes meaningless. As first pointed out by Li *et al.* [Li and Arakawa (1998); Li *et al.* (1999)], the main ingredient which leads to an energy relaxation is the phonon instability against dissociation into other phonons due to the anharmonicity of the vibrations. When we use the phonon concept, we implicitly assume that the vibrations are harmonic. A weak anharmonicity induces a finite lifetime to the phonons. In bulk or QW structures this is not an important effect because the phonon lifetime (4-10 ps) is considerably longer than typical electronic lifetime due to the irreversible emission of LO phonons (0.4-1 ps). In QDs however, this finite lifetime induced by anharmonicity is very important because it is the only mechanism which can trigger the polaron decay (in weakly excited QDs). Thus, we arrive at the novel concept that the energy relaxation in QDs should be seen as the evolution of a small system (the polaron) coupled to a huge thermostat (the two-phonon thermostat) by a small coupling (the effective anharmonicity Hamiltonian which is the restriction of the bare anharmonicity term to the polaron subspace). Note that there is no difficulty in applying the Fermi golden rule for the purpose of calculating polaron lifetimes since we deal with a broad continuum (the two-phonon continuum) and a small interaction term between the discrete polaron states and the thermostat. Attempts to evaluate the polaron lifetime along these lines have been undertaken by Verzelen *et al.* [Verzelen *et al.* (2000)] and Jacak *et al* [Jacak *et al.* (2002)]. A more transparent semi-classical model was put forward by Li *et al.* [Li and Arakawa (1998); Li *et al.* (1999)]. It amounts to writing that the decay frequency of the polaron Γ_{pol} is equal to the decay frequency of the LO phonon Γ_{ph} times

the fraction of the one-phonon state in the polaron wavefunction:

$$\Gamma_{pol} = \Gamma_{ph} \left| \sum_{m,\vec{q}} \langle \psi_{pol} | m, 1_q \rangle \right|^2, \quad (5.35)$$

where $|m, 1_q\rangle$ is a factorized e-ph QD state. There is no restriction in (5.35) on the possibility of polaron relaxation, while more microscopic approaches [Verzelen *et al.* (2000)] put a bound to the polaron relaxation which is that the energy difference between the initial or final polaron states should not exceed the width of the two-phonon thermostat. Otherwise, when comparable, the two models give similar results for Γ_{pol} .

It is interesting to point out that the energy relaxation of QD polarons (i.e. when the electron is strongly coupled to LO phonons) can be less efficient than found for factorized bulk states (when the electron-phonon coupling is weak). This is because from (5.31) $\Gamma_{pol} < \Gamma_{ph}$ and therefore $\tau_{pol} > \tau_{ph} \approx$ a few ps. In addition, it depends very little on the strength of the electron-phonon interaction: the latter sets the polaronic energy scale but never enters again in the energy relaxation formalism. In a weak coupling description instead, the relaxation time is governed by the Fröhlich interaction itself, and is thus the shorter when the electron-phonon interaction is the stronger and when the density of final electronic states is the larger. Finally, let us mention that for fixed material parameters, say GaAs, the energy relaxation is less efficient in a QD than in a QW. Thus, there is in effect a weakening of the energy relaxation efficiency in QDs, but it is of very different physical origin from what was known as the “phonon bottleneck”.

Recent experiments have brought convincing evidence that the polaron description of the interacting e-ph system does explain the energy relaxation in QDs. Sauvage *et al.* [Sauvage *et al.* (2002)] and Zibik *et al.* [Zibik *et al.* (2003)] have performed absorption recovery experiments in InAs/GaAs QDs arrays. The QDs were modulation-doped by 1 to 4 electrons. FIR photons from a free electron laser saturate one of the two linearly polarized “S-P transitions”. At time τ_D later a weak probe with the same photon energy becomes absorbed because some of the excited state population has relaxed down to the ground state. A plot of the probe absorption versus τ_D at fixed $\eta\omega (> \eta\omega_{LO})$ allows to determine the decay time τ , which is identified with the population relaxation time of the upper polaron state to the ground polaron state. Furthermore, it is possible to vary ω in these experiments and therefore to probe the accuracy of (5.35) since varying ω

amounts to varying the sub-class of dots which is probed by the laser. This is also equivalent to varying the detuning δ since $\eta\omega = \epsilon_+ - \epsilon_S$ and ϵ_S varies smoothly with the dot size. Hence, in this situation, one can probe the accuracy of the polaronic theory which states that

$$\Gamma_{pol} = \Gamma_{ph}(1 - |a_+|^2), \quad (5.36)$$

where a_+ is given by (5.33). Figure 5.9 shows a comparison between Zibik *et al.* experiments and the polaron model in the case of dots which contain at most one electron on the average [Zibik *et al.* (2003)]. It is seen that the polaron theory fits nicely to the data. One input parameter is the phonon lifetime, 10 ± 2 ps, which is quite comparable to the value found in GaAs. Note finally the magnitude of the relaxation time: for an “S-P” transition energy around 50 meV, the relaxation time is ≈ 50 ps.

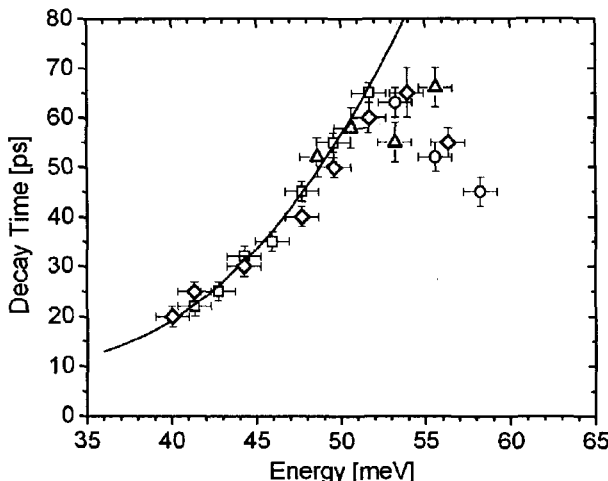


Fig. 5.9 Measured energy dependence of the decay time at $T = 5$ K (solid squares) and calculated polaron decay times (solid line) assuming an optical phonon lifetime of 10 ps. Courtesy L. Wilson [Zibik *et al.* (2003)].

5.5 Excitonic Polarons in Quantum Dots

It is not immediately clear that a Coulomb correlated electron-hole ($e-h$) pair (in short an exciton) should enter into a strong coupling with the opti-

cal phonons, on the grounds that an e-h pair is neutral and thus is insensitive to the Fröhlich coupling to the optical phonon, which is of Coulombic origin. In order to get a better understanding of the importance of the phonon-related couplings involving electron-hole states, let us focus initially on the ground inter-band transition. In the absence of coupling to LO phonons, the ground e-h pair state is mostly made out of two closely resembling wavefunctions with roughly the same symmetry and shape: S_e and S_h . When we evaluate the e-ph and h-ph couplings up to the second order in perturbation, the energy of the ground state $|S_e, S_h, 0_{\vec{q}_i}\rangle$ reads

$$\tilde{\epsilon}_{S_e S_h} \approx \epsilon_{S_e S_h} + \sum_{\nu_e, \nu_h, \vec{q}_i} \frac{|\langle S_e S_h | e^{i\vec{q}_i \cdot \vec{r}_e} - e^{i\vec{q}_i \cdot \vec{r}_h} | \nu_e \nu_h \rangle|^2 |V_{Fr}(\vec{q}_i)|^2}{\epsilon_{S_e S_h} - \epsilon_{\nu_e \nu_h} - \hbar\omega_{LO}(\vec{q}_i)}, \quad (5.37)$$

where $\nu_{e,h}$ run over all the electronic bound states. One has both diagonal and non-diagonal contributions in Eq. (5.37). It turns out that the matrix element for the diagonal contribution ($|\nu_e, \nu_h\rangle = |S_e, S_h\rangle$) is generally much weaker than the ones that involve excited e-h states. Actually, the diagonal coupling of the ground inter-band level to the optical phonons is, as a general rule, very weak in self-assembled GaAs/InAs QDs. The non-diagonal Fröhlich couplings admixes the ground level with more excited e-h states, like the asymmetrical P_e - S_h and S_e - P_h states. These mixings are however small due to the large energy detunings in Eq. (5.37). Since all the one-phonon pair states entering in the sum in Eq. (5.37) lay at higher energies, a red shift of $|S_e, S_h, 0_{\vec{q}_i}\rangle$ ensues, but this shift is quantitatively small, typically less than one meV in actual InAs/GaAs QDs [Verzelen *et al.* (2002)]. So, at the end, the lowest lying pair state is weakly affected by the electron-phonon and hole-phonon interactions. However, the small mixing of the zero-phonon S_e - S_h state with the wavefunction of factorized e-h pair states with 1 (or 2, ..., at higher order in perturbation) phonons is of paramount importance for the optical properties of QDs. Let us quote in the following two major effects regarding the optical response of the ground inter-band transition.

Firstly, the polaron mixings lead to the existence of LO phonon replicas of the zero-phonon lines in the absorption or luminescence spectra of QDs [Fomin *et al.* (1998)]. Their intensity is quite small when the electron and hole envelope functions are alike. In QDs which display very different electron and hole envelope functions, the intensity of the LO phonon replicas are enhanced [Verzelen (2002); Heitz *et al.* (1999); Bissiri *et al.* (2000)]. Note that the comparable magnitudes of the energy

distances between the e-h states and the LO phonon energy invalidates the use of the Huang-Rhys model (see below) to evaluate the intensities of the replicas. The influence of the coupling between the e-h states and the LO phonons on the non linear optical properties of QDs is discussed by Kuhn *et al.* in this volume (see Chapter 6).

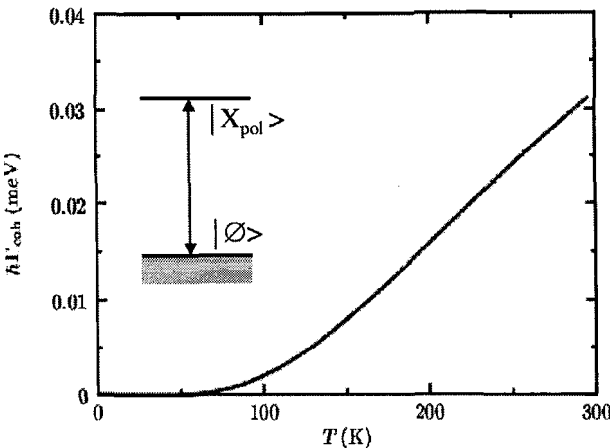


Fig. 5.10 Calculated temperature dependence of the coherence broadening in a InAs/GaAs QD. From [Verzelen *et al.* (2002)].

Secondly, the polaronic mixings lead to the existence of a finite coherence lifetime for the ground excitonic polaron state. Verzelen *et al.* have shown how these couplings imply a thermally activated escape process towards the excited e-h pair states. This escape, which is triggered by the anharmonic couplings, leads to the time decay of the coherence between the QD ground state (empty dot) and the lowest lying exciton state (see Figure 5.10). It is interesting to point out that at room temperature for a typical InAs/GaAs QD the coherence lives at most a few tens of a ps, thereby limiting severely the number of quantum operations one can perform before the decoherence has washed out the fragile quantum superpositions one has created.

Let us now focus on the higher energy exciton-phonon mixed states in QDs. Following the same lines as for *electronic* polarons, Verzelen *et al.* [Verzelen *et al.* (2002)] have demonstrated the formation of *excitonic* po-

laron states when the narrow continuum of the one-phonon replica of the ground state $|S_e, S_h, 1_{\vec{q}}\rangle$ becomes nearly degenerate in energy with any of the zero-phonon states $|S_e, P_h, 0_{\vec{q}_i}\rangle$ or $|P_e, S_h, 0_{\vec{q}_i}\rangle$. Thus, in spite of the electrical neutrality of an e-h pair, the (electrostatic in origin) Fröhlich interaction can lead to resonant polaron couplings when excited e-h pair states are involved, which are the excitonic counterpart of the single particle polarons. In these e-h polarons one of the two particles actually remains a spectator, but an active one since the Coulomb correction to the e-h energy is quite large (some 25 meV in InAs/GaAs dots for S_e - S_h or P_e - P_h states). The magnitude of the anti-crossing between the zero-phonon e-h states and the one-phonon replica of the e-h ground state is similar to the one found in electronic polarons. Also, the electron-hole and LO phonon entanglement properties found for electronic polarons remain true for excitonic polarons. Let us finally note that the formation of QD excitonic polarons also influences significantly the energy relaxation of the excited e-h states (see [Verzelen *et al.* (2002)]). Like in the electronic case, one should invoke the phonon anharmonicity to find a non zero relaxation.

5.6 Diagonal Non-Perturbative Interaction Between Electrons and Acoustic Phonons

As mentioned before, the coupling between the electrons and acoustic phonons is weak and the Fermi golden rule can be used safely. However, it leads to very small transition rates between QD levels. Recent experiments on single QDs (see Figure 5.11) have pointed out the crucial part played by the acoustic phonons in the inter-band optical transitions ([Favero *et al.* (2003)]; see also [Besombes *et al.* (2001)] for similar measurements on shallow QDs formed at QW interfaces). At very low T (say $T < 10K$) the recombination line of a single QD is symmetrical. Raising the temperature leads to the development of an increasing asymmetrical pedestal while the central peak decreases. At $T \approx 60K$ the line is again symmetrical and much broader. The pedestal calls for the participation of phonons to the radiative recombination process, which involve either the absorption (high energy side) or the emission (low energy side) of acoustic phonons. It is possible to perform a perturbative calculation to account, at least partially, for the pedestal. However, this is seldom done because there exists a simpler and more powerful model, the Huang-Rhys (also called independent boson) model, which explains the pedestal

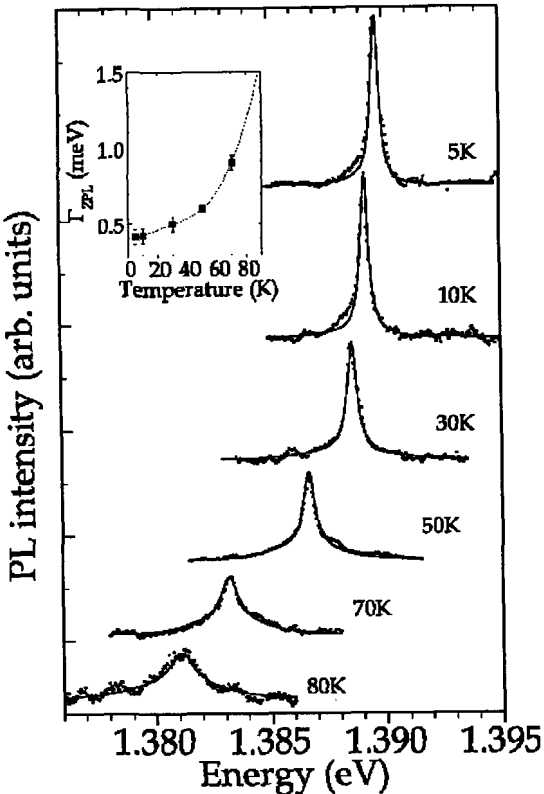


Fig. 5.11 Photoluminescence intensity versus photon energy in a single InAs/GaAs QD at different temperature. The inset shows the temperature dependence of the zero-phonon line. From [Favero *et al.* (2003)].

quite satisfactorily [Huang and Rhys (1950); Duke and Mahan (1965); Mahan (1990)]. The Huang-Rhys model assumes that the splittings between electronic states are much larger than the typical phonon energies. This is the situation met by the electrons and the acoustic phonons in QDs (electronic splittings ≈ 50 meV; typical acoustic phonon energy $\approx 1\text{--}2$ meV) but not by the electrons and the LO phonons. Because of the large electron

energy distances, one expects that the electron-phonon interaction between factorized states with different electronic quantum numbers will be quite small, actually much smaller than the electron-phonon interaction between the factorized states with the same electron quantum number. Under such circumstances the interacting electron-acoustic phonon Hamiltonian can be exactly diagonalized. One starts from

$$H = H_e + \sum_{\vec{q}_i} (b_{\vec{q}_i}^\dagger b_{\vec{q}_i} + \frac{1}{2}) \hbar \omega_{\vec{q}_i} + (V_{\vec{q}_i}^e e^{-i\vec{q}_i \cdot \vec{r}_e} + V_{\vec{q}_i}^h e^{-i\vec{q}_i \cdot \vec{r}_h}) b_{\vec{q}_i}^\dagger + ((V_{\vec{q}_i}^e)^* e^{i\vec{q}_i \cdot \vec{r}_e} + (V_{\vec{q}_i}^h)^* e^{i\vec{q}_i \cdot \vec{r}_h}) b_{\vec{q}_i} \quad (5.38)$$

where H_e is the e-h Hamiltonian, possibly taking the interaction with LO phonons into account. H is projected onto the relevant e-h state $|\psi_X\rangle$ (say the lowest lying Coulomb correlated excitonic polaron state) to become an effective phonon Hamiltonian:

$$H \rightarrow |\psi_X\rangle \langle \psi_X| H |\psi_X\rangle \langle \psi_X| = H_{eff} |\psi_X\rangle \langle \psi_X|. \quad (5.39)$$

The introduction of new creation and annihilation operators:

$$\beta_{\vec{q}_i} = b_{\vec{q}_i} + \frac{\lambda_{\vec{q}_i}}{\hbar \omega_{\vec{q}_i}}, \quad \beta_{\vec{q}_i}^\dagger = b_{\vec{q}_i}^\dagger + \frac{\lambda_{\vec{q}_i}^*}{\hbar \omega_{\vec{q}_i}} \quad (5.40)$$

with

$$\lambda_{\vec{q}_i} = \langle \psi_X | V_{\vec{q}_i}^e e^{-i\vec{q}_i \cdot \vec{r}_e} + V_{\vec{q}_i}^h e^{-i\vec{q}_i \cdot \vec{r}_h} | \psi_X \rangle \quad (5.41)$$

achieves the diagonalization of H_{eff} :

$$H_{eff} = E_X + \sum_{\vec{q}_i} \left(\beta_{\vec{q}_i}^\dagger \beta_{\vec{q}_i} + \frac{1}{2} \right) \hbar \omega_{\vec{q}_i} + \left| \frac{\lambda_{\vec{q}_i}}{\hbar \omega_{\vec{q}_i}} \right|^2. \quad (5.42)$$

Several features are worth mentioning. Firstly, the interacting electron-phonon states remain factorized. This contrasts with the polaron states which are entanglements of electron and LO phonon states. Secondly, the effective Hamiltonian displays the same phonon frequencies as the initial phonon Hamiltonian, a natural consequence of the linearity of the electron-phonon Hamiltonian in b and b^\dagger . More important for explaining the piedestals is the fact that the harmonic oscillators representing the phonons are no longer centered at the equilibrium positions they had without interaction with the e-h degrees of freedom. The new equilibrium positions explicitly depend on the specific e-h state. Thus, during the radiative recombination, there is a possibility that no vibration is involved. This is

the central peak. Or the phonon quantum number can change, which leads to a red shift or a blue shift of the satellites compared to the central line. The fact that the acoustic phonons do show a dispersion implies that the phonon replicas form a band rather than a line, as found for the LO phonon replicas.

In this simplified Huang-Rhys model, the elastic peak remains unbroadened. In experiments it is found broadened, to a much larger extent than inferred from the radiative broadening [Favero *et al.* (2003)]. This calls for further improvements of the electron-phonon theory or for the inclusion of extra broadenings, e.g. that due to the random electrostatic fluctuations around the QDs [Jankovic *et al.* (2004)].

The interaction between e-h pairs with acoustic phonons leads to de-coherence of the ground optical transitions. This was experimentally evidenced by Bori *et al.* [Borri *et al.* (2001)] and explained by Vagov *et al.* [Vagov *et al.* (2002)]. A review of these important findings is contained in the next chapter.

5.7 Conclusions

There is now compelling evidence that the electron-phonon interaction is radically different in QDs than in other heterostructures. Ultimately, this is because the electronic continuums have been peeled off by the three-dimensional size quantization and because the LO phonon continuum is very narrow. These two features conspire to invalidate the Fermi golden rule which is so prevalent in quantum wires, wells and in bulk materials. In turn, the polaron model explains not only the energy levels and far infrared optical transitions but also the energy relaxation. Efforts remain to be made to bring the understanding of the inter-band optical data to the same level of satisfaction as found for intraband data. The relevance of the polaron model to other situations, such as the broadened Landau levels of 2D gases, remains to be established.

Acknowledgments

The Laboratoire Pierre Aigrain ENS is “Laboratoire associé au CNRS et aux Universités Paris 6 et Paris 7”. We are pleased to thank all the members of the SQID consortium for numerous helpful discussions and interactions. We are indebted to our collaborators and students for providing

us with superb experimental data and modelings. These include Professors, Doctors Y. Arakawa, G. Cassabois, L. A. de Vaulchier, I. Favero, Y. Guldner, S. Hameau, T. Inoshita, J.N. Isaia, A. Jankovic, C. Kammerer, Ph. Roussignol, H. Sakaki, A. Vasanelli and, above all, O. Verzelen. One of us (G.B.) would like to express his gratitude to Professors J. Wang and P. Sheng for their kind invitation to the Hong Kong University for Science and Technology where part of this article was written.

Bibliography

- Ando, T., Fowler A. and Stern, F. (1982). Electronic properties of two-dimensional systems, *Rev. Mod. Phys.* **54**: 437.
- Bastard G. and Molinari E., this volume and references cited therein.
- Benisty, H., Sotomayor-Torres, C. M. and Weisbuch, C. (1991) Intrinsic mechanism for the poor luminescence of quantum-box systems, *Phys. Rev. B* **44**: 10945.
- Besombes, L., Kheng, K., Marsal, L. and Mariette, H. (2001). Acoustic phonon broadening mechanism in single quantum dot emission, *Phys. Rev. B* **63**: 155307.
- Bissiri, M., Baldassarri Hoger von Hogerthal, G., Bhatti, A. S., Capizzi, M., Frova, A., Frigeri, P. and Franci, S. (2000). Optical evidence of polaron interaction in InAs/GaAs quantum dots, *Phys. Rev. B* **62**: 4642.
- Bockelmann, U. and Bastard, G. (1990). Phonon scattering and energy relaxation in two-, one-, and zero-dimensional electron, gases, *Phys. Rev. B* **42**: 8947.
- Bockelmann, U. and Egeler, T. (1992). Electron relaxation in quantum dots by means of Auger processes, *Phys. Rev. B* **46**: 15574.
- Borri, P., Langbein, W., Schneider, S., Woggon, U., Sellin, R. L., Ouyang, D. and Bimberg, D. (2001). Ultralong dephasing time in InGaAs quantum dots, *Phys. Rev. Lett.* **87**: 157401.
- Cohen-Tannoudji, C., Dupont-Roc, J. and Grynberg, G. (1988). *Processus d'interaction entre photons et atomes*, InterEditions/Editions du CNRS, Paris.
- Davydov, A. (1980), *Théorie du Solide*, Mir, Moscou.
- Duke, C. B. and Mahan, G. D. (1965). Phonon-broadened impurity spectra. I. Density of states, *Phys. Rev.* **139**: 1965.
- Fafard, S., Leon, R., Leonard, D., Merz, J. L. and Petroff, P. M. (1995). Phonons and radiative recombination in self-assembled quantum dots, *Phys. Rev. B* **52**: 5752.
- Favero, I., Cassabois, G., Darson, J. D., Voisin, C., Tignon, J., Delalande, C., Roussignol, Ph., Ferreira, R., Bastard, G. and Gerard, J. M. (2003). Acoustic phonon sidebands in the emission line of single InAs/GaAs quantum dots, *Phys. Rev. B* **68**: 233301.
- Ferreira, R. and Bastard, G. (1989). Evaluation of some scattering times for elec-

- trons in unbiased and biased single- and multiple-quantum-well structures, *Phys. Rev. B* **40**: 1074.
- Ferreira, R. and Bastard, G. (1999). Phonon-assisted capture and intradot Auger relaxation in quantum dots, *Appl. Phys. Lett.* **74**: 2818.
- Fomin, V. M., Gladilin, V. N., Devreese, J. T., Pokatilov, E. P., Balaban, S. N. and Klimin, S. N. (1998). Photoluminescence of spherical quantum dots, *Phys. Rev. B* **57**: 2415.
- Hameau, S., Guldner, Y., Verzelen, O., Ferreira, R., Bastard, G., Zeman, J., Lemaitre, A. and Gerard, J. M. (1999). Strong electron-phonon coupling regime in quantum dots: evidence for everlasting resonant polarons, *Phys. Rev. Lett.* **83**: 4152.
- Hameau, S., Isaia, J. N., Guldner, Y., Verzelen, O., Ferreira, R., Bastard, G., Zeman, J. and Gerard, J. M. (2002). Far-infrared magnetospectroscopy of polaron states in self-assembled InAs/GaAs quantum dots, *Phys. Rev. B* **65**: 085316.
- Heitz, R., Grundmann, M., Ledentsov, N. N., Eckey, L., Veit, M., Bimberg, D., Ustinov, V. M., Egorov, A. Yu., Zhukov, A. E., Kop'ev, P. S. and Alferov, Zh. I. (1996). Multiphonon-relaxation processes in self-organized InAs/GaAs quantum dots, *Appl. Phys. Lett.* **68**: 361.
- Heitz, R., Veit, M., Ledentsov, N. N., Hoffmann, A., Bimberg, D., Ustinov, V. M., Kop'ev, P. S. and Alferov, Zh. I. (1997). Energy relaxation by multiphonon processes in InAs/GaAs quantum dots, *Phys. Rev. B* **56**: 10435.
- Heitz, R., Mukhametzhanov, I., Stier, O., Madhukar, A. and Bimberg, D. (1999). Enhanced polar exciton-LO phonon interaction in quantum dots, *Phys. Rev. Lett.* **83**: 4654.
- Heitz, R., Born, H., Gutfarth, F., Stier, O., Schliwa, A., Hoffmann, A. and Bimberg, D. (2001). Existence of a phonon bottleneck for excitons in quantum dots, *Phys. Rev. B* **64**: 241305.
- Htoon, H., Kulik, D., Baklenov, O., Holmes Jr., A. L., Takagahara, T. and Shih, C. K. (2001). Carrier relaxation and quantum decoherence of excited states in self-assembled quantum dots, *Phys. Rev. B* **63**: 241303.
- Huang, K. and Rhys, A. (1950). Theory of light absorption and non-radiative transitions in F-centres, *Proc. R. Soc. London, Ser. A* **204**: 406.
- Inoshita, T. and Sakaki, H. (1992). Electron relaxation in quantum dot: significance of multi-phonon processes, *Phys. Rev. B* **46**: 7260.
- Inoshita, T. and Sakaki, H. (1997). Density of states and phonon-induced relaxation of electrons in semiconductor quantum dots, *Phys. Rev. B* **56**: 4355.
- Jacak, L., Krasnyj, J., Jacak, D. and Machnikowski, P. (2002). Anharmonicity-induced polaron relaxation in GaAs/InAs quantum dots, *Phys. Rev. B* **65**: 113305.
- Jankovic, A., Ferreira, R. and Bastard, G. (2004). Non-perturbative optical response of a "fluctuating" single quantum dot, *Physica E* **21**: 252.
- Jusserand, B. (2002). "Electron and Photon Confinement in Semiconductor Nanostructures", *Proceedings of the Varenna Summer School. Course CL*, p. 63; and references therein.
- Kral, K. and Khas, K. (1998). Electron self-energy in quantum dots, *Phys. Rev.*

- B* **57**: 2061.
- Lee, I., Goodnick, S. M., Gulia, M., Molinari, E. and Lugli, P. (1995). Microscopic calculations of the electron-optical-phonon interaction in ultrathin GaAs/Al_xGa_{1-x} As alloy quantum-well systems, *Phys. Rev. B* **51**: 7046.
- Lemaitre, A., Ashmore, A. D., Finley, J. J., Mowbray, D. J., Skolnick, M. S., Hopkinson, M. and Krauss, T. F. (2001). Enhanced phonon-assisted absorption in single InAs/GaAs quantum dots, *Phys. Rev. B* **63**: 161309.
- Li, X. Q. and Arakawa, Y. (1998). Anharmonic decay of confined optical phonons in quantum dots, *Phys. Rev. B* **57**: 12285.
- Li, X. Q., Nakayama, H. and Arakawa, Y. (1999). Phonon bottleneck in quantum dots: role of lifetime of the confined optical phonons, *Phys. Rev. B* **59**: 5069.
- Mahan, G. D. (1990). *Many-Particle Physics*, 2nd ed. (Plenum Press, New York, 1990)
- Müller, T., Schrey, F. F., Strasser, G. and Unterrainer, K. (2003). Ultrafast interband spectroscopy of electron capture and relaxation in InAs/GaAs quantum dots, *Appl. Phys. Lett.* **83**: 3572.
- Oulton, R., Finley, J. J., Mowbray, D. J., Skolnick, M. S., Hopkinson, M., Steer, M. J. and Liu, H. (2002). *Physics of Semiconductors 2002* (Eds: A. R. Long and J. H. Davies, IOP Conference Series Number 171).
- Raymond, S., Fafard, S., Charbonneau, S., Leon, R., Leonard, D., Petroff, P. M. and Merz, J. L. (1995). Photocarrier recombination in Al_yIn_{1-y}As/Al_xGa_{1-x}As self-assembled quantum dots, *Phys. Rev. B* **52**: 17238.
- Ridley, B.K. (1988). *Quantum processes in semiconductors*, Clarendon Press, Oxford.
- Rossi, F. and Kuhn, T. (2002). Theory of ultrafast phenomena in photoexcited semiconductors, *Rev. Mod. Phys.* **74**: 895.
- Sauvage, S., Boucaud, P., Lobo, R. P. S. M., Bras, F., Fishmann, G., Prazeres, R., Glotin, F., Ortega, J. M. and Gerard, J. M. (2002). Long polaron lifetime in InAs/GaAs self-assembled quantum dots, *Phys. Rev. Lett.* **88**: 177402.
- Schmidt, K. H., Medeiros-Ribeiro, G., Oestreich, M., Petroff, P. M. and Dohler, G. H. (1996). Carrier relaxation and electronic structure in InAs self-assembled quantum dots, *Phys. Rev. B* **54**: 11346.
- Shah, J. (Ed) (1992). *Hot carriers in semiconductor nanostructures: Physics and applications*, Academic Press, London.
- Stauber, T., Zimmermann, R. and Castella, H. (2000). Electron-phonon interaction in quantum dots: a solvable model, *Phys. Rev. B* **62**: 7336.
- Steer, M. J., Mowbray, D. J., Tribe, W. R., Skolnick, M. S., Sturge, M. D., Hopkinson, M., Cullis, A. G., Whitehous, C. R. and Murray, R. (1996). Electronic energy levels and energy relaxation mechanisms in self-organized InAs/GaAs quantum dots, *Phys. Rev. B* **54**: 17738.
- Urayama, J., Norris, T. B., Singh, J. and Bhattacharya, P. (2001). Observation of phonon bottleneck in quantum dot electronic relaxation, *Phys. Rev. Lett.* **86**: 4930.
- Uskov, A. V., McInemey, J., Adler, F., Schweitzer, H. and Pilkuhn, M. H. (1998).

- Auger carrier capture kinetics in self-assembled quantum dot structures, *Appl. Phys. Lett.* **72**: 58.
- Vagov, A., Axt, V. M. and Kuhn, T. (2002). Electron-phonon dynamics in optically excited quantum dots: exact solution for multiple ultra short laser pulses, *Phys. Rev. B* **66**: 165312.
- Vallee, F. and Bogani, F. (1991). Coherent time-resolved investigations of LO-phonon dynamics in GaAs, *Phys. Rev. B* **43**: 12049.
- Vallee, F. (1994). Time-resolved investigations of coherent LO-phonon relaxation in III-V semiconductors, *Phys. Rev. B* **49**: 2460.
- Verzelen, O., Ferreira, R., Bastard, G., Inoshita, T. and Sakaki, H. (2002). Polaron effects in quantum dots, *Phys. Stat. Sol. (a)*, **190**: 213.
- Verzelen, O. (2002). Interaction électron-phonon LO dans les boîtes quantiques d'InAs/GaAs, PhD Thesis (Paris 2002) unpublished.
- Verzelen, O., Ferreira, R. and Bastard, G. (2000). Polaron lifetime and energy relaxation in semiconductor quantum dots, *Phys. Rev. B* **62**: 4809.
- Verzelen, O., Ferreira, R. and Bastard, G. (2002). Excitonic polarons in semiconductor quantum dots, *Phys. Rev. Lett.* **88**: 146803.
- Yu, P. Y. and Cardona, M. (1999), *Fundamentals of Semiconductors: Physics and materials properties*, Springer-Verlag, Berlin, Second Edition.
- Zibik, E. A., Wilson, L. R., Green, R. P., Wells, J. P. R., Phillips, P. J., Carder, D. A., Cockburn, J. W., Skolnick, M. S., Steer, M. J., Liu, H. Y. and Hopkinson, M. (2003). *ITQW 2003*. Evolene (Switzerland).

This page intentionally left blank

Chapter 6

Phonon-Induced Decoherence in Semiconductor Quantum Dots

V. M. Axt, A. Vagov,¹ B. Krummheuer, T. Kuhn,

*Institut für Festkörpertheorie, Westfälische-Wilhelms Universität,
Wilhelm-Klemm-Str. 10, 48149 Münster, Germany*

P. Machnikowski,² J. Krasnyj,³ L. Jacak

*Institute of Physics, Wrocław University of Technology,
Wybrzeże Wyspiańskiego 27, 50-370 Wrocław, Poland*

6.1 Introduction

As anticipated in the introductory part of this book (see Chapter 1), the understanding of how initially well defined quantum mechanical phase relations are lost is without any doubt of central importance for most device applications of semiconductor quantum dots (QDs). This holds equally well for proposed schemes where QDs are used as key ingredients of quantum information processing [Biolatti *et al.* (2000); Li *et al.* (2003)] or quantum encryption devices [Stevenson *et al.* (2002)], as well as for optoelectronic applications such as new types of lasers [Bimberg *et al.* (1998); Jacak *et al.* (2002a)] or single photon sources [Michler *et al.* (2000)]. While in most cases decoherence is a limiting factor for device operations it can also be a desirable feature, e.g. a rapid thermalization of excitonic occupations may be favorable for laser action [Bimberg *et al.* (1998); Jacak *et al.* (2002a)]. In general, decoherence takes place due to the cou-

¹current address: Physics Department, University of Antwerp, Belgium

²current address: Institut für Festkörpertheorie, Universität Münster, Germany

³current address: Institute of Mathematics, University of Opole, Poland

pling of the discrete dot excitations to the environment. There are many potential sources for such couplings including: interactions with phonons [Borri *et al.* (2001); Besombes *et al.* (2001); Krummheuer *et al.* (2002)] or with the radiation field [Bayer and Forchel (2002)] as well as charge fluctuations in the surrounding material [Itakura and Tokura (2003)]. It turns out that decoherence in QDs proceeds not as a simple exponential decay that can be fully characterized by some time constants. Instead, a non-trivial dynamical behavior is observed which is by itself of physical interest in addition to its importance for device applications. Typically, the polarization in self-assembled QDs is found to decay in two stages that, at not too high temperatures, are well separated, i.e., an initial rapid drop of the signal which is non-exponential and typically ends after a few picoseconds, is followed by an almost exponential decay on a much longer time scale. This gives rise to strongly non-Lorentzian shapes of both emission [Besombes *et al.* (2001)] and absorption [Krummheuer *et al.* (2002)] lines of single QDs consisting of a relatively sharp line superimposed on a broad background. Most clearly and quantitatively this behavior has been analyzed in four-wave-mixing (FWM) experiments on inhomogeneously broadened ensembles of QDs [Borri *et al.* (2001); Birkedal *et al.* (2001); Borri *et al.* (2003)]. For applications where decoherence is an obstacle, the long-time decay can be very favorable for device operations, having time constants of up to few hundreds of picoseconds at low temperatures. However, the rather short time scale for the initial decay can potentially introduce severe constraints; whether or not these constraints have actual consequences for specific applications depends in addition on the total amount by which the coherence is reduced. The latter changes with temperature and after the initial drop is completed there is still a partial coherence left in the system which can be of substantial size at low temperatures [Krummheuer *et al.* (2002); Vagov *et al.* (2003a)]. It turns out that this initial decoherence in strongly confined self-assembled QDs is almost entirely due to couplings to acoustic phonons [Vagov *et al.* (2004)].

Apart from FWM signals many other properties of coherent optical excitations of QDs are also affected by decoherence. In particular, Rabi oscillations, which are of key importance for most quantum computational protocols (see Chapter 7), exhibit a rather strong damping. This has been found in experiments on QD ensembles [Borri *et al.* (2002)] where the damping can be attributed at least partially to fluctuations of the dipole matrix elements. However, it has also been observed for signals from single

dots [Kamada *et al.* (2001); Stievater *et al.* (2001); Zrenner *et al.* (2002)]. Recent theoretical studies indicate that again the phonon-induced decoherence may yield a sizable contribution which sets an intrinsic limit to the fidelity of operations based on Rabi rotations [Förstner *et al.* (2003); Machnikowski and Jacak (2004b)].

Also in extended semiconductors phonons provide for important decoherence channels. In these systems the decoherence is mainly caused by relaxation processes where the electronic energies are redistributed by phonon-induced transitions between different electronic levels. In QDs such processes take place if the charges are initially promoted to intra-band excited states [Jacak *et al.* (2002b); Jacak *et al.* (2003a)] but are largely suppressed for electrons in the ground state strongly confined within a QD. Consequently, phonon assisted transitions that transfer an electron from one level to another are of minor importance for dots in the strong electronic confinement limit provided the temperature is not too high. But even if phonon-induced electronic transitions are completely neglected, phonons can still cause substantial decoherence, namely by carrier-phonon interactions that do not change the carrier occupations and therefore do not lead to electronic relaxation. Such processes are commonly referred to as *pure dephasing* [Krummheuer *et al.* (2002); Besombes *et al.* (2001)]. It turns out that, in marked contrast to the behavior of extended semiconductors, phonon-induced pure dephasing can become a dominant decoherence mechanism for strongly confined QDs.

In this chapter we shall explore the implications of pure dephasing for the dynamics of optically excited QDs. The chapter is organized as follows: after specifying the pertinent model we will explain how analytical expressions can be obtained for all elements of the electronic and phononic density matrix provided the excitation consists of a sequence of *ultrafast* pulses. Within this ultrashort pulse limit we then discuss different aspects of the combined dynamics of photoexcited carriers and phonons ranging from the initial decay of the linear as well as the FWM polarization via the coherent control of carrier densities to the emission of phonon-wave packets. A comparison with recent FWM experiments [Vagov *et al.* (2004)] reveals that phonon-induced pure dephasing is indeed the dominant mechanism for the initial decay. Interestingly, the measurements confirm a highly unusual non-monotonous temperature dependence of the initial decay time which has been predicted theoretically on the basis of our pure-dephasing model [Vagov *et al.* (2003a)]. Analytical solutions are, however, only available in

the ultra-short pulse limit. In order to deal with issues that do crucially depend on the pulse lengths or on the spectral selectivity of the excitation, different approaches have to be used. We shall present pulse length dependent results concerning the damping of Rabi oscillations obtained by a perturbative treatment of the carrier-phonon interaction. Furthermore, competing dephasing mechanisms depend differently on the pulse length. It is shown that by adjusting the spectral properties of the exciting pulses an optimal trade-off between competing mechanisms can be made such that the fidelity of quantum computational operations is maximized.

6.2 Model for Phonon-Induced Pure Dephasing

Our theoretical discussion is based on the model for phonon-induced pure dephasing of optically excited QDs presented in [Krummheuer *et al.* (2002); Besombes *et al.* (2001)]. Assuming that the QDs are in the strong confinement limit, the electronic degrees of freedom are represented by a two-level system interacting with laser light and linearly coupled to phonons. The corresponding Hamiltonian is given by

$$\begin{aligned} H = & \hbar\Omega c^\dagger c - (MEc^\dagger d^\dagger + M^*E^*dc) + \sum_{\xi} \hbar\omega_{\xi} b_{\xi}^\dagger b_{\xi} \\ & + \sum_{\xi} \hbar \left[(g_{\xi}^e b_{\xi} + g_{\xi}^{e*} b_{\xi}^\dagger) c^\dagger c - (g_{\xi}^h b_{\xi} + g_{\xi}^{h*} b_{\xi}^\dagger) d^\dagger d \right]. \end{aligned} \quad (6.1)$$

Here, c, d, b_{ξ} are destruction operators for electrons, holes, and phonons, respectively, while $c^\dagger, d^\dagger, b_{\xi}^\dagger$ are the corresponding creation operators and ξ is a mode index. Many of our general results, in particular the analytical formulae in the short-pulse limit [Vagov *et al.* (2002)], can be derived for any type of phonon modes. However, in order to be specific, we shall concentrate in our later numerical studies on bulk phonons. This assumption is valid provided that the lattice properties are not much affected by the electronic confinement and thus confined phonon modes can be disregarded. Then the combined index $\xi = (j, \mathbf{q})$ comprises a phonon wave vector \mathbf{q} and a branch index that can stand for $j = \text{LO}, \text{LA}, \text{TA}$ corresponding to longitudinal optical (LO), longitudinal acoustic (LA) or transverse acoustic (TA) phonon modes, respectively. $g_{\xi}^{e,h}$ are phonon coupling constants: LO phonons primarily interact with carriers via the Fröhlich coupling, for LA phonons usually the deformation potential coupling is most important but for materials without inversion symmetry also piezo-electric interactions have to be

taken into account [Krummheuer *et al.* (2002); Krummheuer *et al.* (2004b); Krummheuer *et al.* (2004a)]. The latter also provide the dominant coupling for TA modes. M is the component of the dipole matrix element in the direction of the laser field polarization and $E(t)$ denotes the amplitude of the laser field. $\hbar\Omega$ is the energy of an electron occupying a conduction band dot state. We have chosen the energy of the hole to define the zero of energy. It should be noted that if the exciton binding energy is smaller than the separation of the single particle energies the mixing of different states by the Coulomb interaction can be neglected and therefore excitonic effects can be accounted for in our model simply by lowering the gap by an amount given by the electron-hole Coulomb matrix element [Schmitt-Rink *et al.* (1987)]. If Coulomb induced mixing occurs but the energies of neighboring excitonic levels are still well separated then a Hamiltonian of the form Eq. (6.1) can still be used; but in addition to interpreting $\hbar\Omega$ as an exciton energy one has to use excitonic wave functions for the evaluation of the matrix elements $g_{\xi}^{e,h}$ and M [Krummheuer *et al.* (2004b); Krummheuer *et al.* (2004a); Jacak *et al.* (2003b)]. For all the results presented here standard InAs/GaAs system parameters [see e.g. [Krummheuer *et al.* (2002); Axt *et al.* (2003)]] have been taken.

The above defined model contains two well-studied limiting cases: without the coupling to the light field it reduces to the *independent Boson model* which has been applied in the past to quite different physical situations such as the theory of F-centers or the phonon-broadened density of electronic states for different types of impurities [Huang and Rhys (1950); Duke and Mahan (1965)]. When instead the carrier-light coupling is retained and the carrier-phonon interactions are neglected then the model generates the *optical Bloch equations* which are applied extensively for optical studies of atoms. Formally, the Hamiltonian has the form of a spin-Boson model, but with a time dependent coupling caused by the time dependence of the laser amplitude. So far no general solution is available representing the dynamics defined by the Hamiltonian Eq. (6.1) for arbitrarily shaped pulses. This has only been achieved in the limit of ultrafast excitation, i.e. for an excitation by a sequence of δ -shaped pulses [Vagov *et al.* (2002); Vagov *et al.* (2003a)]. In the next section we shall first present results obtained in this limit and discuss finite pulse excitations afterwards in a separate section.

6.3 Analytical Results for Excitations with Ultrafast Pulses

In order to derive analytical results the dynamics of our model has been represented in [Vagov *et al.* (2002)] in terms of three generating functions for phonon-assisted density matrices defined by

$$Y(\alpha_\xi, \beta_\xi, t) = \left\langle d^\dagger c e^{\sum_\xi \alpha_\xi b_\xi^\dagger} e^{\sum_\xi \beta_\xi b_\xi} \right\rangle, \quad (6.2)$$

$$C(\alpha_\xi, \beta_\xi, t) = \left\langle c^\dagger c e^{\sum_\xi \alpha_\xi b_\xi^\dagger} e^{\sum_\xi \beta_\xi b_\xi} \right\rangle, \quad (6.3)$$

$$F(\alpha_\xi, \beta_\xi, t) = \left\langle e^{\sum_\xi \alpha_\xi b_\xi^\dagger} e^{\sum_\xi \beta_\xi b_\xi} \right\rangle, \quad (6.4)$$

where for each phonon mode two arbitrary parameters α_ξ, β_ξ have been introduced. The property of being a generating function means that once the dependence of Y , C and F on α_ξ, β_ξ has been determined, all elements of the electronic or phononic density matrix can be obtained by evaluating the generating functions or their derivatives with respect to the parameters α_ξ, β_ξ at $\alpha_\xi = \beta_\xi = 0$. In particular, the optical polarization induced in the dot is proportional to $Y(\alpha_\xi = \beta_\xi = 0, t)$ while the electronic occupation of the lowest dot excitation is given by $C(\alpha_\xi = \beta_\xi = 0, t)$. Thus, Y and C can be regarded as exponentially phonon-assisted generalizations of the standard variables used to represent the dynamics of a two-level system, namely: the transition density and the occupation of the upper level. The generating function F contains in addition the information on the lattice degrees of freedom, including non-equilibrium phonon occupations and coherent phonons. The most important property of the generating functions is, however, that by straightforward setting up of the Heisenberg equations for corresponding operators a closed set of equations of motion is obtained for Y, C and F without invoking any approximations [Vagov *et al.* (2002)]. Thus, these non-linear coupled partial differential equations completely represent the dynamics of our model without further restrictions. Recently, we have solved the equations for an excitation by an arbitrary sequence of ultrafast (δ -shaped) pulses [Vagov *et al.* (2002)]. It should be stressed that this solution is non-perturbative with respect to both the carrier-phonon and the carrier-light coupling and is therefore not limited to low excitation densities or weak phonon couplings. Of course, the mathematical idealization of δ -pulses restricts the applicability of the results. In practice, the theory applies to pulses that fulfill two requirements: (a) the pulses should be spectrally selective such that essentially only the two-level transition is

excited. This sets a lower limit to the pulse length; (b) after the selectivity of the excitation has been accounted for by retaining only two electronic levels in the model, the δ -pulse solution is applicable provided the pulses are much shorter than the typical time scale for the evolution of the phonon degrees of freedom. As discussed in detail in [Vagov *et al.* (2002)] there is usually a sufficiently large pulse length window where both requirements are simultaneously fulfilled.

In the simplest special case the dot is excited by a single δ -pulse arriving at time $t = 0$ with pulse area A and optical phase φ . In order to present the solution in a compact form it is useful to set $Y(\alpha_\xi, t) \equiv Y(-\alpha_\xi^*, \alpha_\xi, t)$ and analogous definitions for $C(\alpha_\xi, t)$ and $F(\alpha_\xi, t)$ (the full dependence on α_ξ and β_ξ can be recovered when α_ξ and α_ξ^* are considered as independent arguments). With these notations the solution reads:

$$\begin{aligned} Y(\alpha_\xi, t) &= \frac{i\theta(t)}{2} \sin(A) \\ &\times e^{\left\{ -i\bar{\Omega}t + i\varphi + \sum_\xi [\gamma_\xi^*(\alpha_\xi + \gamma_\xi)(e^{-i\omega_\xi t} - 1) - N_\xi(\alpha_\xi + \gamma_\xi)e^{-i\omega_\xi t} - \gamma_\xi|^2] \right\}}, \\ C(\alpha_\xi, t) &= \theta(t) \sin^2\left(\frac{A}{2}\right) e^{\sum_\xi \left\{ 2i\text{Im}[\gamma_\xi^*\alpha_\xi(e^{-i\omega_\xi t} - 1)] - N_\xi|\alpha_\xi|^2 \right\}}, \\ F(\alpha_\xi, t) &= e^{-\sum_\xi N_\xi|\alpha_\xi|^2} \left\{ 1 + \theta(t) \sin^2\left(\frac{A}{2}\right) \left[e^{2i\text{Im}[\sum_\xi \gamma_\xi^*\alpha_\xi(e^{-i\omega_\xi t} - 1)]} - 1 \right] \right\}, \end{aligned} \quad (6.5)$$

where $\gamma_\xi \equiv (g_\xi^e - g_\xi^h)/\omega_\xi$, N_ξ is the thermal occupation of the phonon mode ξ and $\bar{\Omega} \equiv \Omega - \sum_\xi |\gamma_\xi|^2 \omega_\xi$ is the polaron shifted optical transition frequency. Clearly, all generating functions and therefore all components of the density matrix oscillate as a function of the pulse area A . This is the signature of Rabi-oscillations in the ultrafast pulse limit. Obviously these oscillations are undamped, indicating that the phonon coupling can yield a damping of the Rabi oscillations only for finite pulse lengths (see Section 6.4.1).

6.3.1 Linear single-dot spectra

From the above formulae it is easy to extract the linear response. It should be noted that in the linear regime the solution to a pulse of general shape can be obtained from the δ -pulse solution by a simple convolution. Thus, the short-pulse limit does not impose any restrictions here. As shown in [Krummheuer *et al.* (2002)] the linear polarization $P(t)$ obtained from our model typically decreases with time only towards some plateau value and

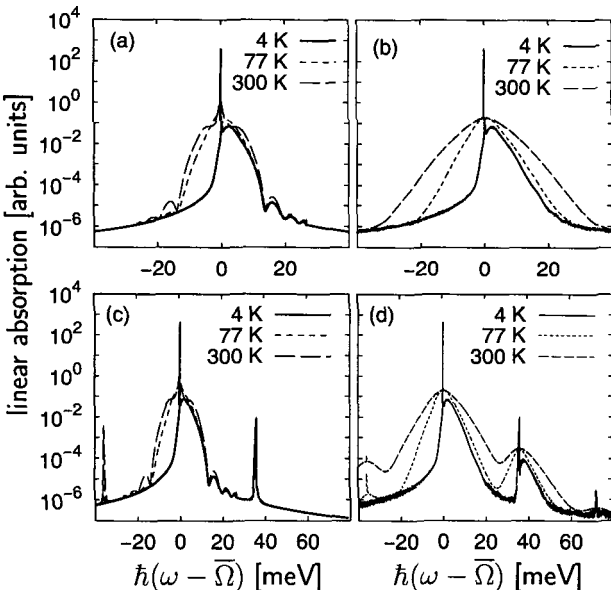


Fig. 6.1 Linear absorption spectra for a small GaAs quantum dot: (a), (c) correlation expansion accounting only for single phonon processes; (b), (d) exact results. The upper parts are obtained keeping only the deformation potential coupling to LA phonons while all couplings to all phonon modes are accounted for in the lower parts.

does not reach zero asymptotically. In fact, by analyzing the analytical result it has been shown that the asymptotics of $P(t)$ is determined by the behavior of γ_ξ in the vicinity of $\mathbf{q} = 0$. It turns out that an asymptotic exponential decay of $P(t)$ would require a higher divergence of γ_ξ for $\mathbf{q} \rightarrow 0$ than is realized for all common coupling mechanisms. The finite asymptotics of $P(t)$ reflects the fact that pure dephasing is unable to produce the long-time decay observed in experiments while it reproduces the rapid initial decay.

Linear absorption spectra are proportional to the imaginary part of the Fourier transform of $P(t)$. We have included the long-time decay by multiplying our model polarization by a factor e^{-t/t_0} with $t_0 = 500$ ps which is of the order of the radiative lifetime. The resulting spectra are plotted in Figure 6.1 for three temperatures. For these calculations we have used a dot model described in detail in [Krummheuer *et al.* (2002)] with a harmonic confinement potential in the $x-y$ -plane and infinite barriers in z -direction. The extension of the dot in the plane as measured by the radius where the electron density is reduced to half its maximum

value has been set equal to the width of the potential well in z -direction. The phonon dispersions have been parameterized in the form valid for a standard diatomic linear chain model adjusted to the phonon dispersion relation given in the literature. It turns out, however, that the extension of the carrier wave functions in momentum space restricts the effectively coupled phonon modes to a region near the center of the Brillouin zone where – without losing much accuracy – linear dispersions can be assumed for acoustic phonons while optical phonons are essentially dispersionless. The right hand part of Figure 6.1 shows the result of the full model while the results shown on the left hand side have been obtained by using the leading order correlation expansion for phonon assisted variables [Rossi and Kuhn (2002)], i.e. a commonly used approximation that keeps only single phonon processes. The upper panels are calculated accounting only for the deformation potential coupling while all phonon couplings are taken into account in the lower panels. The spectrum comprises in all cases a narrow zero-phonon line broadened only by the radiative lifetime superimposed on a broad non-Lorentzian background provided by acoustic phonons. In Figure 6.1(d), where all phonons are fully included, this pattern is repeated at the positions of the LO phonon sidebands. The background spectra change from a strongly asymmetric shape at low temperatures towards an essentially symmetric form at room temperature, which, however, is still not well represented by a Lorentzian. The non-Lorentzian shape clearly reflects the non-exponential decay in the time domain. The comparison between the full theory and the results of the correlation expansion reveals the role of multi-phonon processes, which are missing in the latter case. The correlation expansion obviously reproduces the width of the full calculation only at low temperatures; at elevated temperatures multi-phonon processes become important and contribute significantly to the linewidth. Furthermore, sharp structures show up in the approximate spectra which are absent in the exact result. These structures occur at energies where a linear absorption with the assistance of only a single phonon is suppressed by unfavorable form factors. The full theory does not exhibit these features, because multi-phonon contributions compensate the suppression. Interestingly, in the correlation expansion the broad background is missing at the position of the LO phonon sideband. This can be understood by noting that one LO phonon is needed to produce the sideband and the background is then produced by additional acoustic phonon couplings. It is therefore a multi-phonon effect where a LO phonon and further acoustic phonons are involved. Comparing the upper with the lower parts of Figure 6.1 in the

vicinity of the zero-phonon line essentially the same spectra are found for the full model and when only the deformation potential is accounted for. Thus, apart from providing the LO sidebands, LO phonons have not much influence on the spectral shape and therefore are of minor importance for the decoherence.

6.3.2 *The initial decay of four-wave-mixing signals*

Non-Lorentzian lineshapes have been observed in FWM spectra from inhomogeneously broadened ensembles of QDs [Borri *et al.* (2001)]. These measurements are in good qualitative agreement with the linear response discussed in the previous subsection. However, a quantitative description of non-linear signals – such as the FWM emission – in general requires the direct modeling of the actual signal [Vagov *et al.* (2003a); Axt *et al.* (2003)]. In particular, there is no simple relation between the linear response of a single dot and the FWM amplitude emitted from a strongly inhomogeneously broadened dot ensemble [Vagov *et al.* (2003a)]. This finding is in sharp contrast to the standard textbook result valid for a dephasing described by a single decay time T_2 , which states that the latter should be proportional to the absolute square of the former. However, for the pure dephasing model there are substantial quantitative differences between these quantities, demonstrating that pure dephasing provides for a decoherence mechanism that is qualitatively different from phenomenological Markovian decay models.

For single dot FWM signals, on the other hand, there is a simple relation to the linear response: the two-pulse FWM signal obtained for zero pulse delay is proportional to the linear signal. These and many more generic properties of single dot FWM signals have been derived from our analytical formulae in [Vagov *et al.* (2003a)]. However, FWM signals of single QDs are still hard to measure, although there is considerable progress concerning the detection of coherent non-linear optical signals from single dots [Guenther *et al.* (2002); Stievater *et al.* (2002); Li *et al.* (2003)]. Therefore, experiments performed on dot ensembles are better suited for comparing the predictions of the pure dephasing theory with measured data. In the following we shall discuss in particular the predictions of the pure dephasing theory concerning the initial decoherence as monitored by two-pulse FWM signals. In a recent study the theory has been directly compared with corresponding experiments [Vagov *et al.* (2004)]. Such investigations were expected to provide a decisive test for the pure

dephasing theory, because on the basis of this theory an unusual behavior was expected [Vagov *et al.* (2003a); Axt *et al.* (2003)] namely, the initial decay time should at low temperatures *increase* with rising temperature, while the usual decrease of the decoherence time with increasing temperatures should be observed only for higher temperatures. This prediction is highly unusual especially in view of the fact that from the existing experiments [Borri *et al.* (2001)] it was already known that the long-time decay follows – in agreement with corresponding theories [Takagahara (1999); Uskov *et al.* (2000)] – the intuitive expectation, i.e. the decay time monotonously decreases with rising temperature. Experimentally testing such an unusual prediction thus provides a criterion to decide whether the physical nature of the initial decay mechanism is correctly assigned to pure dephasing.

For strongly inhomogeneously broadened dot ensembles the FWM signal is a sharp photon echo in real time [Borri *et al.* (2001)]. In such a case, the information on the initial decoherence is most conveniently extracted from the time-integrated FWM amplitudes. After taking the ensemble average of our analytical single dot results and performing the time integration we obtain for the measured signal the simple final expression [Vagov *et al.* (2003a)]:

$$P_{\text{FWM}} = f \exp \left[-8 \sum_{\xi} |\gamma_{\xi}|^2 (1 + 2N_{\xi}) \sin^4 \left(\frac{\omega_{\xi}\tau}{2} \right) \right], \quad (6.6)$$

where $\tau > 0$ is the relative time delay between the exciting pulses. The prefactor f does not depend on τ and the temperature T . It contains the information on the pulse area dependence which is not important for the present discussion. As precise information about details of the QD structure is usually not available we assume a parabolic non-isotropic confinement potential, rotationally symmetric around the growth direction axis z . Moreover, from the discussion of the analytic properties of the solution in [Vagov *et al.* (2003a)] and also from our numerical experience, we have learned that the resulting signals are not very sensitive to the detailed form of the confinement potential, e.g. parabolic or box shape. Typically, the overall extension of the carrier wave functions is the most important characteristic of the dot, because it determines the region in the Brillouin zone where phonons are effectively coupled. The assumption of a parabolic confinement for the present calculations implies that the ground state wave function is a Gaussian with two parameters: the lateral diameter $a_{e(h)}$ and the full z -width $b_{e(h)}$ where the

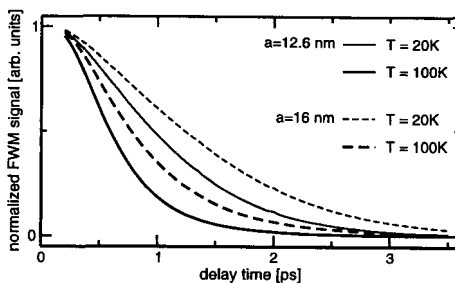


Fig. 6.2 Normalized time-integrated FWM amplitudes plotted vs. delay τ at $T = 20$ K and 100 K for size parameters $a = 12.6$ nm, $b = 2.4$ nm and $a = 16$ nm, $b = 2.4$ nm.

electron (hole) density has decreased by $1/e$ from its peak value. When in addition equal potential shapes are assumed for electrons and holes one can express the localization ratios a_h/a_e and b_h/b_e in terms of the electron/hole mass ratios for the in-plane and growth direction masses. This procedure leaves $a \equiv a_e$ and $b \equiv b_e$ as the only free sample dependent parameters of the theory since all other material parameters entering our formulae are available from the literature [Krummheuer *et al.* (2002); Axt *et al.* (2003)].

In Figure 6.2 we have displayed FWM signals calculated according to Eq. (6.6) for two temperatures as a function of the delay time. In order to concentrate on the initial decay properties separated from the long time behavior we have normalized the results by subtracting the asymptotic plateau value and dividing by the signal maximum. The curves show a smooth non-exponential decay on a picosecond time scale. These numerical FWM traces have been compared in [Vagov *et al.* (2004)] with measurements performed on two self-assembled InGaAs samples. The two samples differed essentially only in their in-plane average dot sizes. Taking the size parameters a and b as the only fitting parameters good quantitative agreement was found with the experimental results for a, b values that were well consistent with other independent estimates. In particular, it was shown that the characteristic non-exponential delay time decay of the FWM signals is well represented by the analytical formula Eq. (6.6).

In order to quantify the amount of coherence that is lost in the initial phase before the long-time decay becomes effective, we have determined the fraction by which the signal has dropped after the initial decay is completed. In Figure 6.3(a) we have plotted the fractional drop vs. temperature obtained from Eq. (6.6). We find that the fraction rises

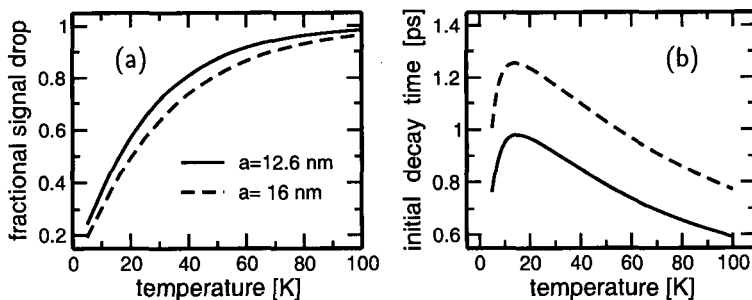


Fig. 6.3 Temperature dependence of: (a) fractional signal drop, (b) initial decoherence time, calculated with the same parameters as in Figure 6.2.

monotonously with temperature indicating that pure dephasing leads to stronger decoherence for higher temperatures [Besombes *et al.* (2001); Vagov *et al.* (2002)]. For both dot sizes roughly 25% of the coherence is lost at low temperatures while at about 100 K the coherence is lost almost completely. These numbers are again in quantitative agreement with the measurements [Vagov *et al.* (2004)]. The precise numerical values for the amount of lost coherence depend, however, strongly on the material as well as on geometrical factors such as the dot sizes [Krummheuer *et al.* (2004b); Krummheuer *et al.* (2004a)].

A measure for the time scale on which the initial decoherence takes place is the delay time τ_{initial} at which the normalized signal (see Figure 6.2) has dropped to half of its initial amplitude. The extracted τ_{initial} are plotted in Figure 6.3(a) vs. temperature. The figure confirms the expected tendency of a faster decoherence for smaller extension of the exciton wavefunction. The most striking feature is however that τ_{initial} clearly is a *non-monotonous* function of T , increasing at low and decreasing at higher temperatures. Its maximum is reached at slightly different T values for different samples. Even this unusual feature has been quantitatively confirmed in the experiments [Vagov *et al.* (2004)] indicating that the initial decoherence is indeed dominated by pure dephasing. The observed non-monotonous temperature dependence of τ_{initial} can be explained as follows: At $T = 0$ the effective phonon coupling, i.e. the angle average of $q^2|\gamma_q|^2(1 + 2N_q)$, peaks at a finite q value [Vagov *et al.* (2003a)]. With increasing T the peak broadens and moves towards $q = 0$ due to the singularity of the Bose distribution N_q . Thus, at low temperatures the corresponding phonon-sidebands give ultrafast signals the character of an overdamped oscillation. In principle, even a smooth continuum of acoustic phonons may result in well

resolved oscillations for certain material parameters [Vagov *et al.* (2003a); Axt *et al.* (2003)], but for typical values the damping is so strong that the oscillation is visible only for the first half period. In such a case, the effective initial decay time is essentially determined by the period of the oscillation which increases with rising temperature, leading to the unusual rise of τ_{initial} at low T values [Vagov *et al.* (2003a)]. The high temperature behavior is dominated by the effective damping which reflects the total width of the coupled phonon sidebands. The latter increases with temperature, resulting in the observed decrease of τ_{initial} [Li and Arakawa (1999); Vagov *et al.* (2003a)]. Finally, it is worth noting that essential features of the curves cannot be changed by variations of a or b . In particular, the non-monotonous T -dependence of τ_{initial} is always found [Vagov *et al.* (2004)]. Moreover, the parameters have little impact on the shape of the curves and the position of the maximum. The predominant effect of size variations is a shift of the overall time scale.

6.3.3 *Impact of pure dephasing on electronic and phononic occupations*

The signals discussed so far are related to the optical emission and absorption and thus test only properties of the transition density Y defined in Eq. (6.2). However, the phonon-induced decoherence also leaves its traces in the occupation numbers of electrons and phonons. Let us start with the discussion of the electronic densities. At first sight it may seem contradictory that pure dephasing should affect electronic densities, because the corresponding interaction processes by definition do not change the carrier occupation. However, pure dephasing does change phase relations and therefore it affects the way carriers are generated by a laser pulse. It also can restrict the possibilities of removing carriers from the conduction band by photon induced transitions to the valence band. Thus, the combined action of the pure dephasing type carrier-phonon coupling and the laser field can lead to pronounced signatures of decoherence reflected in the carrier occupation. This is very directly seen from coherent control studies, where two short phase-locked laser pulses are used to control the carrier density. The resulting electron density after the second pulse can be easily calculated for our model by using our analytical solutions for a two-pulse excitation [Vagov *et al.* (2002)]. The solution exhibits the well known coherent control oscillations of the carrier density, where changes of the delay τ of the order of the optical period, i.e., on a femtosecond time

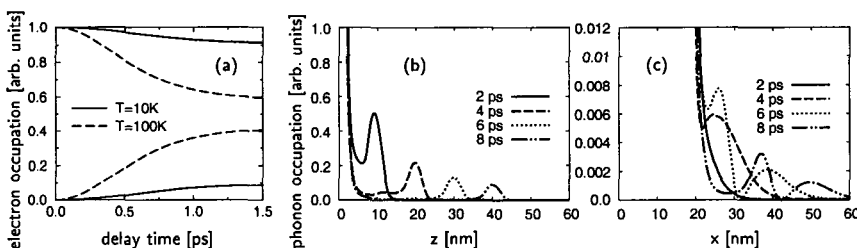


Fig. 6.4 (a) Upper and lower envelopes of the coherent control oscillations performed by the electron occupation in response to two phase-locked ultrafast pulses plotted vs the pulse delay. The pulse areas of both pulses are taken equal $A_1 = A_2 = \pi/2$. (b), (c) spatial non-equilibrium phonon distributions for selected times after a single pulse excitation of a GaAs dot with an external static electric field applied in x -direction: plotted are distributions along the z -axis (b) and x axis (c).

scale, lead to large changes of the carrier density. Let us consider in the following the special case of excitation by two $\pi/2$ -pulses. The first pulse then creates a linear superposition with equal probabilities of ground and excited states. Without phonons, after the second pulse the dot could reach complete excitation or, if the control is destructive, the carriers generated by the first pulse could be completely removed by the second. Figure 6.4(a) shows for two temperatures the upper and lower envelope of the coherent control oscillations obtained within our pure dephasing model. Clearly, the ability to remove the carriers with the second pulse is limited because of the interaction of the carriers with phonons. Upper and lower bounds of the oscillations come closer to each other for higher temperatures and longer delay times. Obviously, the quantum mechanical phase relations required for the destructive or constructive interference that leads to the control of the carrier density are disturbed by the phonons. Thus, the changes of the coherent control envelopes can be regarded as a direct measure for the phonon-induced decoherence.

There is also a very direct connection between decoherence and changes in the phonon system, as the total production of non-thermal phonons turns out to be governed by the same function that determines the decoherence of the linear optical polarization [Vagov *et al.* (2002)]. In fact the optical excitation of a QD affects the phonon dynamics in many ways, e.g., the dot becomes a source for coherent phonons, i.e., expectation values of the phonon amplitudes $\langle b_\xi \rangle$ are built up resulting in finite lattice displacements and corresponding local changes of the relative volume [Vagov

et al. (2003b)]. In addition, non-equilibrium phonon occupations are also generated. The latter contribute to the phonon-induced heat transport that can be detected by bolometric measurements [Hawker *et al.* (1999)]. A detailed analysis of dynamical changes in the spatial distribution of non-thermal phonons reveals [Vagov *et al.* (2002); Krummheuer *et al.* (2004b); Jacak *et al.* (2003b)] that the the spatial phonon distribution obtained after optical excitation with a single ultrafast pulse consists of two distinct parts: (i) an occupation localized in the region of the dot and (ii) a propagating phonon wave packet leaving the dot. Part (i) corresponds to a stable polaron formed in the QD, typically on a ps time scale. Roughly, this is the time needed for the wave packet to leave the dot. After the packet has left, a permanent lattice distortion remains in the dot vicinity that does not change with time. It should be noted that for the emission of the phonon wave packet no electronic relaxation is needed: the energy that is transported by the phonon wave is provided by the polaron formation energy. Figures 6.4(b) and (c) show snapshots of phonon wave packets emitted from a GaAs QD with parabolic confinement in $x-y$ -direction and a deep box-shaped potential in growth direction. In addition, an external static electric field was applied in x -direction. The presence of static fields has been found to modify the decoherence no matter whether the field is externally applied [Krummheuer *et al.* (2002)] or provided by internal fields as, e.g., in GaN dots [Krummheuer *et al.* (2004a)]. The field induced charge separation in the dot strongly enhances polar electron-phonon coupling mechanisms, in particular the piezo-electric coupling can become the dominant coupling mechanism for acoustic phonons. For the GaN dots studied in [Krummheuer *et al.* (2004b)] the piezo-electric coupling was strong enough that phonon wave packets traveling with the sound velocities of the LA and TA modes could be separately resolved (note: the TA modes do not couple via the deformation potential). In contrast, for the GaAs results shown in Figure 6.4 essentially only wave packets propagating with the LA velocity are seen. Interestingly, there is only a single phonon pulse emitted in growth direction [cf. Figure 6.4(b)] while two pulses emerge along the axis of the external field [cf. Figure 6.4(c)]. The double phonon pulse is generated because separate wave packets are emitted due to the couplings to electrons and holes. The spatial separation of the corresponding phonon pulses directly reflects the field induced average distance between electrons and holes.

6.4 Influences of Temporal and Spectral Properties of the Laser Excitation on the Decoherence

Let us now turn to the case of excitation by laser pulses with a finite duration. In this case no exact analytical solution of the model is known and one has to rely on a perturbative treatment of electron-phonon interaction. For the examples studied in this section we will apply the leading order (Born) approximation. The main difference compared to the ultrashort pulse limit is the fact that now the decoherence during the excitation process plays an important role. We will start by analyzing the phonon-induced damping of Rabi oscillations and then discuss the combined impact of pure dephasing and radiative decay on gate operations of qubits realized by excitonic excitations. In the latter case it is shown that by adjusting the spectral properties of the laser an optimized trade-off between these competing decoherence channels can be made.

6.4.1 *Phonon-induced damping of Rabi oscillations in quantum dots*

The experimental observation of Rabi oscillations in QDs [Kamada *et al.* (2001); Stievater *et al.* (2001); Zrenner *et al.* (2002); Borri *et al.* (2002)] is one of the first essential steps towards achieving the full coherent control over these systems. In all existing measurements of Rabi oscillations a strong damping has been observed, especially for stronger pulses. In principle, this might also be explained by experimental conditions or environmental perturbation, e.g. scattering by weakly localized excitons around an interface fluctuation QD (further confirmed by increasing decay for stronger pulses) [Stievater *et al.* (2001)], tunneling to leads in the photodiode structure (on ~ 10 ps time scale) [Zrenner *et al.* (2002)], or dipole moment distribution in the QD ensemble [Borri *et al.* (2001)]. One might thus believe that all the perturbations come from sources that may be removed or minimized by technology improvement and by optimizing the experimental conditions and hence produce no fundamental obstacle to arbitrarily perfect quantum control over the excitonic states. However, in any case the QDs are inherently coupled to the surrounding crystal lattice. As already shown in the preceding sections of this chapter, various decoherence effects observed in the experiment may be quantitatively accounted for by invoking the pure dephasing model described by Eq. (6.1), where without static fields, the deformation potential coupling to LA modes

dominates the decoherence in InAs/GaAs-type systems for the time scales relevant for the present discussion [Krummheuer *et al.* (2002)].

We shall assume that the electronic part of the system is initially in its ground state ϱ_0 (no exciton) while the lattice modes are in thermal equilibrium. In order to describe the phonon-related damping of Rabi oscillations it is necessary to deal with finite pulse solutions that account non-perturbatively for the carrier-light interaction. To this end we make use of an expansion of the system evolution operator in Born approximation where only the carrier-phonon interaction is treated as a perturbation. The lattice degrees of freedom are then traced out leading to the reduced density matrix for the carrier subsystem, which contains all the information accessible by optical methods (see [Alicki *et al.* (2002); Machnikowski and Jacak (2004a)]). The resulting reduced density matrix at time t may be written as $\varrho(t) = U(t)(\varrho_0 + \varrho_1)U^\dagger(t)$, where $U(t)$ is the evolution operator for the carrier system coupled to laser light but unperturbed by phonons and ϱ_1 describes the phonon-induced perturbation. The matrix elements of the latter, in the basis of empty dot ($|0\rangle$) and one exciton ($|1\rangle$) states, may be written as

$$\langle m|\varrho_1|n\rangle = - \int_{-\infty}^{\infty} d\omega \frac{R(\omega)}{\omega^2} S_{mn}(\omega). \quad (6.7)$$

In addition, at the same order of perturbation theory corrections to the unitary time evolution of the reduced density matrix appear describing energy shifts and renormalizations of the light coupling which lead, e.g. to an intensity dependence of the observed Rabi frequency [Förstner *et al.* (2003)]. Being unitary, they do not contribute to the damping of Rabi rotations and therefore they will be disregarded in the following. The function $R(\omega)$ is the spectral density of the reservoir, fully characterizing the lattice properties at this order of perturbation treatment. It depends on the material parameters and QD size via the coupling constants (see [Machnikowski and Jacak (2004a)] for explicit formulae). The functions $S_{mn}(\omega)$ contain the complete information on the optically controlled carrier dynamics. If we assume that the final state is measured after a time which is long compared to the phonon oscillation periods, they may be written as

$$\begin{aligned} S_{00}(\omega) &= -S_{11} = \frac{1}{4} [\sin^2 \alpha + |K_s(\omega)|^2], \\ S_{01}(\omega) &= S_{10}^* = \frac{1}{8} [\sin 2\alpha + 2\text{Re}K_s(\omega)K_c^*(\omega)], \end{aligned}$$

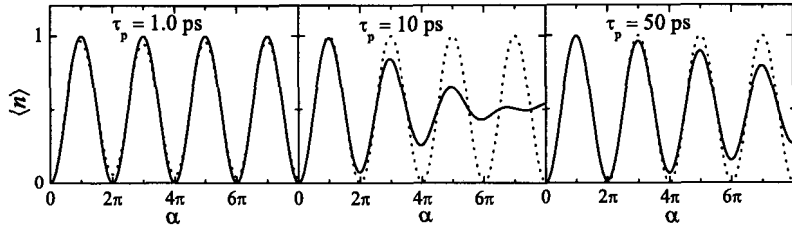


Fig. 6.5 Rabi oscillations calculated for $T = 10$ K and various fixed pulse durations τ_p (full-width-half-maximum of the pulse envelope) as indicated, plotted vs the pulse-area (α is rotation angle on the Bloch sphere). Dotted line show the unperturbed oscillations.

with

$$K_s(\omega) = \int_{-\infty}^{\infty} d\tau e^{i\omega\tau} \frac{d}{d\tau} \sin F(\tau), \quad K_c(\omega) = \int_{-\infty}^{\infty} d\tau e^{i\omega\tau} \frac{d}{d\tau} \cos F(\tau), \quad (6.8)$$

where $F(t)$ is the rotation (on the Bloch sphere) performed on the exciton state up to time t and α is the total angle of rotation.

The quantity of interest is the final dot occupation, $\langle n \rangle = \langle 1 | \rho(\infty) | 1 \rangle$, induced by the control pulse. In a typical experimental situation the pulse has a fixed length but variable amplitude. The results of the theoretical calculations for Gaussian pulses are shown in Figure 6.5. The oscillations are almost perfect for very short pulses (~ 1 ps), then lose their quality for longer pulse durations (~ 10 ps). Although this might be expected from any simple decoherence model, the striking feature is that the effect dramatically grows for higher oscillations, despite the fact that the whole process has exactly constant duration. Even more surprising is the improvement of the quality of oscillations for long pulses (~ 50 ps) where, in addition, the first oscillation is nearly perfect.

This non-monotonous pulse-length dependence of the damping may be understood by invoking a semi-classical picture of resonant carrier-lattice interaction. While in the linear limit the system response depends only on the spectral decomposition of the pulse, the situation is different when a strong pulse induces an oscillating charge distribution in the system. Classically, this would act as a driving force for the lattice dynamics. If the induced carrier dynamics is much faster than phonon oscillations the lattice has no time to react until the optical excitation is finished. The subsequent dynamics will lead to exciton dressing, accompanied by emission of phonon packets, and will partly destroy coherence of superposition states [Borri *et al.* (2001); Vagov *et al.* (2002); Jacak *et al.* (2003b)] but cannot

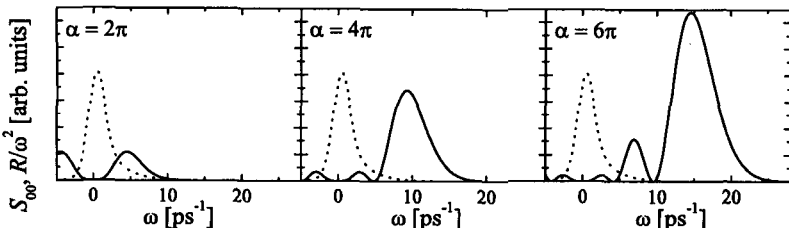


Fig. 6.6 The non-linear pulse spectrum $S_{00}(\omega)$ (solid) for the pulse duration $\tau_p = 1$ ps (for a fixed pulse shape and given α , the functions (6.8) actually depend only on $\omega\tau_p$, so the characteristics for other durations are easily obtained by scaling), for rotation angles α as shown, and the phonon spectral density $R(\omega)/\omega^2$ (dashed) for deformation potential coupling to LA phonons at $T = 10$ K.

change the exciton occupation number. That is why Rabi oscillations in the ultrafast pulse limit are undamped as also seen from our analytical formulae 6.5. In the opposite limit, the carrier dynamics is slow enough for the lattice to follow adiabatically. The intermediate case corresponds to modifying the charge distribution in the QD with frequencies resonant with the lattice modes which leads to increased interaction with phonons and to decrease of the carrier coherence (see also [Axt *et al.* (1999)] for a simple, single-mode model).

This resonance idea is quantified by the formulae (6.7) in terms of the overlap between the spectral characteristics of the optically induced dynamics, $S_{mn}(\omega)$, and of the lattice response $R(\omega)$. The spectral function $S_{00}(\omega)$ is shown in Figure 6.6 for various Rabi rotation angles. For growing number of rotations n , the non-linear pulse spectrum $S_{00}(\omega)$ develops a series of maxima of increasing strength. The position of the last and highest maximum corresponds approximately to $2\pi n/\tau_p$, in accordance with the semiclassical resonance concept. However, spectral components are also present at all the frequencies $2\pi n'/\tau_p$, $n' < n$, which is due to the turning on/off of the pulse (for high n , the low-frequency part of $S_{00}(\omega)$ does not evolve with n [Machnikowski and Jacak (2004a)]). There are, therefore, two ways of minimizing the overlap and thus, according to Eq. (6.7) the phonon-induced perturbation: either the pulse must be so short that all the maxima of $S_{00}(\omega)$ are pushed to the right into the exponentially vanishing tail of the reservoir spectral density $R(\omega)$, or the pulse must be very long, to “squeeze” the spectral function near $\omega = 0$ and thus reduce its area. In the latter case, the maxima developing with growing number of oscillations will eventually overlap with $R(\omega)$ destroying the coherence.

Although it might seem that speeding up the process is the preferred

solution, in reality it is limited, e.g. by the presence of excited states and non-adiabatically enhanced LO phonon coupling [Fomin *et al.* (1998); Machnikowski and Jacak (2004b); Jacak *et al.* (2004)]. Moreover, in the case of short pulses the dynamics, even within the present model, is actually not fully coherent, as seen from our previous discussion of the coherent control of the carrier density [Vagov *et al.* (2002)] (Section 6.3.3), where we found that the superposition created by the first pulse decoheres due to pure dephasing processes so that the second pulse cannot create an exciton with unit probability. It may be shown [Machnikowski and Jacak (2004a)] that for longer pulses the destructive effect is smaller since the lattice partly manages to follow the evolution of charge distribution during the optical operation. Finally, if the carrier dynamics are slow compared to the lattice response times the lattice distortion follows adiabatically the changes in the charge distribution and the superposition created by the first pulse is an eigenstate of the interacting carrier-lattice system, hence does not undergo any decoherence and the final effect is the same for any delay time (its quality being limited by decoherence effects during pulsing).

The above analysis shows that damping of pulse-area-dependent Rabi oscillations due to the interaction with lattice modes is a fundamental effect of non-Markovian character: it is due to a semiclassical resonance between optically induced confined charge dynamics and lattice modes. The possibility of minimizing the decoherence either by speeding up or by slowing down the dynamics is limited. Thus, it is impossible to perform an arbitrary number of fully coherent Rabi oscillations on an exciton confined in a quantum dot.

6.4.2 *Optimal gating strategy: a trade-off between different types of decoherence*

In this section we analyze the consequences of the pure dephasing phenomena for the possible implementation [Biolatti *et al.* (2000)] of a quantum bit using the optically controlled excitonic degree of freedom in a QD [Al-icki *et al.* (2004)]. Apart from being interesting from the point of view of the physical processes discussed in this chapter, this issue has also some more general aspects. In fact, one usually considers the decoherence time of the system τ_d and the time of performing operation (quantum gate) τ_p , so that the error is given by the ratio $\tilde{\delta} = \tau_p/\tau_d$ [DiVincenzo (1995)]. This suggests one should search for systems with $\tilde{\delta}$ as small as possible, and the obvious strategy to diminish the error is to apply fast gates, which

may be achieved by selecting materials to provide favorable spectral characteristics [De Rinaldis *et al.* (2002)] or by applying techniques that reduce unwanted transitions within the register space [Chen *et al.* (2001); Piermarocchi *et al.* (2002)] as well as outside this space (leakage) [Tian and Lloyd (2000); Wu *et al.* (2002)]. One then tacitly assumes that the process of decoherence is independent of running the gate, which formally means that it is a Markovian process, where the error, to first order, grows linearly in time. However, the picosecond time scale of the phonon reservoir memory, as observed experimentally [Borri *et al.* (2001)], is longer than the suggested sub-picosecond control times necessary to compete with the nanosecond lifetime of an exciton. The resulting decoherence effect is inherently non-Markovian and corresponds to the general scheme of *minimal decoherence* [Alicki *et al.* (2002)]. As we discuss below, the error contribution related to the pure dephasing effect grows for shorter control pulses, precluding the error minimization by gate speed-up.

The quality of a coherent manipulation of the qubit system is customarily quantified in terms of the fidelity which measures the overlap between the intended (unperturbed) final state and the actual one (affected by the coupling to environment), $F = 1 - \delta = \langle \psi(t) \varrho_C(t) \psi(t) \rangle$, where $\psi(t)$ is the unperturbed final state and $\varrho_C(t)$ is the reduced density matrix of the qubit subsystem. The error δ can be expressed by the correction to the density matrix in the interaction picture. If the latter is calculated in the leading order (Born) approximation [Alicki *et al.* (2004); Alicki *et al.* (2002)], then the error averaged over the initial qubit states is

$$\delta = \int \frac{d\omega}{\omega^2} R(\omega) \overline{S(\omega)}, \quad (6.9)$$

where, as in the previous section, $R(\omega)$ is the spectral density of the phonon reservoir and $\overline{S(\omega)}$ is the spectral characteristics for a given control pulse here, however, averaged over the initial states,

$$\overline{S(\omega)} = \frac{1}{3}(|F_-(\omega)|^2 + |F_+(\omega)|^2), \quad F_{\pm} = \int_{-\infty}^{+\infty} dt \frac{d}{dt} e^{\pm iF(t)} e^{i\omega t},$$

and $F(t)$ is the rotation angle on the Bloch sphere performed by the control pulse up to time t .

At $T = 0$ and assuming the deformation potential coupling to LA phonons to be dominant, the spectral density exhibits a $\sim \omega^3$ behavior at low frequencies. Then, for Gaussian pulses and pulse lengths τ_p long compared to the inverse phonon cut-off frequency the error may be shown

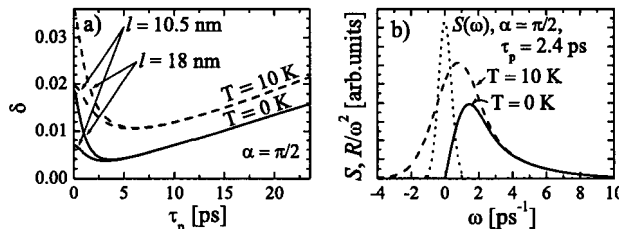


Fig. 6.7 (a) Combined Markovian and non-Markovian error for the temperatures and confinement sizes (FWHM of the electron density) as shown. The Markovian decoherence times are inferred from the experimental data [Borri *et al.* (2001)]. (b) Spectral characteristics of the phonon reservoir and of the control operation.

[Alicki *et al.* (2004)] to scale as τ_p^{-2} . Therefore, minimizing this error requires long pulses leading, however, to an increased probability of exciton decay during the operation since this latter grows linearly with the gate duration and becomes the dominating source of error for long pulses. This trade-off situation, resulting from the combination of a non-Markovian contribution related to pure dephasing with a Markovian contribution due to exciton recombination, gives rise to the existence of a certain optimal pulse duration, below which a further speed-up of the control operation increases the error, instead of reducing it as expected for purely Markovian models.

The error for various pulse durations, taking into account the cut-off and anisotropy of the dot shape and allowing for finite temperatures, is shown in Figure 6.7. The size-dependent cut-off is reflected by a shift of the optimal parameters for the two dot sizes: larger dots admit slightly faster gates and lead to a lower error. The optimal gating time found for InAs/GaAs QDs interacting with bulk phonons and Gaussian pulses is of the order of 1 ps, well within the experimental possibility and far from resonance with excited states or LO phonon transitions. The minimal error is in this case higher than that admitted by fault-tolerant schemes known so far. Thus, it follows that diminishing the responsible constants γ_M (by enhancing the exciton lifetime, e.g. by elimination of radiative losses [Troiani *et al.* (2003)]) and γ_{nM} (by optimizing the system parameters, e.g. by engineering of phonon modes) is an important task towards a semiconductor implementation of a quantum computer. In addition, pulse shaping might be used to further reduce the error [Chen *et al.* (2001); Piermarocchi *et al.* (2002)]. Finally, the requirements for fault-tolerant computation schemes might be reduced by improved strategies.

6.5 Conclusions

We have analyzed the consequences of phonon-induced pure dephasing on the decoherence of strongly confined semiconductor QDs. Pure dephasing has been shown to be the dominant source of decoherence in the initial phase subsequent to an impulsive optical excitation as well as during the evolution induced by a finite pulse. For ultrafast pulses exact analytical results have been discussed showing a non-exponential decay corresponding to non-Lorentzian lineshapes. Interestingly, pure dephasing leads to an unusual non-monotonous temperature dependence of the initial decoherence which has been observed recently in FWM experiments in quantitative agreement with the theoretical predictions. In addition, the decoherence resulting from phonon-induced pure dephasing can be monitored in the coherent control of the carrier density and is also responsible for the formation of stable acoustic polarons in the QD; a process accompanied by the emission of propagating phonon-wave packets that release the formation energy. For pulses with durations comparable with the typical time scale introduced by the coupling to the lattice, the decoherence during the excitation process is of central importance. Here, no analytical results are known and an approximate treatment has to be used instead. In this regime a pronounced damping of Rabi rotations is obtained which decreases for shorter as well as for longer pulses. This type of damping sets an intrinsic limit to the fidelity of Rabi rotations which cannot be reduced by improving the sample quality. However, as it is induced by the carrier-phonon interaction it depends crucially on the phonon density of states and might be reduced by engineering the phonon coupling using samples with confined phonon modes. Finally, it is shown that for a given pulse shape an optimal pulse length can be defined such that the fidelity of gate operations of qubits defined in terms of excitonic excitations is maximized. The optimal pulse length establishes the best trade-off between the non-Markovian decoherence due to pure dephasing and the Markovian loss of coherence provided by the radiative decay.

Acknowledgments

A.V. is grateful for the support of a DWTC fellowship. P.M. and L.J. were partly supported by the Polish Government Grant No. PBZ-MIN-

008/P03/2003. P.M. acknowledges support of the Humboldt Foundation.

Bibliography

- Alicki, R., Horodecki, M., Horodecki, P. and Horodecki, R. (2002). Dynamical description of quantum computing: generic nonlocality of quantum noise, *Phys. Rev. A* **65**: 062101.
- Alicki, R., Horodecki, M., Horodecki, P., Horodecki, R., Jacak, L. and Machnikowski, P. (2004). Optimal strategy of quantum computing and trade-off between opposite types of decoherence, *quant-ph/0302058*: unpublished.
- Axt, V. M., Herbst, M. and Kuhn, T. (1999). Coherent control of phonon quantum beats, *Superlattices and Microstructures* **26**: 117–28.
- Axt, V. M., Krummheuer, B., Vagov, A. and Kuhn, T. (2003). Analytical results for nonlinear optical signals from quantum dots coupled to phonons, *Phys. Status Solidi B* **238**: 581–8.
- Bayer, M. and Forchel, A. (2002). Temperature dependence of the exciton homogeneous linewidth in In0.60Ga0.40As/GaAs self-assembled quantum dots, *Phys. Rev. B* **65**: 041308.
- Besombes, L., Kheng, K., Marsal, L. and Mariette, H. (2001). Acoustic phonon broadening mechanism in single quantum dot emission, *Phys. Rev. B* **63**: 155307.
- Bimberg, D., Grundmann, M. and Ledentsov, N. N. (1998). *Quantum Dot Heterostructures* (John Wiley and Sons, Chichester).
- Biolatti, E., Iotti, R. C., Zanardi, P. and Rossi, F. (2000). Quantum information processing with semiconductor macroatoms, *Phys. Rev. Lett.* **85**: 5647–50.
- Birkedal, D., Leosson, K. and Hvam, J. M. (2001). Long lived coherence in self-assembled quantum dots, *Phys. Rev. Lett.* **87**: 227401.
- Borri, P., Langbein, W., Schneider, S., Woggon, U., Sellin, R. L., Ouyang, D. and Bimberg, D. (2001). Ultralong dephasing time in InGaAs quantum dots, *Phys. Rev. Lett.* **87**: 157401.
- Borri, P., Langbein, W., Schneider, S., Woggon, U., Sellin, R. L., Ouyang, D. and Bimberg, D. (2002). Rabi oscillations in the excitonic ground-state transition of InGaAs quantum dots, *Phys. Rev. B* **66**: 081306(R).
- Borri, P., Langbein, W., Woggon, U., Schwab, M., Bayer, M., Fafard, S., Wasilewski, Z. and Hawrylak, P. (2003). Exciton dephasing in quantum dot molecules, *Phys. Rev. Lett.* **91**: 267401.
- Chen, P., Piermarocchi, C. and Sham, L. J. (2001). Control of exciton dynamics in nanodots for quantum operations, *Phys. Rev. Lett.* **87**: 067401.
- De Rinaldis, S., D'Amico, I., Biolatti, E., Rinaldi, R., Cingolani, R. and Rossi, F. (2002). Intrinsic exciton-exciton coupling in GaN-based quantum dots: Application to solid-state quantum computing, *Phys. Rev. B* **65**: 081309(R).
- DiVincenzo, D. P. (1995). Quantum computation, *Science* **270**: 255–61.
- Duke, C. B. and Mahan, G. (1965). Phonon-broadened impurity spectra. I. density of states, *Phys. Rev.* **139**: A1965–82.

- Fomin, V. M., Gladilin, V. N., Devreese, J. T., Pokatilov, E. P., Balaban, S. N. and Klimin, S. N. (1998). Photoluminescence of spherical quantum dots, *Phys. Rev. B* **57**: 2415–25.
- Förstner, J., Weber, C., Danckwerts, J. and Knorr, A. (2003). Phonon-assisted damping of Rabi oscillations in semiconductor quantum dots, *Phys. Rev. Lett.* **91**: 127401.
- Guenther, T., Lienau, C., Elsaesser, T., Glanemann, M., Axt, V. M., Kuhn, T., Eshlaghi, S. and Wieck, A. D. (2002). Coherent nonlinear optical response of single quantum dots studied by ultrafast near-field spectroscopy, *Phys. Rev. Lett.* **89**: 057401.
- Hawker, P., Kent, A. J. and Henini, M. (1999). Energy relaxation by photoexcited carriers in the InAs/GaAs quantum dot system: bolometric detection of strong acoustic-phonon emission, *Appl. Phys. Lett.* **75**: 3832–4.
- Huang, K. and Rhys, A. (1950). Theory of light absorption and non-radiative transitions in F-centers, *Proc. Roy. Soc. London, Ser. A* **204**: 406–23.
- Itakura, T. and Tokura, Y. (2003). Dephasing due to background charge fluctuations, *Phys. Rev. B* **67**: 195320.
- Jacak, L., Krasnyj, J., Jacak, D. and Bujkiewicz, L. (2002a). Far-infrared laser action from quantum dots created by electric-field focusing, *Phys. Rev. A* **65**: 063813.
- Jacak, L., Krasnyj, J., Jacak, D. and Machnikowski, P. (2002b). Anharmonicity-induced polaron relaxation in GaAs/InAs quantum dots, *Phys. Rev. B* **65**: 113305.
- Jacak, L., Krasnyj, J., Jacak, D. and Machnikowski, P. (2003a). Magneto-polaron in a weakly elliptical InAs/GaAs quantum dot, *Phys. Rev. B* **67**: 035303.
- Jacak, L., Machnikowski, P., Krasnyj, J. and Zoller, P. (2003b). Coherent and incoherent phonon processes in artificial atoms, *Eur. Phys. J. D* **22**: 319–31.
- Jacak, L., Machnikowski, P. and Krasnyj, J. (2004). Fast control of quantum states in quantum dots: limits due to decoherence, *cond-mat/0307536*: to be published.
- Kamada, H., Gotoh, H., Temmyo, J., Takagahara, T. and Ando, H. (2001). Exciton Rabi oscillations in a single quantum dot, *Phys. Rev. Lett.* **87**: 246401.
- Krummheuer, B., Axt, V. M. and Kuhn, T. (2002). Theory of pure dephasing and the resulting absorption lineshape of semiconductor quantum dots, *Phys. Rev. B* **65**: 195313.
- Krummheuer, B., Axt, V. M., Kuhn, T., D'Amico, I. and Rossi, F. (2004a). Pure dephasing in GaAs and GaN quantum dot structures proposed for quantum computation schemes, *Phys. Rev. B*: submitted.
- Krummheuer, B., Vagov, A., Axt, V. M., Kuhn, T., D'Amico, I. and Rossi, F. (2004b). Ultrafast carrier and phonon dynamics in GaAs and GaN quantum dots, *Semicond. Sci. Technol.*: in press.
- Li, X.-Q. and Arakawa, Y. (1999). Optical linewidths in an individual quantum dot, *Phys. Rev. B* **60**: 1915–20.
- Li, X. Q., Wu, Y. W., Steel, D., Gammon, D., Stievater, T. H., Katzer, D. S., Park, D., Piermarocchi, C. and Sham, L. J. (2003). An all-optical quantum

- gate in a semiconductor quantum dot, *Science* **301**: 809–11.
- Machnikowski, P. and Jacak, L. (2004a). Limitation to coherent control in quantum dots due to lattice dynamics, *cond-mat/0305165*: unpublished.
- Machnikowski, P. and Jacak, L. (2004b). Damping of Rabi oscillations in quantum dots due to lattice dynamics, *cond-mat/0307615*, *Semicond. Sci. Technol.*: in press.
- Michler, P., Kiraz, A., Becher, C., Schoenfeld, W. V., Petroff, P., Zhang, L. D., Hu, E. and Imamoglu, A. (2000). A quantum dot single-photon turnstile device, *Science* **290**: 2282.
- Piermarocchi, C., Chen, P., Dale, Y. S. and Sham, L. J. (2002). Theory of fast quantum control of exciton dynamics in semiconductor quantum dots, *Phys. Rev. B* **65**: 075307.
- Rossi, F. and Kuhn, T. (2002). Theory of ultrafast phenomena in photoexcited semiconductors, *Rev. Mod. Phys.* **74**: 895–950.
- Schmitt-Rink, S., Miller, D. A. B. and Chemla, D. S. (1987). Theory of the linear and nonlinear optical properties of semiconductor microcrystallites, *Phys. Rev. B* **35**: 8113–25.
- Stevenson, R. M., Thompson, R. M., Shields, A. J., Farrer, I., Kardynal, B. E., Ritchie, D. A. and Pepper, M. (2002). Quantum dots as a photon source for passive quantum key encoding, *Phys. Rev. B* **66**: 081302.
- Stievater, T. H., Li, X., Steel, D. G., Gammon, D., Katzer, D. S., Park, D., Piermarocchi, C. and Sham, L. J. (2001). Rabi oscillations of excitons in single quantum dots, *Phys. Rev. Lett.* **87**: 133603.
- Stievater, T. H., Li, X., Steel, D. G., Gammon, D., Katzer, D. S. and Park, D. (2002). Transient nonlinear spectroscopy of excitons and biexcitons in single quantum dots, *Phys. Rev. B* **65**: 205319.
- Takagahara, T. (1999). Theory of exciton dephasing in semiconductor quantum dots, *Phys. Rev. B* **60**: 2638–52.
- Tian, L. and Lloyd, S. (2000). Resonant cancellation of off-resonant effects in a multilevel qubit, *Phys. Rev. A* **62**: 050301.
- Troiani, F., Molinari, E. and Hohenester, U. (2003). High-finesse optical quantum gates for electron spins in artificial molecules, *Phys. Rev. Lett.* **90**: 206802.
- Uskov, A. V., Jauho, A.-P., Tromborg, B., Mørk, J. and Lang, R. (2000). Dephasing times in quantum dots due to elastic LO phonon-carrier collisions, *Phys. Rev. Lett.* **85**: 1516–9.
- Vagov, A., Axt, V. M. and Kuhn, T. (2002). Electron-phonon dynamics in optically excited quantum dots: Exact solution for multiple ultrashort laser pulses, *Phys. Rev. B* **66**: 165312.
- Vagov, A., Axt, V. M. and Kuhn, T. (2003a). Impact of pure dephasing on the nonlinear optical response of single quantum dots and dot ensembles, *Phys. Rev. B* **67**: 115338.
- Vagov, A., Axt, V. M. and Kuhn, T. (2003b). Nonperturbative treatment of quantum dots coupled to light and phonons, *Physica E* **17**: 11–4.
- Vagov, A., Axt, V. M., Kuhn, T., Langbein, W., Borri, P. and Woggon, U. (2004). Non-monotonous temperature dependence of the initial decoherence in quantum dots, *Phys. Rev. Lett.*: submitted.

- Wu, L.-A., Byrd, M. S. and Lidar, D. A. (2002). Efficient universal leakage elimination for physical and encoded qubits, *Phys. Rev. Lett.* **89**: 127901.
- Zrenner, A., Beham, E., Stufler, S., Findeis, F., Bichler, M. and Abstreiter, G. (2002). Coherent properties of a two-level system based on a quantum-dot photodiode, *Nature* **418**: 612–14.

Chapter 7

All-Optical Schemes for Quantum Information Processing with Semiconductor Macroatoms

I. D'Amico, E. Pazy¹ and P. Zanardi

Institute for Scientific Interchange (ISI)

Villa Gualino

viale Settimio Severo 65

10133 Torino, Italy

E. Biolatti, R.C. Iotti and F. Rossi

Dipartimento di Fisica, Politecnico di Torino

Corso Duca degli Abruzzi 24

10129 Torino, Italy

F. Troiani, U. Hohenester² and E. Molinari

INFM National Center on nanoStructures and bioSystems at Surfaces (S3)

Dipartimento di Fisica, Università di Modena e Reggio Emilia

Via Campi 213/A, 41100 Modena, Italy

7.1 Introduction

It has been recently recognized that processing information in a quantum-mechanical fashion can provide, in some cases, a huge computational speed-up with respect to *any* classical device [DiVincenzo and Bennet (2000)]. Just to mention the two best known quantum algorithms, a quantum com-

¹present affiliation: Department of Physics, Ben-Gurion University of the Negev, Beer-Sheva 84105, Israel

²present affiliation: Institut für Theoretische Physik, Karl-Franzens-Universität Graz, Universitätspatz 5, 8010 Graz, Austria

puter would allow for ultrafast factoring of large integer numbers or would efficiently perform database search. From the fundamental point of view, the novel computational power owned by such devices relies on two basic quantum features: (i) superposition of states, i.e., linear structure of the state-space, and (ii) quantum entanglement, i.e., tensor-product structure of a multipartite state-space. These two ingredients, along with the unitary character of quantum dynamics, lie at the heart of the additional capability provided by quantum information/computation (QIC) processing. The first one endow a quantum computer with a sort of massive built-in parallelism while the latter makes it possible to use uniquely quantum correlations, i.e., entanglement, for designing efficient algorithms.

Even though from the theoretical point of view QIC can be already considered as a well-established field, a major challenge arises when one starts to move toward the experimental side, addressing the problem of concrete implementations. Indeed, from the practical point of view this goal is exceptionally demanding: once a system with a well-defined state-space has been identified, one should be able to perform precise state preparation (*input*), any — arbitrarily long — coherent state manipulation (*data processing*), and state measurement (*output*) as well. In analogy to classical computation, such manipulations are thought of as a sequence (*network*) of elementary logic quantum gates, e.g., universal sets of single plus two quantum-bit (*qubit*) operations. Such quantum gates, in turn, have to be realized exploiting physically affordable coupling mechanisms, in terms of, e.g., single- and two-body interactions.

The primary obstacle toward a straightforward implementation of this idealized scheme is the destruction of the unitary nature of quantum evolution due to the unavoidable coupling of the computational degrees of freedom to their environment. Indeed, any quantum computer is an open system; it follows that, typically on a very short time scale, a system prepared in a pure quantum state (coherent superposition) decays into a statistical (incoherent) mixture. This process is known as *decoherence*: it represents a kind of noise peculiar to quantum mechanics; it spoils quantum computation making it basically a classical process.

Mostly due to the need of low decoherence rates, the first proposals for experimental realizations of quantum-information processing devices originated from specialties in atomic physics [Cirac and Zoller (1995); Pellizzari *et al.* (1995); Monroe *et al.* (1995); Sorensen and Molmer (1999)], in quantum optics [Turchette *et al.* (1995); Imamoglu *et al.* (1999)], and in nuclear and electron magnetic-resonance spectroscopy [Gershenfeld and

Chuang (1997)]. On the other hand practically relevant quantum computations require a large number of quantum-hardware units (qubits) that are known to be hardly achievable in terms of such systems.

In contrast, in spite of the serious difficulties related to the “fast” decoherence times, a solid-state implementation of QIC seems to be the only way to benefit synergistically from the recent progress in ultrafast optoelectronics [Shah (1996)] as well as in meso/nanostructure fabrication and characterization [Jacak *et al.* (1998)]. Among the proposed solid-state implementations one should mention those in superconducting device physics [Shnirman *et al.* (1997); Mooij *et al.* (1999)], in electron physics, and in meso- and nanoscopic physics [Loss and DiVincenzo (1998)].

In this chapter we shall address the problem of a semiconductor-based realization of QIC using charge and/or spin degrees of freedom. Along this line, we shall present an all-optical implementation [Biolatti *et al.* (2000); Biolatti *et al.* (2002); De Rinaldis *et al.* (2002)] of QIC processing with semiconductor quantum dots (QDs) — often called macroatoms [Jacak *et al.* (1998)] — where the computational degrees of freedom are inter-band optical transitions (excitonic states) manipulated/controlled by ultrafast sequences of multicolor laser-pulse trains; this kind of implementation scheme has indeed stimulated a significant experimental activity aimed at realizing basic QIC with QDs [Li *et al.* (2003)]. Moreover, we shall review a recently proposed scheme [Pazy *et al.* (2003)] based on a proper combination of charge and spin degrees of freedom.

The present chapter is organized as follows: after having recalled the fundamentals of QIC, in Section 7.2 we shall present and discuss a number of proposed all-optical implementation schemes. Coupled-dot encoding schemes are discussed in Section 7.2.2; more specifically, Sections 7.2.2.1 and 7.2.2.2 will describe how to implement such coupled-dot quantum encoding/manipulation strategy in GaAs- and GaN-based quasi zero-dimensional (0D) nanostructures, respectively. Section 7.2.3 discusses the possibility to combine charge and spin degrees of freedom, aiming at identifying fast quantum gates which do not translate into fast decoherence times. In Section 7.3 we shall finally summarize and draw some conclusions.

7.2 All-Optical Quantum Information/Computation with Semiconductor Macroatoms

The first semiconductor-based QIC proposal [Loss and DiVincenzo (1998)] relies on spin dynamics in QDs; it exploits the low decoherence of spin degrees of freedom in comparison to the one of charge excitations (see Section 7.2.3). On the other hand, as originally envisioned in [Zanardi and Rossi (1998)], gating of charge excitations could be performed by exploiting *present* ultrafast laser technology, that allows to generate and manipulate electron-hole quantum states on a sub-picosecond time scale [Shah (1996); Bonadeo *et al.* (1998a)]. In this respect decoherence times on nano/microsecond scales can be regarded as “long” ones. Following this spirit, the first *all-optical* implementation schemes with semiconductor macroatoms/molecules have been recently put forward [Troiani *et al.* (2000); Biolatti *et al.* (2000); Biolatti *et al.* (2002); De Rinaldis *et al.* (2002)].

The scheme proposed by Troiani and co-workers [Troiani *et al.* (2000)], is based on ultrafast optical manipulations of ground as well as excited excitonic transitions in a single quantum-dot structure. In contrast, in the scheme proposed by Biolatti and co-workers [Biolatti *et al.* (2000); Biolatti *et al.* (2002)] the quantum information is encoded in the ground state excitons of Coulomb-coupled quantum-dot molecules. More specifically, the original proposal [Biolatti *et al.* (2000); Biolatti *et al.* (2002)], discussed in Section 7.2.2.1, deals with Coulomb-coupled GaAs-based QD structures; as we shall see, in this scheme an applied external field is needed. In order to overcome such requirement/limitation, De Rinaldis and co-workers have recently proposed a modified version [De Rinaldis *et al.* (2002)] of the original scheme; the latter, based on GaN QD structures, is described in Section 7.2.2.2.

7.2.1 Single-dot encoding schemes

The implementation of quantum gates in a single dot is expected to provide a first proof-of-principle of QIC schemes based on the use of inter-band excitations as computational degrees of freedom [Troiani *et al.* (2000)]. As discussed in more detail in the following, the coupled-dot encoding is needed in order for such schemes to be scalable; however, most of the required physical ingredients are already given in single dots, where some of them, such as the Coulomb-induced exciton-exciton coupling, are more easily en-

gineered and observed. A detailed description of a specific QD is beyond the scope of our work, and is not relevant at the present stage of our discussion. However, some physical features do play a crucial role in the proposed scheme: among these, we mention here the Coulomb renormalizations of the exciton levels and the energy separations between the relevant and the “unwanted” optical transitions, whose inverse values (times \hbar) approximately give the minimum duration of the quantum gates. In the following we consider a GaAs/AlGaAs QD, which we model by means of a prototypical confinement potential, parabolic in the (x, y) -plane and box-like along z : $V^{(e,h)}(\mathbf{r}) = \frac{1}{2}m_{e,h}^*\omega_{e,h}^2(x^2 + y^2) + V_{e,h}^z\theta(|z| - l/2)$. The single-particle states $|\mu_{e,h}\rangle$ and energies $\epsilon_{\mu_{e,h}}^{e,h}$ for electrons and holes are obtained by numerically solving the three-dimensional single-particle Schrödinger equation within the envelope-function and effective-mass approximations.

As an important step within our proposal, we use the fact that in most semiconductors electron-hole pairs with given spin orientation can be selectively created by photons with a well-defined circular polarization. Throughout the present paragraph, we shall only consider excitons with parallel spin orientations because of their strongly reduced available phase space and the resulting simplified optical density of states. Moreover, we can restrict ourselves to single excitons and biexcitons. We expand the exciton and biexciton states within the subspaces of spin-selective electron-hole excitations, and directly diagonalize the Hamiltonian matrix, including the Coulomb terms, within the resulting basis (further details on the model are provided in Chapter 5). Finally, the optical properties of the dot result from the inter-band transitions corresponding to the creation (annihilation) of an electron-hole pair.

In Figure 7.1 we show the linear optical response of the dot as a function of its initial state. In the top line (a) the dot is prepared in its ground state $|G\rangle$ (i.e., no electron-hole pairs): two pronounced absorption peaks appear (labeled with X_0 and X_1) with an energy splitting of the order of the single-particle interlevel spacings $\hbar\omega_e + \hbar\omega_h$. In fact, a closer inspection of the exciton wavefunctions reveals that the dominant contribution to the ground state exciton X_0 is given by the energetically lowest electron and hole single-particle states (with s -type character), while that of the X_1 exciton comes from the electron and hole first excited (p -type) orbitals. In Figure 7.1b the initial state is $|X_0\rangle$; because of state filling, the character of the corresponding optical transition changes from absorption to gain (i.e., negative absorption). Moreover, the higher-energetic transition is shifted from ω_{X_1} to $\omega_{X_1} - \Delta$, with $\Delta \approx 8$ meV: this pronounced red shift mainly

arises from the exchange interaction between the two electrons and that between the two holes. As an important point, the dominant contribution (more than 95%) to the biexcitonic wavefunction comes from excitons X_0 and X_1 : we are therefore allowed to label this state with $|X_0 + X_1\rangle \simeq \hat{\sigma}_{X_0}^\dagger \hat{\sigma}_{X_1}^\dagger |G\rangle$, where the exciton creation operators $\hat{\sigma}_{X_{0,1}}^\dagger$ are defined such that $\hat{\sigma}_{X_{0,1}}^\dagger |G\rangle = |X_{0,1}\rangle$. Analogous considerations apply to the Figures 7.1(c,d), that report the optical responses of the dot prepared in state X_1 and $X_0 + X_1$, respectively.

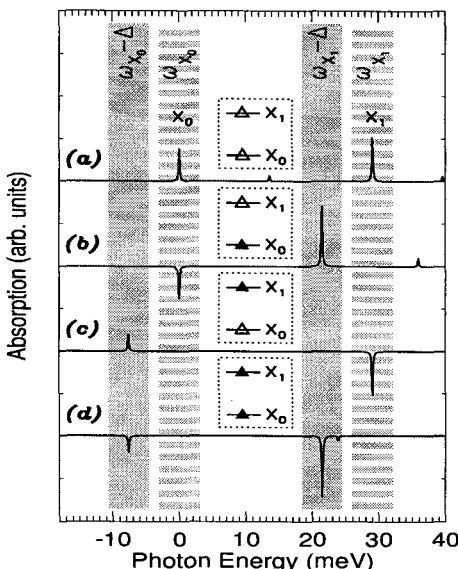


Fig. 7.1 Optical response of the GaAs/AlGaAs semiconductor quantum dot described in the text: the interlevel spacings due to the in-plane parabolic potential are $\omega_o^{(e)} = 20$ meV for electrons and $\omega_o^{(h)} = 3.5$ meV for holes; the quantum-well confinement along z is characterized by a width of 10 nm, a depth of 400 meV for electrons and of 215 meV for holes. The four lines correspond to the optical response of the dot initially prepared in (a) the vacuum state $|G\rangle$, (b) the exciton $|X_0\rangle$ state (exciton ground state), (c) the exciton $|X_1\rangle$ state, (d) the biexciton state $|X_0 + X_1\rangle$ state. Photon energy zero corresponds to the transition between the vacuum- and the exciton ground state.

Within the present scheme, the manipulation of the QD state is performed by means of ultrafast laser pulses: each of these creates an inter-band polarization, i.e., a superposition between different inter-band excitations, which propagate in phase with the driving laser. In order to illustrate

the essence of our scheme, we consider the time-evolution induced by laser pulse with rectangular-shaped envelope and with central frequency $\omega_{X_0} - \Delta$; besides, we assume that only resonant transitions at $\omega_{X_0} - \Delta$ are affected by the laser (results of more realistic simulations will be presented further below). Having rephrased the basis states in terms of their logical value ($|00\rangle \equiv |G\rangle$, $|01\rangle \equiv |X_0\rangle$, $|10\rangle \equiv |X_1\rangle$, $|11\rangle \equiv |X_0 + X_1\rangle$), the effective qubit-light Hamiltonian reads

$$\mathcal{H}_{\text{op}} = -\frac{1}{2}M\mathcal{E}_o(t) \left(e^{i\omega t}|11\rangle\langle 01| + e^{-i\omega t}|01\rangle\langle 11| \right)_{\omega=\omega_{X_0}-\Delta}, \quad (7.1)$$

with the dipole-matrix element $M = \langle X_0|\hat{P}|X_0 + X_1\rangle$, the inter-band-polarization operator $\hat{P} = \sum_{\mu_e, \nu_h} M_{\mu_e \nu_h}^* \hat{d}_{\nu_h} \hat{c}_{\mu_e}$; \hat{c}_{μ_e} (\hat{d}_{ν_h}) is the electron (hole) destruction operator and $M_{\mu_e \nu_h}$ is the dipole-matrix element for the optical transition between μ_e and ν_h . The time evolution induced by a pulse of duration T corresponds to the following unitary transformation:

$$\begin{aligned} \mathcal{U}(t > T, 0) = \\ |00\rangle & \quad (00| + |01) \quad e^{-iE_{X_0}t} \quad (01| + \\ |10\rangle & \quad e^{-iE_{X_1}t} \cos(\Omega_R T) \quad (10| + |10) \quad -ie^{-iE_{X_1}t} \sin(\Omega_R T) \quad (11| + \\ |11\rangle & \quad -ie^{-iE_{X_0+X_1}t} \sin(\Omega_R T) \quad (10| + |11) \quad e^{-iE_{X_0+X_1}t} \cos(\Omega_R T) \quad (11| , \end{aligned}$$

where $\Omega_R = M\mathcal{E}_o$ is the Rabi frequency. Apparently, $\mathcal{U}(t, 0)$ manipulates the first qubit only if the second qubit is set equal to one. The details of such manipulations depend on the specific choices for t and T ; e.g., for $\Omega_R T \bmod 2\pi = \pm\frac{\pi}{2}$ (i.e., $\pi/2$ -pulse), $E_{X_0} t \bmod 2\pi = 0$, $E_{X_1} t \bmod 2\pi = \pm\frac{\pi}{2}$, and $E_{X_0+X_1} t \bmod 2\pi = \pm\frac{\pi}{2}$, the above unitary transformation precisely corresponds to a controlled NOT (C-NOT) operation. By inspection of Figure 1, we observe that a completely analogous scheme, although with different conditional qubit settings, applies for the optical transitions at different photon energies (the conditional dependence is indicated at the top of Figure 7.1). Within our proposed scheme, the unconditioned qubit operations (i.e., rotation of a single qubit), which are requested besides the C-NOT operations for the implementation of a universal set of gates, can be simply achieved by combining two conditional operations at different photon energies: e.g., in order to perform a NOT operation on the first qubit (independent of the setting of the second qubit) we first have to perform a C-NOT operation at frequency $\omega_{X_0} - \Delta$, followed by a C-NOT operation at ω_{X_0} (see also Figure 7.2; other single-qubit rotations can be performed by choosing different durations T of the laser pulses).

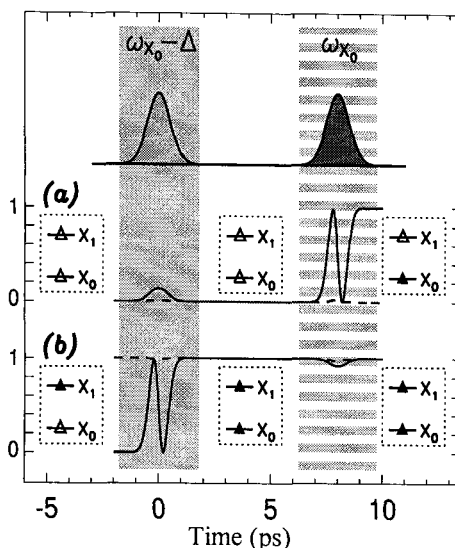


Fig. 7.2 Results of our simulations (neglecting dephasing) of the quantum dot time-evolution by means of two laser pulses with Gaussian profiles. The solid (dashed) lines represent the population of the $|X_0\rangle$ ($|X_1\rangle$) state corresponding to the dot being prepared (a) in the vacuum state $|00\rangle$ and (b) in the exciton state $|X_1\rangle = |01\rangle$. The sequence of pulses and the corresponding photon energies are indicated at the top of the figure; for the envelopes of the laser pulses we use Gaussians $\propto \exp(-t^2/2\tau^2)$, with $\tau = 0.5$ ps. The pulse at time zero corresponds to a C-NOT operation where the $|X_1\rangle$ exciton acts as the control-qubit; the second pulse implements an analogous gate, but here the control qubit must be in its 0 state in order for the target qubit to be flipped: the overall sequence corresponds to an unconditional NOT operation applied to the first qubit.

We finally consider the possible experimental realization of our proposed scheme. Quite generally, the feasibility of quantum-information processing depends on the number of qubit operations which can be performed on the time scale of dephasing. We therefore have to estimate the time required for performing single qubit manipulations (i.e., the duration T_{pulse} of the laser pulse) and the typical dephasing times ($T_{\text{dephasing}}$). In order to perform qubit manipulations without affecting unwanted transitions, the spectral width of the laser pulse must be narrow as compared to the energy separation between neighboring peaks; from the basic relation $\Delta \times T_{\text{pulse}} \sim \hbar$ we can estimate a lower limit of $T_{\text{pulse}} \gtrsim 0.1$ ps (note that much longer pulses would be required in case of non-spin-selective excitations, where the typical energy splitting of peaks in the optical spectra would be of the order of 1 meV). We have also simulated single- and two-qubit gates assuming

for the laser pulses some Gaussian profiles, which minimize the spectral width, and therefore the leakage and the error rates. Figure 7.2 shows typical results of our simulations; for conceptual clarity, we have chosen rather strong laser pulses to demonstrate that even for such high electric fields the laser only manipulates components of the state vector with appropriate energies. From our simulations we safely conclude that manipulation times of the order of $T_{\text{pulse}} \approx 0.25$ ps completely suffice to suppress any population of components of the state vector at non-matching energies.

Recent experimental results have demonstrated the feasibility of the present scheme. Indeed, the required quantum mechanical behaviors, such as Rabi oscillations (of excitons and biexcitons), entanglement and quantum interference, have been optically induced and observed both in naturally formed and in self-assembled QDs (see [Li *et al.* (2003)] and references therein): in the former one can profit from the large dipole moment associated to the inter-band transitions; the latter are more promising in view of their stronger confinement regime and of the better control of the dot geometry allowed by the self-assembly growth process [Jacak *et al.* (1998)]. These results are indeed encouraging; however, one should keep in mind that single QDs are not suited for the QIC implementation beyond the 2-3 qubit limit. This is essentially due to the tensorial structure of the Hilbert space, which is required by the most efficient quantum algorithms and calls for the quantum hardware to consist in a collection of subsystems.

7.2.2 Coupled-dot encoding schemes

7.2.2.1 GaAs-based quantum hardware

As multi-dot quantum hardware, we consider a vertically-staked array of GaAs-based self-assembled QD structures, whose unit cell $a + b$ is schematically depicted in Figure 7.3A. Here, the in-plane carrier confinement is described by a two-dimensional (xy) parabolic potential, while along the growth (z) direction we deal with a square-like potential profile. The latter is tailored in such a way to allow for an energy-selective creation/destruction of bound excitons in dots a and b . The inter-dot barrier width (~ 50 Å) is such to prevent single-particle tunneling and at the same time to allow for significant inter-dot Coulomb coupling. Moreover, in order to induce a significant exciton-exciton dipole coupling [Biolatti *et al.* (2000); Biolatti *et al.* (2002); D'Amico and Rossi (2001)], an in-plane static electric field F is applied.

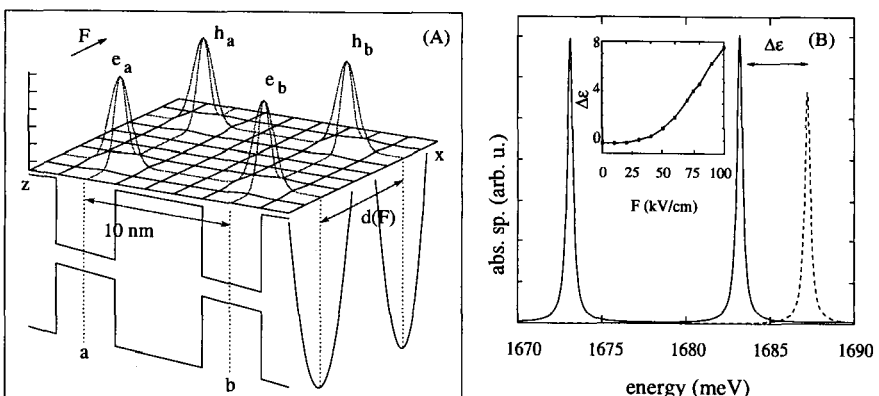


Fig. 7.3 (A) Schematic representation of the electron and hole charge distribution as well as of the confinement potential profile in our Coulomb-coupled GaAs-based QD structure. (B) Excitonic (solid curve) and biexcitonic response (dashed curve) of the GaAs-based coupled QD structure in (A) for an in-plane field $F = 75 \text{ kV/cm}$. The biexcitonic shift $\Delta\epsilon$ as a function of the in-plane field F is also reported in the inset (see text).

As a starting point, let us discuss the optical response of the *semiconductor macromolecule* ($a + b$) in Figure 7.3A to a single- as well as a double-pulse sequence. The excitonic spectrum in the presence of an in-plane electric field $F = 75 \text{ kV/cm}$ is shown in Figure 7.3B (solid curve). This is compared to the so-called biexcitonic spectrum (dashed curve); the latter describes the generation of a second electron-hole pair in the presence of a previously created exciton. The crucial feature in Figure 7.3B is the magnitude of the “biexcitonic shift” $\Delta\epsilon$ [Jacak *et al.* (1998)], i.e., the energy difference between the excitonic and the biexcitonic transitions (see solid and dashed curves). As discussed in [D’Amico and Rossi (2001)], this is due to the in-plane field F , which induces an electron-hole charge separation along the field direction. This, in turn, gives rise to significant dipole-dipole coupling between adjacent excitonic states (see Figure 7.3A).

The central idea in this QD-based QIC proposal is to exploit such few-exciton effect to design *conditional operations*: the presence of an exciton in a quantum dot can prevent the generation of a second exciton by varying the detuning and thus controlling the resonance condition in the photo-generation process. In order to define the computational space for our QIC scheme, let us introduce the excitonic occupation number operators \hat{n}_l , where l denotes the generic QD in the array. The two states with

eigenvalues $n_l = 0$ and $n_l = 1$ correspond, respectively, to the absence (no conduction-band electrons) and to the presence of a ground state exciton (a Coulomb-correlated electron-hole pair) in dot l . Each single QD in the array can be regarded as a qubit, its quantum state is a vector in a subspace whose two-dimensional basis is given by $|0\rangle_l$ and $|1\rangle_l$. The whole computational state-space \mathcal{H} is then spanned by the basis $|\mathbf{n}\rangle = \otimes_l |n_l\rangle$, ($n_l = 0, 1$). The full many-body Hamiltonian describing our interacting electron-hole system restricted to the above computational space \mathcal{H} reduces to

$$\tilde{\mathbf{H}}_o = \sum_l \mathcal{E}_l \hat{n}_l + \frac{1}{2} \sum_{l \neq l'} \Delta \mathcal{E}_{ll'} \hat{n}_l \hat{n}_{l'} . \quad (7.2)$$

Here, \mathcal{E}_l denotes the energy of the ground state exciton in dot l while $\Delta \mathcal{E}_{ll'}$ is the biexcitonic shift due to the Coulomb interaction between dots l and l' , previously introduced (see Figure 7.3B). The effective Hamiltonian in (7.2) has exactly the same structure of the one proposed by Lloyd in his pioneering paper on quantum cellular automata, and it is the model Hamiltonian currently used in most of the NMR quantum-computing schemes. As it can be trivially derived from (7.2), the single-exciton energy \mathcal{E}_l is simply renormalized by the biexcitonic shift $\Delta \mathcal{E}_{ll'}$, induced by the presence of a second exciton in dot l' . The dependence of the single-qubit energy on the occupation of the neighboring sites, $\tilde{\mathcal{E}}_l = \mathcal{E}_l + \sum_{l' \neq l} \Delta \mathcal{E}_{ll'} n_{l'}$, is the crucial ingredient that allows for the implementation of a *conditional* dynamics required for universal QIC. In order to illustrate this idea, let us focus again on the two-QD structure, i.e., two-qubit system, of Figure 7.3A and fix our attention on one of the two dots, say dot b . The effective energy gap between $|0\rangle_b$ and $|1\rangle_b$ depends now on the occupation of dot a . This elementary remark suggests to design properly tailored laser-pulse sequences to implement controlled-not logic gates among the two QDs as well as single-qubit rotations. Indeed, by sending an ultrafast laser π -pulse with central energy $\hbar\omega_b[n_a] = \mathcal{E}_b + \Delta \mathcal{E}_{ba} n_a$, the transition $|n_b\rangle_b \rightarrow |1 - n_b\rangle_b$ (π rotation) of the *target* qubit (dot b) is obtained if and only if the *control* qubit (dot a) is in the state $|n_a\rangle_a$. In the very same way, by using a laser pulse with central energy $\hbar\omega_a[n_b]$, the role of the target and control qubit is interchanged. By denoting with U_l^n the unitary transformation induced by the laser π -pulse of central frequency $\omega_l[n]$, the above conditional gate corresponds to the transformation $U_b^{n_a}$. Moreover, one can easily check that the two-color pulse sequence $U_l^0 U_l^1$ achieves the unconditional π rotation of the l -th qubit.

In order to test the viability of the proposed QIC strategy, we have

performed a few simulated experiments of basic quantum-information processing. They are based on a numerical solution of the Liouville-von Neumann equation describing the exact quantum-mechanical evolution of the many-exciton system (7.2) within our computational subspace \mathcal{H} in the presence of environment-induced decoherence processes. The latter are accounted for in our density-matrix formalism by means of a standard T_1T_2 model: we employ a band-to-band recombination time $T_1 = 1\text{ ns}$ and we describe phonon-induced decoherence processes in terms of an exciton-phonon dephasing time $T_2 = 50\text{ ps}$, which is fully compatible with recent experimental findings [Bonadeo *et al.* (1998a); Borri *et al.* (2001)]. A detailed analysis of phonon-induced decoherence in optically excited QD structures can be found in [Krummheuer *et al.* (2002); Vagov *et al.* (2002)].

The above simulation scheme has been applied to the coupled-QD structure of Figure 7.3A in the presence of an in-plane static field $F = 75\text{ kV/cm}$: $\mathcal{E}_a = 1.673\text{ eV}$, $\mathcal{E}_b = 1.683\text{ eV}$, and $\Delta\mathcal{E} = 4\text{ meV}$ (see inset in Figure 7.3B).

We shall start our time-dependent analysis by simulating a basic conditional two-qubit operation, the so-called *controlled not* (CNOT) gate. Our first simulated experiment is shown in Figure 7.4A. The multi-color laser-pulse train (see central panel) is able to perform first a π rotation of the qubit a ($|0\rangle_a \rightarrow |1\rangle_a$); then, the second pulse is tuned to the frequency $\mathcal{E}_b + \Delta\mathcal{E}$, thus performing a π rotation of the qubit b ($|0\rangle_b \rightarrow |1\rangle_b$), since this corresponds to its renormalized transition energy when the neighbor qubit a is in state $|1\rangle_a$. The scenario described so far is confirmed by the time evolution of the exciton occupation numbers n_a and n_b (upper panel) as well as of the diagonal elements of the density matrix in our four-dimensional computational basis (lower panel).

This realizes the first part of the well-known CNOT gate: the target qubit b is rotated if the control qubit a is in state $|1\rangle_a$. To complete it, one has to show that the state of the target qubit b remains unchanged if the control qubit a is in state $|0\rangle_a$. This has been checked by a second simulated experiment (not reported here) where the first pulse, being now off-resonant (with respect to dot a), does not change the computational state of the system. As a consequence, the second pulse is no more into resonance with the excitonic-transition energy of dot b , since the latter is no more renormalized by the excitonic occupation of dot a . Therefore, the initial state of the system is $|0, 0\rangle$ and the final one is again $|0, 0\rangle$.

The simulated experiments discussed so far clearly show the potential realization of the CNOT gate, thus confirming the validity of the proposed

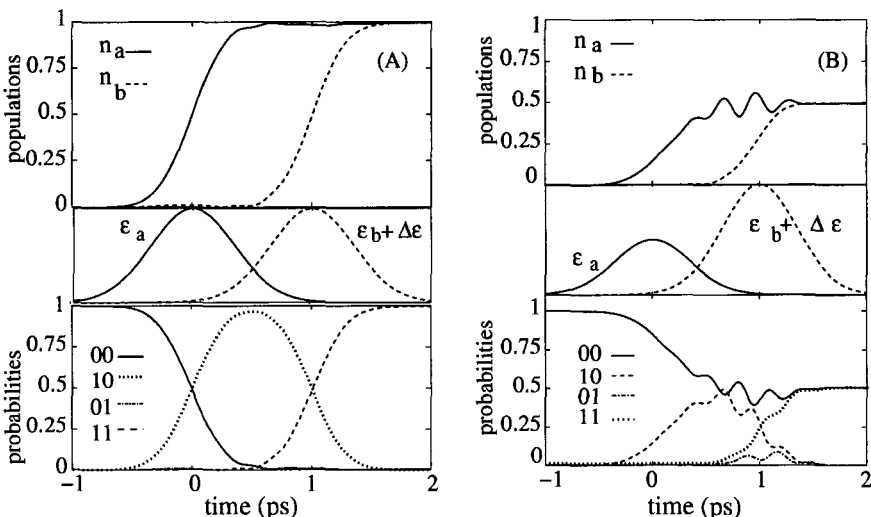


Fig. 7.4 Time-dependent simulation of a CNOT quantum gate (A) realizing the prescription $(|1,0\rangle \rightarrow |1,1\rangle)$, and (B) transforming the factorized state $|0,0\rangle + |1,0\rangle$ into a maximally entangled state $|0,0\rangle + |1,1\rangle$ (see text). Exciton populations n_a and n_b (upper panels) and diagonal density-matrix elements (lower panels) as a function of time. The laser-pulse sequences are also sketched.

semiconductor-based QIC strategy. However, the analysis presented so far deals with factorized states only. It is well known [DiVincenzo and Bennet (2000)] that the key ingredient in any QIC is entanglement. Generally speaking, this corresponds to a non-trivial linear combination of our basis states.

We shall now show that the CNOT gate previously discussed is able to transform a factorized state into a maximally entangled one. Figure 7.4B shows a simulated two-qubit operation driven again by a two-color laser-pulse sequence (see central panel). Initially, the system is in the state $|0,0\rangle$. The first laser pulse (at $t = 0$) is tailored in such a way to induce now a $\frac{\pi}{2}$ rotation of the qubit a : $|0,0\rangle \rightarrow (|0,0\rangle + |1,0\rangle)/\sqrt{2}$. At time $t = 1$ ps a second pulse induces a conditional π rotation of the qubit b : $|0,0\rangle + |1,0\rangle \rightarrow |0,0\rangle + |1,1\rangle$. This last operation plays a central role in any QIC, since it transforms a *factorized* state $((|0\rangle_a + |1\rangle_a) \otimes |0\rangle_b)$ into an *entangled* state $(|0\rangle_a \otimes |0\rangle_b + |1\rangle_a \otimes |1\rangle_b)$.

The experiments simulated above (see Figures 7.4A and 7.4B) clearly show that the gating time is fully compatible with the typical decoherence

time scale of QD structures; indeed, this is also confirmed by a number of recent experiments demonstrating Rabi oscillations in QDs [Kamada *et al.* (2001); Stievater *et al.* (2001)]. Moreover, our simulated experiments show that the energy scale of the biexcitonic splitting $\Delta\mathcal{E}$ in our QD molecule (see inset in Figure 7.3B) is compatible with the sub-picosecond operation time scale of modern ultrafast laser technology [Shah (1996)].

7.2.2.2 *GaN-based quantum hardware*

As anticipated, one of the major technological problems in implementing the solid-state quantum gate previously discussed [Biolatti *et al.* (2000); Biolatti *et al.* (2002)] is the need of an external electric field to drive two-qubit conditional operations. Indeed, from the technological point of view, this requires the presence of electrical contacts which limit the time response of the system and strongly complicate the physical interconnection of the device. The ideal scheme would thus be a QD structure with built-in electric fields. GaN-based QDs seem to match these requirements quite well [Andreev and O'Reilly (2000); Arlery *et al.* (1999); Widmann *et al.* (1998a); Widmann *et al.* (1998b)], as they are known to exhibit strong built-in polarization and piezoelectric field (of the order of MV/cm).

To overcome this limitation, we have recently proposed an all-optical quantum gate based on GaN QD molecules [De Rinaldis *et al.* (2002)]. The central idea is to properly tailor the internal field such to induce built-in excitonic dipoles. This will result in an intrinsic exciton-exciton coupling, i.e., without the need of additional external fields. We shall show that the biexcitonic shift due to such dipole-dipole interaction is again of the order of a few meV, thus allowing for sub-picosecond quantum state manipulations via ultrafast laser-pulse sequences.

As already mentioned, one of the most interesting features of GaN heterostructures is the strong built-in electric field: this is induced both by the spontaneous polarization and by the piezoelectric field. Contrary to GaN quantum wells — where the major role is played by the spontaneous polarization charge accumulated at the GaN/AlGaN interfaces while strain-induced piezoelectric fields have a minor importance [Cingolani *et al.* (2000)] — in GaN QDs piezoelectric effects become relevant because of the non-central symmetry of the wurzite structure. Moreover, since the dimensions of GaN and AlN unit cell differ slightly from those of an ideal hexagonal crystal, a spontaneous electrostatic polarization is present as well [An-

dreev and O'Reilly (2000); Arlery *et al.* (1999); Widmann *et al.* (1998a); Widmann *et al.* (1998b)]. As shown in [Andreev and O'Reilly (2000); Arlery *et al.* (1999); Widmann *et al.* (1998a); Widmann *et al.* (1998b)], the strain-induced piezoelectric potential and the spontaneous-polarization contribution are of similar magnitude and equal sign, both oriented along the growth direction. The magnitude of the intrinsic electric field along the growth direction is almost the same inside and outside the dot, but it is opposite in sign.

The resulting internal field can be tailored by varying the size of the dot: The models usually considered for its estimation neglect the in-plane shape of the QD; the latter will be primarily responsible for the relatively strong in-plane carrier confinement [Andreev and O'Reilly (2000); Arlery *et al.* (1999); Widmann *et al.* (1998a); Widmann *et al.* (1998b)], which — as for the case of GaAs-based structures — can be well described in terms of a two-dimensional (2D) parabolic potential. Such built-in electric field induces electron-hole charge separation, which results in a charge dipole — also called excitonic dipole — in each QD. This, in turn, will generate an effective inter-dot dipole-dipole coupling. For the case of two stacked QDs *a* and *b* along the growth (*z*) direction (see Figure 7.5) — for which such intrinsic excitonic dipole $\mathbf{p} \parallel \hat{z}$ — we get:

$$\Delta\mathcal{E} = -2 \frac{p_a p_b}{Z^3}, \quad (7.3)$$

where *Z* is the distance between the two dipoles.

The general scheme of our two-qubit quantum gate consists of two stacked dots of slightly different size. For the sake of clarity, here we discuss the case of two coupled dots with identical bases, stacked along the growth axis, and having height of 2.5 and 2.7 nm, respectively. Analogous results would be obtained by two dots of same height and different base-radius. The resulting difference in the potential-well width ($\simeq 0.2$ nm) allows us to shift the excitonic transitions (see below). Moreover, the barrier width is chosen such to prevent single-particle tunneling but to allow at the same time for significant dipole-dipole Coulomb coupling. Such internal field strongly modifies the conduction-band and valence-band edges along the growth directions (see Figure 7.5); this causes the spatial separation of the carrier states and the creation of the desired intrinsic dipoles as can be seen in Figure 7.5. Here, the internal field shifts in opposite directions the electron and the hole charges: electrons are forced to move towards the top of the dot (right) and holes are driven towards its bottom (left). So,

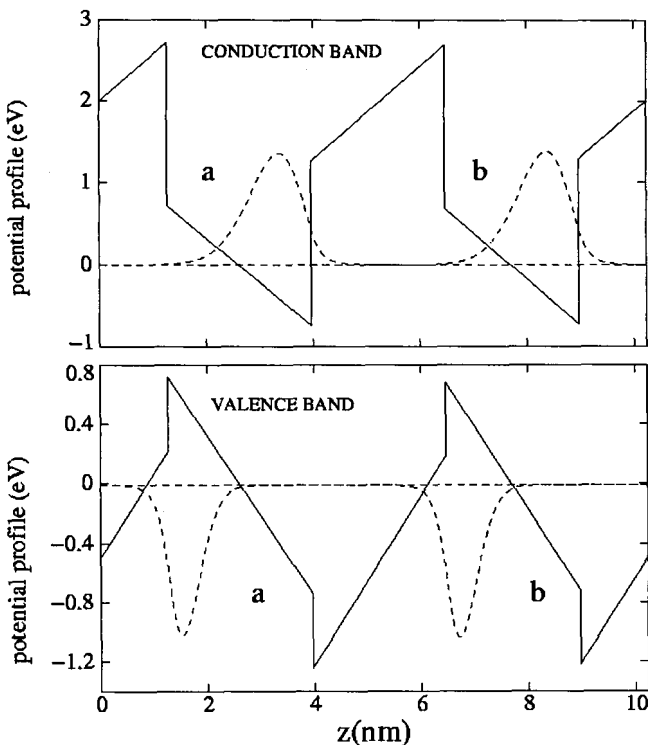


Fig. 7.5 Effects of the intrinsic electric field in a GaN-based QD molecule: schematic representation of the square-well potential profile for electrons and holes along the growth direction modified by the internal field (solid lines) and single-particle spatial charge distributions for electrons (e_a and e_b) and holes (h_a and h_b) (dashed curves).

if we consider two dots (*a* and *b*) along the growth direction and with one exciton each, we are left with two aligned dipoles which are both pointing in the same direction. As recalled before, this results in a negative dipole-dipole coupling term (see Eq.(7.3)). The energy shift $\Delta\mathcal{E}$ is opposite and its absolute value is doubled with respect to the configuration discussed in Section 7.2.2.1, in which the two dipoles are still parallel but lying side by side.

Let us now discuss the optical response of our *GaN macromolecule (a+b)* in Figure 7.5. Our calculations are based on the fully three-dimensional approach of Reference [Biolatti *et al.* (2000); Biolatti *et al.* (2002)]. The excitonic absorption spectrum in the presence of the intrinsic field is shown

in Figure 7.6 (solid curve). The two lowest optical transitions correspond to the formation of direct ground state excitons in dot *a* and *b*, respectively. Due to the strong built-in electric field in such heterostructures, it is known

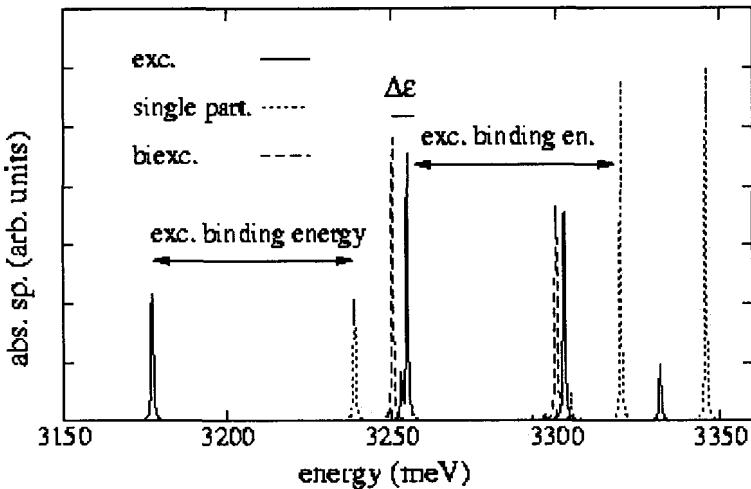


Fig. 7.6 Optical response of the GaN-based QD macromolecule in Figure 7.5: excitonic (solid curve) and biexcitonic absorption (dashed curve); the single-particle spectrum is also reported (dotted curve) as well as the corresponding exciton binding energy (see text).

that the excitonic transitions energies are red-shifted and, as it can be seen in Figure 7.6, the inter-band emission is fractions of eV below the GaN bulk bandgap energy (3.5 eV) (see also Figure 7.5). It is worth noticing that the difference in the ground state excitonic transitions of the two dots is one order of magnitude bigger than the one employed in [Biolatti *et al.* (2000); Biolatti *et al.* (2002)], and this is due to the presence of the strong intrinsic electric field in the growth direction. Moreover, the two ground state transitions have different amplitudes, due to the non-symmetric structure we are considering: indeed, the two dots have different heights along the growth direction, which implies that the internal electric field experienced by the carriers in each dot is not the same. As a result the oscillator strength — i.e., the overlap of electron and hole single-particle wavefunctions — changes according to the specific dot. The peaks which occur at higher energies correspond to optical transitions involving excited states of the in-plane parabolic potential in each QD.

We stress that, since the electric field is in the growth direction, the in-plane 2D confinement potentials for electrons and holes exhibit the same symmetry axis. It follows that, due to parity arguments, only a few inter-band optical transitions are allowed, which makes the interpretation as well as the energy-selective addressing of specific lines in the spectrum much easier. This is a distinguished advantage of the proposed GaN-based scheme, compared to the GaAs-based implementation previously discussed, where the presence of the in-plane field breaks all inter-band selection rules related to the 2D cylindrical symmetry of single-particle wavefunctions. This feature may be of crucial importance when considering energy-selective addressing schemes, since it allows to employ shorter light pulses, i.e., pulses with a larger spectral width.

Let us now discuss the biexcitonic spectrum (dashed curve in Figure 7.6); it describes the generation of a second electron-hole pair in the presence of a previously created exciton. Once again, the crucial feature in Figure 7.6 is the magnitude of the “biexcitonic shift” [Jacak *et al.* (1998)], i.e., the energy difference between the excitonic and the biexcitonic transition (see solid and dashed curves). For the QD structure under investigation we get an energy splitting of 4.4 meV, which is quite comparable to the one in [Biolatti *et al.* (2000); Biolatti *et al.* (2002)] and can still be resolved by sub-picosecond optical excitations.

In order to test the viability of this novel semiconductor-based quantum hardware in the framework of the quantum-computing scheme proposed in Section 7.2.2.1, we have performed a few simulated experiments of basic QIC processing. Our time-dependent simulations are based on the realistic state-of-the-art multi-QD structure depicted in Figure 7.5, for which $\mathcal{E}_a = 3.177 \text{ eV}$, $\mathcal{E}_b = 3.255 \text{ eV}$, and $\Delta\mathcal{E} = -4.4 \text{ meV}$ (see Figure 7.6). Our simulations are based again on a numerical solution of the Liouville-von Neumann equation; in this case inter-band recombination is described in terms of a $T_1 = 1 \text{ ns}$ while exciton-phonon dephasing is accounted for by a time $T_2 = 30 \text{ ps}$. We have repeated for the novel GaN structure the time-dependent analysis performed in Section 7.2.2.1, i.e., we have simulated again a CNOT quantum gate.

Figure 7.7A shows a simulated sequence of two-qubit operations driven by a two-color laser-pulse sequence (dashed curve in the upper panel). This realizes again the CNOT previously discussed (see Figure 7.4): the state of the second quantum dot is changed if and only if the first dot is in the state $|1\rangle$. Indeed, the multi-color laser-pulse train is able to perform first a π rotation of the qubit a ($|0\rangle_a \rightarrow |1\rangle_a$); then, the second pulse

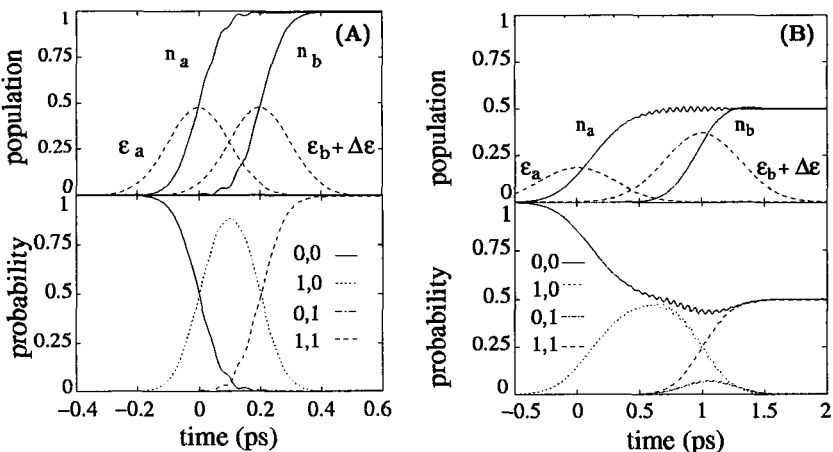


Fig. 7.7 Same as in Figure 7.4 but for the GaN-based molecule depicted in Figure 7.5 (see text).

is tuned to the frequency $\mathcal{E}_b + \Delta\mathcal{E}$, thus performing a π rotation of the qubit b ($|0\rangle_b \rightarrow |1\rangle_b$), since this corresponds to its renormalized transition energy when the neighbor qubit a is in state $|1\rangle_a$. The scenario described so far is confirmed by the time evolution of the exciton occupation numbers n_a and n_b (upper panel) as well as of the diagonal elements of the density matrix in our four-dimensional computational basis (lower panel). We stress that, again, the operation is performed on a sub-picosecond time scale; in particular, the time delay between the pulses is only $\delta t = 0.2$ ps.

Let us now come again to the ultrafast generation of entangled states shown in Figure 7.7B. As for the CNOT gate simulated in (A), initially, the system is in the state $|0,0\rangle \equiv |0\rangle_a \otimes |0\rangle_b$. The first laser pulse (at $t = 0$) is now tailored in such a way to induce a $\frac{\pi}{2}$ rotation of the qubit a : $|0,0\rangle \rightarrow (|0,0\rangle + |1,0\rangle)/\sqrt{2}$. At time $t = 0.4$ ps a second pulse induces a conditional π -rotation of the qubit b : $|0,0\rangle + |1,0\rangle \rightarrow |0,0\rangle + |1,1\rangle$. We stress again that the conditional operation simulated in Figure 7.7B plays a central role in any quantum information processing.

The experiments simulated above (see Figure 7.7) clearly show that the energy scale of the biexcitonic splitting $\Delta\mathcal{E}$ in our QD molecule — which is now totally driven/controlled by the built-in polarization field — is compatible with the sub-picosecond operation time scale of modern ultrafast laser technology [Shah (1996)].

7.2.3 Combination of charge and spin degrees of freedom

The implementation schemes discussed so far are both based on charge degrees of freedom corresponding to inter-band optical excitations in semiconductors. As such, on the one hand, they can be easily manipulated/controlled on a sub-picosecond time scale via properly tailored sequences of multicolor laser pulses; on the other hand, however, such excitonic states are known to suffer from relatively fast decoherence processes and are ultimately limited by inter-band radiative recombination. In this respect, the use of spin degrees of freedom seems to be preferable, as originally pointed out in [Loss and DiVincenzo (1998)]. It is then clear that the most desirable scenario would be a combination of charge and spin degrees of freedom able to merge the best of the two worlds.

In this spirit, we have recently proposed a novel implementation scheme for an all optical spin-based QIC with QDs [Pazy *et al.* (2003)]. While our qubit is the spin of an excess electron in a QD, quantum gate operations rely on swapping spin superpositions via short laser pulses to charged excitonic states. Thus we merge ideas from both the fields of spintronics and optoelectronics: using spin as quantum memory, and charge for the interaction between qubits, we can benefit (i) from the “low” spin decoherence rates of conduction electrons [Kikkawa *et al.* (1997)], and (ii) from ultrafast (sub-picosecond) optical gating of charge excitations. Coherent optical control [Imamoglu *et al.* (1999); Gupta *et al.* (2001)] of spins and excitons, and the interaction between excitons will allow the implementation of single and two-qubit gates, i.e., the full set of quantum operations to implement quantum computing.

More specifically, in [Pazy *et al.* (2003)] we consider an excess electron in a semiconductor QD, its spin degrees of freedom defining the qubit $|0\rangle$, $|1\rangle$. Our quantum register consists of an array of QDs each dot containing one excess conduction electron. Our primary goal was the implementation of a two-qubit phase gate. The dynamics required to perform the gate operation exploits a *Pauli-blocking* mechanism, as observed experimentally in QDs [Bonadeo *et al.* (1998b); Chen *et al.* (2000)]. We assume that the QDs can be individually addressed via laser excitation, by energy-selective addressing enabled by the size fluctuations of self-assembled QDs. As schematically depicted in Figures 7.8 and 7.9, the control of the phase accumulated by Coulomb interactions is obtained by shining a σ^+ polarized laser pulse on the QD, due to the Pauli exclusion principle a $|M_j^e = -1/2, M_j^h = +3/2\rangle$ electron-heavy hole pair is created

in the s-shell only if the excess electron — already present in the QD — has a spin projection $1/2$ (see Figure 7.8). Thus with a π -pulse we ob-

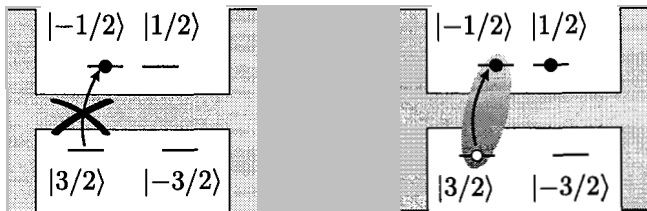


Fig. 7.8 Quantum dots and energy level scheme. Left: the excess electron is in state $| -1/2 \rangle \equiv | 0 \rangle$ and the transition induced by a σ^+ -polarized light is blocked. Right: the excess electron is in $| +1/2 \rangle \equiv | 1 \rangle$ and the exciton can be excited. After Reference [Pazy *et al.* (2003)].

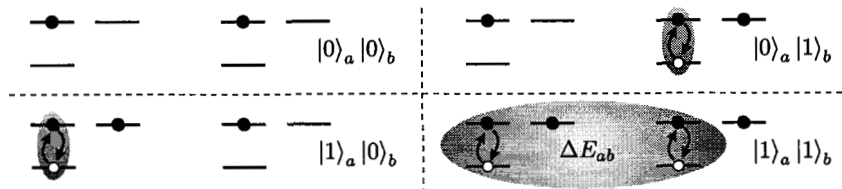


Fig. 7.9 Dynamics of the two-qubit gate for the computational basis states $|\alpha\rangle_a \otimes |\beta\rangle_b$ ($\alpha, \beta \in \{0, 1\}$). In the ideal case of perfect Pauli blocking, the effective dipole-dipole interaction is present only for the $|11\rangle$ component. After Reference [Pazy *et al.* (2003)].

tain an exciton conditional to the spin state (qubit) of the original excess electron. In this way one obtains precise spin control of the switching on (and off) of further Coulomb interactions. In particular, this allows the switching on of exciton-exciton interactions on neighboring quantum dots previously discussed conditional to the spins (qubits) being in state $|1\rangle \otimes |1\rangle$ (see Figure 7.9). We emphasize that the presence of the photo-generated electron-hole pair is only required during the gating, after which the latter will be annihilated via a second laser pulse. Thus excitonic interactions can be switched on and off, in contrast to the proposals based on charge excitations previously discussed. We stress that the two-pulse sequence previously discussed may also be replaced by a properly tailored single-pulse sequence, as shown in Figure 7.10 and discussed in [Pazy *et al.* (2003)].

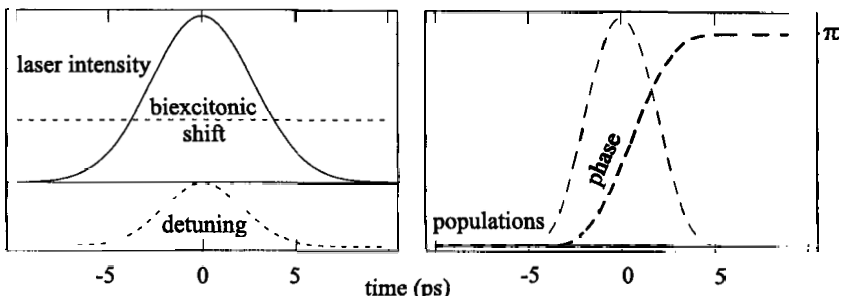


Fig. 7.10 Left panel: Pulse shapes and biexcitonic shift. Right panel: Biexcitonic population obtained starting from an initial state $|11\rangle$ (dashed line), $|00\rangle$, $|01\rangle$ or $|10\rangle$ (indistinguishable on the plot scale – solid line), and accumulated phase. We obtain the desired value $\theta = \pi$ while the population eventually left in the unwanted (single- and bi-) exciton states remains at most of the order of 10^{-6} . After Reference [Pazy *et al.* (2003)].

The simulated experiments reported in Figure 7.10 clearly show that the proposed implementation scheme benefits from the vast time scale separation between excitonic and spin dephasing processes. Whereas the proposed qubit is given by the spin of a conduction electron and thus decoheres on a microsecond time scale, our conditional two-qubit phase gate is driven/controlled by Coulomb interaction on a picosecond time scale. The ratio between gate operation time and the coherence time of the quantum memory is therefore of the order of 10^5 .

The above charge+spin implementation strategy has been extended to single-qubit operations (see Figure 7.11), thus leading to a full optically-driven spin-based QIC scheme. More specifically, what we have proposed



Fig. 7.11 Scheme for all-optical single-qubit rotations involving light holes. After Reference [Pazy *et al.* (2003)].

is to implement the single qubit gate via a Raman process involving the lowest light hole states $M_j^h = \pm 1/2$ which however, being excited hole

states, suffer from significant decoherence. On the other hand QDs can be grown where strain in II-VI semiconductors can shift the energy of the light holes to become the energetically lowest holes states in the dot, avoiding the above mentioned decoherence problems. In this case, we can apply the following pulse sequence: first a linearly polarized laser coupling the light-hole subband and the bottom of the conduction band (see Figure 7.11). Due to the Pauli principle, a π -pulse of such a light will promote an electron only into the unoccupied qubit state – processes (1) in Figure 7.11. The hole thus created is then recombined with the original excess electron via a further π -pulse of σ^+ light propagating in the plane orthogonal to the QD symmetry axis – processes (2) in Figure 7.11. By adjusting the duration and phase of the pulses, the net effect of the above pulse sequence is a coherent rotation between $|0\rangle$ and $|1\rangle$ on the fast ps time scale. Finally, we note that the two-qubit gate described above can also be adapted to this inverted heavy-light hole configuration.

7.2.3.1 *Artificial molecules as qubits and Raman adiabatic passages for the optical gating*

As already mentioned in the discussion of the above proposal, a major advancement towards a QD-based implementation of QIC would result from combining the most favorable features of the exciton-based schemes (ultra-fast optical gating, efficient Coulomb coupling between the qubits) with the long-lived memory of the electron spins. This is also the ultimate goal of the following implementation scheme [Troiani *et al.* (2003)], which relies on an efficient interplay between the spin and the charge degrees of freedom of the confined carriers: the former store the information, the latter provide the auxiliary states required for their optical manipulation. As an essential step within the quantum gate implementation, we propose to map literally the spin state $|\chi\rangle$ of each electron onto its charge state $\phi(\mathbf{r})$ by means of optically-induced (Raman) transitions: more specifically, $|0\rangle \equiv |\downarrow\rangle$ and $|1\rangle \equiv |\uparrow\rangle$ are mapped onto spatially separated orbitals, $\phi_{\downarrow,\uparrow}(\mathbf{r})$, and therefore produce different electrostatic fields, which are felt by the neighboring electrons (qubits). If simultaneously applied to two neighboring qubits, the overall process thus results in an effective spin-spin coupling, mediated by a Coulomb (dipole-dipole) interaction, that carries the information and thus allows the implementation of the conditional dynamics.

Let us start the discussion of the scheme by considering the physical implementation of the qubit, which we identify with the spin of an excess

electron confined in two vertically-coupled QDs (see Figure 7.12). An electric field is applied in the growth direction with a twofold purpose: first, it transfers the (single) excess electron from a nearby *n*-type reservoir to the artificial molecule, where further charging is suppressed because of the Coulomb blockade; second, it enhances the electron localization in one of the two dots (labeled as large, *L*, as compared to the small one, *S*). Although at this stage we shall not be too specific about the details of the quantum-dot molecule (model calculations will be presented in the following), we assume that in presence of a uniform magnetic field along *x* the electron eigenstates become a direct product of orbital and spin degrees of freedom, respectively

$$\begin{aligned} |0,1\rangle &= |L\rangle \otimes |S_x = \mp \frac{1}{2}\rangle \\ |2\rangle &= |S\rangle \otimes |S_x = -\frac{1}{2}\rangle, \end{aligned} \quad (7.4)$$

with $|L\rangle$ ($|S\rangle$) the orbital part associated to localization in the large (small) dot, and $|S_x = \pm \frac{1}{2}\rangle$ the spin part; states $|0\rangle$ and $|1\rangle$ will serve us for the qubit encoding, whereas state $|2\rangle$ is an auxiliary state, which will be used during gating. Finally, we introduce as a fourth (auxiliary) state $|3\rangle$, which allows optical coupling between the electrons states of Eq. (7.4), the negatively charged exciton state $|X^-\rangle$ [Hartmann *et al.* (2000)], i.e., an electron-hole complex consisting of two electrons and a single hole; besides, we assume that in the presence of the strong confinement along *z* the hole acquires a well-defined symmetry because of the splitting of heavy- and light-hole states. Thus, in the qubit manipulation by means of external laser pulses the light polarization allows to control the spin degrees of freedom (e.g., to individually address the 0–3 and 1–3 transitions), whereas the light frequency serves as a control for the orbital part [Turchette *et al.* (1995); Imamoglu *et al.* (1999)] (e.g., to individually address 0–3 and 2–3). The resulting optical selection rules are sketched in Figure 7.12. As a relevant point, the states encoding the information are stable against the fast relaxation of the orbital degrees of freedom, because they both correspond to the lowest orbital $\langle r|L\rangle = \phi_{0,1}(r)$. The auxiliary state $|2\rangle$ corresponds to an intraband excitation: however, (i) it is only going to be occupied during gating (see below), and (ii) its inter-dot relaxation towards the lowest orbital $|L\rangle$ is highly inefficient as compared to an analogous intradot process. In fact, this is one of the main reasons why we propose the qubit identification with an artificial molecule: the presence of an auxiliary state which is stable on the gating time scale and spatially separated from the ones encoding the information.

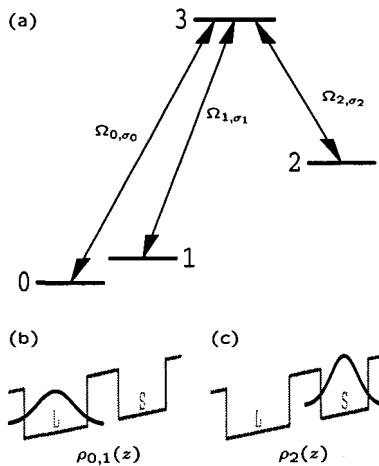


Fig. 7.12 Schematic representation of our proposed qubit implementation, which consists of two vertically coupled quantum dots in presence of an external electric field. (a) Level scheme as described in the text: single-electron states $|0\rangle$ and $|1\rangle$ (electron in large dot L and $|S_x = \mp\frac{1}{2}\rangle$, respectively) which are used to encode the quantum information; auxiliary state $|2\rangle$ (electron in small dot S and $|S_x = -\frac{1}{2}\rangle$); charged-exciton state $|3\rangle$ which allows optical coupling between all single-electron states through frequency-selective and linearly polarized laser pulses (Rabi energies Ω_{i,σ_i} , light polarizations $\sigma_{1,2} = x$ and $\sigma_1 = y$). (b) ((c)) schematic of the electron distribution along z corresponding to state L (S).

One of the main limits of the QIC schemes involving the inter-band excitations is the loss of information due to the radiative recombination of the electron-hole pairs. In order to suppress this channel of decoherence, we propose to perform all the quantum gates solely by means of stimulated Raman adiabatic passages (STIRAPs). This technique, which was originally developed in the field of atomic physics [Bergmann *et al.*(1998)], allows to channel the system between two long-lived states $|\psi_i\rangle$ and $|\psi_f\rangle$, by exploiting their optical coupling to interconnecting leaky states, but without ever populating them. A STIRAP can be essentially thought of as the adiabatic evolution of a renormalized (dressed) radiation-matter state, which is coherently driven by a sequence of laser pulses in such a way that (i) it coincides with $|\psi_i\rangle$ and $|\psi_f\rangle$ at the beginning and at the end of the process, respectively, and (ii) remains orthogonal to all the leaky states throughout its time evolution. As a further advantage, such control does not require a detailed knowledge of the system parameters (i.e., oscillator strengths) and therefore is of very robust nature, thus rendering this scheme

ideal for quantum control in the solid state [Hohenester *et al.* (2000); Goan and Milburn (2001); Pazy *et al.* (2001); Cortez. *et al.* (2002); D'Amico and Rossi (2002)].

Quite generally, the required sequence of the laser pulses depends on the initial state in which the system is prepared, whereas a quantum gate is supposed to be effective on a general and unknown state. However, specific level shemes allow to overcome this problem and to make quantum gates out of proper sequences of adiabatic passages. In particular, in a recent paper Kis and Renzoni [Kis and Renzoni (2002)] extended the three-level version of the STIRAP by adding a long-lived auxiliary state (here $|2\rangle$), and showed that this allows to perform any unitary transformation within the subspace $\{|0\rangle, |1\rangle\}$, without the knowledge of the initial state being required. For the sake of clarity, let us briefly rephrase the main steps of this control within the present scheme: suppose that initially the system wavefunction is $|\Psi\rangle = |L\rangle \otimes (\alpha|S_x = -\frac{1}{2}\rangle + \beta|S_x = +\frac{1}{2}\rangle) \equiv \alpha|0\rangle + \beta|1\rangle$. Next, the quantum dot structure is subject to a first STIRAP, consisting of a sequence of three laser pulses: the first one (Stokes pulse) couples the states 2 and 3; the second and third ones (pump pulses) affect the 0-3 and 1-3 transitions, with Rabi frequencies $\Omega_0(t) = \Omega(t) \cos \chi$ and $\Omega_1(t) = \Omega(t) \exp(i\eta) \sin \chi$, respectively [Kis and Renzoni (2002)] (here $\Omega(t)$ is the envelope, χ and η are phase factors). The pump lasers define two orthogonal dressed states, $|S_C(\eta, \chi)\rangle$ and $|S_{NC}(\eta, \chi)\rangle$, in terms of which we can express any initial state: $|\Psi_i\rangle = \alpha'|S_C\rangle + \beta'|S_{NC}\rangle$. The effect of the first pulse sequence is essentially that of transferring the $|S_C\rangle$ (coupled) component of $|\Psi\rangle$ in the state $|2\rangle$, while leaving unaffected the $|S_{NC}\rangle$ (non-coupled) part. Incidentally, with a specific choice of the laser parameters ($\chi = -\pi/2$ and $\eta = 0$) $|S_C\rangle = |1\rangle$ and this first sequence maps the information stored in the electron spin onto the orbital degrees of freedom:

$$|\Psi\rangle \longrightarrow (\alpha|L\rangle + \beta|S\rangle) \otimes |S_x = -1/2\rangle = \alpha|0\rangle + \beta|2\rangle; \quad (7.5)$$

as discussed in the following, this possibility is crucial to the implementation of the conditional dynamics within the present scheme. The single-qubit rotation is completed by a second, reversed STIRAP (pump pulses before the Stokes one), that moves the $|2\rangle$ component of the state vector back to $|S_C\rangle$, giving rise to a final state $|\Psi_f\rangle = \alpha'|S_C\rangle + e^{i\delta}\beta'|S_{NC}\rangle$. It is easily shown that this particular rotation actually corresponds to the most general transformation of the SU_2 group as a function of χ , η and δ , all depending from the relative phases of the laser pulses. Note that the different energies

of the electron states (0, 1 and 2) considered in the present case result in additional dynamic phase factors, which should be incorporated into the quantum algorithm.

As already mentioned, the key point in the implementation of the conditional (controlled) dynamics within the present scheme is represented by the electrostatic potential changes resulting from the population of the auxiliary state 2. In Figure 7.13 we show, for example, the evolution corresponding to a C-NOT gate applied to an initial state $|1\rangle_c \otimes |0\rangle_t$, where c and t denote the control and target qubit, respectively. In the idle state the information of both qubits is encoded in the respective electron spins; a first STIRAP process applied to the control qubit then maps the $|S_x = +\frac{1}{2}\rangle$ component onto the orbital $[\phi_2(\mathbf{r})]_c$ independent of the target qubit setting, as shown in Figure 7.13b. In what follows, we shall exploit the fact that this modified charge distribution exerts a potential change on the target qubit and leads to different transition frequencies. Thus, in the next step, Figure 7.13c, the double STIRAP pulse sequence discussed above is applied to the target qubit with the modified laser frequencies; apparently, this procedure rotates the target qubit dependent on the control qubit setting. Finally, the quantum information of the control qubit is mapped back to the spin degrees of freedom, Figure 7.13d.

By now the strength of our present proposal should have become obvious: its ability to map the quantum information between spin and orbital degrees of freedom. On the one hand, this allows for a high-finesse gating through stimulated Raman adiabatic passage. On the other hand, it becomes possible to turn on selectively qubit-qubit interactions only during gating; this inter-qubit control emerges naturally for the double-dot structure under investigation without requiring additional time-dependent electric or magnetic fields. Thus, the present scheme fully benefits from the long spin coherence and the ultrafast optical gating.

As a final step, we comment on the possibility of designing a quantum dot structure with the desired level scheme of Figure 7.12. Quite generally, the relevant features for the implementation of such a scheme are the following: (i) single-electron wavefunctions localized in either dot, in order to minimize the environment losses during gating and to maximize the difference between the dipole moments associated to $\phi_0^e(\mathbf{r}) = \phi_1^e(\mathbf{r})$ and $\phi_2^e(\mathbf{r})$; (ii) a charged-exciton state with the hole delocalized over the double-dot structure (such that all transitions between 0–3, 1–3, and 2–3 acquire comparable oscillator strengths); (iii) energetically well separated transition frequencies ω_0 and ω_2 , in order to spectrally resolve the 0–3 and 2–3 transitions,

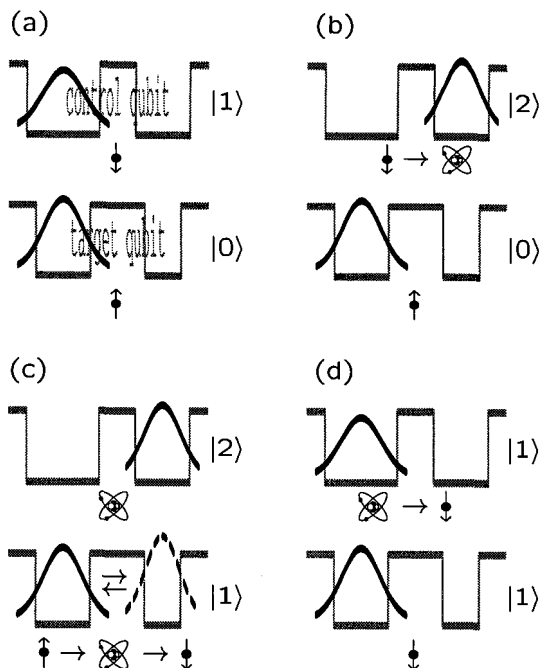


Fig. 7.13 Implementation of the controlled-NOT gate for an initial state $|1\rangle_c \otimes |0\rangle_t$ (panel (a)); (b) a first sequence of adiabatic passages applied to the control qubit transfers the electron to the smaller dot S_c and changes the electrostatic potential; (c) a NOT transformation is applied to the target qubit with the laser frequencies tuned to the modified transition energies; (d) a final STIRAP sequence brings back the control qubit to its initial state. The symbols below each dot-molecule indicate the nature of information storage (spin or orbital) at different stages of the quantum gate.

that are induced by optical fields with the same polarization. Model calculations were performed to demonstrate that such manifold requirements can indeed be simultaneously fulfilled. We calculate the single- and few-particle states for prototypical GaAs/AlGaAs double-dot structures within the envelope-function and effective-mass approximations, assuming a prototypical confinement potential which is double-well like along z and parabolic in the in-plane directions. In addition, we consider: a slight asymmetry in the double-dot structure (well widths of $l_L = 3.5\text{nm}$ and $l_S = 3.6\text{nm}$, respectively, and an inter-dot distance $d = 7\text{nm}$); an applied electric field; the consideration of a charged-exciton state with light-hole character, in order to enhance the inter-dot tunneling of holes (alternatively, it might be advantageous to use type-II quantum dots where the hole is only Coulomb-bound

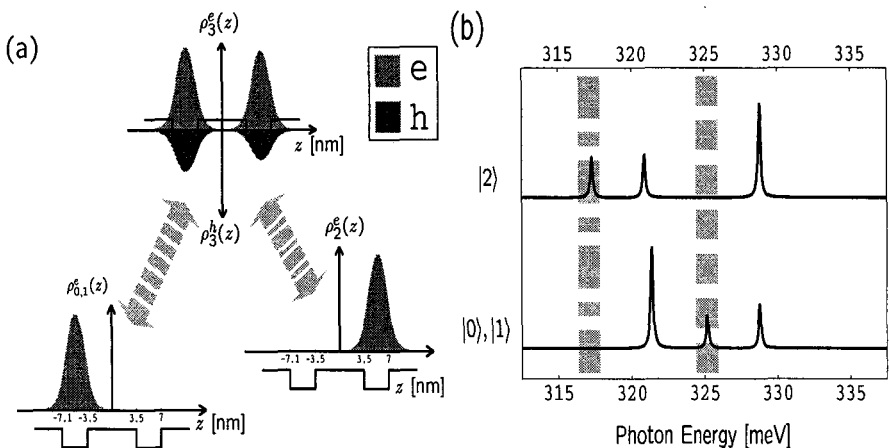


Fig. 7.14 Results of our calculations. (a) Spatial distributions along z for the electron states 0, 1, 2 (lower plots) and for the exciton state X^- (upper plot; light and dark gray corresponds to electrons and holes, respectively). The lateral confinement of the carriers is produced by a parabolic potential, with $\hbar\omega_{e,h} = 60, 50$ meV, while the applied electric field is $\mathbf{F} = -3\hat{z} + 50(\hat{x} + \hat{y})$ kV/cm. (b) Absorption spectra corresponding to the three possible initial states 0, 1 (lower spectrum) and 2 (upper spectrum), where the photon zero corresponds to the semiconductor bandgap. The shaded regions indicate the energies of the pump and Stokes pulses. The Zeeman splitting of the 0 and 1 states, induced by the magnetic field is neglected in the calculations. The physical parameters (GaAs) are the following: $m_{e,h}^* = 0.067, 0.80 m_0$, band offsets $V_0^{e,h} = 400, 215$ meV, dielectric constant $\epsilon = 12.9$.

and its wavefunction becomes strongly delocalized).

Results of our calculations are shown in Figure 7.14. Panel (a) shows the carrier distributions along z : the two lower plots represent the single-electron densities $\rho_i^e(z) = |\phi_i^e(z)|^2$; the small overlap between $\phi_{0,1}^e$ and ϕ_2^e allows to almost completely suppress environment losses due to phonon-assisted tunneling during gating, as discussed in more detail by Pazy *et al.* [Goan and Milburn (2001); Pazy *et al.* (2001); Cortez. *et al.* (2002); D'Amico and Rossi (2002)], where lifetimes of the order of nanoseconds were estimated; in the upper part of panel (a) we report the electron (light gray) and hole (dark gray) densities $\rho_3^{e,h}(z) = \int dx dy \langle 3 | \hat{\psi}_{e,h}^\dagger(\mathbf{r}) \hat{\psi}_{e,h}(\mathbf{r}) | 3 \rangle$ and $\hat{\psi}_{e,h}(\mathbf{r})$ the field operator for electrons and holes, respectively. While the use of light fields with linear polarizations allows the coupling of the charged exciton with electron states sharing the orbital state and with opposite spins, the present overlap of $\rho^h(z)$ with both $\rho_{0,1}^e(z)$ and $\rho_2^e(z)$ ensures comparable

oscillator strengths to transitions involving states where electrons are localized in opposite dots (irrespective of their spin orientations). This indeed can be seen in Figure 3b where we plot the absorption spectra associated to the three initial states, with the transitions 0–3 (1–3) and 2–3 indicated by the shaded regions. The additional peaks with larger oscillator strength are attributed to additional intradot transitions; however, the energetic separation between the peaks is of the order of a few meV and is thus certainly large enough to suppress such undesired transitions by use of laser-pulse widths of the order of tens of picoseconds (for more sophisticated quantum control strategies see [Borzì *et al.* (2002)]). Thus, although more realistic calculations including finer details of the material and dot parameters, e.g., strain distributions or piezoelectric fields, might introduce moderate modifications, we believe that our model calculations clearly demonstrate that the level scheme of Figure 7.12 can be designed in state-of-the-art quantum dot samples and could open the possibility for much more efficient and sophisticated quantum gates.

7.3 Summary and Conclusions

In summary, we have reviewed potential semiconductor-based schemes for the implementation of QIC processing devices. After a brief introduction on the fundamentals of QIC theory, we have presented and discussed an all-optical approach based on inter-band excitations (excitonic states) in coupled QD structures; we have seen that energy-selected optical transitions in realistic state-of-the-art semiconductor macroatoms/molecules are good candidates for quantum information encoding and manipulation. As confirmed by our simulated experiments, for both GaAs- and GaN-based nanostructures the sub-picosecond time scale of ultrafast laser spectroscopy allows for a relatively large number of elementary operations. This is particularly important for the case of charge plus spin implementation schemes, which allow — in principle — 10^5 quantum operation within the spin decoherence time. It should be stressed that, in addition to the implementation of basic QIC operations, one needs to perform a corresponding quantum-state read out; to this end, a number of ideas have been recently put forward [Goan and Milburn (2001); Pazy *et al.* (2001); Cortez. *et al.* (2002); D'Amico and Rossi (2002)].

We can therefore conclude that, in spite of a number of technological limitations, state-of-the-art semiconductor nanostructures — like Coulomb-

coupled QDs — constitute potential candidates for the realization of prototypical QIC processing devices.

Acknowledgments

We wish to thank Tommaso Calarco, Sergio De Rinaldis, and Peter Zoller for their relevant contributions to part of the research activity reviewed in the paper. We are also grateful to David DiVincenzo and Seth Lloyd for stimulating and fruitful discussions.

This work has been supported in part by the European Commission through the Research Project *Semiconductor-based implementation of Quantum Information Devices (SQID)* within the *Future and Emerging Technologies (FET)* programme.

Bibliography

- Andreev, R.D. and O'Reilly, E.O. (2000). Theory of the electronic structure of GaN/AlN hexagonal quantum dots, *Phys. Rev. B* **62**: 15851.
- Arlery, M., Rouvière, J.L., Widmann, F., Daudin, B., Feuillet, G. and Mariette, H. (1999). Quantitative characterization of GaN quantum-dot structures in AlN by high-resolution transmission electron microscopy, *Appl. Phys. Lett.* **74**: 3287.
- Bergmann, K., Theuer, H. and Shore, B.W. (1998). Coherent population transfer among quantum states of atoms and molecules, *Rev. Mod. Phys.* **70**: 1003.
- Biolatti, E., Iotti, R.C., Zanardi, P. and Rossi, F. (2000). Quantum Information Processing with Semiconductor Macroatoms, *Phys. Rev. Lett.* **85**: 5647.
- Biolatti, E., D'Amico, I., Zanardi, P. and Rossi, F. (2002). Electro-optical properties of semiconductor quantum dots: Application to quantum information processing, *Phys. Rev. B* **65**: 075306.
- Bonadeo, N.H., Erland, J., Gammon, D., Park, D., Katzer, D.S. and Steel, D.G. (1998). Coherent Optical Control of the Quantum State of a Single Quantum Dot, *Science* **282**: 1473.
- Bonadeo, N.H., Gang Chen, Gammon, D., Katzer, D.S., Park, D. and Steel, D.G. (1998). Nonlinear Nano-Optics: Probing One Exciton at a Time *Phys. Rev. Lett.* **81**: 2759.
- Borri, P., Langbein, W., Schneider, S., Woggon, U., Sellin, R.L., Ouyang, D. and Bimberg, D. (2001). Ultralong Dephasing Time in InGaAs Quantum Dots *Phys. Rev. Lett.* **87**: 157401.
- Borzì A., Stadler, G. and Hohenester, U. (2002). Optimal quantum control in nanostructures: Theory and application to a generic three-level system, *Phys. Rev. A* **66**: 053811.

- Chen, G., Bonadeo, N.H., Steel, D.G., Gammon, D., Katzer, D.S., Park, D. and Sham, L.J. (2000). Optically Induced Entanglement of Excitons in a Single Quantum Dot, *Science* **289**: 1906.
- Cingolani, R., Botchkarev, A., Tang, H., Morkoc, H., Traetta, G., Coli, G., Lomascolo, M., Di Carlo, A., Della Sala, F. and Lugli, P. (2000). Spontaneous polarization and piezoelectric field in GaN/Al_{0.15}Ga_{0.85}N quantum wells: Impact on the optical spectra, *Phys. Rev. B* **61**: 2711.
- Cirac, J.I. and Zoller, P. (1995). Quantum Computations with Cold Trapped Ions, *Phys. Rev. Lett.* **74**: 4091.
- Cortez, S., Krebs, O., Laurent, S., Senes, M., Marie, X., Voisin, P., Ferreira, R., Bastard, G., Grard, J-M. and Amand, T. (2002). Optically Driven Spin Memory in n-Doped InAs-GaAs Quantum Dots, *Phys. Rev. Lett.* **89**: 207401.
- D'Amico, I. and Rossi, F. (2001). Field-induced Coulomb coupling in semiconductor macroatoms: Application to "single-electron" quantum devices, *Appl. Phys. Lett.* **79**: 1676.
- D'Amico, I. and Rossi, F. (2002). All-Optical Single-Electron Read-Out Devices Based on GaN Quantum Dots, *Appl. Phys. Lett.*, **81**: 5213.
- De Rinaldis, S., D'Amico, I., Biolatti, E., Rinaldi, R., Cingolani, R. and Rossi, F. (2002). Intrinsic exciton-exciton coupling in GaN-based quantum dots: Application to solid-state quantum computing, *Phys. Rev. B* **65**: 081309.
- DiVincenzo, D.P. and Bennet, C. (2000). Quantum information and computation, *Nature* **404**: 247, and references therein.
- Gershenfeld, N. and Chuang, I. (1997). Bulk Spin-Resonance Quantum Computation, *Science* **275**: 350.
- Goan, H.-S. and Milburn, G.J. (2001). Dynamics of a mesoscopic charge quantum bit under continuous quantum measurement, *Phys. Rev. B* **64**: 235307.
- Gupta, J.A., Knobel, R., Samarth, N. and Awschalom, D.D. (2001). Ultrafast Manipulation of Electron Spin Coherence, *Science* **292**: 2458.
- Hartmann, A., Ducommun, Y., Kapon, E., Hohenester, U. and Molinari, E. (2000). Few-Particle Effects in Semiconductor Quantum Dots: Observation of Multicharged Excitons, *Phys. Rev. Lett.* **84**: 5648.
- Hohenester, U., Troiani, F., Molinari, E., Panzarini, G. and Machiavello, C. (2000). Coherent population transfer in coupled semiconductor quantum dots, *Appl. Phys. Lett.* **77**: 1864.
- Imamoglu, A., Awschalom, D.D., Burkard, G., DiVincenzo, D.P., Loss, D., Sherwin, M. and Small, A. (1999). Quantum Information Processing Using Quantum Dot Spins and Cavity QED, *Phys. Rev. Lett.* **83**: 4204.
- Jacak, L., Hawrylak, P., Wojs, A. (1998). *Quantum Dots* (Springer, Berlin).
- Kamada, H., Gotoh, H., Temmyo, J., Takagahara, T. and Ando, H. (2001). Exciton Rabi Oscillation in a Single Quantum Dot, *Phys. Rev. Lett.* **87**: 246401.
- Kikkawa, J.M., Smorchkova, I.P., Samarth, N. and Awschalom, D.D. (1997). Room-Temperature Spin Memory in Two-Dimensional Electron Gases, *Science* **277**: 1284.
- Kis, Z. and Renzoni, F. (2002). Qubit rotation by stimulated Raman adiabatic passage, *Phys. Rev. A* **65**: 032318.

- Krummheuer, B., Axt, V.M. and Kuhn, T. (2002). Theory of pure dephasing and the resulting absorption line shape in semiconductor quantum dots, *Phys. Rev. B* **65**: 195313.
- Li, X., Yanwen Wu, Steel, D.G., Gammon, D., Stievater, T.H., Katzer, D.S., Park, D., Piermarocchi, C. and Sham, L.J. (2003). An All-Optical Quantum Gate in a Semiconductor Quantum Dot, *Science* **301**: 809.
- Loss, D. and DiVincenzo, D.P. (1998). Quantum computation with quantum dots, *Phys. Rev. A* **57**: 120.
- Monroe, C., Meekhof, D.M., King, B.E., Itano, W.M. and Wineland, D.J. (1995). Demonstration of a Fundamental Quantum Logic Gate, *Phys. Rev. Lett.* **75**: 4714.
- Mooij, J.E., Orlando, T.P., Levitov, L., Lin Tian, van der Wal, C.H. and Lloyd, S. (1999). Josephson Persistent-Current Qubit, *Science* **285**: 1036.
- Pazy, E., D'Amico, I., Zanardi, P. and Rossi, F. (2001). Storage Qubits and Their Potential Implementation Through a Semiconductor Double Quantum Dot, *Phys. Rev. B* **64**: 195320.
- Pazy, E., Biolatti, E., Calarco, T., D'Amico, I., Zanardi, P., Rossi, F. and Zoller, P. (2003). Spin-based optical quantum gates via Pauli blocking in semiconductor quantum dots, *Europhys. Lett.* **62**: 175.
- Pellizzari, T., Gardiner, S. A., Cirac, J. I. and Zoller, P. (1995). Decoherence, Continuous Observation, and Quantum Computing: A Cavity QED Model, *Phys. Rev. Lett.* **75**: 3788.
- Shah, J. (1996). *Ultrafast Spectroscopy of Semiconductors and Semiconductor Nanostructures* (Springer, Berlin).
- Shnirman, A., Schön, G. and Hermon, Z. (1997). Quantum Manipulations of Small Josephson Junctions, *Phys. Rev. Lett.* **79**: 2371.
- Sorensen, A. and Mølmer, K. (1999). Quantum Computation with Ions in Thermal Motion, *Phys. Rev. Lett.* **82**: 1971.
- Stievater, T.H., Xiaojin Li, Steel, D.G., Gammon, D., Katzer, D.S., Park, D., Piermarocchi, C. and Sham, L.J. (2001). Rabi Oscillations of Excitons in Single Quantum Dots, *Phys. Rev. Lett.* **87**: 133603.
- Troiani, F., Hohenester, U. and Molinari, E. (2000). Exploiting exciton-exciton interactions in semiconductor quantum dots for quantum-information processing, *Phys. Rev. B* **62**: 2263.
- Troiani, F., Hohenester, U. and Molinari, E. (2003). High-Finesse Optical Quantum Gates for Electron Spins in Artificial Molecules, *Phys. Rev. Lett.* **90**: 206802.
- Turchette, Q.A., Hood, C.J., Lange, W., Mabuchi, H. and Kimble, H.J. (1995). Measurement of Conditional Phase Shifts for Quantum Logic, *Phys. Rev. Lett.* **75**: 4710.
- Vagov, A., Axt, V.M. and Kuhn, T. (2002). Electron-phonon dynamics in optically excited quantum dots: Exact solution for multiple ultrashort laser pulses, *Phys. Rev. B* **66**: 165312.
- Widmann, F., Simon, J., Daudin, B., Feuillet, G., Rouvire, J.L., Pelekanos, N.T. and Fishman, G. (1998). Blue-light emission from GaN self-assembled quantum dots due to giant piezoelectric effect, *Phys. Rev. B* **58**: 15989.

- Widmann, F., Daudin, B., Feuillet, G., Samson, Y., Rouvière, J.L. and Pelekanos, N. (1998). Growth kinetics and optical properties of self-organized GaN quantum dots, *J. Appl. Phys.* **83**: 7618.
- Zanardi, P. and Rossi, F. (1998). Quantum Information in Semiconductors: Noiseless Encoding in a Quantum-Dot Array, *Phys. Rev. Lett.* **81**: 4752.

Chapter 8

Novel Devices for the Measurement of Electronic States in Semiconductor Quantum Dots

I. D'Amico

Institute for Scientific Interchange (ISI)

Villa Gualino

viale Settimio Severo 65

10133 Torino, Italy

F. Rossi

Dipartimento di Fisica, Politecnico di Torino

Corso Duca degli Abruzzi 24

10129 Torino, Italy

8.1 Introduction

As underlined in previous chapters (see Chapters 1 and 4), few particle Coulomb interactions are enhanced in quantum dot based nanostructures as well as being crucial for the functioning of quantum computing devices based on excitonic conditional dynamics. Unfortunately exact diagonalization calculations of the related many-body Hamiltonian are usually cumbersome and computationally time consuming [Biolatti *et al.* (2000); Biolatti *et al.* (2002)]. In this chapter we shall review simplified models able to properly describe excitonic binding as well as inter-dot Coulomb coupling in GaAs-based (see Section 8.2) [D'Amico and Rossi (2001)] as well as GaN-based (see Section 8.3) [D'Amico and Rossi (2002)] quantum dots (QDs). Their analytical solution allows to identify suitable parameter sets needed to employ coupled QD structure as semiconductor-based hardware for quantum information processing (see Chapter 7) as well as

to describe novel devices based on the control of exciton-exciton as well as exciton-single particle Coulomb coupling in semiconductor quantum dots. Such interactions are controlled and magnified by the presence of a static external or built-in electric field. In this context we will describe in detail two measuring devices. The first is a semiconductor based implementation of the quantum storage bit (see Section 8.4) [Pazy *et al.* (2001)], which allows for a qubit measurement scheme based on stimulated Raman adiabatic passage (STIRAP); the second is an all-optical read-out device (see Section 8.5), which uses GaN-based QDs as hardware and detects the charge state of a nanoscopic system.

Quantum dots represent the extreme evolution of low dimensional structures. In contrast to quantum wells and wires, they exhibit a discrete — i.e., atomic-like — energy spectrum and their optical response is dominated by few-particle/exciton effects. During the 90s, self-assembling techniques for QDs have been developed (particularly used is the Stranski-Krastanow growth mode). These techniques allow for a control of the areal density (between 10^9 to 10^{12} cm^{-2}) by varying the total deposition of the material for the QD layer. The in-plane average size of the dots usually vary between 10 to 50 nm, with a size fluctuation in the same sample which can be reduced to few percents depending on the growing conditions. Such a spontaneous size fluctuation is responsible for the inhomogeneous broadening of the photoluminescence spectrum but can be also used to implement energy-selective addressing schemes (See Chapter 7). Self-assembled QDs show high optical efficiency due both to the strong carrier confinement (and to the resulting higher coupling with electromagnetic fields) and to the absence of material degradation which can instead be induced, when QDs are produced by nano-lithography techniques. Self-assembled QDs present a symmetric in-plane confinement potential (which paves the road to an easier engineering of their electronic structure) and a stronger confinement in the growth direction. The possibility of optically-driving their excitations allows for ultrafast state manipulation and coherent control of the few particle dynamics, a basic request for quantum computing devices [Biolatti *et al.* (2000); Biolatti *et al.* (2002)]. As discussed in Chapter 2, due to strain propagation through the barrier which separates different QD layers, similar-size QDs tend to vertically-align, enhancing vertical coupling between different QDs. Such structures, which have been proposed as qubit arrays in quantum information/computation schemes (See Chapter 7) [Biolatti *et al.* (2000); Biolatti *et al.* (2002); De Rinaldis *et al.* (2002a)], will be the subject of the present chapter.

Self-organized QDs have been successfully fabricated using a wide range of semiconductor materials; they include III-V QD structures based on GaAs as well as on GaN compounds. The characterization of GaN-based quantum dots is still incomplete, but interesting properties such as their long spin decoherence time [Beschoten *et al.* (2001)] or the presence of a built-in electric field as strong as few MeV/cm [Andreev and O'Reilly (2000); Arlery *et al.* (1999); Widmann *et al.* (1998a); Widmann *et al.* (1998b)] have already been demonstrated. GaN systems have a wider bandgap (3.5 eV) compared to GaAs-based ones (1.5 eV). Moreover, whereas GaAs and most of the other III-V compounds have a cubic (zincblende) structure, GaN (as well as other nitrides) has a hexagonal (wurzite) structure which leads to strong built-in piezoelectric fields (of the order of MV/cm). As a consequence, in these nanostructures excitonic transitions are red-shifted, and the corresponding inter-band emission is fractions of eV below the bulk GaN bandgap. The strong built-in electric field which characterizes wurzite GaN heterostructures, is the sum of the spontaneous polarization and the piezoelectric field. Spontaneous polarization charge accumulates at the GaN/AlN interfaces as a consequence of a slight distortion of GaN and AlN unit cells, compared to those of an ideal hexagonal crystal. Piezoelectric fields are caused by uniform strain along the (0001) direction. Contrary to GaN/AlGaN quantum wells —where the spontaneous-polarization contribution is dominant [Cingolani *et al.* (2000)]— in QDs the strain-induced piezoelectric field and the spontaneous-polarization potential are of similar magnitude and sign, both oriented along the growth direction. The strength of the intrinsic field along such direction is almost the same inside and outside the dot, but it is antiparallel to the growth direction inside the QDs, inverting its sign outside [Andreev and O'Reilly (2000); Arlery *et al.* (1999); Widmann *et al.* (1998a); Widmann *et al.* (1998b)]. Its importance in relation to single-electron devices lays on the possibility of creating strong bonds between neighboring quantum dots which can be switched on and off optically. Under its action in fact, electrons and holes are driven in opposite directions, so to create electrical dipoles which interact with energies of the order of few meV (see Figure 7.5) [De Rinaldis *et al.* (2002a); De Rinaldis *et al.* (2002b)]; this effect is, for example, the key ingredient for the GaN-based quantum computation/information processing device described in Chapter 7 [De Rinaldis *et al.* (2002a)].

The aim of this chapter is first of all to provide simple tools for estimating few particle Coulomb interactions and to study how Coulomb correlated

few-electron/exciton states are affected by the presence of a static external or built-in electric field (see Sections 8.2 [D'Amico and Rossi (2001)] and 8.3 [D'Amico and Rossi (2002)]). The analytical models described here represent an ideal tool to scan the parameter space, which usually depends non trivially on many variables, and to quickly obtain the optimal structure parameters for QD-based single-electron/exciton devices. We shall then use such an analytical approach to (i) single out systems with large exciton-exciton interaction energies (biexcitonic shift) – crucial property in ultrafast all-optical conditional quantum gates [Biolatti *et al.* (2000); Biolatti *et al.* (2002); De Rinaldis *et al.* (2002a)] – and (ii) analyze single particle-exciton interactions in view of device applications, such as the ones proposed in Section 8.4 (storage qubit [Pazy *et al.* (2001)]) and in Section 8.5 (read-out device [D'Amico and Rossi (2002)]).

8.2 Field-Induced Exciton-Exciton Coupling in Semiconductor Quantum Dots with no Intrinsic Bias

We shall start by considering how the electric field acts on an exciton in a single QD. If the field is absent, charge neutrality is observed. Indeed, assuming that electron and hole experience the same quantum confinement, it is possible to show that there is almost no net Coulomb interaction among excitons belonging to the same degenerate “shell” [Hawrylak *et al.* (2000); Bayer *et al.* (2000)].

In contrast, an external electric field pulls apart charges opposite in sign, i.e. electrons and holes, as it can be seen in the panel (A) of Figure 8.1: each exciton is turned into an electrical dipole and the transition energies are red-shifted according to the Stark shift. The net Coulomb interaction among excitons is now different from zero even if we consider two excitons in the same shell and with the same single-particle carrier confinement for electrons and holes.

In Figure 8.1 we show the value of the biexcitonic shift $\Delta\mathcal{E}$ as a function of the applied electric field. Here, this quantity is obtained by a direct diagonalization of the three-dimensional Hamiltonian describing the Coulomb-correlated few-particle system quantum confined within a realistic GaAs-based QD structure [Biolatti *et al.* (2000); Biolatti *et al.* (2002)]. It is worth pointing out that, in the single-QD case (panel (B)), the biexcitonic shift can be not only tuned at will, but its sign can even be reversed: in fact, for small values of the field E this is mainly due to the exchange

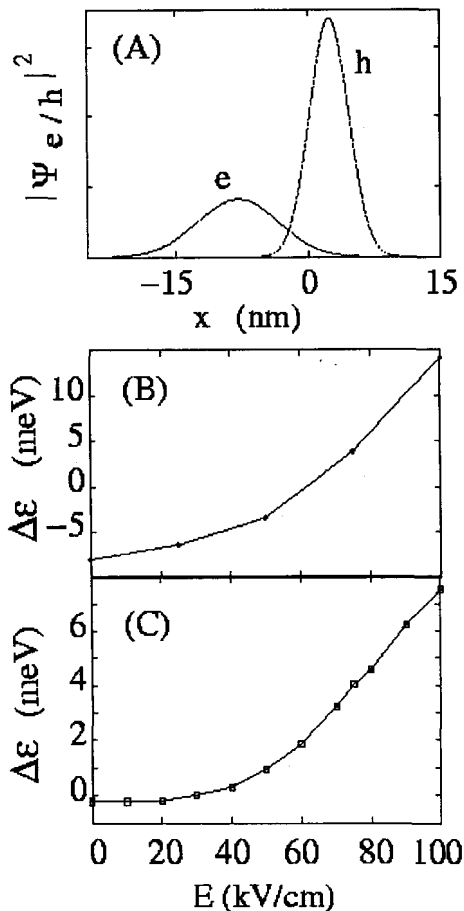


Fig. 8.1 (A) Electron and hole particle densities corresponding to the excitonic ground state along the direction of the applied electric field. (B) Biexcitonic shift $\Delta\epsilon$ as a function of the applied field for the two-exciton ground state in a single dot, obtained via an exact-diagonalization approach. Here, realistic GaAs-based QD structure parameters are taken into account. (C) Biexcitonic shift $\Delta\epsilon$ as a function of the applied field for a two-exciton ground state in a double-dot structure.

term and is negative. When the field is increased, it tends to align the two dipoles so that $\Delta\epsilon$ first vanishes and then becomes positive: the external electric field, removing part of the system symmetries, allows us to *turn on* at will and to *tune* exciton-exciton interactions.

Let us now consider the interaction between excitons localized in two

neighboring QDs stacked in the growth direction: in this case, even for different electron and hole charge distributions, the interaction between excitons sitting in different and far enough QDs will be negligible in the absence of the external field (see Figure 8.1 C). When a constant in-plane electric field is applied, we create again electron-hole dipoles inside each QD, which are now parallel and pointing toward the same direction. Therefore, the polarized excitons will now interact with a positive $\Delta\mathcal{E}$, roughly proportional to the square of the field-induced excitonic dipole and inversely proportional to the third power of the inter-dot distance. This implies that, to exploit this interaction, the quantum dots must be close enough to allow for a non-vanishing dipole-dipole interaction energy but far enough to prevent single-particle tunneling phenomena. Once more, the presence of an in-plane field is found to turn on exciton-exciton interactions, thus allowing for the formation of *tunable bonds* between QDs, i.e., for the creation of *artificial macromolecules*.

We shall now show that the field-induced effects previously introduced can be described in terms of a simple analytical model. To this purpose, the QD carrier confinement along the growth (z) direction can be modeled as a narrow harmonic potential (or as a square box) $V(z)$; the confinement in the QD (\vec{r}) plane is described as a two-dimensional (2D) parabolic potential. By denoting with \vec{E} the in-plane electric field, the single-exciton Hamiltonian will then be

$$\mathbf{H} = \sum_{i=e,h} \left[\frac{\mathbf{p}_i^2}{2m_i} + \frac{1}{2}m_i\omega_i^2 \left| \vec{r}_i \pm \vec{d}_i \right|^2 + V_i(z_i) \right] - \frac{e^2}{\epsilon \sqrt{|\vec{r}_e - \vec{r}_h|^2 + |z_e - z_h|^2}} , \quad (8.1)$$

where the \pm sign and the subscripts e and h refer, respectively, to electron and hole. Here, $\vec{d}_i = e\vec{E}/(m_i\omega_i^2)$ is the single-particle charge displacement induced by the field. We want to show that, under suitable conditions, Eq. (8.1) can be analytically solved and all the important quantities can be easily estimated with a good degree of accuracy.

Due to the strong single-particle confinement along the z direction, we will approximate $|z_e - z_h|^2$ with its average value l^2 . We choose l to be twice the average length related to the ground state of an *infinite-height* square well of width a , i.e., $l = (2a/\pi)\sqrt{(\pi^2 - 6)/12}$. It is then possible to separate the Hamiltonian (8.1) as $\mathbf{H} = \mathbf{H}_{||}(\{\vec{r}_i\}) + \mathbf{H}_{\perp}(z_e) + \mathbf{H}_{\perp}(z_h)$ where $\mathbf{H}_{\perp}(z_i) = p_{z_i}^2/2m_i + V_i(z_i)$ is the single-particle Hamiltonian along

the growth direction —exactly solvable for the case of a parabolic potential as well as of an infinite-height square well. By further defining the center of mass (CM) and relative coordinates $\vec{R} = [m_e(\vec{r}_e + \vec{d}_e) + m_h(\vec{r}_h - \vec{d}_h)]/M$, with $M = m_e + m_h$, and $\vec{r} = \vec{r}_h - \vec{r}_e$, the in-plane Hamiltonian $\mathbf{H}_{\parallel}(\{\vec{r}_i\})$ becomes

$$\begin{aligned}\mathbf{H}_{\parallel}(\vec{R}, \vec{r}) = & \frac{P^2}{2M} + \frac{1}{2}M\omega_R^2 R^2 + \frac{p}{2\mu} + \frac{1}{2}\mu\omega_r^2 |\vec{d} - \vec{r}|^2 \\ & + \mu(\omega_e^2 - \omega_h^2)\vec{R} \cdot (\vec{d} - \vec{r}) - \frac{e^2}{\epsilon\sqrt{r^2 + l^2}},\end{aligned}\quad (8.2)$$

where $\mu = m_e m_h / M$ is the reduced mass, $\omega_R^2 = [(\omega_e^2 + \omega_h^2)/2](1 + \Delta)$, $\omega_r^2 = [(\omega_e^2 + \omega_h^2)/2](1 - \Delta)$, $\Delta = [(m_e - m_h)/M](\omega_e^2 - \omega_h^2)/(\omega_e^2 + \omega_h^2)$ and

$$\vec{d} = \vec{d}_e + \vec{d}_h = e\vec{E}\left(\frac{1}{m_e\omega_e^2} + \frac{1}{m_h\omega_h^2}\right) \quad (8.3)$$

denotes the total electron-hole in-plane displacement.

In the limit $(\omega_e^2 - \omega_h^2)/(\omega_e^2 + \omega_h^2) \ll 1$, the two coordinates are only weakly coupled, and the Schrödinger equation associated to the CM coordinate \vec{R} is exactly solvable. In the general case we will concentrate on the ground state, though the generalization to higher states is straightforward. We can approximate the ground state of \mathbf{H}_{\parallel} as $\Psi(\vec{r}, \vec{R}) = \Psi_x(x)\chi(y, \mathbf{R})$, with $\chi(y, \mathbf{R}) = \frac{1}{(\lambda_r^2\pi)^{1/4}} e^{-\frac{y^2}{2\lambda_r^2}} \frac{1}{(\lambda_R^2\pi)^{1/2}} e^{-\frac{R^2}{2\lambda_R^2}}$, where x and y denote, respectively, the components of \vec{r} parallel and perpendicular to the field \vec{E} , $\lambda_r = \sqrt{\hbar/(\mu\omega_r)}$ and $\lambda_R = \sqrt{\hbar/(M\omega_R)}$. By averaging \mathbf{H}_{\parallel} over $\chi(y, \mathbf{R})$, we obtain the effective Hamiltonian $\mathbf{H}_{eff} = \frac{1}{2}\hbar\omega_r + \hbar\omega_R + \frac{p_x^2}{2\mu} + V_{eff}(x)$, characterized by the effective potential

$$V_{eff}(x) = \frac{1}{2}\mu\omega_r^2(x - d)^2 + V_C\left(\frac{x^2 + l^2}{2\lambda_r^2}\right) \quad (8.4)$$

with $V_C(u) = -e^2/(\epsilon\sqrt{\pi}\lambda_r)e^u K_0(u)$, K_0 being the zero-order Bessel function.

If we are interested in the low-energy states, we can approximate V_{eff} around its minimum V_0 with a parabolic potential, i.e., $V_{eff}(x) \approx V_0 + \frac{1}{2}\mu\tilde{\omega}^2(x - x_0)^2$, where $V_0 \equiv V_{eff}(x_0)$ and $\mu\tilde{\omega}^2 \equiv \partial^2 V_{eff}/\partial x^2|_{x_0}$. Within such approximation scheme, the eigenvalues and eigenfunctions of \mathbf{H}_{eff} can be evaluated analytically and, in particular, the approximate ground state eigenfunction becomes $\Psi_x(x) = (\mu\tilde{\omega}/\hbar\pi)^{\frac{1}{4}} e^{-\frac{1}{2}\frac{\mu\tilde{\omega}}{\hbar}(x - x_0)^2}$.

In the case of strong enough fields, the main effect of the attractive Coulomb interaction is to reduce the electron-hole displacement from d to x_0 . For intermediate and strong fields, we can then write the effective displacement as $x_0 = d - \Delta x$, with $\Delta x \ll d$. By inserting x_0 into $\partial V_{eff}/\partial x|_{x_0} = 0$, and considering, in the resulting equation, terms up to first order in Δx , In this regime an analytical expression for Δx can be obtained

$$\frac{\Delta x}{d} = -\frac{\lambda_r}{a^*} \frac{\exp(\xi)}{\sqrt{\pi}} \frac{\Delta K}{1 - \frac{\lambda_r}{a^*} \frac{\exp(\xi)}{\sqrt{\pi}} \left[\frac{d^2}{\lambda_r^2} A(\Delta K, K_1) + \Delta K \right]}, \quad (8.5)$$

with $\xi = (d^2 + l^2)/2\lambda_r^2$, K_1 the first-order Bessel function, $\Delta K = K_0(\xi) - K_1(\xi)$, $A(\Delta K, K_1) = 2\Delta K + K_1(\xi)/\xi$ and $a^* = \hbar^2\epsilon/\mu e^2$ the reduced Bohr radius.

The ratio $\Delta x/d$ as a function of the applied field is shown in the inset of Figure 8.2. It is important to point out that the analytical expression of Δx contains as a multiplying factor the ratio between the reduced Bohr radius a^* and λ_r , which is a measure of the system confinement.

In a similar way, setting $\tilde{\omega} = \omega_r + \Delta\omega$ in $\mu\tilde{\omega} = \partial^2 V_{eff}/\partial x^2|_{x_0}$, we can calculate the effect of the Coulomb attraction on the potential shape

$$\begin{aligned} \frac{\Delta\omega}{\omega_r} = & -\frac{\lambda_r}{a^*} \frac{\exp(\xi)}{2\sqrt{\pi}} \left(\frac{d^2}{\lambda_r^2} A(\Delta K, K_1) + \Delta K - \right. \\ & \left. \frac{\Delta x}{d} \frac{d^2}{\lambda_r^2} \left\{ \frac{d^2}{\lambda_r^2} \left[2A(\Delta K, K_1) - \frac{1}{\xi} \left(\Delta K + 2\frac{K_1(\xi)}{\xi} \right) \right] + \right. \right. \\ & \left. \left. 3A(\Delta K, K_1) \right\} \right). \end{aligned} \quad (8.6)$$

In the limit $\lambda_r^2/d^2 \ll 1$ (strong fields, see Eq. (8.3)), $\Delta\omega/\omega_r = -\Delta x/d \propto -(\lambda_r/a^*)(\lambda_r^3/d^3)$, showing that, in this regime, Coulomb corrections decrease very fast for increasing field. The condition $\Delta x/d \lesssim 20\%$ quantitatively defines the “intermediate and strong” electric-field regime. It is easy to show that, in the regime of interest, the correction on the wave function due to $\Delta\omega/\omega_r$ is negligible with respect to the correction given by the shift $\Delta x/d$.

The most important quantity for implementing the quantum computing scheme of Section 7.2.2.1 is the biexcitonic shift. This is in our case the energy shift due to the Coulomb interaction between two excitons sitting in neighboring dots. We can approximate the biexcitonic ground state as the product of two excitonic wavefunctions sitting in different dots and built according to the model just described. The wave function in the z -direction

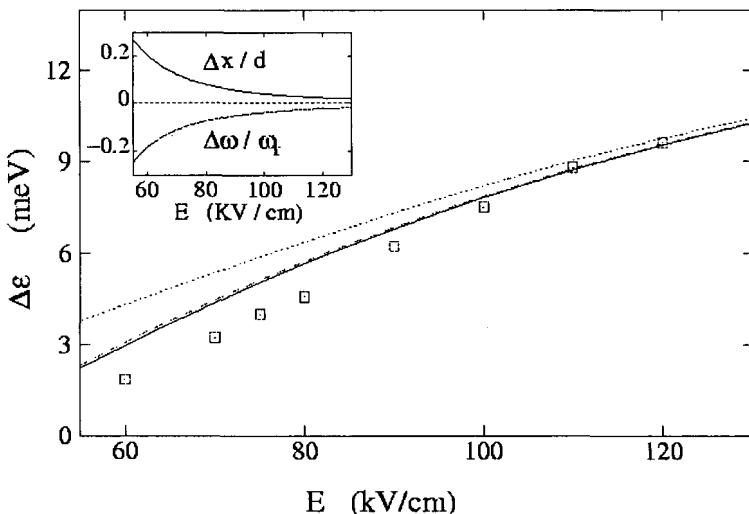


Fig. 8.2 Biexcitonic shift $\Delta\epsilon$ vs external field E for a system characterized by the parameters $m_e = 0.067m_0$, $m_h = 0.34m_0$ (m_0 being the free-electron mass), $\hbar\omega_e = 30$ meV and $\hbar\omega_h = 24$ meV. The dipole-dipole coupling energy, i.e., the biexcitonic shift, is reported as a function of the in-plane field E . The squares indicate the results of the fully three-dimensional calculation, the solid line represents the results of the proposed model, the dotted line is the result obtained when Coulomb correlations are completely neglected, and the dashed line corresponds to setting $\Delta\omega = 0$ in the model. The inset presents the behavior of the two key quantities $\Delta\omega/\omega_r$ and $\Delta x/d$ as a function of the external field.

is approximated by a Gaussian of width $l/2$ and the two dots are taken to have the same width a , i.e. the average of the two dots widths. This is reasonable since, for construction, the two dots have almost the same width and single particle tunneling between the two dots is highly suppressed. The desired biexcitonic shift $\Delta\epsilon$ is then obtained averaging the corresponding two-exciton Hamiltonian over such factorized ground state. In this approximation $\Delta\epsilon$ becomes an easy-to-calculate sum of at most two-dimensional integrals. In the corresponding validity region the model provides a good estimate for $\Delta\epsilon$: Figure 8.2 shows the comparison between the exact results (squares), the approximate result (solid curve) and the results obtained by neglecting completely Coulomb correlation in the wave functions (dotted line). The dashed curve shows the approximated results obtained setting $\Delta\omega/\omega_r = 0$: as anticipated before, this correction is generally negligible.

We now want to show how this model can become a powerful tool to

analyze the complex parameter space related to a certain device scheme.

In order to implement the quantum computing scheme described in Section 7.2.2.1, system parameters such as ω_e , ω_h and \vec{E} must satisfy specific requirements which determine the parameter space available for building our system. Let's analyze the constraints in details. First of all, (i) in order to have well defined qubits, tunneling between dots must be suppressed, i.e. minimum distance between neighboring dots depends on the inter-dot potential barrier height. In agreement with state of the art nanostructure technology, we have chosen a barrier height of 1 eV (e) and 0.58 eV (h) and a distance $D = 100 \text{ \AA}$ between the centers of two consecutive dots for our calculations. On the other side, (ii) to implement our quantum computing scheme, Coulomb interaction between consecutive dots must be strong enough to produce a biexcitonic shift of the order of few meV (at least 3-4 meV). This can be obtained either by tailoring the distance between the two dots in a suitable way or by varying the strength of the external electric field \vec{E} , since as a rough approximation,

$$\Delta\mathcal{E} \propto \frac{d^2}{D^3}, \quad (8.7)$$

and d is given by Eq. (8.3). Unfortunately, (iii) a secondary effect of a strong electric field is to decrease the oscillator strength, and, accordingly, the system response to driving laser pulses: the electric field in fact separates the electronic and hole single particle wave-functions decreasing their overlap (see Figure 8.1). If we now consider the confining parabolic potentials, (iv) in order to have well defined quantum dots, the system must be in a strong confinement regime, i.e. the characteristic length $\lambda_r \sim 1/\sqrt{\omega_e^2 + \omega_h^2}$ associated to the parabolic potential in Eq. (8.2) must be smaller than the corresponding effective Bohr radius a^* . On the other side, (v) as shown by Eq. (8.7) and Eq. (8.3), a too strong oscillator confinement would in turn heavily decrease the biexcitonic shift $\Delta\mathcal{E}$. Last but not least, (vi) in order to be able to perform quantum computing operations, we must be able to address specific excitations of the system unambiguously. This means that the peaks of interest in the optical spectrum (lowest single exciton state in dot a , lowest single exciton state in dot b and lowest biexcitonic state) must be well defined and well isolated from peaks due to other excitations. This determines additional constraints on the value of $\hbar\omega_e$ and $\hbar\omega_h$, since, in the regime we describe, single particle excitations are well defined. In particular, under the hypothesis $\hbar\omega_e > \hbar\omega_h$ (reasonable since $m_h > m_e$), the closest additional peak in the spectrum corresponds to one

electron in the ground state plus one hole in the first excited state and both in dot a. Defining δ_E as the energy difference between the two excitonic ground states in dot a and dot b, we must then try to maximize $\hbar\omega_h - \delta_E$. As it is easy to understand from the above discussion, in order to satisfy all the requirements (i)-(vi) at the same time, the system parameters must be fine tuned so that a quick way to scan the whole parameter space becomes necessary. The available parameter space for a reasonable field of $E = 75$ kV/cm is shown in Figure 8.3. It has been calculated using the model introduced in this section, that allows for a quick screening of the whole parameter space. The typical error in the calculated values of $\Delta\mathcal{E}$ is 10-20%. The constraints imposed for the results shown in Figure 8.3 are $\Delta\mathcal{E} \geq 3.5$ meV, oscillator strength greater than 0.15, $\hbar\omega_e > \hbar\omega_h$, $\hbar\omega_h - \delta_E \geq 10$ meV, $\lambda_r/a^* \leq 0.6$. Based on these results we have chosen the final parameters for the simulations presented in Section 7.2.2.1.

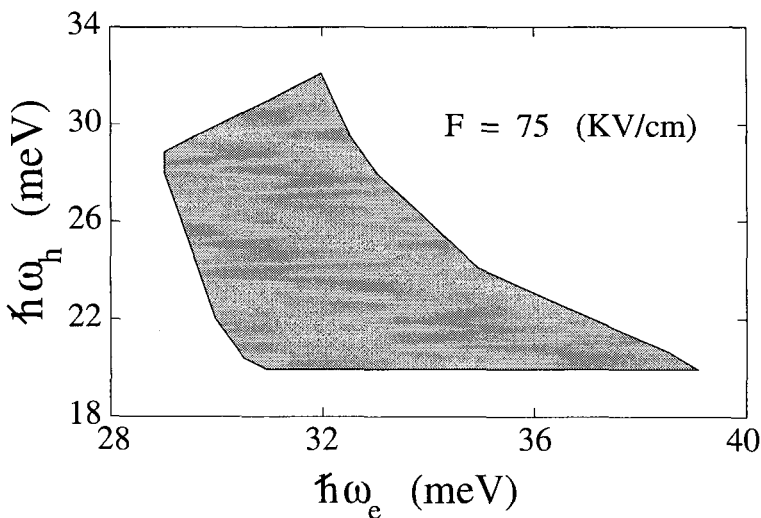


Fig. 8.3 Plot of the parameter space available for constructing the two qubit gate, as calculated using the proposed analytical model. Here, the constraints imposed are $\Delta\mathcal{E} \geq 3.5$ meV, oscillator strength greater than 0.15, $\hbar\omega_e > \hbar\omega_h$, $\hbar\omega_h - \delta_E \geq 10$ meV (δ_E being the energy difference between the lowest excitonic transitions for the two neighboring QDs), $\lambda_r/a^* \leq 0.6$.

8.3 Modeling Few Particle Interactions in Quantum Dots with Intrinsic Bias

In this section we shall analyze peculiarities of exciton-exciton inter-dot coupling in GaN-based quantum dots.

We will first present a fully three-dimensional study of the multiexciton optical response of vertically stacked quantum dots via a direct-diagonalization approach. In particular, we focus on the inter-dot exciton-exciton coupling, key ingredient in the all-optical quantum processor proposed in Section 7.2.2.2 and we demonstrate that there is a large window of realistic parameters for which both biexcitonic shift and oscillator strength are compatible with such implementation scheme [De Rinaldis *et al.* (2002a)].

In the second part of the section we will introduce a semi-analytical method to estimate few particle interactions between stacked quantum dots with an intrinsic bias. This model provides a high degree of accuracy in calculating both exciton-exciton and single particle-exciton coupling strengths, and allows for an easy modeling of devices (see for example the read-out device [D'Amico and Rossi (2002)] in Section 8.5).

8.3.1 *Engineering electronic structure and optical spectrum in coupled GaN quantum dots*

As already underlined, the peculiarity of wurzite GaN heterostructures is the strong built-in electric field which is the sum of the spontaneous polarization and the piezoelectric field. We calculate the built-in electric field in GaN QDs and AlN barriers according to [Cingolani *et al.* (2000)]

$$F_d = \frac{L_{br}(P_{tot}^{br} - P_{tot}^d)}{\epsilon_0(L_d\epsilon_{br} + L_{br}\epsilon_d)} , \quad (8.8)$$

where $\epsilon_{br,(d)}$ is the relative dielectric constant of the barrier (of the quantum dot), $P_{tot}^{br,(d)}$ is the total polarization of the barrier (of the quantum dot), and $L_{br,(d)}$ is the width of the barrier (the height of the dot). The value of the field in the barrier F_{br} is obtained by exchanging the indexes br and d . Equation (8.8) is derived for an alternating sequence of quantum wells and barriers, but it is also a good approximation in the case of an array of similar QDs in the growth (z) direction. The lateral shape of the QD is simply approximated by a bi-dimensional parabolic potential which mimics the strong in-plane carrier confinement caused by the built-in electric field

and preserves the spherical symmetry of the ground state [Andreev and O'Reilly (2000); Arlery *et al.* (1999); Widmann *et al.* (1998a); Widmann *et al.* (1998b)]. Our approach is supported by the agreement with the experimental findings in Reference [Andreev and O'Reilly (2000); Arlery *et al.* (1999); Widmann *et al.* (1998a); Widmann *et al.* (1998b)]. The intrinsic field is the sum of the spontaneous polarization charge that accumulates at GaN/AlN interfaces and the piezoelectric one. All the parameters are taken from [Cingolani *et al.* (2000)] (adapted for the case $x=1$ for Al percentage in the barrier).

We shall focus on the interplay between single-particle carrier confinement and two-body Coulomb interactions and in particular, we shall analyze exciton-exciton dipole coupling versus oscillator strength. The relevance of our analysis is twofold: (i) we address a distinguished few-particle phenomenon typical of nitride QDs, i.e., the presence of an intrinsic exciton-exciton dipole coupling induced by built-in polarization fields; (ii) we provide detailed information on the set of parameters needed for the experimental realization of the quantum information processing strategy proposed in Section 7.2.2.2 [De Rinaldis *et al.* (2002a)].

In our analysis we vary the dot height from 2 to 4 nm and the QD-base diameter from 10 to 17 nm, assuming a linear dependence between these two parameters in agreement with experimental and theoretical findings [Andreev and O'Reilly (2000); Arlery *et al.* (1999); Widmann *et al.* (1998a); Widmann *et al.* (1998b)]. The difference between the well width of two neighboring QDs is assumed to be 8% to allow energy-selective generation of ground state excitons in neighboring QDs. The barrier width is such to prevent single-particle tunneling and to allow at the same time significant dipole-dipole Coulomb coupling: the giant internal field in fact causes the separation of electrons and holes, creating intrinsic dipoles. If we consider two stacked dots occupied by one exciton each, the resulting charge distribution can be seen as two dipoles aligned along the growth direction, so to be negatively coupled (See Figure 7.5).

As previously mentioned, the theoretical approach here employed to study the optical response of our GaN nanostructure is a fully three-dimensional exact-diagonalization scheme [Biolatti *et al.* (2000); Biolatti *et al.* (2002)]. More specifically, we consider electrons (e) and holes (h) confined within stacked QDs as depicted in Figure 7.5; the confinement potential is modeled as parabolic in the $x - y$ plane and as a square-well potential modified by the built-in electric field along the growth (z) di-

rection. We focus on the excitonic and biexcitonic optical spectra in the presence of the built-in electric field. For all the structures considered, the two lowest optical transitions correspond to the formation of direct ground state excitons in dot *a* and *b*, respectively. Here, we shall consider parallel-spin configurations only.

Let us consider the biexcitonic shift corresponding to the energy difference between the ground state biexcitonic transition (given a ground state exciton in dot *a*) and the ground state excitonic transition of dot *b*. This quantity —a “measure” of the ground state exciton-exciton coupling— plays a crucial role in all-optical quantum processor of Section 7.2.2.2. Figure 8.4a shows how the biexcitonic shift increases with the height of the dot. The barrier width is kept fixed and equal to 2.5 nm. In curve (A) both the height and the diameter D of the dots are varied according to the relation $D = 3.5L_d + 3$ nm [Andreev and O'Reilly (2000); Arlery *et al.* (1999); Widmann *et al.* (1998a); Widmann *et al.* (1998b)], while in (B) only the height of the dot is changed. We notice that, for realistic parameters, it is possible to achieve biexcitonic shifts up to 9.1 meV.

Contrary to what happens in stacked GaAs-based QDs (see Section 4.6) in GaN QDs, over the range of parameters used, the lowest states preserve their atomic-like shape even for barriers as low as 2.5 nm. In these structures both electron and hole effective masses and valence/conduction-band discontinuities are much higher than in GaAs, therefore decreasing the atomic-like wavefunction overlap responsible for the molecular bonding. The excitonic dipole length is roughly proportional to the height of the dot because of the strong built-in electric field; therefore it is crucial to evaluate the dependence of the exciton-exciton interaction on the height of the QDs. Even the spreading of the wavefunction affects the biexcitonic shift, as one can notice by comparing curves A and B in Figure 8.4. The biexcitonic shift is larger (up to 20% for the parameters considered here) when the wavefunction is more localized, since the system is closer to the idealized “point-like” particle case (see curve C in the same figure). Our results demonstrate that there exists a wide range of parameters for which the biexcitonic shift is at least a few meV. This is a central prerequisite for realizing energy-selective addressing with sub-picosecond laser pulses, as requested, for example, by all-optical quantum information processing schemes [Biolatti *et al.* (2000); Biolatti *et al.* (2002); De Rinaldis *et al.* (2002a)].

The best strategy to achieve large biexcitonic shift is to grow “high” and “small diameter” dots. The drawback is that the oscillator strength

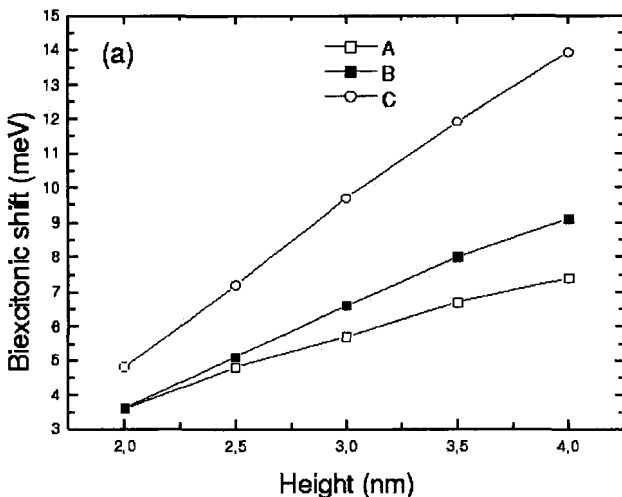


Fig. 8.4 Biexcitonic shift (upper panel) of the ground state transition in dot b for two coupled GaN dots separated by a barrier of 2.5 nm vs QD height. In curve (B) only the height of the dots is changed ($D = 10$ nm), while in curve (A) D is varied proportionally to the height from 10 to 17 nm. Curve (C) shows the biexcitonic shift in the point-like charge approximation. The parameters used are : effective masses $m_e = 0.2m_0$ and $m_h = m_0$; in-plane parabolic confinement energy $\hbar\omega_e = 74$ meV and $\hbar\omega_h = 33$ meV for the (B) curve; $\hbar\omega_e = 74 \div 290$ meV, $\hbar\omega_h = 33 \div 130$ meV for the (A) curve.

(OS) of the ground state transition strongly decreases with the height of the dot, since it is proportional to the overlap of electron and hole wave functions. A small value of the OS enhances the well-known difficulties of single-dot signal detection.

In the range of height values considered in Figure 8.4, the OS varies over three orders of magnitude, so care must be taken in a future quantum information processing experiment in order to optimize at the same time biexcitonic shift and OS. We suggest as a reasonable figure of merit the product between the biexcitonic shift and the logarithm of the oscillator strength. Such quantity is plotted in Figure 8.5 and it is the largest for a QD height of $2.5 \div 3$ nm.

8.3.2 Semi-analytical model

We shall devote the next pages to the description of a semi-analytical model able to describe with high accuracy few particle interactions in quantum dots with intrinsic bias.

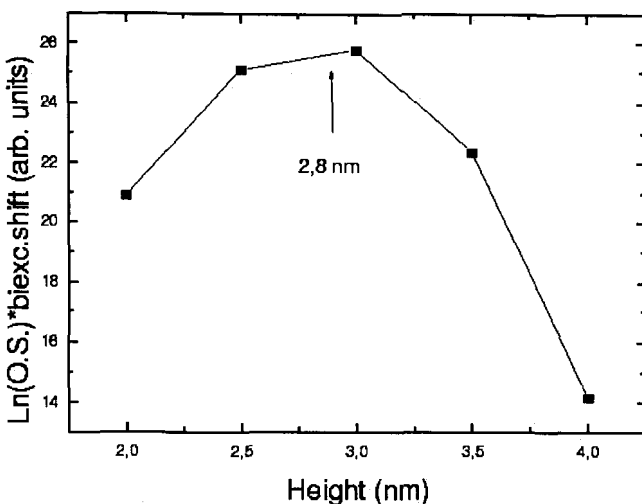


Fig. 8.5 Figure of merit (biexcitonic shift times logarithm of oscillator strength) vs QD height. The arrow indicates the maximum obtained by a parabolic fit.

8.3.2.1 Single exciton system

Let us consider a single electron-hole correlated pair confined in a QD with a built-in electric field oriented along the growth direction. We will present calculations done using parameters related to GaN-based QD structures. We shall work in the envelope function approximation and focus on the system ground state, though the method described can be easily extended to the other low-energy level states. The Hamiltonian of the excitonic system is

$$H = \sum_{\alpha=e,h} \left[\frac{p_\alpha^2}{2m_\alpha} + \frac{1}{2} m_\alpha \omega_\alpha^2 (x_\alpha^2 + y_\alpha^2) + V_z(z_\alpha) \right] - eEz_e + eEz_h - \frac{e^2}{\epsilon |\vec{r}_e - \vec{r}_h|} \quad (8.9)$$

where the terms in square bracket correspond to the Hamiltonian of a particle confined by a parabolic potential in the in-plane directions and by the stronger confining potentials V_z in the growth direction (usually modeled as a square potential). E is the built-in electric field, e is the absolute value of the electron charge and ϵ the dielectric constant of the medium. In the following we shall use Greek letters to indicate the indexes e, h correspond-

ing respectively to electrons and holes. If we consider the one-dimensional Hamiltonian $H_{z(e/h)}^0 = (p_{z(e/h)}^2/2m_{e/h}) + V_z(z_{e/h}) \mp eEz_{e/h}$, its ground state $\psi_{e/h}(z_{e/h})$ can be easily calculated by exact diagonalization. We can then resort to the separable effective Hamiltonian $\tilde{H} = H_{ze}^0 + H_{zh}^0 + H_I$ where

$$H_I(\vec{R}, \vec{r}) = \left[\frac{p_R^2}{2M} + \frac{1}{2} M \omega_R^2 R^2 \right] + \left[\frac{p_r^2}{2\mu} + \frac{1}{2} \mu \omega_r^2 r^2 - \frac{e^2}{\epsilon \sqrt{r^2 + \langle (z_e - z_h)^2 \rangle}} \right] + \mu(\omega_e^2 - \omega_h^2) \vec{R} \cdot \vec{r}. \quad (8.10)$$

Here $\vec{R} = [m_e(x_e, y_e) + m_h(x_h, y_h)]/M$ and $\vec{r} = (x_e - x_h, y_e - y_h)$ are the in-plane center of mass and relative coordinates, $M = m_e + m_h$, $\mu = m_e m_h / M$, $\omega_R^2 = (m_e \omega_e^2 + m_h \omega_h^2) / M$, $\omega_r^2 = (m_h \omega_e^2 + m_e \omega_h^2) / M$ and $\langle (z_e - z_h)^2 \rangle \equiv \langle \psi_e(z_e) \psi_h(z_h) | (z_e - z_h)^2 | \psi_e(z_e) \psi_h(z_h) \rangle$. The original problem Eq. (8.9) has now been reduced to solving the Schrödinger equation for $H_I(x, y)$. By approximating the ground state solution of H_I with the factorized form $\psi_R(\vec{R}) \psi_{rel}(\vec{r})$, where $\psi_R(\vec{R}) = \sqrt{M \omega_R / \hbar \pi} \exp(-M \omega_R R^2 / 2\hbar)$, we get

$$\tilde{H}_{rel}(r) = \langle \psi_R | H_I | \psi_R \rangle = \hbar \omega_R + \frac{p_r^2}{2\mu} + V(r) \quad (8.11)$$

with $V(r) = \frac{1}{2} \mu \omega_r^2 r^2 - e^2 / \epsilon \sqrt{r^2 + \langle (z_e - z_h)^2 \rangle}$. For calculating the properties of low-energy states, $V(r)$ can be approximated around its minimum as $V(r) \approx V_0 + \mu \tilde{\omega}_r^2 r^2 / 2$ where

$$\mu \tilde{\omega}_r^2 = \mu \omega_r^2 + \frac{e^2}{\epsilon \langle (z_e - z_h)^2 \rangle^{3/2}}. \quad (8.12)$$

We underline that the expression (8.12) includes corrections due to the Coulomb interaction between electron and hole. As we shall see later, such corrections strongly influence the precision of the approximation. The eigenvalue problem related to Eq. (8.11) is now exactly solvable and its ground state is given by $\psi_{rel}(r) = \sqrt{\mu \tilde{\omega}_r / \hbar \pi} \exp(-\mu \tilde{\omega}_r r^2 / 2\hbar)$. The approximated form for the total excitonic wavefunction is then

$$\psi_{exc} \approx \psi_e(z_e) \psi_h(z_h) \psi_R(R) \psi_{rel}(r). \quad (8.13)$$

8.3.2.2 Biexciton system

If the barrier between two stacked quantum dots QD0 and QD1 is such that particle tunneling is negligible, or if the mismatch between relevant single particle levels in QD0 and QD1 is sufficiently large due to the built-in electric field and to the size difference between the two dots, each direct low

energy exciton in the macromolecule QD0 + QD1 will be strictly confined to a single dot, so that when considering a biexciton formed by one exciton in QD0 and the second in QD1, we can safely approximate its wavefunction as the product of the two excitonic wavefunctions, i.e. $\psi_{bi} \approx \psi_{exc0}\psi_{exc1}$, where 0, 1 indicates QD0 or QD1. As discussed in the previous section, in GaN-based structures this condition is not very strict, in fact the confinement of low energy direct excitons to a single GaN-based QD is a very robust feature for varying QD size and inter-dot barrier.

Let us now consider the biexcitonic shift $\Delta\epsilon$, essential for performing, for example, conditional operations in the quantum computational schemes of Section 7.2.2.2. As discussed in Section 8.2 it is then crucial to have a quick way to estimate $\Delta\epsilon$ in order to define the correct range for the structure parameters. For the case we are analyzing, a good approximation for $\Delta\epsilon$ will be the Coulomb interaction average $\Delta\epsilon = \sum_{\alpha,\beta=e,h} \Delta\epsilon_{\alpha0,\beta1}$ with

$$\Delta\epsilon_{\alpha0,\beta1} = sign_{\alpha,\beta} \langle \psi_{exc,0} \psi_{exc,1} | \frac{e^2}{\epsilon |\vec{r}_{\alpha0} - \vec{r}_{\beta1}|} | \psi_{exc,0} \psi_{exc,1} \rangle \quad (8.14)$$

with $sign_{\alpha,\beta} = -1$ if $\alpha \neq \beta$, 1 otherwise. $\Delta\epsilon_{\alpha0,\beta1}$ represents the Coulomb interaction between particle α in QD0 and particle β in QD1 in the presence of the other particles composing the biexciton (i.e. partially including correlation effects). The calculation of the exact biexcitonic shift $\Delta\epsilon$ is cumbersome [Biolatti *et al.* (2000); Biolatti *et al.* (2002)], even using the approximation Eq. (8.14), so it is highly desirable to derive a precise but much simpler estimate for it.

Let us focus on $\Delta\epsilon_{\alpha0,\beta1}$. This is an integral over the coordinates of all the four particles considered: in general in fact, due to Coulomb interaction, it is not possible to *exactly* factorize $\psi_{exc,i}$ into single particle components. Let us now consider a ground state biexciton and approximate $\psi_{exc,i}$ with Eq. (8.13). We stress that, though factorized, such expression *includes* the Coulomb interaction between the electron and the hole in the same QD to a certain extent. This is possible because the factorization is over the *collective* coordinates *internal* to the single QD.

For its particularly simple form and being the potential a two-body interaction, it is however possible to integrate analytically over $\vec{r}_{\bar{\alpha}0}$ and $\vec{r}_{\bar{\beta}1}$, where $\bar{\alpha} = e$ (h) if $\alpha = h$ (e) (and similar for $\bar{\beta}$), even if $\psi_{exc,i}$ is given in respect to the center of mass and relative coordinates *internal* to the

single quantum dot. The result of such integration is given by

$$|\Delta\epsilon_{\alpha 0, \beta 1}| = C_{\bar{\alpha} 0} C_{\bar{\beta} 1} \int dz_{\alpha 0} dz_{\beta 1} |\psi_{\alpha 0}(z_{\alpha 0})|^2 |\psi_{\beta 1}(z_{\beta 1})|^2 \int dx_{\alpha 0} dx_{\beta 1} dy_{\alpha 0} dy_{\beta 1} \frac{e^2 \exp[-(D_{\alpha 0} x_{\alpha 0}^2 + D_{\beta 1} x_{\beta 1}^2) - (D_{\alpha 0} y_{\alpha 0}^2 + D_{\beta 1} y_{\beta 1}^2)]}{\epsilon \sqrt{(x_{\alpha 0} - x_{\beta 1})^2 + (y_{\alpha 0} - y_{\beta 1})^2 + (z_{\alpha 0} - z_{\beta 1})^2}}, \quad (8.15)$$

where

$$D_{e/h, i} = \left[\frac{\mu}{\hbar} \left(B_{e/h} - \frac{(\omega_R - \tilde{\omega}_r)^2}{B_{h/e}} \right) \right]_i, \quad (8.16)$$

$i = 0, 1$ indicates to which QD the parameters involved belong, $B_{e/h} = [\tilde{\omega}_r + \omega_R(m_{e/h}/m_{h/e})]$ and

$$C_{(e/h)i} = \left(\frac{M \tilde{\omega}_r \omega_R}{\pi B_{e/h} \hbar} \right)_i. \quad (8.17)$$

If we define the in-plane center of mass and relative coordinates between two particles in *different* quantum dots

$$\vec{R}_{01} = D_{\alpha 0}(x_{\alpha 0}, y_{\alpha 0}) + D_{\beta 1}(x_{\beta 1}, y_{\beta 1}) \quad (8.18)$$

$$\vec{r}_{01} = (x_{\alpha 0} - x_{\beta 1}, y_{\alpha 0} - y_{\beta 1}), \quad (8.19)$$

it is possible to integrate analytically over \vec{R}_{01} and \vec{r}_{01} obtaining

$$|\Delta\epsilon_{\alpha 0, \beta 1}| = \sqrt{\pi} \sqrt{\tilde{D}_{\alpha 0, \beta 1}} \frac{e^2}{\epsilon} \int dz_{\alpha 0} dz_{\beta 1} |\psi_{\alpha}(z_{\alpha 0})|^2 |\psi_{\beta}(z_{\beta 1})|^2 \exp[(z_{\alpha 0} - z_{\beta 1})^2 \tilde{D}_{\alpha 0, \beta 1}] \times \left[1 - \phi \left(\sqrt{(z_{\alpha 0} - z_{\beta 1})^2 \tilde{D}_{\alpha 0, \beta 1}} \right) \right]. \quad (8.20)$$

Here $\phi(x) = (2/\sqrt{\pi}) \int_0^x \exp(-t^2) dt$ the error function and $\tilde{D}_{\alpha 0, \beta 1} = D_{\alpha 0} D_{\beta 1} / (D_{\alpha 0} + D_{\beta 1})$. With the use of Eq. (8.13) the twelve-dimensional integral in Eq. (8.14) has been reduced to the two-dimensional integral in Eq. (8.20).

The expression (8.20) can be additionally simplified if we approximate the electron and hole single particle wave-functions along the z direction with the Gaussian $\psi_{\alpha, i}(z_{\alpha, i}) \approx \exp[-(z_{\alpha, i} - \langle z_{\alpha, i} \rangle)^2 / 2\lambda_{\alpha, i}^2] / \sqrt{\sqrt{\pi}\lambda_{\alpha, i}}$ where $\langle z_{\alpha, i} \rangle = \langle \psi_{zi}(z_{\alpha, i}) | \hat{z} | \psi_{zi}(z_{\alpha, i}) \rangle$ and $\lambda_{\alpha, i}^2 \equiv 2\langle \psi_{zi}(z_{\alpha, i}) | \hat{z}^2 | \psi_{zi}(z_{\alpha, i}) \rangle$.

After some elementary manipulations Eq. (8.20) reduces to the *one-dimensional integral*

$$|\Delta\epsilon_{\alpha0,\beta1}| = \frac{e^2}{\epsilon} \sqrt{\frac{1}{\lambda_{\alpha0}^2 + \lambda_{\beta1}^2}} \sqrt{\tilde{D}_{\alpha0,\beta1}} \int_{-\infty}^{\infty} dz \exp \left[-\frac{z^2}{\lambda_{\alpha0}^2 + \lambda_{\beta1}^2} \right] \exp[(z + \Delta z_{\alpha0,\beta1})^2 \tilde{D}_{\alpha0,\beta1}] \times \left\{ 1 - \phi \left[\sqrt{(z + \Delta z_{\alpha0,\beta1})^2 \tilde{D}_{\alpha0,\beta1}} \right] \right\}, \quad (8.21)$$

where $\Delta z_{\alpha0,\beta1} \equiv \langle z_{\alpha0} \rangle - \langle z_{\beta1} \rangle$.

Figure 8.6 shows biexcitonic shift values associated to the system QD0+QD1, when the barrier width w is varied between 2 and 4 nm and QD heights are respectively 2.5 and 2.7 nm. $\Delta\epsilon$ is obtained using Eq. (8.21) (solid line), and compared to the “exact” results calculated by direct diagonalization of the fully interacting three-dimensional biexcitonic Hamiltonian. As can be seen in Figure 8.6, Eq. (8.21) (which uses a Gaussian form for $\psi_{\alpha,i}$) captures most of the information: its estimates are in fact at most 7% from the exact values. The curve labeled by C include Coulomb correlation effects in the excitonic wave-functions, while the NC one does not. We stress that, in this formulation, *including Coulomb interaction does not imply more complex calculations*, since it is done by the simple substitution $\omega_r \rightarrow \tilde{\omega}_r$ (see Eq. (8.12)). The precision of the results is highly affected by such correction.

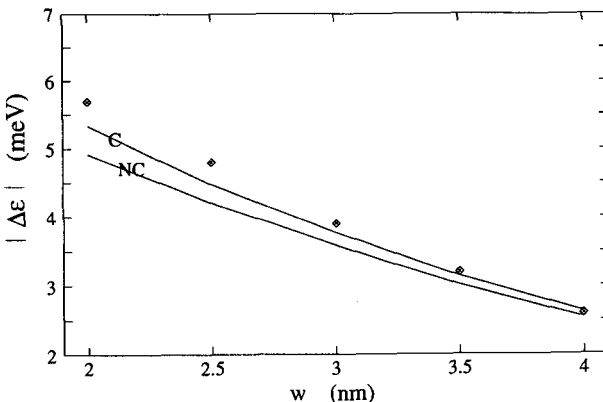


Fig. 8.6 Biexcitonic shift $\Delta\epsilon$ vs barrier width w obtained using Eq. (8.21) (solid line). Diamonds correspond to the results obtained by “exact” diagonalization. Curves C (NC) include (do not include) Coulomb corrections.

8.4 Semiconductor Double Quantum Dot as Storage Qubit

The last part of this chapter is devoted to the description of measuring devices, useful both for quantum computing purposes as well as for detecting charge variations in nanoscopic structures.

One of the main problems with solid state quantum computing proposals based on the charge degrees of freedom, is to find a way to overcome “fast” decoherence times. A major step in overcoming this problem has been the idea of using ultrafast gate operations driven by laser pulses which address energy-selected inter-band optical transitions. In the original proposal described in Section 7.2.2.1 [Biolatti *et al.* (2000); Biolatti *et al.* (2002)] the qubit is implemented using excitonic degrees of freedom; in this section we present a possible scheme to measure the state of a qubit in a solid state quantum computing implementation which can be used to complement such a proposal.

Most of the proposals for measuring the quantum state of a solid state implemented qubit [Gurvitz (1997); Korotkov (1999); Korotkov (2001); Shnirman and Schön (1998)] involve continuous measurement schemes, for example, schemes in which the current through a point-contact is being continuously measured. Regarding the proposal of Section 7.2.2.1, continuous measurements schemes suffer major drawbacks because of the decoherence effects of the unavoidable current fluctuations involved. We are going to show a possible way to overcome these problems via the use of a “storage qubit”. First we will introduce the definition of the storage qubit, and then we will present a possible implementation using a double quantum dot structure.

8.4.1 *Definition*

The key idea is to transfer the information from the computational qubit (C-qubit) to another qubit (the storage qubit or S-qubit) where the information can reside for a long time, i.e. the S-qubit posses a large T_1 compared to the C-qubit. Short T_1 (in this case the finite excitonic lifetime) in fact limits the available time for the measurement process, even when no gating operations are being performed. In addition the use of a S-qubit can increase the spatial distance between the qubit and the measurement device, decreasing the decoherence rate when no measurement is taking place. Due to its relatively large T_1 , the information inside the S-qubit can be extracted for example by continuous measurement schemes, without affecting the C-

qubit.

The S-qubit must measure the C-qubit in a time that is “short” compared to the decoherence time, and store the information. The generic way to describe this measurement is through the “controlled not” gate, which is also referred to as the measurement gate.

We now consider a possible implementation of a S-qubit which could be used for measuring the quantum state of C-qubits in the scheme of Section 7.2.2.1. Here the qubit is implemented through the excitonic degrees of freedom of a QD. The two possible states of the C-qubit, $|0_{QB}\rangle$ and $|1_{QB}\rangle$ consist of the absence and presence of a ground state exciton in the QD respectively.

The S-qubit designed to measure the excitonic state of the C-qubit, consists of two coupled semiconductor QDs. Through the application of an external gate voltage a surplus hole occupies the double dot (DD) system. The S-qubit states are thus defined as excess hole in right QD, $|R\rangle$ and excess hole in the left QD, $|L\rangle$. The original symmetry between the two states is lifted through the application of an electric field $F = 15\text{kV/cm}$ in the growth direction [Hohenester *et al.* (2000)]. Due to this field the energy levels are lowered in the left dot with respect to the right. For measuring the C-qubit we propose the use of coherent population transfer in coupled semiconductor QDs, as proposed in [Hohenester *et al.* (2000)]. The coherent population transfer (in this case the transfer of excess hole from the left to the right QD) is achieved through a Stimulated Raman Adiabatic Passage (STIRAP) [Bergmann *et al.* (1998)]. The idea is to use the Coulomb interaction, between the exciton in the C-qubit and the surplus hole in the DD to detune the coherent population transfer in the DD (see Figure 8.7).

To consider the DD an actual implementation of a S-qubit, one should check first, that the measured information about the state of the QD stored inside the DD is actually long-lived, and second, that the measurement of the C-qubit by the S-qubit is fast and reliable.

It can be shown that the states $|R\rangle$ and $|L\rangle$ are long-lasting, i.e. the tunneling between them is highly improbable on a time scale set by the decoherence process T_2 , or by the exciton recombination time T_1 of the QD. This is due to the relative large distance (100\AA) and high energy barrier (200 meV) between the two dots (we are considering ground state holes). Additionally the presence of an externally applied electric field along the growth direction introduces an energy level mismatch of tenths of meV between the two dots which strongly inhibits tunneling from $|L\rangle$ to $|R\rangle$.

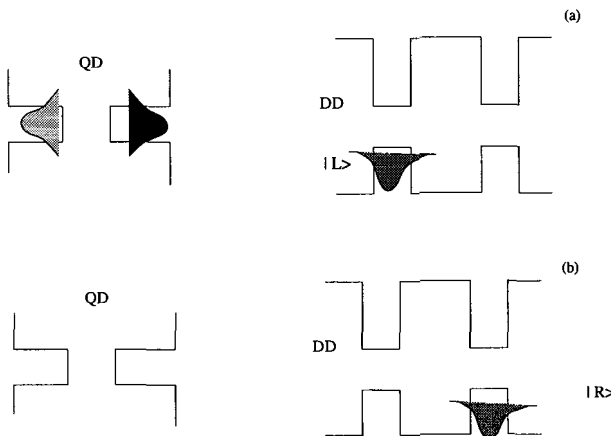


Fig. 8.7 Schematic illustration of the implemented qubit (QD) - storage qubit (DD) structure. The double dot states are labeled $|L\rangle$ and $|R\rangle$ and correspond to a hole in the left dot or in the right respectively. The degeneracy between these two states is lifted by an external electric field. (a) State of DD corresponding to an exciton in the QD the STIRAP is detuned and the hole remains in state $|L\rangle$. (b) State of DD corresponding to no exciton in the QD, STIRAP is not detuned and hole is transferred to state $|R\rangle$.

For the measurement to be fast, the typical time for extracting information on the excitonic state of the C-qubit should be much shorter than T_1 and T_2 ; for the measurement to be reliable, the energy shift of the DD states due to the existence of an exciton in the C-qubit should be larger than the energy uncertainty of the laser pulses and larger than the typical width of the energy levels due to interaction with the environment.

The estimates presented in the following are based on the same parameters used in [Hohenester *et al.* (2000)], except for the distance between the two QDs which has been extended to 100 Å. This particular choice of distance will be discussed extensively when describing the measurement scheme.

8.4.2 Measurement using a STIRAP process

The STIRAP process (see also Section 7.2.3.1) is based on three states, two of which are the long-lived lower energy states $|R\rangle$ and $|L\rangle$, while the third is a higher energy state, in this case a charged exciton labeled $|X^+\rangle$. Between $|R\rangle$ and $|L\rangle$ there are no dipole allowed transitions, while both these levels are dipole coupled to $|X^+\rangle$. Through the use of two delayed

laser pulses, coherent population transfer can be achieved between $|L\rangle$ and $|R\rangle$ without ever occupying $|X^+\rangle$. The first pulse (“Stokes”), is tuned to the $L\text{-}X^+$ resonance and the second pulse (“pump”) is tuned to the $R\text{-}X^+$ resonance.

For the STIRAP process to be effective the coupling of the excited state $|X^+\rangle$ to the two long lived states should be of the same order. Moreover the two long lived states should be non-degenerate. Hohenester and co-workers [Hohenester *et al.* (2000)] propose applying an electric field in the growth direction to lift the original degeneracy of $|R\rangle$ and $|L\rangle$ and choose an excited state $|X^+\rangle$ with electronic wave function split between the two QDs. In this way the coupling between $|X^+\rangle$ and the two localized states $|R\rangle$ and $|L\rangle$ can be of the same order. In the scheme we propose for implementing the S-qubit, we have increased the spatial separation between the two wells to $r = 100 \text{ \AA}$. This localizes the ground state and the first excited states of the electron in one of the QDs. To have an electron wave function¹ which is equally spread over the two QDs, as needed for an effective STIRAP process, we propose two options. The first is to use a charged exciton in which the holes are in the ground states in both QD and the electron is in a level with energy comparable to the confining potential. In this case $|X^+\rangle$ is composed of two holes localized in the two QDs and an electron wave function which is split between the wells, as sketched in Figure 8.8.

A second possibility is to keep the holes in their ground state while the electron is excited to a continuum level above the QD confining potential. In this case the charged exciton state is a hybrid state of a confined exciton state for the hole and a bulk exciton state for the electron. The typical length scale for the hole wave function is given in this case by the confining potential width, $l = 50 \text{ \AA}$ and for the electron by the Bohr radius, $a_B \approx 100 \text{ \AA}$. Both the above possibilities for $|X^+\rangle$ are very susceptible to decoherence, especially the hybrid state where the electron, in a continuum level, is bound to the hole by Coulomb interaction only: outside the QD the electron is not shielded by the QD confining potential from interacting with phonons or other decohering mechanisms.

The measurement of the C-qubit state (exciton or absence of exciton in the QD) exploits the Coulomb interaction between the exciton in the C-qubit and the charged states in the DD. Such an interaction shifts the energy levels in the DD and may detune coherent population transfer: the presence

¹We are in the strong confinement regime (the confining potential width is much smaller than the Bohr radius) thus it is meaningful to describe the state in terms of an electron and hole wave functions, rather than using an excitonic wave function.

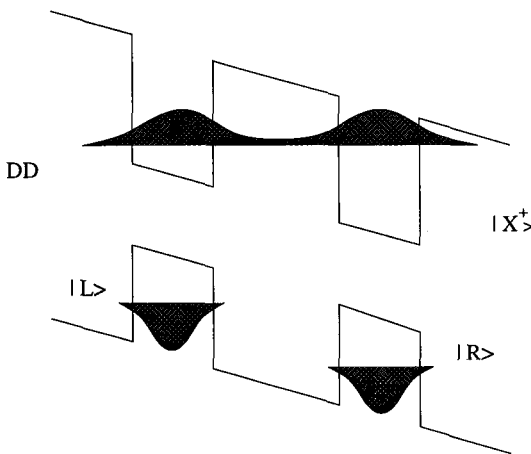


Fig. 8.8 Schematic illustration of the charged exciton state in the double dot structure, $|X^+\rangle$. The two holes are in their ground states, while the electron is an excited state such that its wave function is split between the QDs.

of an exciton in the C-qubit manifest itself by detuning the STIRAP process and so preventing the coherent transfer of the excess hole from the left QD to the right QD of the DD (see Figure 8.7).

Concerning decoherence, one requires from the measurement device, i.e. the DD, to not decohere the QD when no measurement is taking place. This requirement is fulfilled since the presence of the hole in the DD apparatus does not disturb the QD states but rather causes a constant (time independent on the scale of the computation time) shift of the energy levels. Thus the measuring device will not affect the quantum computer when the measurement is not taking place.

Regarding the typical time on which the measurement takes place, the measurement of the state of the C-qubit by the DD occurs on a time scale which is given by the duration of the laser pulses “Stokes” (“pump”) which induce the coherent population transfer. The duration of the laser pulses is of the order of 10 ps [Hohenester *et al.* (2000)], thus the typical time for extracting information on the state of the C-qubit is fast compared to the excitons dephasing and recombination times (the dephasing time being of the order of 100 ps [Hohenester *et al.* (2000)]).

The measurement process of the C-qubit by the DD is done by detuning the STIRAP process: the idea is that the STIRAP will take place *only* when there is *no* exciton in the QD. For the STIRAP to occur, (i) the adiabatic

condition $\Omega\tau \gg 1$ must be fulfilled (τ the duration of the pulses overlap and Ω the typical Rabi frequency associated with the STIRAP process) and (ii) energy conservation during the transfer must be preserved [Elk (1995); Laine and Stenholm (1996)], i.e. the initial and final levels must be in resonance.

We shall now discuss how the presence of an exciton in the C-qubit affects the constraints just mentioned, destroying the probability for a STIRAP process to occur by detuning it. Let us consider a detuning Δ_p of the pump laser from resonance with the $L-X^+$ transition and a detuning of the Stokes laser from the $R-X^+$ transition Δ_s . The Hamiltonian for the three-level system within the rotating wave approximation then has the form [Bergmann *et al.* (1998)]

$$H = \frac{\hbar}{2} [(\Omega_p|X^+\rangle\langle L| + \Omega_s|X^+\rangle\langle R| + h.c.) + 2\Delta_p|X^+\rangle\langle X^+| + 2(\Delta_p - \Delta_s)|R\rangle\langle R|] , \quad (8.22)$$

where Ω_p and Ω_s are the coupling Rabi frequencies, corresponding to the pump and Stokes respectively.

8.4.2.1 Failure of the adiabatic condition

If the two photon resonance condition applies, i.e. $\Delta_p = \Delta_s$, the instantaneous eigenstates and eigenfunction of the Hamiltonian Eq. (8.22) are given by

$$\begin{aligned} |a_0\rangle &= \cos\theta|L\rangle - \sin\theta|R\rangle, & \omega_0 &= 0 \\ |a_{\pm}\rangle &\propto \sin\theta|L\rangle \pm \cot^{\pm 1}\phi|X^+\rangle + \cos\theta|R\rangle, & \omega_{\pm} &= \Delta_p \pm \sqrt{\Delta_p^2 + \Omega_p^2 + \Omega_s^2}, \end{aligned}$$

where θ is the mixing angle defined by $\tan\theta = \frac{\Omega_p}{\Omega_s}$ and ϕ depends on the detuning and Rabi frequencies and is of no importance in the following discussion. $|a_0\rangle$ is referred to as the “dark state” since it includes no contributions from the “leaky state” $|X^+\rangle$.

The adiabatic transfer (constraint (i)) is fulfilled when $|\omega^{\pm} - \omega_0|\tau \gg 1$. For the parameters used by Hohenester *et al.* [Hohenester *et al.* (2000)] ($\Omega_{s,p} = 1.0 \text{ meV}$, $\tau = 10 \text{ ps}$) when the laser detuning Δ_p becomes of the order of the effective Rabi frequency, $\Omega_{eff} = \sqrt{\Omega_p^2 + \Omega_s^2}$, this condition is no longer satisfied. In this case the STIRAP process is detuned when the levels in the DD are perturbed such that the energy difference used in the transition $L-X^+$ is shifted by more than 1.0 meV . When the adiabatic

condition is no longer fulfilled there is a non-vanishing probability for occupying the leaky state. Once the leaky state is occupied there is high probability of a transition to a state different from the three states used for the STIRAP process. In this way the hole transfer from the left QD to the right does not take place.

By modeling the involved (excitonic and hole) wave functions as products of Gaussians, whose parameters have been carefully selected based on the structure and material features (for details see [Pazy *et al.* (2001)]), we have been able to estimate both the shift of the energy levels in the DD (see Figure 8.9) and the difference in the energy shifts of the $|R\rangle$ and $|L\rangle$ states (see Figure 8.10) due to the presence of an exciton in the C-qubit. We have estimated that, *both* when the electron wave function in $|X^+\rangle$ is split between the two QD, or when its energy is above the confining potential we obtain an energy level shift in the DD bigger than 1.0 meV for distances between DD and C-qubit up to 150 Å it is therefore not crucial to have a specific configuration for the excited electron wave function (see Figure 8.9).

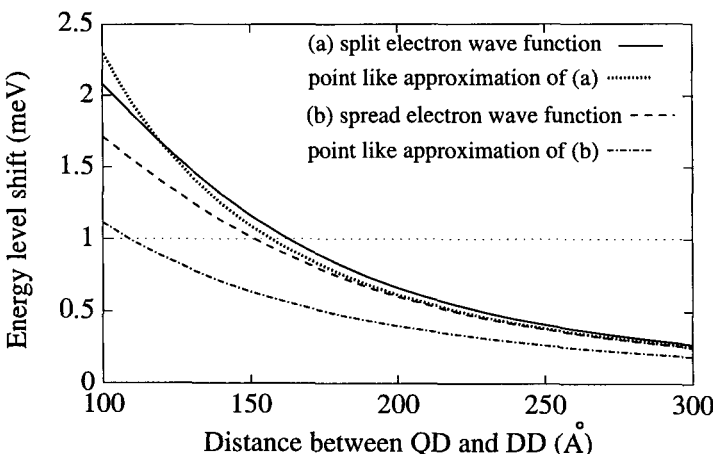


Fig. 8.9 Shift of energy levels of the DD as a function of the distance from the QD. The distance is measured from the center of the electron wave function in the QD to the center of the left (closest) QD of the DD configuration. For the case of an excited electron state spread over the dots we took the typical length scale for the wave function, in the growth direction, to be 100 Å. Results are presented for Gaussian and “point like” wave functions for two cases: electron wave function split between the QDs and electron wave function spread over the two QDs.

8.4.2.2 Failure of the energy conservation requirement

When $\Delta_p \neq \Delta_s$, the STIRAP process is destroyed much sooner. For $\epsilon \equiv \Delta_p - \Delta_s \neq 0$ the zero eigenvalue moves to a value of the order of $\tilde{\omega}_0 \simeq 2\Omega_p^2 \epsilon / \Omega_{eff}^2$ and the (ex) dark state, $|a_0\rangle$, now includes contributions from the leaky state, $|X^+\rangle$, which are of the same order of $\tilde{\omega}_0$. Since in this case the energy conservation requirement is not fulfilled, i.e. the final and initial levels are not in resonance, in order to see if the STIRAP process takes place one needs to compare the energy uncertainty of the pulse with the difference in the energy shift of the initial and final states. Therefore the condition for the STIRAP to take place is given by $\epsilon\tau \leq 1$. Since $\tau = 10$ ps, an energy shift larger than 0.5 meV is sufficient. In Figure 8.10 we show the difference in energy between the initial state, $|L\rangle$ and the final state,

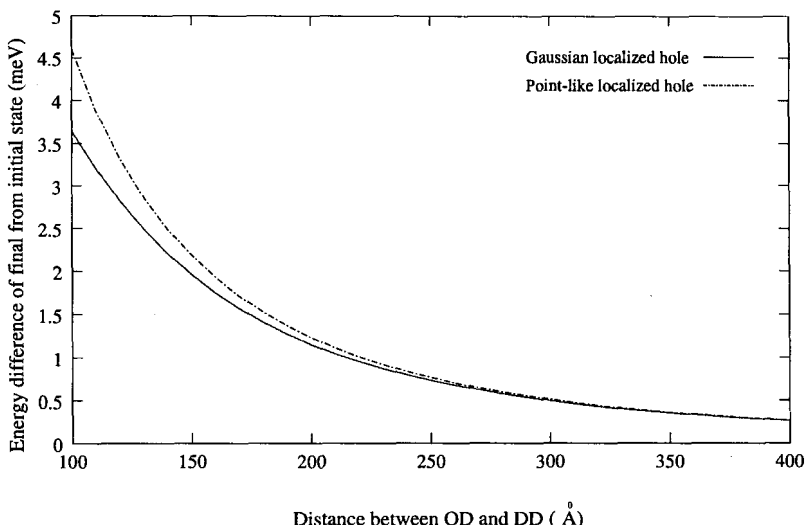


Fig. 8.10 Difference of the shift of initial state, $|L\rangle$ and the final state, $|R\rangle$, of the STIRAP process in the DD when there is an exciton in the QD as a function of the distance from the QD (the distance is measured in the same way as described for Figure 8.9). Results are presented for Gaussian and “point like” wave functions.

$|R\rangle$, of the DD when there is an exciton in the C-qubit. This energy difference is much more sensitive to the presence of an exciton in the QD and is shown to be greater than 0.5 meV up to distances of 300 Å between the QD and DD centers (for details of the calculation see [Pazy *et al.* (2001)]).

The reason it is much easier to detune the transition with respect to

the initial and final states (hole in $|L\rangle$, hole in $|R\rangle$) rather than the initial (or final) state with regards to the intermediate state is due to the different charge configurations. The intermediate, leaky, state ($|X^+\rangle$) couples in a weaker way to an exciton in the QD since the detuning is basically due to a dipole-dipole interaction, whereas for the initial and final states the detuning is due to a charge-dipole interaction.

We think that the idea of a storage qubit reviewed in this section can greatly help practical implementation of quantum computer devices. Apart from measuring the quantum computer's qubit state, a storage qubit stores the information for a time longer than the decoherence times which characterize the computing qubits. Additionally, by incrementing with its physical size the spatial separation between the computing qubits and the final measuring devices, the storage qubit may allow to use conventional methods, e.g. a SET or a point contact [Gurvitz (1997); Korotkov (1999); Korotkov (2001); Shnirman and Schön (1998)] to extract the information, without the latter affecting the coherence of the computing qubits.

8.5 All-Optical Read-Out Device

The last section of this chapter is devoted to the proposal for an all optical read-out device based on a semiconductor quantum dot. The device is centered on the idea of exploiting the shift in the QD ground state excitonic transition due to Coulomb interaction with external charges. Similar to the biexcitonic shift, in fact, Coulomb interaction modifies the transition energy in the absorption spectrum corresponding to the creation of an exciton in a certain dot in the presence of an electron (hole) trapped in the vicinity.² The dipole-monopole interaction decreases as d/w^2 , d the dipole length, w the distance between the dipole and the charge, i.e. much slower than the dipole-dipole interaction characterizing the biexcitonic shift. This implies that, it should be possible to detect such a shift (and thus the electron (hole) presence) even if the dot and the trapped charge are relatively far apart.

Let us now focus on a specific system (though the following discussion can generalized to structures with different geometry or material) and consider the response of an array of slightly different stacked GaN dots (Figure 8.11b), whose height is ~ 2.5 nm and which are separated by barriers 2.5 nm wide. In the hypothesis that the electron (hole) is trapped in dot

²For detection of charged excitons in *the same* QD see [Findeis *et al.* (2001)].

QD0, we can calculate, by using Eq. (8.21) and by not including Coulomb interaction in the wave functions related to QD0, the energy shift connected to the creation of an exciton in QDN ($N=1,2,3,\dots$), where N is the coordination number in respect to QD0. The calculated shift $\Delta\epsilon_{tri}$ is plotted in Figure 8.11a in respect to the distance between QD0 and QDN centers. The coordination number of the latter dot is indicated on the curves as well. The curve labeled by e (h) corresponds to the presence of an electron (hole) in QD0. For $N = 1$, $\Delta\epsilon_{tri} \sim 10\text{meV}$, but even considering N as high as 5, the energy shift is still of the order of $\sim 0.5\text{meV}$, i.e. could be resolved by laser pulses as short as 2-3 ps. The asymmetry between the “e” and the “h” curves reflects the corresponding asymmetry between electron and hole wavefunctions.

Starting from these simple observations, we can think of a non-invasive optical read-out device for a memory which has been written as the presence (state 1) or the absence (state 0) of a charge in each QD [Finley *et al.* (1998)]: state 1 (0) will correspond to the absence (presence) of the chosen excitonic peak in the absorption spectrum. This scheme could be also helpful, in the measuring process of quantum computing devices [Pazy *et al.* (2001); Bayer *et al.* (2001); Tanamoto (2000)] and could in general be an alternative to the reading done, for example, by point contacts, since it avoids charge fluctuations due to the presence of currents in the system. This device may be employed also to monitor the net charge status of a certain mesoscopic system S. For far enough distances between the “written” device S and the “reading” QDN, the interaction becomes in fact proportional to the total net charge inside S, so in principle $\delta \approx n\Delta\epsilon_{tri}$, where δ is the shift of the chosen excitonic transition ϵ_N due to the coupling between QDN and S. A measure of δ could be then used to count the electrons (holes) that have been injected in S.

The device functioning is sketched in Figure 8.12: for simplicity we suppose that one electron (upper panel) or a negative net charge (lower panel) may be stored in S. In the first case we direct on QDN a polarized laser pulse centered on the excitonic transition energy $\epsilon_N + \Delta\epsilon_{tri}$, which include the shift due to the interaction with the possible electron in S (upper panel). The pulse must be long enough to energy-discriminate between ϵ_N and $\epsilon_N + \Delta\epsilon_{tri}$. An exciton will be generated in QDN if and only if there is a single electron in S. For measuring an unknown net charge instead (lower panel), we can think of illuminating QDN with a shorter pulse, corresponding to an energy spreading of $n\Delta\epsilon_{tri}$, n of the order of the maximum net charge we can expect in S. In this case an exciton will be

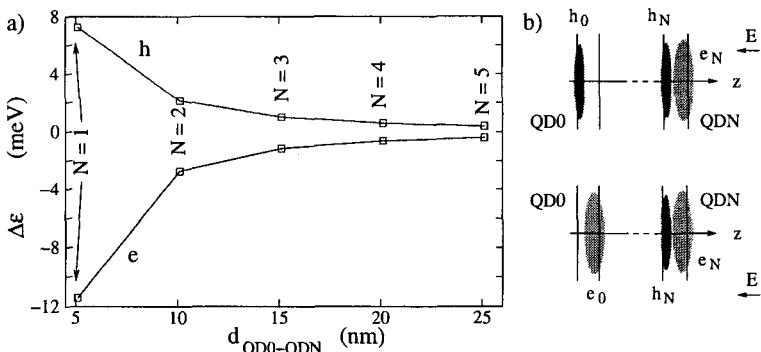


Fig. 8.11 a) Charge-exciton interaction $\Delta\epsilon$ vs distance between “written” QD0 and “reading” QDN. The coordination number N is indicated for each point. Curve “e” (“h”) corresponds to an electron (hole) in QD0. b) Schematic view of the stacked-QD array QD0, ...QDN, when QD0 is occupied by an electron (bottom panel) or by a hole (upper panel). The position along the growth direction occupied by each dot is marked by couples of parallel lines. The electronic (light gray, e_i) and hole (dark gray, h_i) clouds are sketched as well.

always generated in QDN, but the shift δ of such a transition in respect to the benchmark ϵ_N corresponding to no exciton in S will be a measure of the net charge in S. We underline that the same measure may be repeated at will by the use of laser pulse trains, as long as the charge to be measured remains in S. This procedure enhances considerably the efficiency of the read-out scheme.

The desired QDN excitonic transition can be generated by energy selective schemes [Biolatti *et al.* (2000); Biolatti *et al.* (2002)] (if QDN and S are too close to be spatially resolved by the laser pulse) or near-field techniques. A plus of the proposed device is that, by using a long distance interaction, the presence of the exciton in the reading dot would not perturb the system in the written one significantly. In general an important advantage of our reading scheme is that it does not perturb the system during the time in which the process leading to the charge storage in QD0 (for example a computation) is carried out, since the exciton in QDN is created *only* at the time in which a measurement is requested.

Moreover we underline that our scheme does not require S to be subjected to an electric field (either intrinsic or applied). In this frame it is in principle sufficient to grow a single GaN QD in the vicinity of the memory which needs to be read, or, if we consider for example a stack of GaAs QDs, the external electric field can be applied to the reading GaAs QD only. The

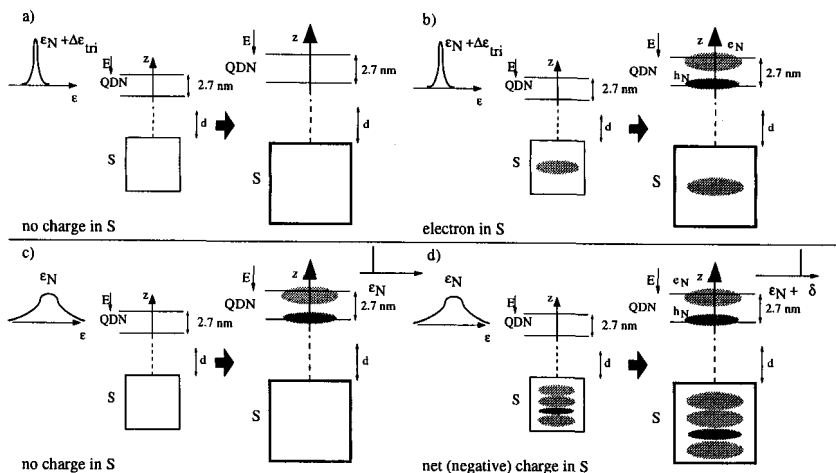


Fig. 8.12 Upper panel: detection of a *known* number of charges (a single electron in the figure). The laser pulse is a peak narrow in energy around the transition energy expected when including Coulomb interaction between QDN and S. Panel a) no charge in S, the pulse does not generate any exciton in QDN; Panel b) electron in S, the pulse generates the corresponding exciton in QDN (conditional dynamics).

Lower panel: detection of an *unknown* net charge in S. The laser pulse is a peak relatively broad in energy centered around the excitonic transition energy expected when Coulomb interaction between QDN and S is *not* included. Panel c) no charge in S, the pulse generates an exciton in QDN at the absorption energy ϵ_N (upper right corner of the panel); Panel d) net charge in S, the pulse generates an exciton in QDN at the absorption energy $\epsilon_N + \delta$, where $\delta \approx n\Delta\epsilon_{tri}$, n the net number of charges in S (upper right corner of the panel).

written unity, in turn, can be a generic nanoscopic charge-based memory (for example a gate-defined QD), while the geometry of the device can be different from the one depicted in Figure 8.12, as long as the distances between the written and reading unities are of the same order.

The main advantage of using GaN quantum dots is the strong *built-in* electric field which on one side simplifies the setup and on the other will never let the trapped exciton ionize. If then the geometry is the one depicted in Figure 8.12, Coulomb interactions between QDN and S result maximized since (i) in GaN QDs dipoles are naturally *aligned* along the growth direction, and (ii) due to the strength of the built-in field the wavefunction spreading in the growth direction is reduced. We finally underline that the parameters used in our calculations are in the reach of present experimental techniques.

Acknowledgments

We are grateful to S. De Rinaldis and E. Pazy for their essential contributions to part of the work reviewed in this chapter as well as to E. Biolatti, R. Ionicioiu, R. Rinaldi, and P. Zanardi for stimulating and fruitful discussions.

This work was supported in part by the European Commission through the Research Project *SQID* within the *Future and Emerging Technologies* (FET) programme.

Bibliography

- Andreev, R.D. and O'Reilly, E.O. (2000). Theory of the electronic structure of GaN/AlN hexagonal quantum dots, *Phys. Rev. B* **62**: 15851.
- Arlery, M., Rouvière, J.L., Widmann, F., Daudin, B., Feuillet, G. and Mariette, H. (1999). Quantitative characterization of GaN quantum-dot structures in AlN by high-resolution transmission electron microscopy, *Appl. Phys. Lett.* **74**: 3287.
- Bayer, M., Stern, O., Hawrylak, P., Fafard, S. and Forchel, A. (2000). Hidden symmetries in the energy levels of excitonic 'artificial atoms', *Nature* **405**: 923.
- Bayer, M., Hawrylak, P., Hinzer, K., Fafard, S., Korkusinski, M., Wasilewski, Z.R., Stern, O. and Forchel, A. (2001). Coupling and Entangling of Quantum States in Quantum Dot Molecules, *Science* **291**: 451.
- Bergmann, K., Theuer, H. and Shore, B.W. (1998). Coherent population transfer among quantum states of atoms and molecules, *Rev. Mod. Phys.* **70**: 1003.
- Beschoten, B., Johnston-Halperin, E., Young, D.K., Poggio, M., Grimaldi, J.E., Keller, S., DenBaars, S.P., Mishra, U.K., Hu, E.L. and Awschalom, D.D. (2001). Spin coherence and dephasing in GaN, *Phys. Rev. B* **63**: 121202.
- Biolatti, E., Iotti, R.C., Zanardi, P. and Rossi, F. (2000). Quantum Information Processing with Semiconductor Macroatoms, *Phys. Rev. Lett.* **85**: 5647.
- Biolatti, E., D'Amico, I., Zanardi, P. and Rossi, F. (2002). Electro-optical properties of semiconductor quantum dots: Application to quantum information processing, *Phys. Rev. B* **65**: 075306.
- Cingolani, R., Botchkarev, A., Tang, H., Morkoc, H., Traetta, G., Coli, G., Lomascolo, M., Di Carlo, A., Della Sala, F. and Lugli, P. (2000). Spontaneous polarization and piezoelectric field in GaN/Al_{0.15}Ga_{0.85}N quantum wells: Impact on the optical spectra, *Phys. Rev. B* **61**: 2711.
- D'Amico, I. and Rossi, F. (2001). Field-induced Coulomb coupling in semiconductor macroatoms: Application to "single-electron" quantum devices, *Appl. Phys. Lett.* **79**: 1676.
- D'Amico, I. and Rossi, F. (2002). All-Optical Single-Electron Read-Out Devices Based on GaN Quantum Dots, *Appl. Phys. Lett.*, **81**: 5213.

- De Rinaldis, S., D'Amico, I., Biolatti, E., Rinaldi, R., Cingolani, R. and Rossi, F. (2002). Intrinsic exciton-exciton coupling in GaN-based quantum dots: Application to solid-state quantum computing, *Phys. Rev. B* **65**: 081309.
- De Rinaldis, S., D'Amico, I. and Rossi, F. (2002). Exciton-Exciton Interaction Engineering in Coupled GaN Quantum Dots, *Appl. Phys. Lett.* **81**: 4236.
- Elk, M. (1995). Adiabatic transition histories of population transfer in the Lambda system , *Phys. Rev. A* **52**: 4017.
- Laine, T. A. and Stenholm, S. (1996). Adiabatic processes in three-level systems, *Phys. Rev. A* **53**: 2501.
- Findeis, F., Baier, M., Zrenner, A., Bichler, M., Abstreiter, G., Hohenester, U. and Molinari, E. (2001). Optical excitations of a self-assembled artificial ion, *Phys. Rev. B* **63**: 121309.
- Finley, J.J., Skalitz, M., Arzberger, M., Zrenner, A., Böhm, G. and Abstreiter G. (1998). Electrical detection of optically induced charge storage in self-assembled InAs quantum dots, *Appl. Phys. Lett.* **73**: 2618.
- Gurvitz, S. A. (1997). Measurements with a noninvasive detector and dephasing mechanism, *Phys. Rev. B* **56**: 15215.
- Hawrylak, P., Narvaez, G.A., Bayer, M. and Forchel, A. (2000). Excitonic Absorption in a Quantum Dot, *Phys. Rev. Lett.* **85**: 389.
- Hohenester, U., Troiani, F., Molinari, E., Panzarini, G. and Machiavello, C. (2000). Coherent population transfer in coupled semiconductor quantum dots, *Appl. Phys. Lett.* **77**: 1864.
- Korotkov, A. N. (1999). Continuous quantum measurement of a double dot, *Phys. Rev. B* **60**: 5737.
- Korotkov, A. N. (2001). Selective quantum evolution of a qubit state due to continuous measurement, *Phys. Rev. B* **63**: 115403.
- Pazy, E., D'Amico, I., Zanardi, P. and Rossi, F. (2001). Storage qubits and their potential implementation through a semiconductor double quantum dot, *Phys. Rev.B* **64**: 195320.
- Shnirman, A. and Schön, G. (1998). Quantum measurements performed with a single-electron transistor, *Phys. Rev. B* **57**: 15400.
- Tanamoto, T. (2000). Quantum gates by coupled asymmetric quantum dots and controlled-NOT-gate operation *Phys. Rev. A* **61**: 22305.
- Widmann, F., Simon, J., Daudin, B., Feuillet, G., Rouvire, J.L., Pelekanos, N.T. and Fishman, G. (1998). Blue-light emission from GaN self-assembled quantum dots due to giant piezoelectric effect, *Phys. Rev.B* **58**: 15989.
- Widmann, F., Daudin, B., Feuillet, G., Samson, Y., Rouvire, J.L. and Pelekanos, N. (1998). Growth kinetics and optical properties of self-organized GaN quantum dots, *J. Appl. Phys.* **83**: 7618.

Index

- acoustic phonons, 24
all-optical control, 2
all-optical implementations, 251
artificial atoms, 8
atomic physics, 2, 250
Auger effect, 28, 39
autoionization, 23
- bandgap renormalization, 36
biexciton, 157, 158, 164, 170
biexcitonic shift, 258, 259, 262
binding energy, 159
blinking effect, 3, 6
Bohr radius, 152
Boltzmann equation, 183
- carrier-carrier interaction, 32
charge fluctuations, 222
classical computing, 2
classical devices, 183
coherence lifetime, 18
coherent carrier control, 102, 223
coherent control, 103
computational degrees of freedom,
 251
configuration interaction, 162
confinement length, 153
confining potential, 9
correlation, 158, 159, 170, 172
correlations, 167
Coulomb correlation, 157
Coulomb interaction, 33, 151
- decoherence, 52, 250, 252, 260, 262
decoherence mechanisms, 4
decoherence time, 101
density matrix, 18, 183, 223
dephasing, 102
diamagnetic shift, 14
dot ensemble, 7
- effective-mass approximation, 152
electron-hole dipole, 13
electron-hole exchange, 20
electron-phonon interaction, 2
electronic coupling, 3
electronic properties, 2
empirical tight binding, 9
entanglement, 158, 184, 250, 261
envelope function, 157
envelope-function approximation, 9,
 152
excitation-induced dephasing, 103
exciton, 152, 156, 158, 164, 170
exciton binding energy, 33
exciton-exciton coupling, 252
exciton-exciton interaction, 35
excitonic dipole, 102
- far-infrared magnetoabsorption, 28
Fermi Golden Rule, 25, 28, 40
fidelity, 223
Fock-Darwin states, 11
four-wave mixing, 25, 222
Fröhlich coupling, 28

- Ga(In)As/GaAs, 2
- GaAs, 7, 251
- GaN, 251
- GaN-based quantum dots, 285
- heavy hole, 11
- Huang–Rhys model, 31
- InAs, 7
 - inelastic interactions, 184
 - inhomogeneous broadening, 7, 19
 - inter-band coherence, 32
 - inter-band optical transitions, 251
 - inter-dot coupling, 151, 167, 176
 - interface quantum dots, 103
- light hole, 11
- linear-excitation regime, 36
- LO phonons, 22
- macroatomic model, 2, 8
- macroatoms, 2, 251, 252, 278
- macromolecules, 252, 258, 262, 268, 278
- magnetic field, 156
- magnetic-resonance spectroscopy, 250
- mass-reversal effect, 11
- monolayer fluctuation, 153
- multiexciton, 159
- multiexcitons, 160, 161, 165
- multiphonon sidebands, 31
- nanocrystallites, 3
- non-equilibrium phonons, 236
- non-exponential decay, 222
- non-Lorentzian lineshape, 222
- open systems, 250
- optical properties, 2
- optical spectroscopy, 162–165, 173
- optoelectronics, 51
- orbital Zeeman effect, 14
- parabolic potential, 10
- Pauli exclusion principle, 37
- phonon bottleneck, 28, 184
- phonon-induced decoherence, 223
- phonon-wave packets, 223
- phonons, 2
- photoexcited carriers, 223
- photoluminescence, 19
- photoluminescence excitation, 20
- piezoelectric effect, 5
- piezoelectric fields, 9
- polarization, 222
- polaron, 28, 184
- pseudopotentials, 9
- pure dephasing, 31, 223
- quantum algorithms, 249
- quantum computation, 2, 249
- quantum computer, 249
- quantum computing, 1
- quantum confinement, 52, 153, 154, 158, 163, 164
- quantum correlations, 250
- quantum cryptography, 35
- quantum devices, 184
- quantum dot, 2, 251, 258, 284
- quantum evolution, 2
- quantum gates, 250
- quantum Hall effect, 14
- quantum hardware, 16, 251
- quantum information processing, 53
- quantum Monte Carlo, 33
- quantum optics, 250
- qubit, 51, 102, 158, 250, 251, 259
- Rabi oscillations, 103, 222
- radiative broadening, 17
- radiative lifetime, 17
- Raman scattering, 27
- scalability, 252
- scalable quantum gates, 103
- Schrödinger equation, 8, 9, 152
- self-organized, 2
- semiconductor laser, 102
- single-photon sources, 221
- single-QD spectroscopy, 102
- size fluctuation, 7
- size quantization, 2, 3, 8

- solid state, 2, 52
- solid-state implementations, 251
- Sommerfeld factor, 33
- spatial correlation, 151
- spectral hole burning, 29
- spectral wandering, 6
- spin degrees of freedom, 156, 251, 252, 268
- spontaneous formation, 3
- square-well potential, 10
- Stark effect, 13
- state superposition, 250
- STIRAP, 304, 305
- strain-induced alignment, 3
- strong confinement, 153
- strong-confinement regime, 223
- sub-picosecond time scale, 102, 252
- superconducting devices, 52, 251
- thermal population, 8
- trap-dot interaction, 43
- trion, 34
- two-level system, 17
- two-photon absorption, 41
- ultrafast light pulses, 102
- ultrafast optical switching, 52
- ultrashort-pulse limit, 223
- vertical confinement, 10
- wavefunction engineering, 52
- weak confinement, 153
- weak-excitation regime, 103
- wetting layer, 4, 12, 18
- zero-dimensional systems, 2